A study of low energy particles in cosmic rays

H. J. Edwards

Edwards, H. J. (1971) A study of low energy particles in cosmic rays. Doctoral thesis, Durham University.

A STUDY OF LOW ENERGY PARTICLES IN COSMIC RAYS

by

H. J. Edwards, B.Sc.

A Thesis submitted to the
University of Durham
for the Degree of Doctor of Philosophy

April, 1971

CONTENTS

ABSTRACT

A large aperture, scintillation counter telescope capable of efficient mass discrimination against muons (and protons if desired) has been operated in a search for low energy ($\beta \lesssim 0.8$), massive particles in the sea level cosmic radiation, irrespective of their charge.

In the running time, no quark candidates were detected. The rate of low velocity quarks is given with 90% confidence as

$$< 4.9 \times 10^{-10} \mathrm{cm}^{-2}\ \mathrm{sec}^{-1} \mathrm{sterad}^{-1} .$$

The limit refers to particles within well defined velocity bands, these being a function of the particle mass and charge.

Furthermore, from this search, an upper limit of $\sim 10^{-7}$ has been placed on the fraction of U particles in the primary radiation, at low energies. This limit refers to particles with mass values in the range 2 - 50 GeV/c^2. Deuterons have been detected at an intensity of,

$$(4.2^{+3}_{-2.4}) 10^{-9} \mathrm{cm}^{-2} \mathrm{sec}^{-1} \mathrm{sterad}^{-1} (\mathrm{MeV/c})^{-1} \quad \text{at} \quad 1.65\ \mathrm{GeV/c}$$

and $$(4.8^{+6.8}_{-3.3}) 10^{-10} \mathrm{cm}^{-2} \mathrm{sec}^{-1} \mathrm{sterad}^{-1} (\mathrm{MeV/c})^{-1} \quad \text{at} \quad 2.45\ \mathrm{GeV/c}$$

The fall off in the observed deuteron spectrum is consistent with that expected for deuteron production via 'pick up' processes.

For conclusive particle identification from measurements of mass, charge and sign of charge, an ideal design of magnetic spectrometer was considered, which, with a combination of momentum and time of flight measurements, gave a mass precision of 10%.

The air gap magnetic spectrometer constructed, was investigated with respect to its ability to accept and subsequently resolve some familiar, low energy (~ 0.6 GeV), massive particles in the cosmic radiation at sea level. The precision of particle mass determinations was found to be limited by the scattering contribution to the momentum precision and not by the time of flight precision.

A time of flight precision of ± 1ns was attained using a technique which incorporated two 5 cm thick, $1m^2$ area, plastic scintillators separated by 530.4 cm and each viewed edgewise on by a single 56 AVP Mullard photomultiplier, for the determination of the time of flight between the scintillators.

An upper limit of $2.2 \times 10^{-5} cm^{-2} sec^{-1} sterad^{-1}$ was placed on the tachyon flux with velocities > 1.6 c in the cosmic rays at sea level. This limit refers to tachyons able to penetrate the spectrometer and deposit > 1.8MeV in each scintillator.

PREFACE

This thesis describes the work performed by the author in the Physics Department at the University of Durham while she was a Research Student under the supervision of Dr. F. Ashton.

It describes the use of a large aperture, scintillator range telescope in searching for low energy, heavy mass particles in the cosmic radiation. The day to day operation of the scintillator range telescope and the analysis of the results of the heavy mass search have been the responsibility of the author and Dr. G. N. Kelly.

A mass spectrometer incorporating momentum, ionisation loss and time of flight measurements for conclusive particle identification, is subsequently presented in this thesis. The construction of the air gap magnetic spectrometer (e.g. optical system, alignment, electronics, etc.), the operation and analysis associated with the calibration of the spectrometer and time of flight system, in the zero field run and in the measurement of the muon spectrum, have been the responsibility of the author, with the help of Dr. N. I. Smith and Dr. G. N. Kelly in the latter stages of this work.

The work which has been published, in which the present author was a co-author, is presented below.

Evidence against the presence of U particles in the primary radiation has been published in Physical Review Letters (Ashton et al., 1968a).

Preliminary results on a search for low energy muons produced directly by neutral cosmic rays, and not referred to in this thesis, have been presented at the C.E.R.N. Neutrino Meeting and are published in the following

C.E.R.N. report (Ashton et al., 1969b). An extension and conclusion to this work was presented at the International Conference on Cosmic Rays at Budapest in August, 1969 (Ashton et al., 1969c).

The results of the low energy, heavy mass search with the scintillator range telescope have been published in Physics Letters (Ashton et al., 1969d) and presented at the Internation Conference on Cosmic Rays at Budapest (Ashton et al., 1969a).

CHAPTER 1

INTRODUCTION

1.1 The quark model and unitary symmetry

The advent of unitary symmetry and the suggestion by Sakata in 1956, that all hadrons were made up of three subnuclear particles (quarks), one of which held unit electron charge, led directly to an explanation of the known strong interaction conservation laws in charge, Q, baryon number, B and hypercharge, Y. This original quark model also led to the existence of multiplets of particle spin states that transformed into each other under the operators of the unitary group. It successfully constructed an octet of mesons with well defined Q, B, and Y content, which fitted with the observed properties of the then known mesons.

Difficulties, however, arose, when Gell-Mann (1962) and Neeman (1961) observed an octet of spin $\frac{1}{2}$ baryons, as the properties of the Sakata quarks did not enable such a prediction. As these eight baryons needed to each contain three quarks to exhibit the same quark structure under the conditions of unitary symmetry, Gell-Mann (1964) and Zweig (1964), attributed a baryon number of $\frac{1}{3}$ to the constituent quarks, to satisfy the requirement of unitary baryon number for the octet. Fractional charges of e/3, 2e/3, were consequently assigned to the quarks, the remaining quantum numbers as proposed by Gell-Mann are shown in Table 1.1.

To reconstruct the spin 0, meson octet, antiquarks were also assumed to exist.

TABLE 1.1

Quark	Charge	Strangeness	Spin	Baryon number	Mass m_q
a	+2e/3	0	$\frac{1}{2}\hbar$	1/3	m_q
b	- e/3	0	$\frac{1}{2}\hbar$	1/3	$m_q +$ 0.5 MeV/c^2
c	- e/3	+1	$\frac{1}{2}\hbar$	1/3	$m_q +$ 140 MeV/c^2

With the laws of unitary symmetry and the Gell-Mann model incorporating triplets and antitriplets of quarks as the fundamental building blocks of hadron matter, startling success was found not only in reconstructing the known multiplets and their associated Q, B, Y properties but also in predicting the baryon unitary decuplet of spin 3/2. Initially nine of the spin 3/2 states had been discovered which fitted neatly into the predicted scheme and the subsequent discovery of the tenth state, the Ω^-, was a triumph of the group theory approach. The members of each multiplet then emerged from group operations on one such member and were essentially variations of the original member, each variation being no more fundamental than the next and existing simply as a member of the multiplet. To satisfy the observed mass splitting in the multiplets, it was necessary to assure that two of the quarks were approximately of the same mass, while the third had a slightly greater mass. It follows that although SU(3) is only an approximate symmetry, it is remarkably successful in explaining the strong interaction conservation laws and the observed ordering of the hadrons into multiplets. Indeed at present, there is no definitely known hadron which does not fit into the multiplets, constructed under the laws of unitary symmetry on the assumption that hadrons consist of a minimum number of quarks.

In the simplest scheme in which the mesons are $q\bar{q}$ states and the baryons are qqq states, only singlets, octets and decuplets are allowed. In Table 1.2 the quark constituents of a few hadrons are given, a more complete list is given by Kokkedee (1969).

TABLE 1.2

Particle	Quark constituents
p	aab
n	abb
π^+	$a\bar{b}$
k^+	$a\bar{c}$

To account for the known decay modes of hadrons e.g. $n \rightarrow p + e^- + \bar{\nu}_e$ and $k^+ \rightarrow \pi^+ + \pi^o$, it is deduced that the a type quark should be stable and the b, c type quarks unstable, as shown in Table 1.3.

TABLE 1.3

Quark	Possible decay mode	Lifetime
a	stable	stable
b	$b \rightarrow a + e^- + \bar{\nu}_e$	seconds
c	$c \rightarrow b + \pi^o$	$\sim 10^{-10}$ seconds

Recently Morpurgo (1968) has reviewed the status of the fractional charge quark model with respect to its success and difficulties. Apart from the most striking success in the experimental verification of the ordering of hadrons into SU(3) multiplets, the subsequent successes are in its predictions on: the ratio of the proton to neutron magnetic moment; the branching ratios of the leptonic baryon decays; the electromagnetic properties of the baryons; and its application to high energy scattering. The most serious difficulty encountered in all quark models is that of explaining the apparent saturation of quarks. Several attempts have been made to resolve this problem, but only the experimental quark searches can conclusively answer the question as to whether quarks exist or are just a convenient mathematical fiction which facilitates the computation of the consequences of SU(3) symmetry.

To design an experiment to prove their existence depends on the precise knowledge of their mass, production cross section, and if a search is being made in the sea level cosmic radiation, their interaction properties in the atmosphere. As no such properties are known, conjecture on the values of these properties necessarily involves different types of experiments each sensitive to quarks pertaining to the assumed properties.

1.2 Quark mass estimates

An estimate of the quark mass has been made by Morpurgo (1967), from the measured average mass differences of the meson octets with different angular momentum. Assuming the q and $\bar{q}$, in the mesons, are bound in an infinitely deep spherical square well potential of radius r he finds that the energy levels are given by

$$E = \alpha \frac{25m_\pi^2}{m_q} \quad \text{where } \alpha = (3.14)^2,\ (4.5)^2,\ (5.76)^2 \text{ etc. for s, p, d, etc. states, and } r = \frac{1}{5m_\pi c}$$

However, the radius of the well is unknown, but inserting reasonable values gives the results shown in Table 1.4 for the quark mass, m_q.

TABLE 1.4

Radius of well	Mass of quark, m_q
$1/3.5\ m_\pi c$	5 GeV/c^2
$1/5m_\pi c$	10 GeV/c^2
$1/7m_\pi c$	20 GeV/c^2

1.3 Production of quarks

The most likely reactions leading to quark production are as follows:-

the production of $q\bar{q}$ pairs, via $\quad p + N \rightarrow N + N + q + \bar{q} + nB \quad$ 1.1

the dissociation of the nucleon, via $\quad p + N \rightarrow N + 3q + nB \quad$ 1.2

or $(6q + nB)$

where q is a quark, B is a boson (mainly pions), and n is an integer.

In the absence of the knowledge of the relative cross sections for equations 1.1 and 1.2, 1.1 is assumed to be the most important process for quark production in the cosmic radiation, on the basis of the smaller incident threshold energy needed in this interaction coupled with the rapidly falling proton spectrum.

Theoretical estimates for the production cross section of quarks in reactions of type 1.1 give widely differing results.

Chilton et al. (1966) have calculated the production cross section, σ_q, to vary as $\sigma_q \propto m_q^{-2}$, above the threshold, giving cross sections in the region of microbarns. On the other hand, Maksimenko et al. (1966) give statistical model arguments based on the Heisenberg-Landau theory (1956) of high energy nuclear interactions, effecting an exponential mass dependence of production cross section, of the form

$$\sigma_q \approx 1.0\, e^{-m_q/m_\pi} \text{mb}$$

for quarks of mass greater than a few GeV/c^2. Typically for $m_q =$ 3GeV/c^2 $\sigma_q \approx 10^{-7}$ mb. Hagedorn (1967) using a similar statistical model, calculates the production cross sections for hadrons existing in the ground state of a series of resonances and for those which are not. The slope of the cross section variation with quark mass is a factor of 7 greater than that due to Maksimenko et al. However both cross sections are extremely small and that of Maksimenko et al. is thought to give only a minimum estimate of the production cross section.

For incident protons of kinetic energy E the maximum quark mass that can be produced in the reaction 1.1 is $(\sqrt{\frac{E}{2} + 1} - 1)$ GeV/c^2. The maximum quark mass that can be produced at the Serpukhov accelerator is 5 GeV/c^2, at a maximum incident energy of 70 GeV. As no quarks have been found at Serpukhov to a level lower than that predicted by statistical theory, a lower limit is implied on the quark mass of 5 GeV/c^2.

If the predicted quark production cross sections via the statistical model are reliable, then the possibility of experimentally detecting quarks with mass greater than 5 GeV/c^2 in the cosmic radiation is particularly weak. However, while the calculations of Hagedorn and Maksimenko et al. are in good agreement with the cross sections for particle, antiparticle pair production at the accelerators, the fact that the nature of high energy nuclear interactions may be substantially different has been suggested by Adair and Price (1966).

To evaluate the most likely mechanism by which quarks are produced in high energy interactions, it is necessary to consider what is known about the structure of the proton. Electron scattering experiments show that the charge on the proton is not concentrated at a point, but occupies a sphere of radius about 1 fermi. The finite size of the proton is thought to be due to Yukawa interactions of the type

$$p \rightleftharpoons n + \pi^+$$

or rather

$$a \rightleftharpoons b + \pi^+$$

where p, n refer to the proton and neutron, and a,b to the quarks. As most collisions are peripheral it would therefore seem that the most likely quark production channel is a virtual π-π collision, so that $q\bar{q}$ pairs are produced in the same way as e^+e^- pairs in the collisions of high energy charged particles. The Feynman diagram for $q\bar{q}$ production by this channel is shown in Figure 1.1. If this is so, the maximum quark mass that can be produced by protons of kinetic energy E GeV is $\left\{\sqrt{\frac{E}{2}+1} - 1\right\} m_\pi$ GeV/c^2 where m_π is in GeV/c^2. For E = 70 GeV this gives $m_{q_{max}} = 0.7$ GeV/c^2, which is considerably lower than the value of 5 GeV/c^2 found previously. Physically the reason is that, whereas the total energy of the colliding nucleons in the centre of mass system was previously available for $q\bar{q}$ production, with the above mechanism this is reduced by a factor of $\frac{m_\pi}{m_p} \approx 15\%$.

This idea was originally introduced by Peters (1965) in terms of the favoured fireball model of high energy interactions (Cocconi, 1965). Peters suggested that the two fireballs observed in interactions at energies greater than 100 GeV were an excited baryon-antibaryon pair produced in the manner depicted in Figure 1.1. As the threshold energy needed by a proton to produce a proton, antiproton pair, of mass m_p, in a virtual π-π collision is

$$2\left\{\left(\frac{m_p}{m_\pi}\right)^2 - 1\right\} \text{ GeV}$$

then above 91 GeV $p\bar{p}$ pairs will be produced in almost every peripheral collision. This threshold value agrees with the threshold of fireball observation and the model thus explains the large number of high energy nucleons which are known to accompany extensive air showers.

It would seem not unreasonable that $q\bar{q}$ pairs would be produced rather than excited $p\bar{p}$ pairs, once the energy threshold for $q\bar{q}$ production is exceeded. If this is true, then $q\bar{q}$ pairs may be produced in almost every p-p collision at extremely high energies. The future for cosmic ray quark

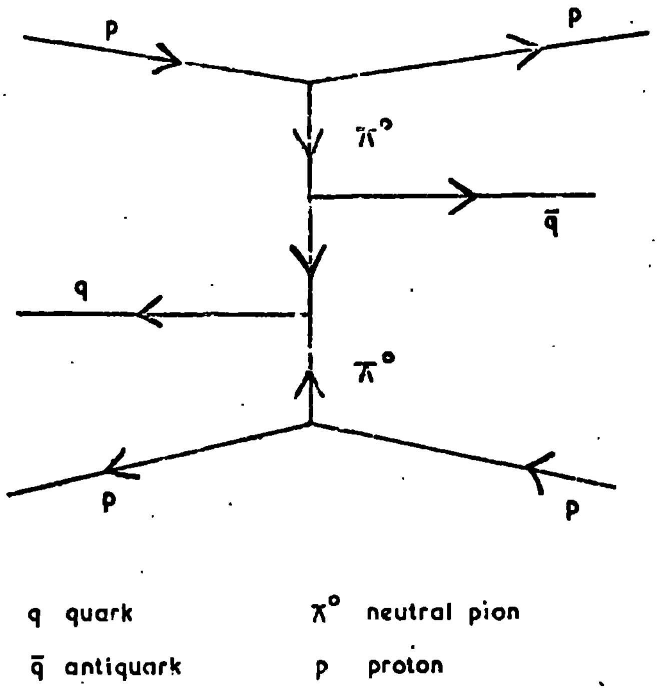

Fig 1.1 Feynmann diagram for quark, antiquark production in a proton-proton collision.

searches brightens accordingly.

It is to be noted that as the $q\bar{q}$ pairs would originate from a virtual π-π collision, their production would not inhibit the formation of extensive air showers at high energies. A forward excited nucleon, carrying most of the incident energy, would still be created and the decay pions from this are more important than fireball pions in generating an extensive air shower. It would seem likely that if the events observed by McCusker and Cairns (1969) close to air shower cores, are really 2/3e quarks, then they have been produced in the above way.

1.4 Propagation of quarks through the atmosphere

A reasonable model of quark interaction with matter in traversing the atmosphere has been considered by Ashton (1965) and shows that if the quark interaction inelasticity is 0.5, then even in the vertical direction, the stable quark component is moderated from relativistic velocities to sub-relativistic velocities at sea level.

1.5 The integral electron charge, quark model

Shortly after the initial Gell-Mann proposal of quarks with fractional electron charge, attempts by several workers (Bacry et al., 1964, and Gursey et al., 1964) have been made to overcome the perhaps distasteful notion of fractional electron charge. Bacry et al. suggest the existence of the hadron states as being composites of two fundamental triplets, termed 'T trions' and 'Ⓗ trions' of unitary baryon number and exhibiting integral electron charge.

From the experimental point of view, quarks of either integral or fractional charge must be searched for.

1.6 Positive results of heavy mass searches in the cosmic radiation

Recent results from the heavy mass searches have indicated the existence of:-

1. Fractionally charged particles (McCusker and Cairns, 1969, followed by Chu et al., 1970) in air shower cores.
2. Heavy mass, relativistic particles of integral charge, delayed with respect to air showers and having interaction lengths 2 to 3 times the pion interaction length (Dardo et al., 1968), interpreted as the stable member of the fundamental triplet.
3. The U particle proposed by Callan and Glashow (1968) as being massive (several GeV/c^2), weakly interacting and of integral charge.

1.7 The present heavy mass searches

Consideration of the possible production and interaction properties of quarks (or triplets) with fractional (or integral) charge, and the recent successes in the heavy mass searches, instigated the experiment described in Chapters 2 and 3 of this thesis. The experiment, comprising of a large aperture, scintillator range telescope, was designed to search for a flux of low energy ($\beta \leq 0.8$), massive ($\gtrsim 1.3$ GeV/c^2) cosmic ray particles at sea level, irrespective of their charge. The particles are identified by their mass and charge, determined from an ionisation, residual range technique.

Subsequently an ideal design and the performance of a magnetic spectrometer and time of flight system, for conclusive particle identification, is described in the remaining chapters 4-8 of this thesis. The improvements of the latter technique, lie in its ability to determine mass, charge and sign of charge, and in its suitability in detecting nuclear interacting particles.

CHAPTER 2

SELECTION OF HEAVY MASS PARTICLES AND MASS DETERMINATION BY AN IONISATION, RESIDUAL RANGE TECHNIQUE

2.1 Introduction

The success of the theoretical concept (see review by Morpurgo, 1968) involving heavy mass quarks as the constituents of baryons and mesons, has led to numerous experiments, all searching for massive particles of either fractional or integral charge.

However, as the results from the accelerating machines implied that the quark mass was greater than the maximum kinematically possible from the available proton accelerator energies, attention was turned to searches in the cosmic radiation, in which no problem of limited incident proton energies existed. Then, to compare with the results of the accelerators, the cosmic ray experiments looking for the production of quark masses > 5 GeV/c^2 needed to have large apertures and long running times. This is a consequence of the integral energy spectrum of primary protons (falling as $E_p^{-1.5}$) reflecting into the production intensity of quarks with mass m_q, approximately as m_q^{-3}.

The methods employed to search for quarks in the cosmic radiation at sea level, are dependent on the charge, mass, production mechanism and interaction properties of quarks with matter in traversing the atmosphere. For this reason the methods can be separated into the following categories:

1. Experiments searching for relativistic, fractionally charged particles.
2. Experiments searching for delayed particles in air showers.
3. Searches for sub-relativistic massive particles.

A detailed survey on the results obtained from experiments of all three types by different research groups has been completed by Kelly (1969). Subsequent to this survey an experiment to search for,

4. fractionally charged particles in air shower cores has been made by McCusker and Cairns (1969).

Only experiments performed by Dardo et al. (1968) (of type 2) and McCusker and Cairns (1969), followed by Chu et al. (1970), (both of type 4) have so far yielded any positive indication as to the existence of unknown massive particles (quarks) in the cosmic radiation.

Consideration of the velocity distribution expected for quarks at sea level by Ashton (1965), under the assumption of a quark interaction inelasticity of 0.5, suggested that under such a mode of interaction the quarks would have sub-relativistic velocities at sea level.

The scintillator range telescope, described in this chapter, was designed to search for low velocity ($\beta \leq 0.8$), heavy mass particles irrespective of their charge, with a detector of a much larger aperture than had previously been used. Identification of the heavy mass particles is deduced from determinations of their mass and charge, and selection of these events for study in background free conditions is by a threshold velocity, residual range technique. The mode of mass and charge determination by an ionisation, residual range technique is given. The validity of this analysis and the mass resolutions attainable with such an instrument, are studied in a preliminary experiment using low energy, sea level protons to trigger the telescope.

2.2 Selection of heavy mass particles

The selection of heavy mass particles by the scintillator range telescope, shown in Figure 2.1, is governed by a threshold velocity, residual range technique, as originally suggested by Ashton (1965). The principle of this method and the important quantities governing the design of such a telescope can be deduced from a consideration of the following expression,

$$R(M,Z,\beta) = \frac{M}{M_p} \times \left(\frac{Z_p}{Z}\right)^2 \times R_p(M_p, Z_p, \beta) \qquad (2.1)$$

where $R(M,Z,\beta)$ is the range of a particle of rest mass Mc^2, charge Ze and velocity βC, and where the suffix p refers to a proton and e is subsequently termed the electron charge. Hence if a demand of $\beta < \beta_T$ is placed on incident particles, and a further demand that they must traverse at least an amount of absorber R_T, then the only particles selected are those satisfying

$$\frac{M}{M_p} \times \left(\frac{Z_p}{Z}\right)^2 > \frac{R_T}{R_p(M_p, Z_p, \beta_T)} \qquad (2.2)$$

Choice of β_T and R_T enables an effective means of mass discrimination against muons (and protons if desired), and are the important parameters in the design of a telescope when studying heavy mass particles of low intensity levels in the cosmic radiation.

As the Cerenkov counters are far superior to the scintillation counters in the region of the threshold, for use as velocity selectors, the former are used for velocity discrimination at a value, β_T. The limiting residual range R_T, which the particles must traverse, is provided by the material beneath the Cerenkov counters in Figure 2.1.

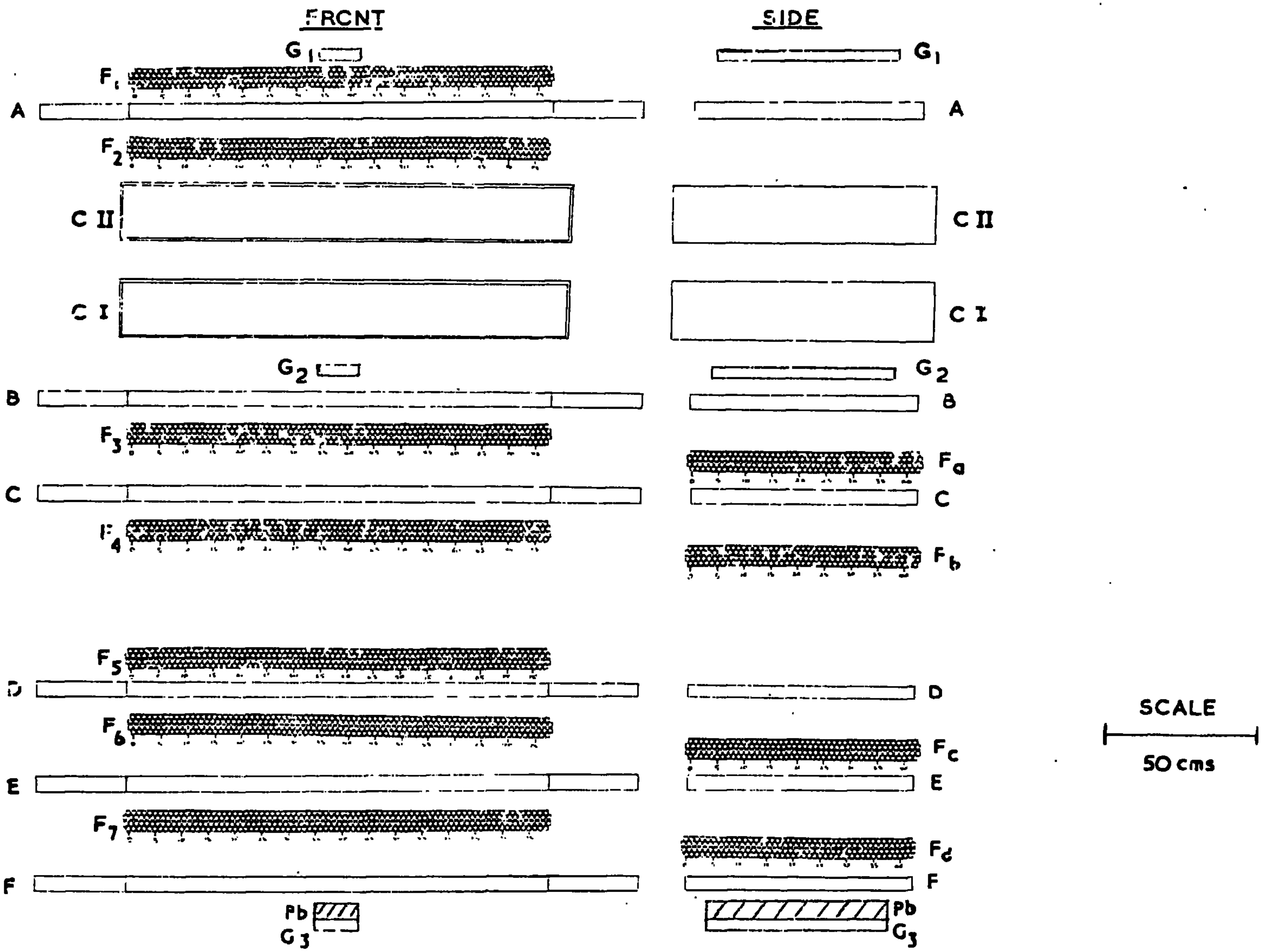

Figure 2.1 The proton telescope: A,B,C,D,E,F are plastic scintillation counters (NE102A); CII,CI are water Cerenkov counters; F_1-F_7 and F_a-F_d are neon flash tube trays; G_1,G_2,G_3 are geiger counter trays.

Variation of β_T and R_T in equation 2.2 enables mass discrimination over a range of several GeV/c^2 as shown in Figure 2.2, where the Cerenkov counter response is plotted as a function of the residual range of a particle, for various particle masses. To reject muons and pions then, the Cerenkov pulse height must be chosen to be less than 0.55 E_c for a limiting residual range, $R_T = 40$ gcm^{-2} water equivalent. E_c is the median muon pulse height obtained in a G calibration of the telescope (see Section 2.5).

2.3 Mass determination

The rate of energy loss from a particle, providing its mass is much heavier than the electron mass, has been given as a good approximation by Rossi (1952) as

$$-\frac{dE}{dx} = \frac{2Cm_e c^2 z^2}{\beta^2}\left\{ \ln\left(\frac{4\, m_e^2\, c^4 \beta^4}{(1-\beta^2)^2\, I^2(Z)}\right) - 2\beta^2 \right\} \qquad (2.3)$$

$$= z^2 D\,(\beta)$$

where m_e is the electron mass, ze is the charge of the particle, M is the particle mass and β the particle velocity.

$C = 0.150\,\frac{Z}{A}$ cm^2/g where Z and A are the atomic number and atomic weight of the medium, respectively, I(Z) is the average ionisation potential of the medium.

Writing $E = (\gamma-1)Mc^2$ then $dE = Mc^2\,\beta(1-\beta^2)^{-3/2}\,d\beta$ and substituting into equation 2.3 one can write

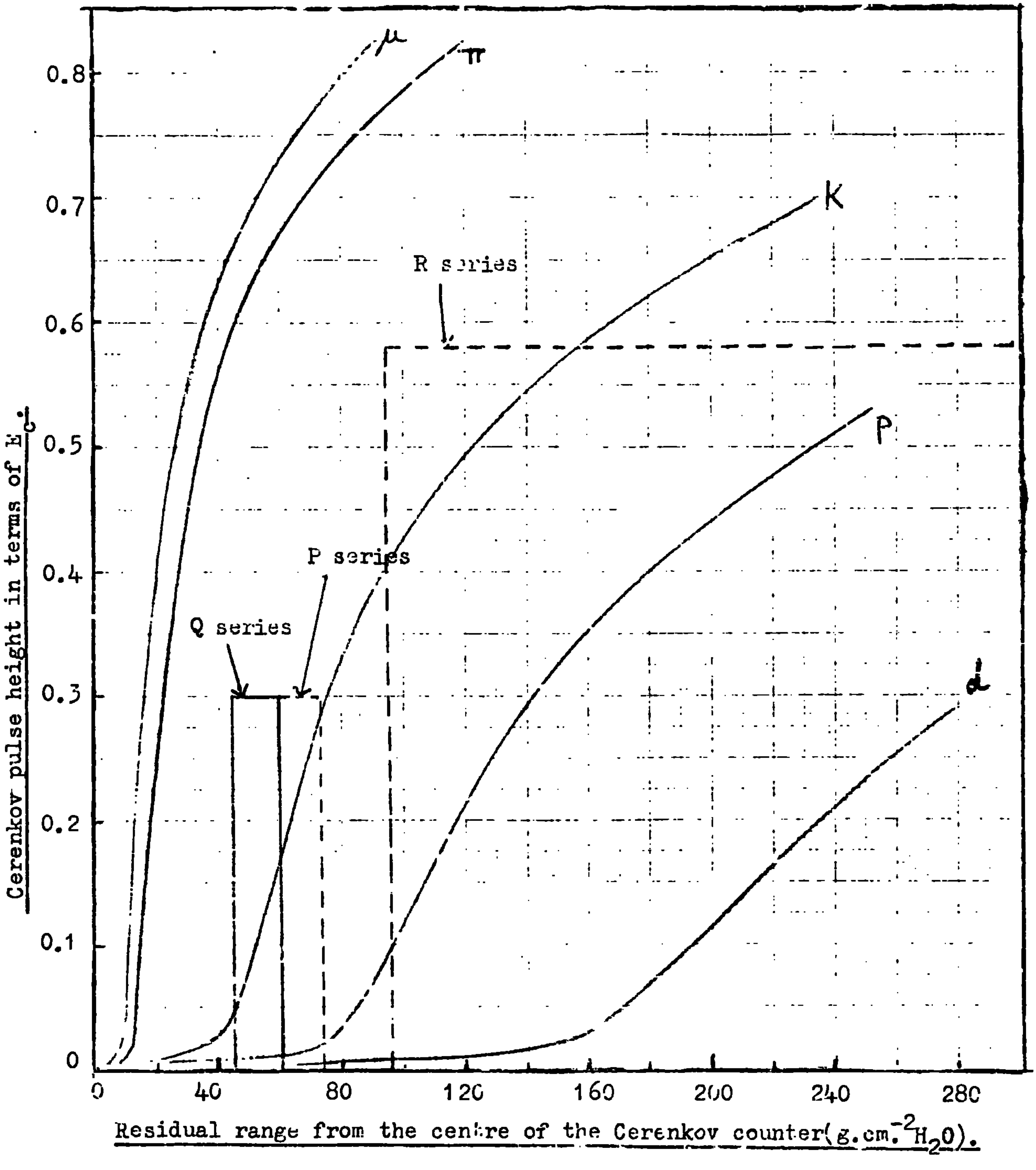

Figure 2.2 Cerenkov pulse height as a function of residual range for particles of different mass, showing the acceptance criteria used in the three series of measurements.

$$\int_0^R dx = \int_0^\beta \frac{\beta}{(1-\beta^2)^{3/2}} \times \frac{Mc^2}{z^2} \times \frac{1}{D(\beta)} d\beta = \frac{Mc^2}{z^2} \times f(\beta)$$

$$R = \frac{Mc^2}{z^2} f(\beta) \qquad \text{where} \quad f(\beta) = \int_0^\beta \frac{\beta}{(1-\beta^2)^{3/2}} \frac{d\beta}{D(\beta)} \qquad (2.4)$$

From equation 2.4, the particle mass is determined if the velocity, β, charge, ze, and residual range, R, of a particle are known.

For a particle traversing a scintillator range telescope, such as the type depicted in Figure 2.1, its residual range can be written as,

$$R = R_i + R_o \qquad (2.5)$$

where R_i is the amount of absorber between the point at which its velocity, β_i, is determined and the bottom of the telescope, and R_o is the residual range of the particle on reaching the bottom of the telescope. From equation 2.5, provided R_o is known, a measurement of the particle velocity at any point in the absorber enables the mass to be determined, as if $z = 1$ then

$$R_o + R_i = Mc^2 \; f(\beta_i) \qquad (2.6)$$

If n measurements ($n \geqslant 2$) are made of the particle velocity at known positions in the absorber, the mass together with the residual range R_o can be obtained from the best fit to n simultaneous equations each containing two variables.

A plot of R_i against $f(\beta_i)$ is a straight line of slope Mc^2 and intercept $- R_o$.

2.4 Basic design of the range telescope

In the scintillator range telescope shown in Figure 2.1, the six NE102A plastic scintillation counters A,B,C,D,E,F are used as velocity sensitive detectors separated by suitable amounts of absorber. These plastic scintillators afford good resolutions and facilitate calibration in a non-monoenergetic cosmic ray beam due to the negligible logarithmic rise in energy loss.

The Cerenkov counters CI, CII were included initially to provide a means of mass discrimination as discussed in Section 2.2. Far more important is the determination of the particle velocity in the Cerenkov counters, which in conjunction with the scintillators gives information on the charge of a particle, provided the velocity is greater then the Cerenkov threshold.

The seven neon flash tube trays $F_1 - F_7$ in the front elevation and the four trays $F_a - F_d$ in the side elevation essentially give visual confirmation of the interpretation of the scintillation and Cerenkov counter responses. They confirm the presence of a single penetrating particle as well as defining the position of each trajectory in the front and side elevations. This enables correction factors to be applied for non-uniformities over the large area scintillation and Cerenkov counters.

There are also three trays of Geiger counters G_1, G_2, G_3, in Figure 2.1, each containing four counters, forming a telescope about the centre of the main telescope where the bottom tray is shielded by lead.

The experimental conditions of the scintillator range telescope, briefly recounted here, have been more fully described by Kelly (1969), where detailed consideration of the three detector types is given. The design and properties of the scintillation counters and neon flash tubes have also been given by Ashton et al. (1968) and those of the Cerenkov counters by Ashton and Kelly (1969).

2.5 Determination of the particle velocity

As the pulse height from a scintillation (and Cerenkov) counter is proportional to the amount of energy deposited, the velocity of a particle travelling through a scintillation (or Cerenkov) counter, can be deduced from the known variation of energy loss with particle velocity, together with a calibration of the counter.

The predicted variations of average ionisation energy loss (Sternheimer 1953 and 1956) and the most probable ionisation energy loss (Symon , 1948) as a function of β, are shown in Figure 2.3. These curves apply for a heavy particle traversing a 5 cm thick plastic scintillator (NE 102A). The latter curve, drawn under the assumption of protons being the ionising particle, is only valid for $\beta > 0.59$. The rapid decrease in the maximum transferable energy from a proton to an electron at values of $\beta < 0.9$, results in only 0.5% difference between the average and the most probable energy loss curves in the lower velocity regions. As the treatment by Symon for the most probable energy loss does not hold for $\beta < 0.59$, the average energy loss deduced by Sternheimer, was considered as a good approximation to the observed energy loss variation with β, in such a scintillator.

The variation of the Cerenkov counter response as a function of the velocity at the centre of the counter is shown in Figure 2.4, calculated under the assumption that the penetrating particles are protons and considering contributions from the water, Perspex container and knock-on electrons. In the lower velocity regions the response for lighter particles will deviate slightly from this curve, due to their more rapid change in velocity over the vertical length of the counter.

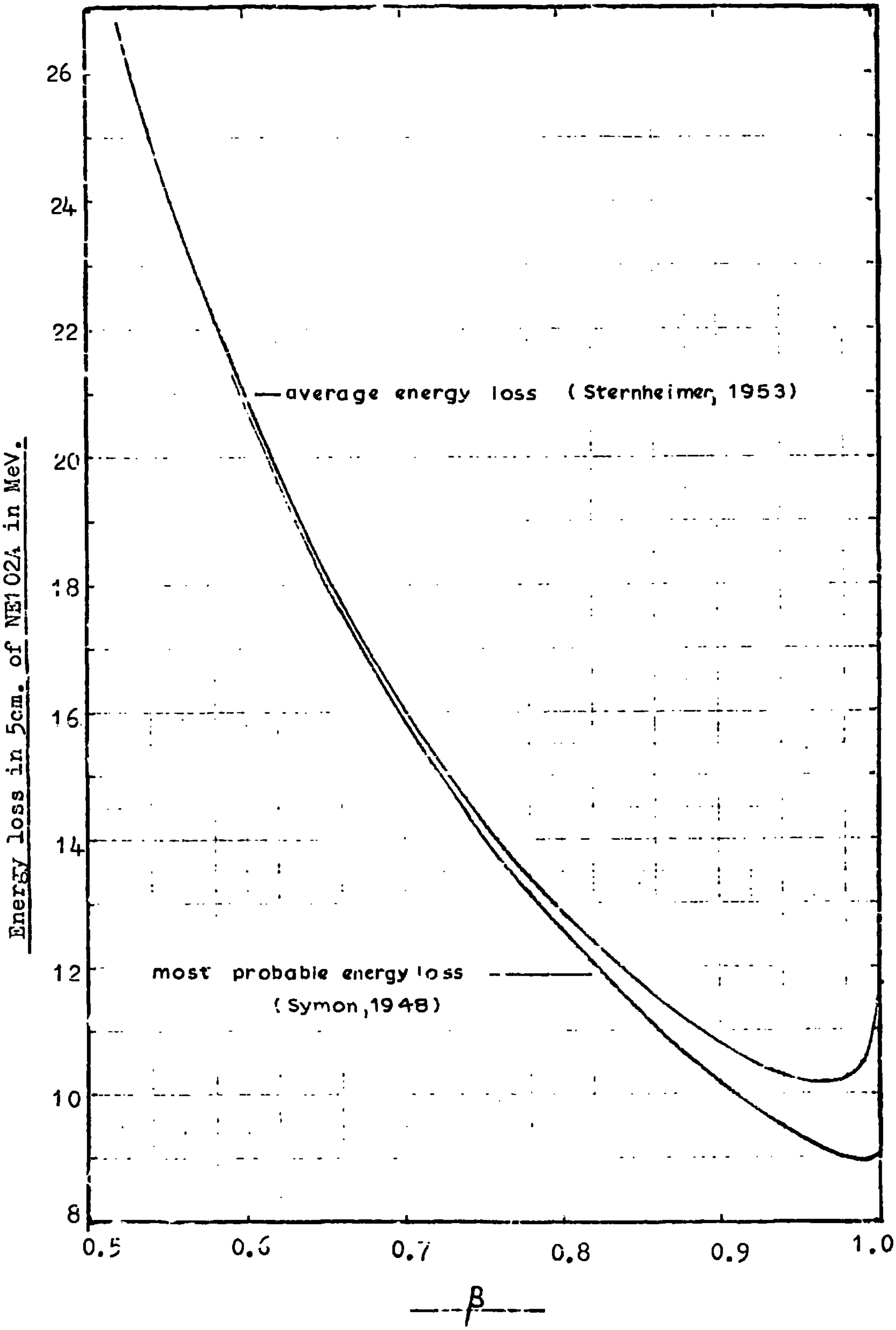

Figure 2.3 The average(upper curve) and most probable(lower curve) energy loss in 5cm. of NE102A as a function of the velocity of the incident particle.

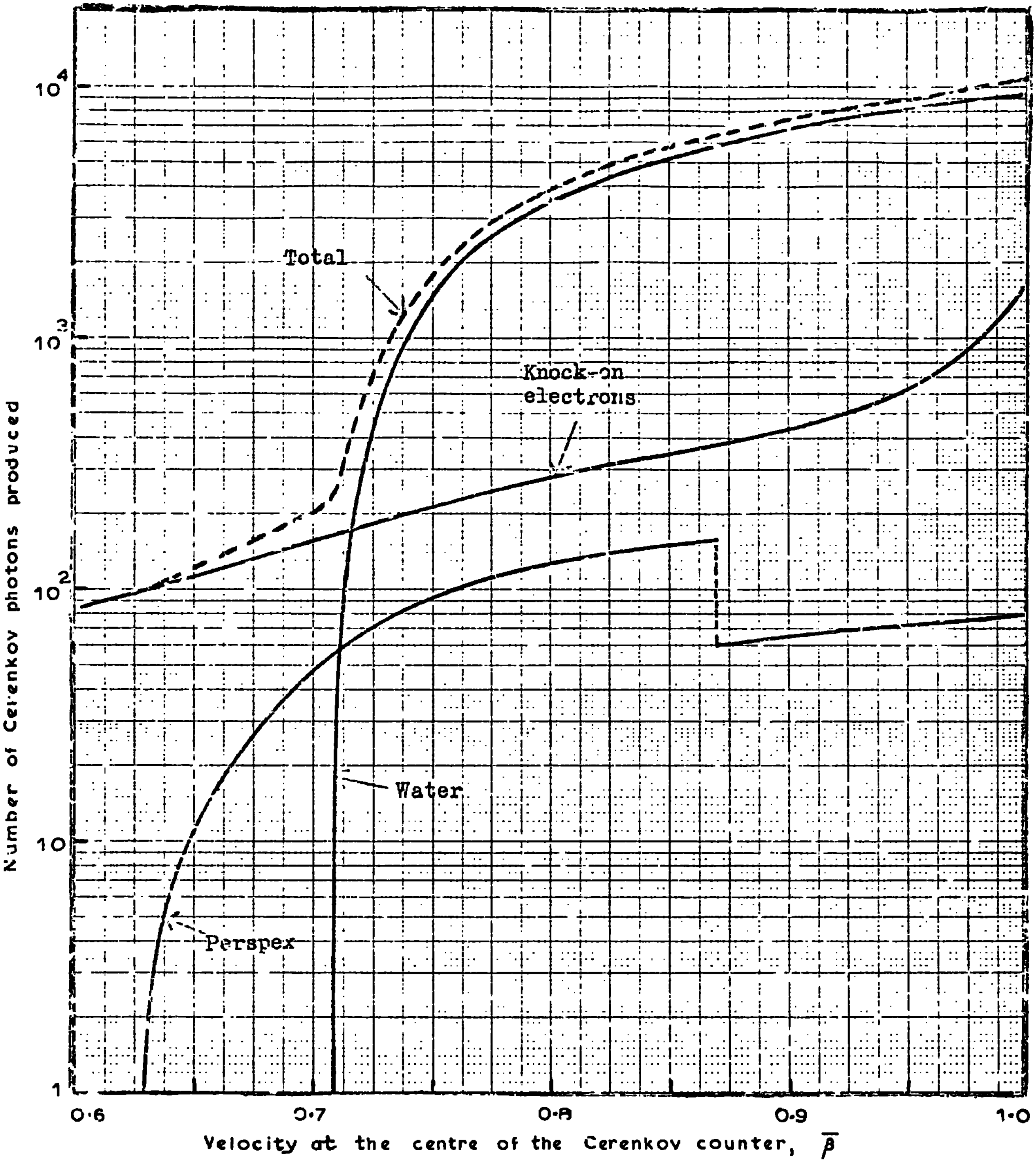

Figure 2.4 The theoretical velocity response of the Cerenkov counters showing the relative contributions from the water, Perspex and knock-on electrons as well as the sum of all three. The curves were evaluated for protons having a velocity, $\bar{\beta}$, at the centre of the counter and hence they would be slightly different in the threshold region for other particles.

Calibration of the scintillation and Cerenkov counters with particles of known velocity, was achieved by selecting muons to traverse within ± 7cm of the centre of the counters by means of the Geiger telescope shown in Figure 2.1 as G_1, G_2, G_3. The presence of the lead above G_3 ensured a minimum muon momentum required to traverse the telescope such that $\beta > 0.98$ in any of the scintillators or Cerenkov counters, thus embracing the region over which the responses for these detectors were fairly uniform, as Figures 2.3 and 2.4 indicate. This was termed a G calibration from which the typical pulse height distributions shown in Figures 2.5 and 2.6 were obtained with the relevant properties given in Table 2.1.

TABLE 2.1

Properties of the muon pulse height distributions	Scintillation counter	Cerenkov counter
Full width of half height of pulse height distribution obtained in a G calibration	25%	35%
Number of photoelectrons collected for a (β=1) particle in a G calibration deduced from a method due to Ashton et al. (1965a)	220	120

The only likely contamination of the muon calibration flux is an estimated negligible contribution of 0.5% from the proton flux.

The most probable pulse height E_s, of the distribution in Figure 2.5, observed in each of the scintillators during a G calibration has been calculated by Kelly (1969) to correspond to an energy deposit of 9.055 MeV.

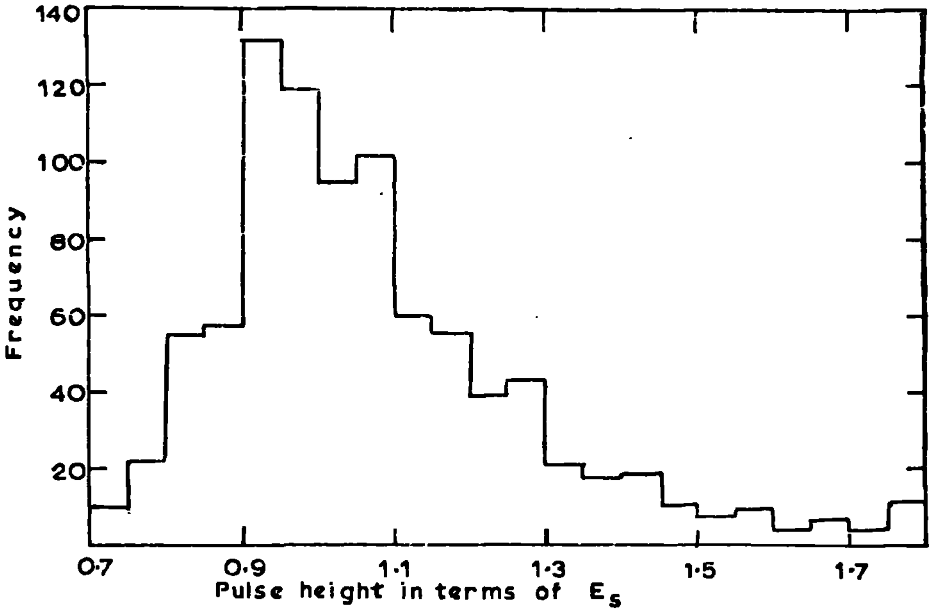

Figure 2.5 Pulse height distribution in a scintillator produced by relativistic muons in a G calibration. E_s is the most probable pulse height of the distribution.

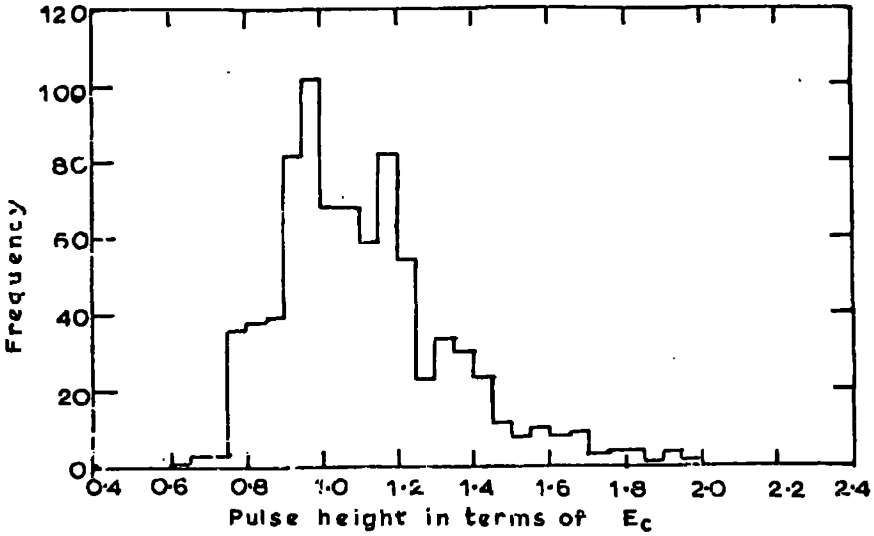

Figure 2.6 Pulse height distribution in a Ceronkov counter produced by relativistic muons selected in a G calibration. E_c is the median pulse height of the above distribution.

In the absence of any theory of most probable Cerenkov response as a function of velocity, the median pulse height, E_c, of the distribution obtained for each counter in a G calibration, is taken to be equal to the response in Figure 2.4 for $\beta=1$, this corresponding to the response for muons of momenta 2 GeV/c, the median momentum in a G calibration.

The velocity of a particle traversing a scintillator (or Cerenkov counter) can thus be evaluated from the measured pulse height relative to the most probable pulse height, E_s (or E_c), in that counter and the energy loss curve in Figure 2.3 (Figure 2.4) where E_s (E_c) refers to the case of $\beta=1$.

2.6 Normalisation of the telescope material

To simplify the mass determination from equation 2.6 in a range telescope containing a variety of materials, it is convenient to normalise all the constituent materials to a standard material, from a consideration of their relative stopping powers.

The normalisation factors were calculated by comparing range values from range energy tables (Serre, 1967) for the constituent materials over energy ranges appropriate to the experimental conditions. The normalisation factor, N, for each constituent material with respect to water is given by:

$$N = \frac{[R_p(600\text{ MeV}) - R_p(120\text{ MeV})]_{\text{water}}}{[R_p(600\text{ MeV}) - R_p(120\text{ MeV})]_{\text{material}}}$$

and is tabulated in Table 2.2 for the various telescope materials.

TABLE 2.2

Material	N
Water	1.00
Soda Glass	0.83
NE 102A	0.99
Perspex	0.97
Aluminium	0.78
Wood (Cellulose)	1.10
Iron	0.69

The range in gcm^{-2} of water equivalent from the top of the telescope to any point part-way down, was evaluated from normalisation of the constituent parts of the telescope by the appropriate factor N.

2.7 Evaluation of f(β)

The variation of f(β) with β, shown in Figure 2.7, was determined from the proton range-energy tables for water, as given by Serre, substituted into equation 2.6, i.e.

$$f(\beta) = \frac{R}{M_p c^2}$$

for a proton of mass M_p and residual range R at a velocity β.

2.8 Operating conditions of the scintillator range telescope in a preliminary proton experiment

In a preliminary experiment, the telescope shown in Figure 2.1 was used

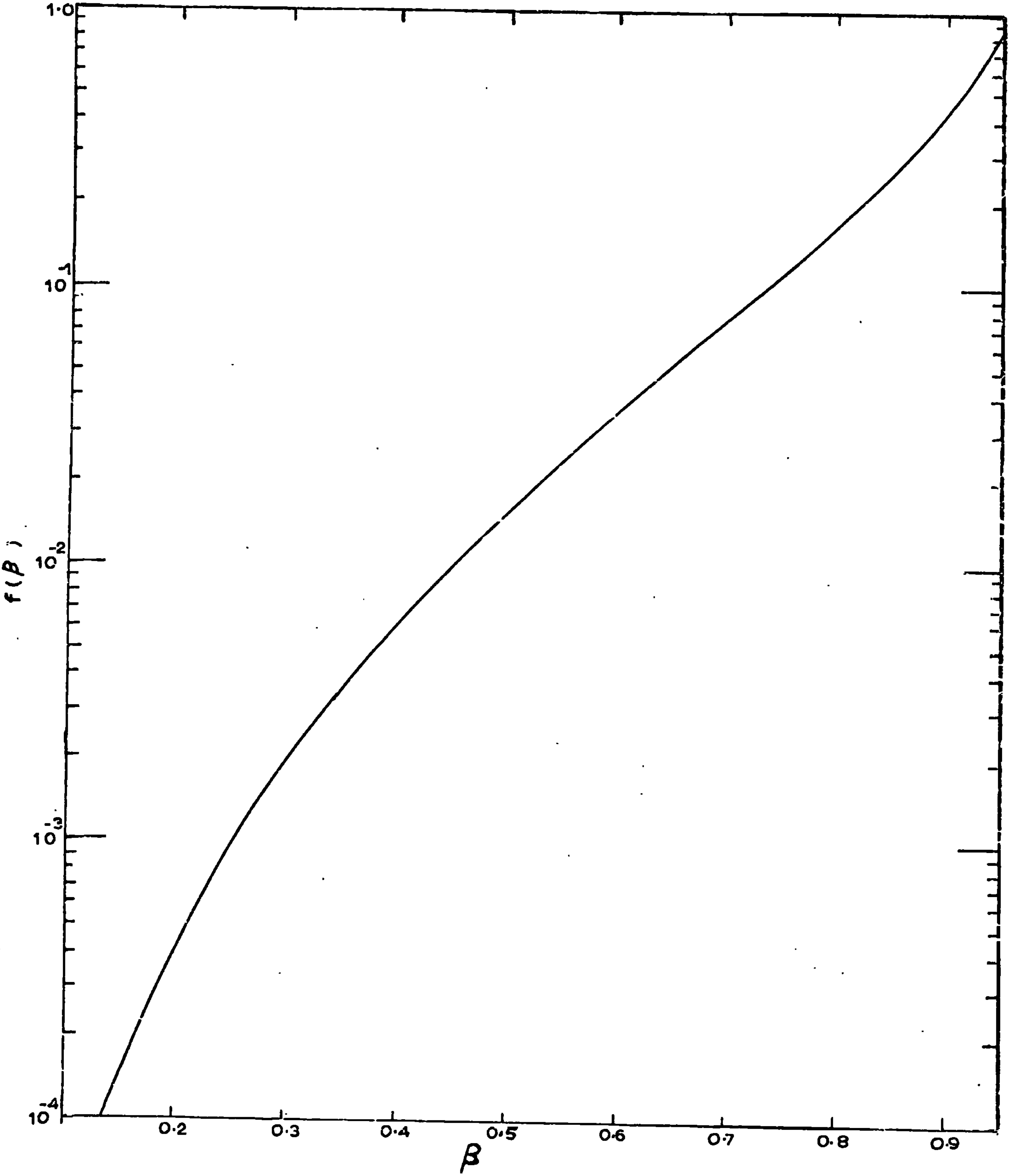

Figure 2.7 The variation of the function $f(\beta)$ for water with β .

to select low energy particles of mass values greater than $\sim$ 300 MeV/c^2 (i.e. mainly protons) by a suitable choice of R_T and β_T to satisfy equation 2.2.

Three series of measurements, P, Q, R, were made in this preliminary experiment, each defining different values of minimum residual range, R_T. The P and Q series selected particles to stop in the region E, F_7, F_d, and D, F_6, F_c, respectively, while the R series selected particles penetrating the whole telescope. The appropriate discrimination levels used in the Cerenkov counter, for each of these series, such that masses $\lesssim$ 300 MeV/c^2 were rejected, are indicated on Figure 2.2. Selection of the desired particles was carried out by Rutherford fast electronic logic. An example of the P series is given in Figure 2.8, where a coincidence ABCDE $\bar{F}$ $\overline{CI}$ was demanded with a resolving time of 55 nanoseconds. The selection systems and discrimination levels used for the three series are shown in Table 2.3.

TABLE 2.3

Series	Selection	Discrimination Levels							
		A	B	C	D	E	F	CII	CI
P series	ABCDE $\bar{F}$ $\overline{CI}$	0.1	0.1	0.1	0.1	0.1	0.05	-	0.3
Q series	ABCD $\bar{\bar{E}}$ $\overline{CI}$	0.1	0.1	0.1	0.1	0.05	-	-	0.3
R series	ABCDEF $\overline{CII}$ $\overline{CI}$	0.1	0.1	0.1	0.1	0.1	0.1	0.58	0.58

The ten pulses (6 scintillator, 2 direct Cerenkov and 2 amplified Cerenkov) separated by suitable time intervals of $\sim$ 300 ns, were displayed on a cathode ray oscilloscope (Tektronix 585A) set at a sweep speed of 0.5 μs/cm.

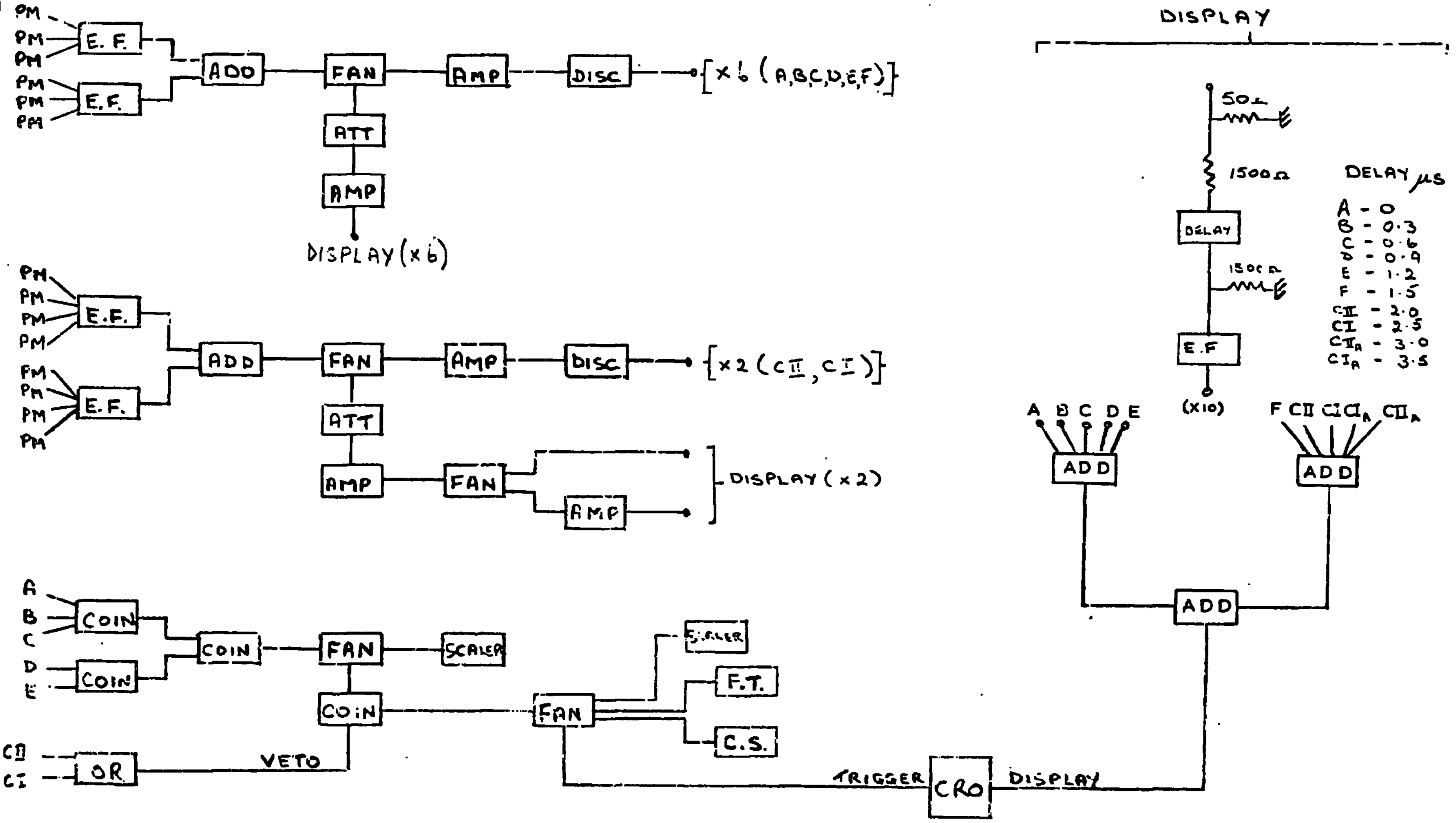

Figure 2.8 The electronic logic used in the P series.

Thus on an event satisfying the electronic logic, the ten pulse heights were displayed and photographed, and the front and side views of the flashed tubes (Figure 2.1) in the particle trajectory were also photographed. Events which triggered the telescope were analysed by projection of the three films onto scanning tables, correlation achieved by means of a clock on each frame. For each selected event, the track coordinates in each flash tube tray, the stopping positions (for P and Q series only), and the response of each detector, were measured.

Imposition of the stopping conditions in the P,Q,R series defined the aperture of the telescope by scintillators A and F for the P and R series, and by scintillators A and E for the Q series. The aperture variation as a function of the angular exponent of the incident radiation is shown in Figure 2.9 for the P and R series only, that of the Q series being slightly greater.

2.9 Mass determination

2.9.1 Initial analysis of events for the determination of their mass

The steps followed to obtain the mass of each selected single track event, from a knowledge of the three dimensional position of the trajectory and the responses of each detector, were as follows:

1. Conversion of output pulse heights to input pulse heights at the emitter follower (Figure 2.8) using calibration curves of the display electronics.
2. Normalisation of the pulse height in terms of E_s (or E_c) for the scintillation (and Cerenkov) counters.

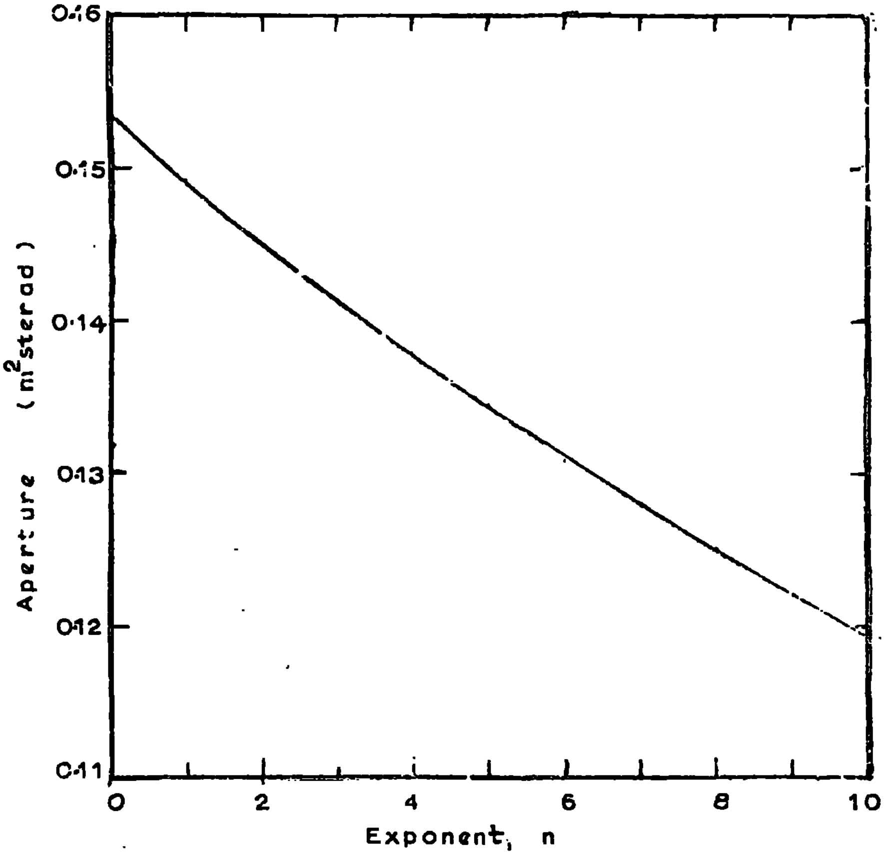

Figure 2.9 The telescope aperture as a function of the angular exponent of the incident radiation, for the aperture defined by scintillators A and F.

3. Correction to normal incidence from multiplication by a factor

$$\cos\theta_T = \cos\left[\tan^{-1}\left(\left\{\tan^2\theta_F + \tan^2\theta_S\right\}^{\frac{1}{2}}\right)\right]$$

where θ_T, θ_F, θ_S are the true zenith, projected, front and side angles, respectively.

4. Correction for the non-uniformity of the counter by means of the curves shown in Figure 2.10 and the co-ordinates of the trajectory at each counter. Where, in the curves for the Cerenkov counters, AB is a line along the centre of the Cerenkov counter, joining the photomultipliers, and CD is a line along the edge.

5. The velocity of the particle at each scintillator and Cerenkov counter was deduced from the appropriate value of the corrected, normalised pulse heights on the curves in Figures 2.3 and 2.4, respectively, where $1E_S$ and $1E_C$ corresponded to a value of $\beta = 1$.

6. The value of $f(\beta_i)$ was finally read from the curve in Figure 2.7.

For each detector i, then from equation 2.6

$$R_i + R_o = \frac{Mc^2}{z^2} \times f(\beta_i) \qquad (2.8)$$

where $f(\beta_i)$ is the measured quantity and R_i the amount of absorber in g cm^{-2} water equivalent to the bottom of the telescope, corrected for the inclination of the trajectory to the vertical.

A further equation resulted from the case in which a particle was observed to stop in the telescope, at which point

$$f(\beta) = 0 \quad \text{and} \quad R_i = -R_o \qquad (2.9)$$

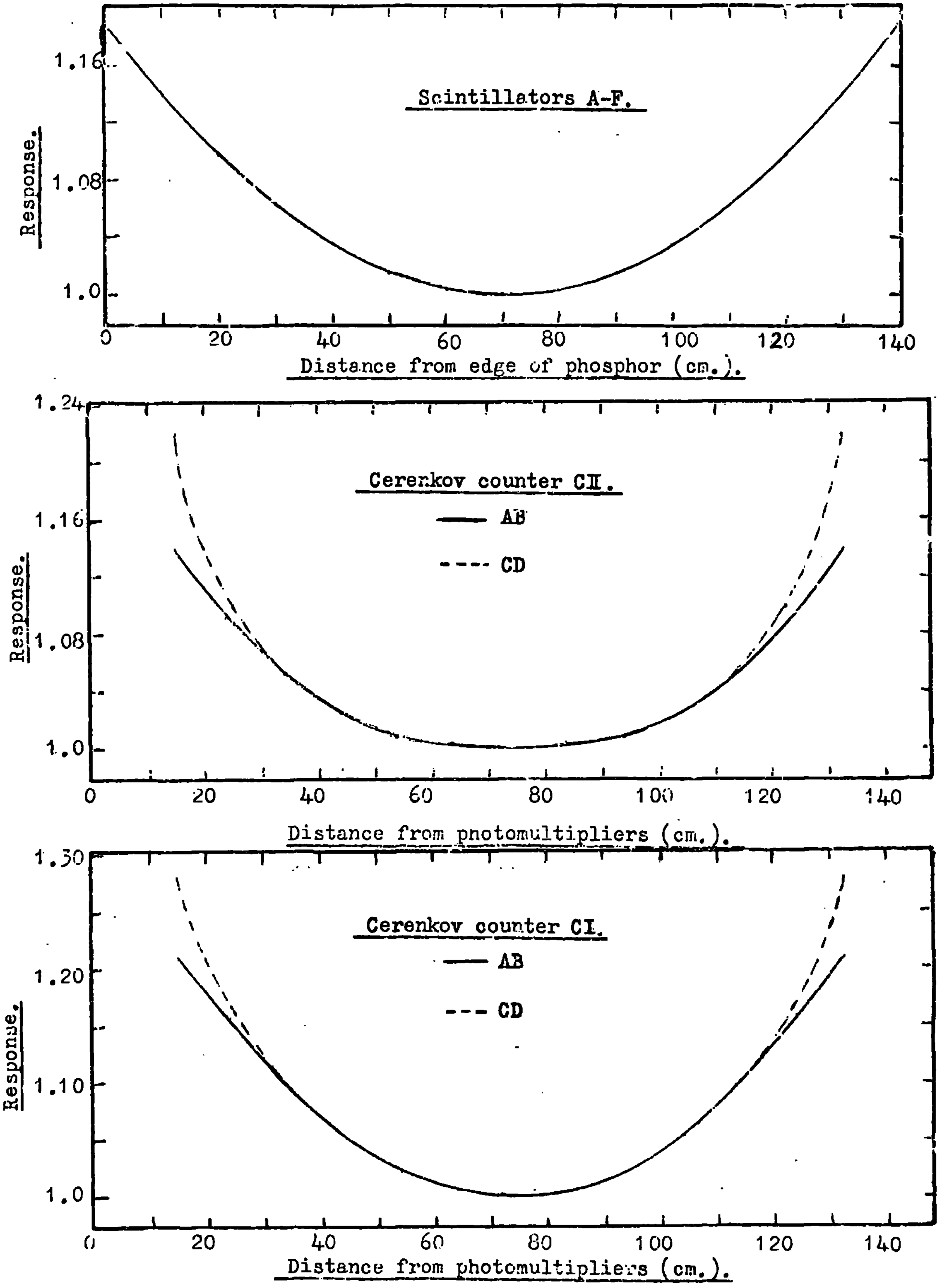

Figure 2.10 The response curves for the scintillators and Cerenkov counters, where the contributions from the photomultipliers at both ends have been summed, and the response normalised to that at the centre of each counter.

The mass M and the residual range R_o were derived from a least squares fit to all the simultaneous equations 2.8, where each equation was assigned a weight dependent on the random errors involved in the analysis of $f(\beta_i)$ or (for equation 2.9) dependent on the error involved in visually detecting the stopping point. The error in $f(\beta_i)$ for the scintillators is a function of several parameters, but there are two of greatest significance, these being the Landau distribution of energy loss (Ashton et al. 1968) and fluctuations in the number of photoelectrons emitted at the photocathode and collected by the photomultiplier.

The errors on the normalised and corrected pulse heights from the Cerenkov counters (and hence on the $f(\beta_i)$ values) were obtained from the standard errors on the measured velocity response of these counters and has been reported by Ashton and Kelly (1969).

2.9.2 Mass determination of a typical event from the preliminary proton experiment

A diagram of a typical event from the P series is shown in Figure 2.11 with the associated R - $f(\beta)$ plot on which the least squares fit to the observed points is indicated. From the slope of the line, a mass of 910 ± 70 MeV/c^2, implies the particle is a proton.

2.10 Observed variation of the mass precision, with different parameters, in the preliminary proton experiment

The precision of mass determination by this method improves with slower particle speeds and is caused by the nature of the curve relating $f(\beta)$ and scintillator pulse heights, where for a constant fractional error in the

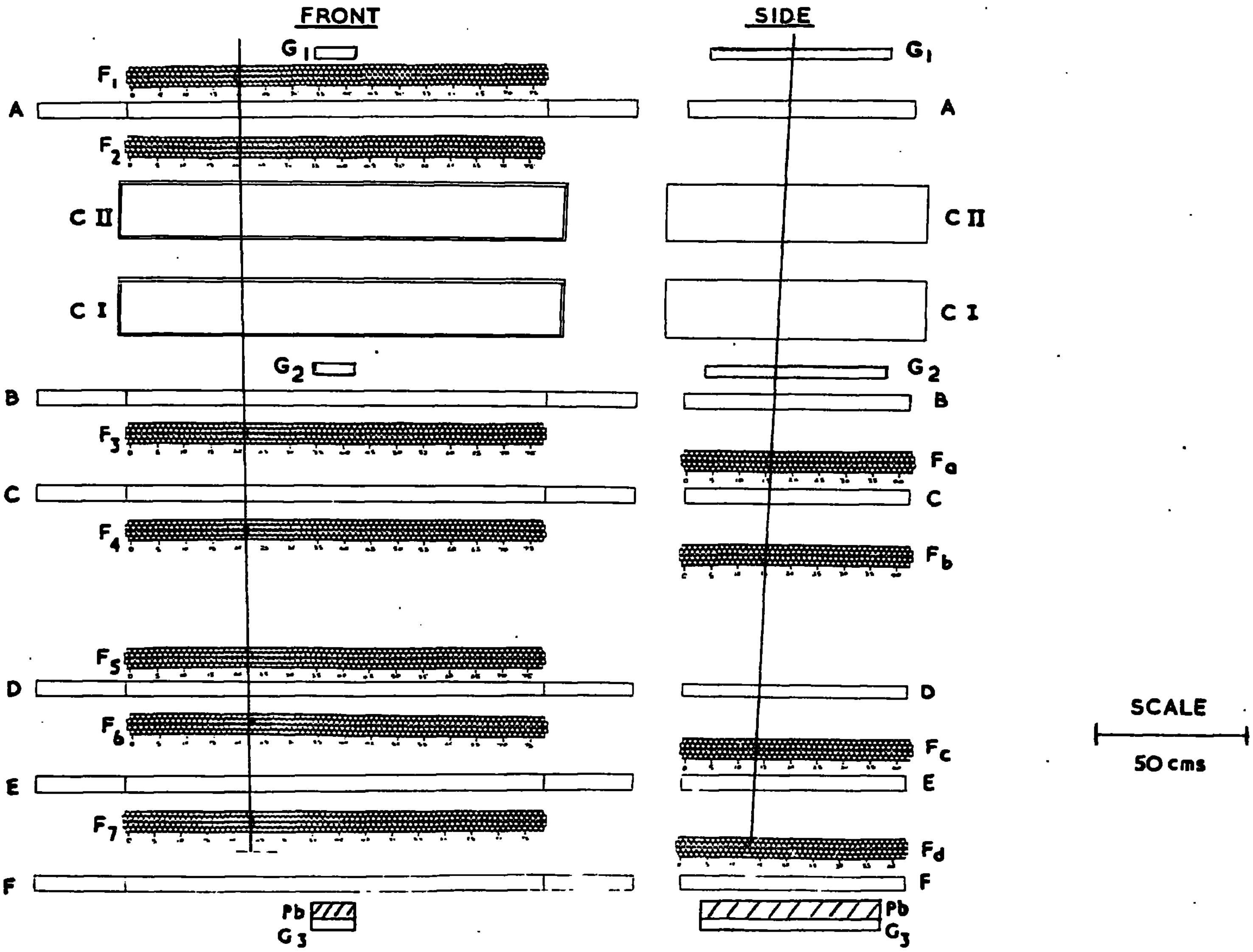

FRONT
SIDE
G1
F1
A
F2
C II
C I
G2
B
F3
C
F4
F5
D
F6
E
F7
F
Pb
G3
Fa
Fb
Fc
Fd
SCALE
50 cms

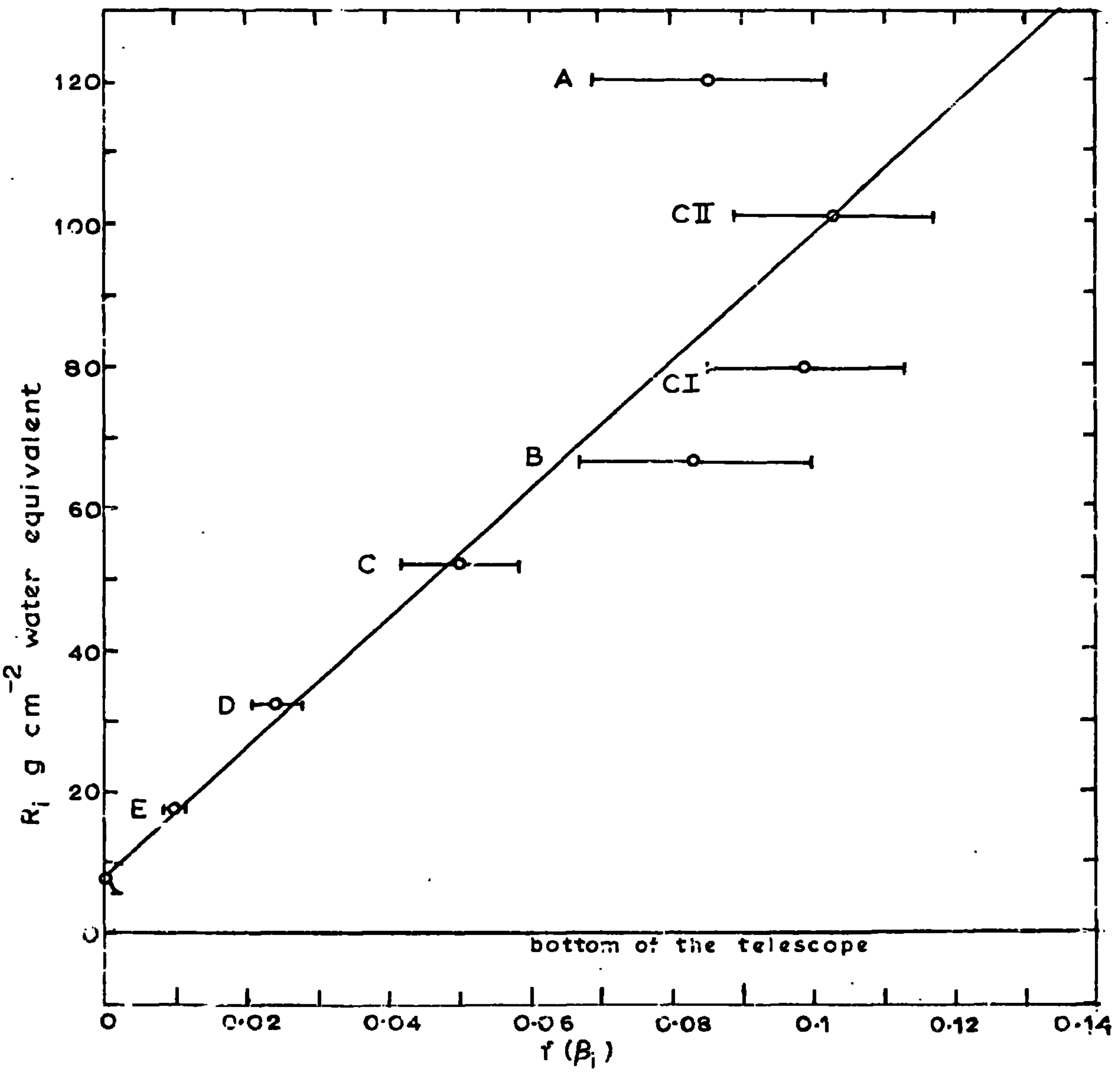

counter	A	CII	CI	B	C	D	E	F
V_N	1·71	0·11	0·076	1·72	2·04	2·65	3·79	0
β	0·71	0·735	0·728	0·71	0·64	0·55	0·45	–

Figure 2.11 A typical event selected in the P series. The event opposite shows the particle stopping in flash tube tray F_d. Above, in the table, the normalised pulse heights in each counter are given together with their corresponding velocities. The R-f(β) plot is shown above and the resulting mass after applying a least squares fit is 910±70 MeV/c^2.

pulse height, the associated error in $f(\beta)$ decreases with increasing pulse height and accordingly the weight increases.

The mass distribution obtained for a total of 799 selected events (assumed to be mainly protons) in the R series is shown in Figure 2.12. The events, when subdivided into incident velocity cells, indicate a trend of the mass distributions shifted with respect to the proton mass to lower mass values as the incident velocity increases. This trend was echoed by the theoretical distributions calculated by a Monte Carlo method which injected protons of known incident velocity into the telescope and calculated their masses after imposing Gaussian errors, which were representative of the experimental conditions, on each of the expected pulse heights. From further Monte Carlo calculations it was revealed that with the telescope shown in Figure 2.1, reliable mass estimates could only be made for particles of mass $2M_p$ and $5M_p$ when their incident velocities were less than 0.71c and 0.56c, respectively.

The mass distributions obtained for stopping particles (mainly protons) in the P and Q series are shown in Figure 2.13. A total of 762 particles are subdivided into scattered ($\geq 4^o$) and unscattered events. The former and latter distributions are observed to have full widths at half height of 550 MeV/c^2 and 350 MeV/c^2, respectively. The increased width of the scattered distribution is caused by the nuclear interactions in the telescope.

2.11 Charge identification

To apply the method of mass identification to fractionally charged

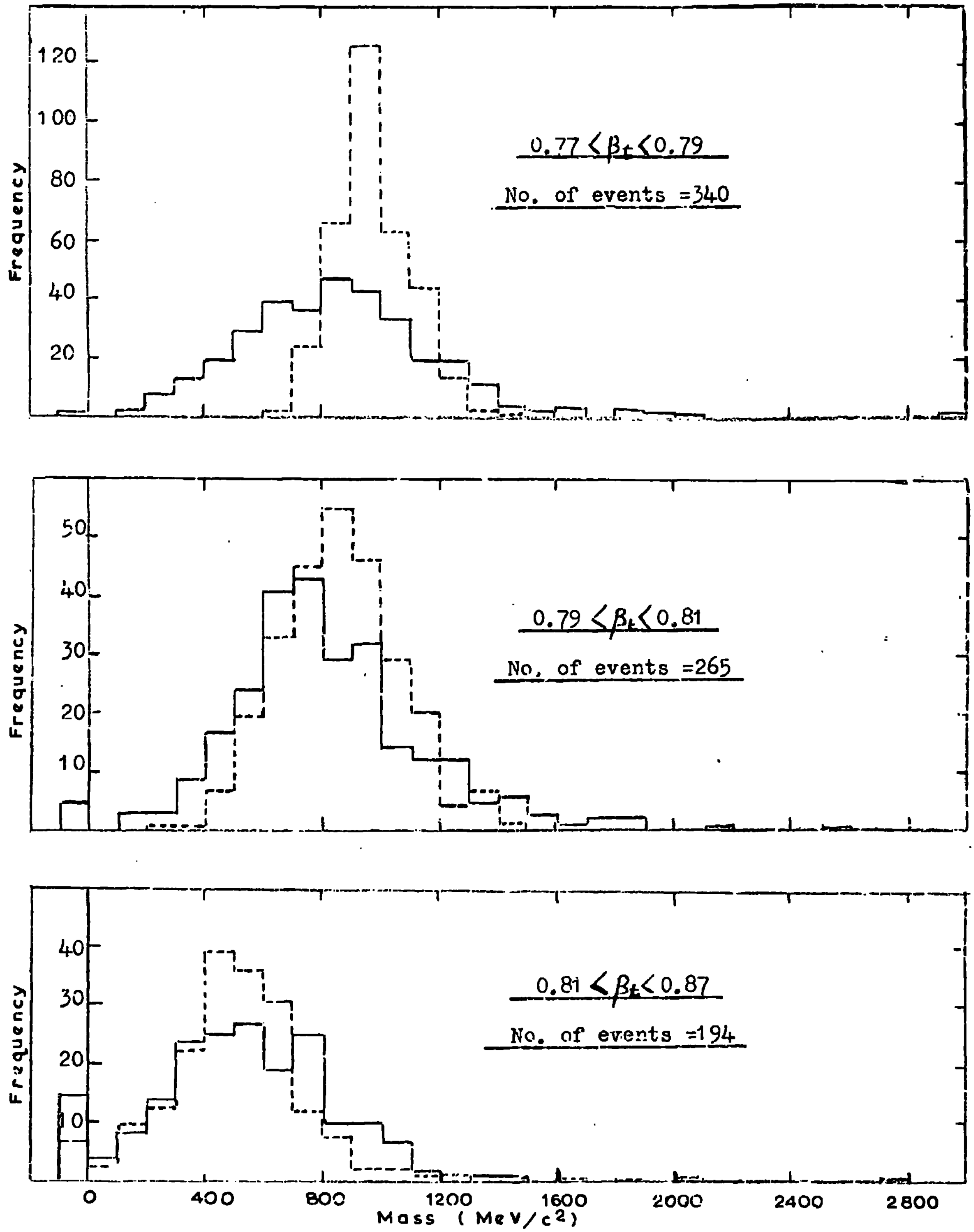

Figure 2.12 The events selected in the R series subdivided in to incident velocity cells, β_t. The full line is the experimental distribution and the dotted the theoretical.

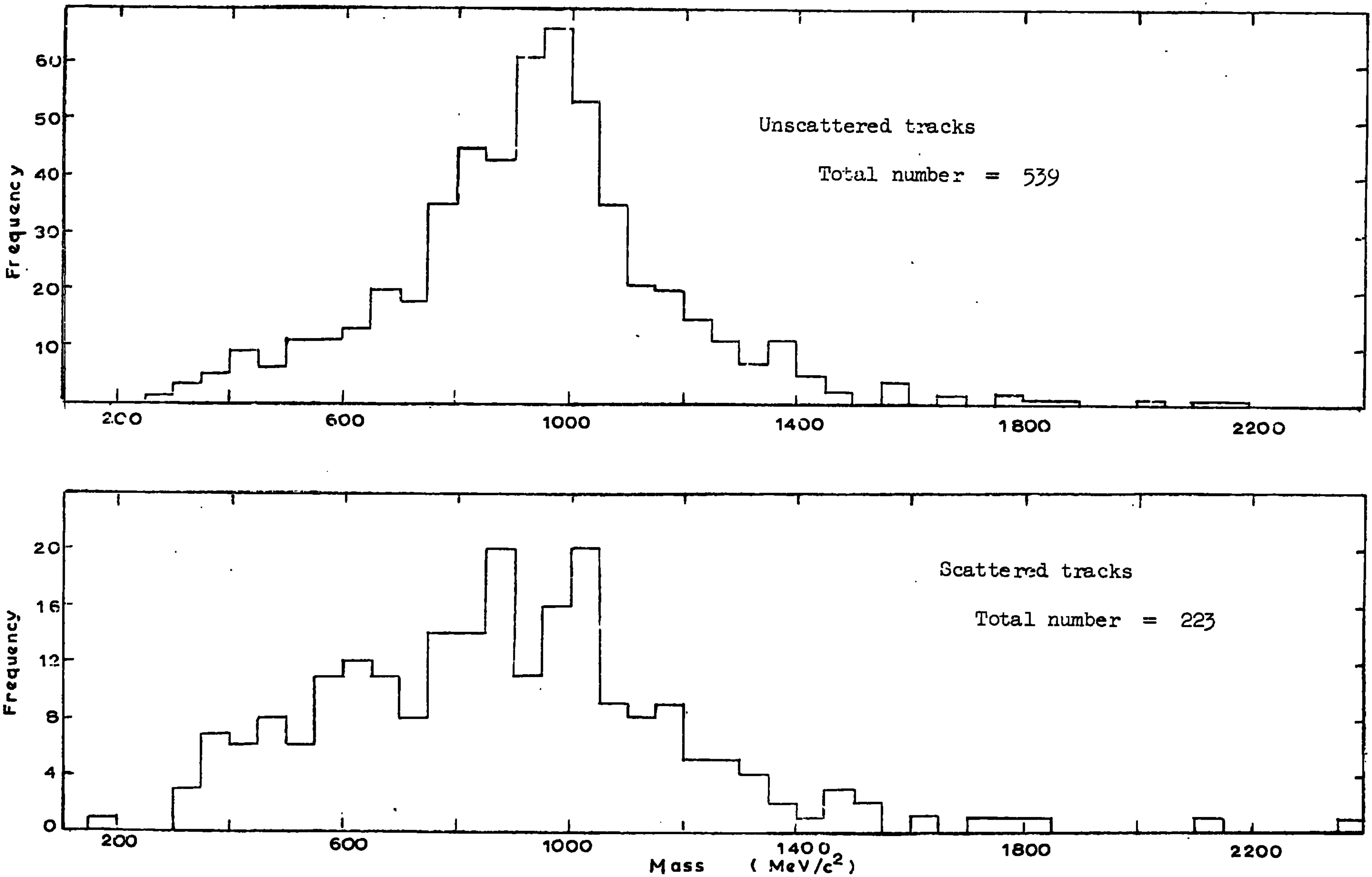

Figure 2.13 Mass distribution of unscattered and scattered particles selected in the P and Q series.

particles of z values 1/3 and 2/3, the value of z must be initially assumed to allow a value of β to be derived at each detector. That is, if the incident particle is assumed to be of charge number z, then the pulse heights, expressed as a ratio of E_s or E_c, must be multiplied by $\frac{1}{z^2}$ before the value of β_i (and hence $f(\beta_i)$) can be found from Figures 2.3 and 2.4. The value of $f(\beta_i)$ is then evaluated so that the least squares fit slope of the R - f(β) plot yields a value of $\frac{Mc^2}{z^2}$ for the assumed z value.

Identification of the appropriate charge and mass, from a range of assumed z values, is found to be possible only if a comparison is made between the β values in the scintillation counters and those in the Cerenkov counters, for each assumed charge. It is found that apart from the case of the true charge, there is a marked disagreement between the velocities in the adjacent scintillators and Cerenkov counters. This disagreement is observed in the results of a charge analysis on the event in Figure 2.11 and is revealed in Table 2.4.

TABLE 2.4

Counter		A	CII	CI	B	C	D	E	F
Corrected and normalised response in terms of E_s or E_c (i.e. in terms of β=1 z=1 particle)		1.71	0.11	0.08	1.72	2.04	2.65	3.79	0
β	z = 1	0.71	0.74	0.73	0.71	0.64	0.55	0.45	0
	z = 2/3	0.45	0.77	0.76	0.45	0.40	<0.40	<0.40	0
	z = 1/3	<0.40	1.0	0.92	<0.40	<0.40	<0.40	<0.40	0

The particle is thus concluded to have charge 1e and a mass 910 ± 70 MeV/c^2, consistent with it being a proton.

2.12 Conclusion

The effect of different parameters of the ionisation, residual range technique on the proton mass precision has been investigated, in the preliminary proton experiment. The conclusions drawn from this preliminary experiment are the following:

1. Good mass resolutions are confined to a small range of mass values, and above a certain mass value (dependent on the amount of material in the telescope) only a minimum mass can be assigned. This is a consequence of the particles change in velocity while penetrating the telescope being comparable to the velocity sensitivity of the telescope detectors.
2. For the selection of a particular mass and velocity range of certain desired particles, a range telescope must be designed to slow these particles down to sufficient speeds to enable accurate mass determinations.
3. When nuclear active particles are selected through a scintillator range telescope, for determination of their mass, a compromise has to be made between tolerable mass resolutions and a tolerable rate of events which necessarily diminishes as the amount of absorber is increased. Spurious results are obtained for the mass estimations of nuclear active particles, as the method of mass analysis breaks down if nuclear interactions become an important mode of energy loss. This effect also increases with increase in the amount of absorbing material.

The agreement between the mass and charge values obtained for stopping unscattered protons and the proton mass and charge, supports the validity of the various aspects of the mass analysis.

The advantages of such a technique lie in the large apertures attainable (several m^2 sterad) allowing low level searches to be carried out in the cosmic radiation, within reasonable time spans, and also in the determination of two particle parameters, those of mass and charge. However, the use of a range telescope is much more suited to accepting weakly interacting particles, where the large amount of absorber needed to stop the particles presents no problem.

In conclusion it is considered that, subject to the suitable conditions above, such a large aperture, scintillator range telescope can be used with confidence to search for low velocity, heavy mass particles in the cosmic radiation and to assign a reliable mass estimate to any such particles accepted.

CHAPTER 3

SEARCH FOR LOW ENERGY, HEAVY MASS PARTICLES IN COSMIC RAYS AT SEA LEVEL

3.1 Introduction

The use of a large aperture, scintillator range telescope in searching for low energy, massive particles, of any charge, incident in the vertical cosmic radiation, stems from an idea by Ashton (1965), who also calculated that for a reasonable quark interaction inelasticity of 0.5 most quarks would be reduced to sub-relativistic velocities at sea level.

Following the technique discussed in Chapter 2 for the determination of the mass and charge of particles stopping in the telescope, by an ionisation, residual range method, mass distributions obtained from the two following experiments, each defining different accepted momentum bands, are analysed in this chapter.

1. The preliminary proton experiment selected low energy particles of mass $\gtrsim 300$ MeV/c^2 and was primarily executed with the purpose of checking the validity of the mode of mass analysis, from a comparison of the observed low energy, proton spectrum with those of other workers. Further, from the observed distribution in proton mass values, to determine the mass resolution attainable with such a telescope. This experiment was also used to search for other low energy, massive particles in the predominating proton distribution.
2. The second, heavy mass search employed a modified version of the previous range telescope to study low energy particles of mass > 1.3 GeV/c^2 (z=1), in a proton free background.

Recently, interest in the possible existence of hitherto unknown, heavy mass particles in the sea level cosmic radiation has been rekindled by results from four independent measurements indicating the presence of such particles.

Dardo et al. (1968) observed relativistic particles of mass in the range 10-15 nucleon masses and charge 1e, at a rate of 10^{-7} cm^{-2} sec^{-1} $sterad^{-1}$ at a depth of 70 m.w.e. (metres water equivalent) underground. These particles, detected from their delay in arrival with respect to muon showers, were observed to have interaction lengths of 2 to 3 pion interaction lengths and to lose only about 5% of their energy in a nucleon-nucleon collision. These observations have prompted a tentative interpretation of the delayed particles as stable members of a heavy fundamental triplet, arising from the dissociation of very high energy, cosmic ray protons in collisions with atmospheric nuclei. The present experiment, searching for sub-relativistic massive particles, (> 1.3 GeV/c^2), would then only be sensitive to such particles if their muon accompaniment were negligible (as events showing previous particles within 200 μs would be automatically rejected) over the area of the telescope, and if a significant number were slowed down to sub-relativistic velocities at sea level. Dardo et al. have indeed suggested that muon showers accompanying these triplets are small (∿ 10 muons) and are contained within a few metres of the triplet. Hence the scintillator range telescope might be sensitive to such sub-relativistic stable triplet members.

McCusker and Cairns (1969) followed by Chu et al. (1970) have independently reported the detection of relativistic particles of charge 2e/3, namely quarks, in the cores of air showers. It seems that the scintillator range telescope, although sensitive to any particle charge, is only applicable to sub-relativistic unaccompanied particles and therefore is not useful for a check on such a result.

The existence of hitherto unknown massive particles, termed U particles, in the primary radiation, has been proposed by Callan and Glashow (1968) to explain the results of Bergeson et al. (1967), who observed an angular distribution of high energy (10^3 - 10^4 GeV), cosmic ray muons underground in marked disagreement with the sec θ enhancement expected if muons are the progeny of pions and kaons. The U particles are suggested to be massive (several GeV/c^2), weakly interacting and present to a level of 10^{-3} of the primary proton flux. The scintillator range telescope, although primarily designed to search for quarks, would also be sensitive to the U particles which were moderated to sub-relativistic velocities at sea level, through ionisation loss in the atmosphere. Thus, such an experiment is expected to give supporting evidence (or otherwise) as to the existence of these particles, from a comparison of the measured U/p ratio with the value of 10^{-3} at the top of the atmosphere, as proposed by Callan and Glashow.

3.2 Measurement of the low energy proton spectrum

The mass distributions of stopping events from the preliminary experiment in which low energy, sea level protons were used to trigger the telescope (in Figure 2.1), are shown in Figure 2.13. The operation of the scintillator telescope in this preliminary experiment is given in Sections 2.4 and 2.8 and the mode of mass analysis in 2.9.

For determination of the proton spectrum, all the stopping events in the

P and Q series are assumed to be protons, subject to a mass discrimination (equation 2.2) that accepted particles of mass $\gtrsim 300$ MeV/c^2. The only likely known contamination is $\sim 2\%$ from deuterons and is relatively of a negligible effect.

The basic information for the P and Q series is shown in Table 3.1.

TABLE 3.1

Series	P	Q
Selection System	$ABCDE\bar{F}\ \overline{CI}$	$ABCD\bar{E}\ \overline{CI}$
Region of stopping	E, F_7, F_d	D,F_6,F_c
Running time, T hours	36.1	27.1
Total number of triggers	2,144	2,799
Number of stopping tracks with scatter $\geqslant 4^{o}$	97	126
Number of stopping tracks with scatter $\leqslant 4^{o}$	256	283
Aperture, A cm^2 sterad	7.9×10^2	9.6×10^2
Accepted momentum band, Δp MeV/c	52.7	57
Mean momentum, MeV/c	1087.3	1032.5
Mean pressure, millibars	1009.3	1012.7

Where the quoted aperture in Figure 2.9 has been corrected for non-uniformity introduced by the supporting steel girders and an exponent of n=8 has been assumed.

The discrimination levels used in each series are given in Table 2.3. The high background of triggers, 13 hr^{-1}, is mainly due to events in which two separate tracks (either unassociated or associated) trigger the coincidence system, such that one particle passes through BCDE missing CI and A, but the other enters A.

Using an observed intensity of protons expressed by

$$N(p)\,dp = \frac{N_o}{3600 \times A \times T \times \Delta p} \quad cm^{-2}sec^{-1}sterad^{-1}(MeV/c)^{-1} \ldots .3.1$$

and normalising to an atmospheric pressure of 10^3 millibars, the observed intensities of protons are $(6.98 \pm 0.38)10^{-8}cm^{-2}sec^{-1}sterad^{-1}(MeV/c)^{-1}$ and $(8.37 \pm 0.43)10^{-8}cm^{-2}sec^{-1}sterad^{-1}(MeV/c)^{-1}$ at mean momenta of 1087 and 1033 MeV/c, respectively.

Correcting the above proton intensities for interaction losses in the telescope is complicated in that not only is the non-interacting component in the accepted momentum band observed, but also protons of higher energy are observed, which interact in the telescope, lose a certain fraction of their energy and then stop in the selected region. Using the inelastic nucleon-nuclei interaction lengths as measured by Chen et al. (1955) (which are fortunately energy independent above 95 MeV) and shown in Figure 3.1 as a function of atomic weight, the observed proton intensities (equation 3.1) were corrected for the inelastic interactions of protons through the telescope. In the absence of accurate inelasticity distributions for nucleon-nuclei interactions, the observed proton intensities were corrected using a value of 0.5 for the inelasticity, k, the statistical errors on the rates being broadened assuming the error in the correction factor to

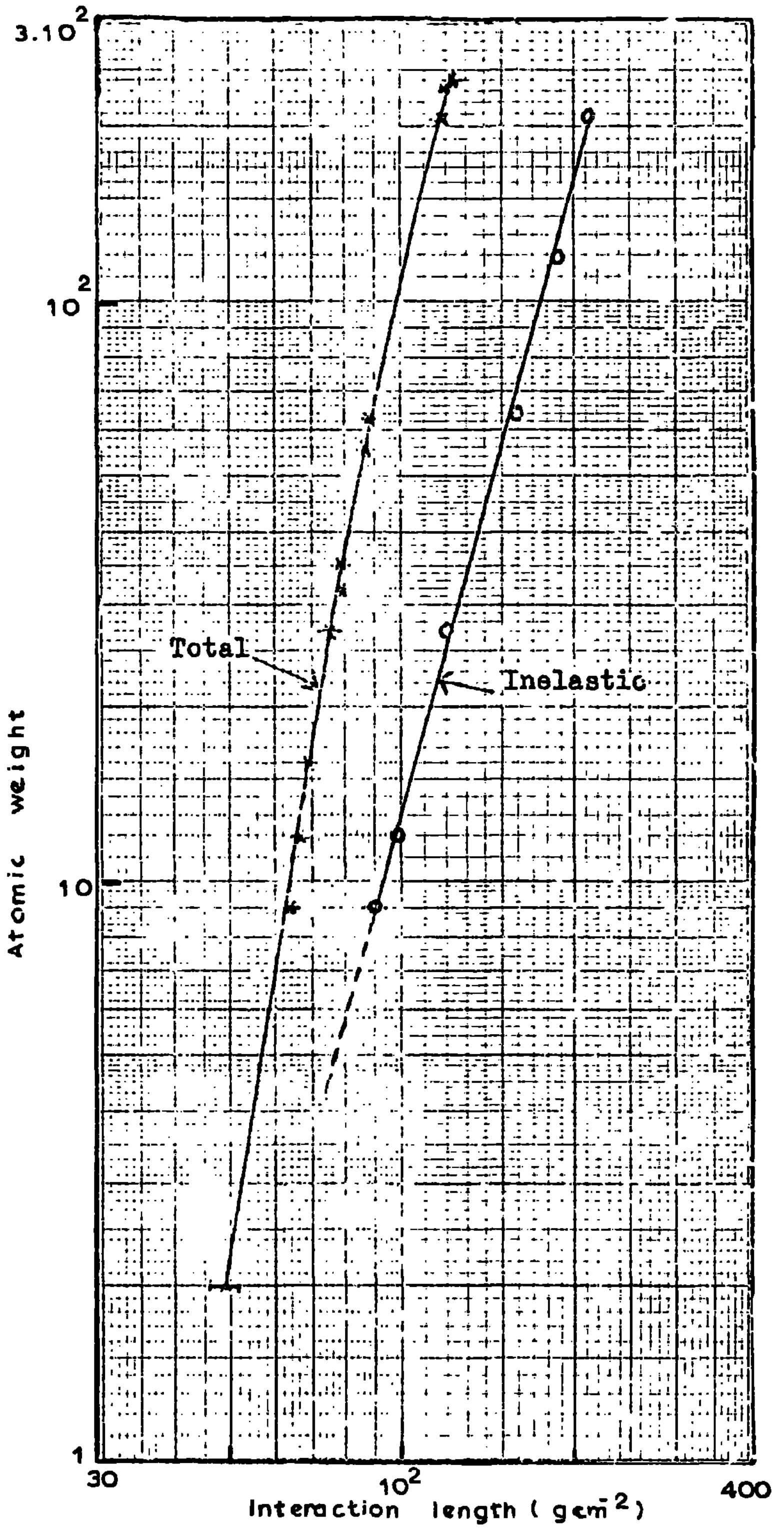

Figure 3.1 Total and inelastic nucleon interaction lengths in various nuclei as a function of atomic weight (Chen et al., 1955).

correspond to the limits k = 0.7 and k = 0.3. The resulting rates of, $(1.03^{+0.13}_{-0.12})10^{-7}$ and $(9.9^{+1.2}_{-0.5})10^{-8}$, $\text{cm}^{-2}\text{sec}^{-1}\text{sterad}^{-1}(\text{MeV/c})^{-1}$ at mean proton momenta of, 1087 and 1033, MeV/c, respectively, are observed to be in good agreement with the results of other workers. The proton intensities as measured by several workers are shown for comparison in Figure 3.2. This agreement substantiates the validity of the various aspects of the ionisation, residual range technique used in the determination of these intensities.

3.3 Measurement of the low energy deuteron intensity at sea level, from the results of the preliminary proton experiment

A significant number of events in the region of the deuteron mass, were observed in the mass distributions of the stopping particles in the preliminary experiment. Due to the limitations of the ionisation, residual range technique in determining accurate mass values (concluded in Section 2.12), only the unscattered mass distribution in Figure 2.13 was considered for the extraction of deuterons from the proton mass tail.

Each particle yielding a mass value greater than 1500 MeV/c^2 was carefully re-analysed. The expected pulse heights, V_e, were calculated assuming that the stopping particle was a deuteron and the particle had stopped at the observed point. An average efficiency of accepting a deuteron of 0.94 resulted from imposing a criteria that $(V_e - V_o)_d$ in each scintillator was within $\pm 2\sigma_e$, where σ_e is the expected error on each pulse height, V_o is the observed pulse height and suffix d refers to a deuteron.

The efficiency for accepting deuterons in a mass band > 1.5 GeV/c^2 is 0.8, assuming the deuteron mass distribution to follow the same shape as

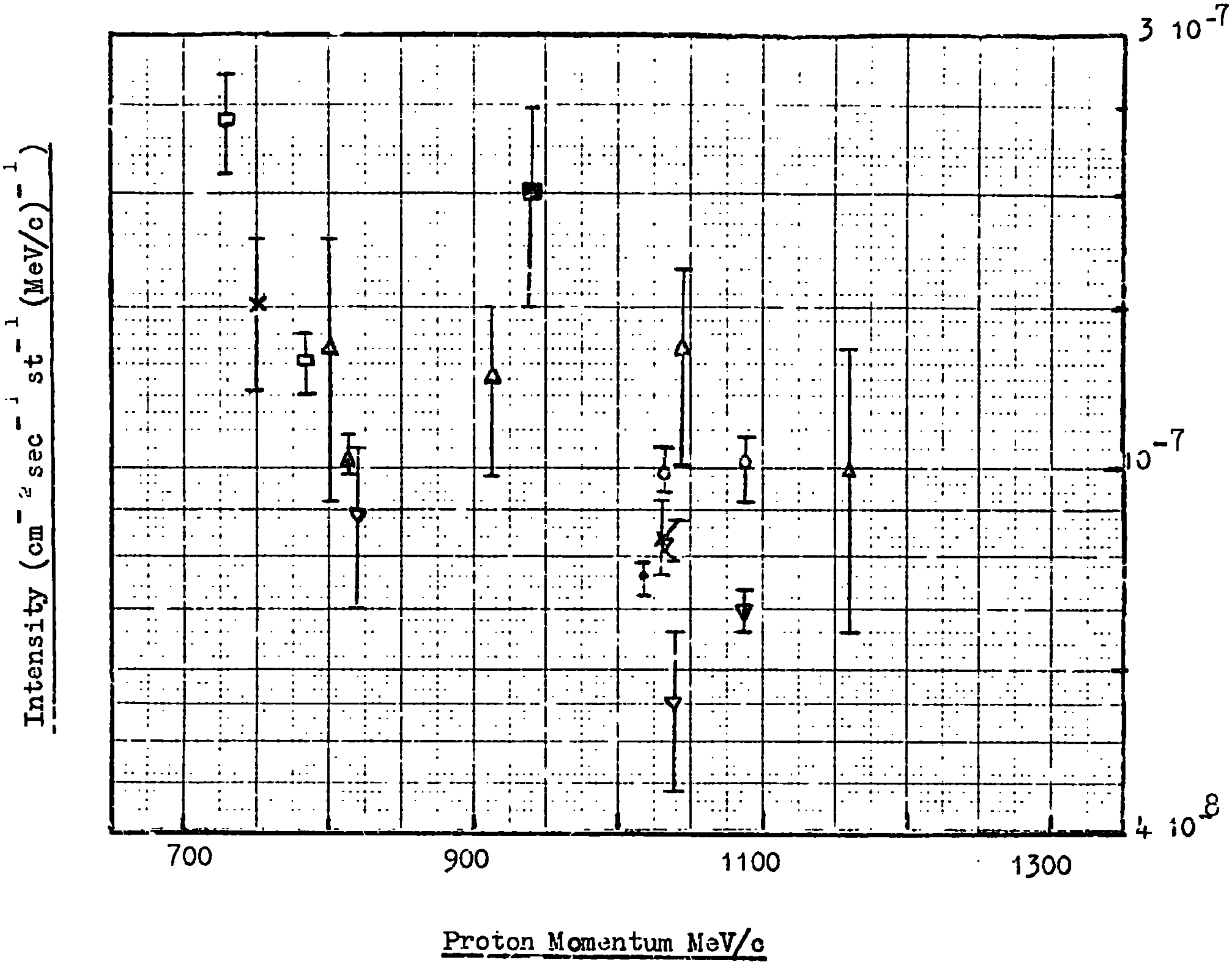

Figure 3.2 Proton Spectrum

- ▼ Present work uncorrected
- ○ Present work corrected
- × Brocke, G. et al. (1964)
- □ McDiarmid, I.B. (1959)
- △ Ballam, J. et al. (1954)
- ● Baccalini, C. et al. (1955)
- ▽ Mylori, M.G. et al. (1951)
- ■ Goldwasser, E.L. et al. (1951)
- ▲ York, C.M. (1952)

that obtained for protons.

From an initial extracted number of 6 deuterons satisfying the above criteria, the corrected number of deuterons in the sample becomes 7.6, corresponding to incident deuterons in the momentum range, 1.565 - 1.725, GeV/c. Assuming a $\cos^8\theta$ zenith angle dependence of incident deuterons, giving a mean telescope aperture of $8.6 \times 10^2 \mathrm{cm}^2$ sterad, the detected intensity of deuterons is $(4.83^{+2.98}_{-1.98}) \times 10^{-10} \mathrm{cm}^{-2} \mathrm{sec}^{-1} \mathrm{sterad}^{-1} (\mathrm{MeV/c})^{-1}$, at a mean momentum of 1.65 GeV/c.

The correction for inelastic interactions of deuterons is relatively simple compared to the correction for proton interaction losses, as, because of the small binding energy holding a deuteron together, disintegration occurs in any inelastic interaction of a deuteron. Correction for these effects assumes the loss of any inelastically interacting deuterons (the elastic interactions, as in the proton case, can be ignored as resulting in negligible energy transfers and small angle scatterings) from the accepted momentum band. The Glauber correction (see Section 8.4) is calculated to be negligible for incident deuterons of mean momenta 1.65 GeV/c and thus the deuteron-nucleus inelastic interaction lengths are half the nucleon-nucleus inelastic interaction lengths shown in Figure 3.1.

The mean number of deuteron inelastic interaction lengths from the top of the telescope to the stopping region is 2.18 and estimating an error of 5% in this value, the corrected intensity of deuterons incident on the telescope is $(4.21^{+2.95}_{-2.38})\ 10^{-9} \mathrm{cm}^{-2} \mathrm{sec}^{-1} \mathrm{sterad}^{-1} (\mathrm{MeV/c})^{-1}$. Taking a value of $3.1 \times 10^{-8}\ \mathrm{cm}^{-2} \mathrm{sec}^{-1} \mathrm{sterad}^{-1} (\mathrm{MeV/c})^{-1}$ for the proton flux at the same momentum (Brooke and Wolfendale, 1964) the incident d/p ratio is

$13.6^{+9.5}_{-7.7}$% at a mean momentum of 1.65 GeV/c. The corrected deuteron intensity is plotted in Figure 3.7 with another measurement of the deuteron intensity at a higher momentum value.

3.4 Heavy mass search in a modified telescope

3.4.1 Study of low energy, heavy mass events in a proton free background

Because of the obvious disadvantages of resolving rare heavy mass events from a large proton background, the scintillator range telescope used in the preliminary experiment was modified with the inclusion of 184 g cm^{-2} of steel in the telescope, as shown in Figure 3.3. The primary factor governing the design of this modification in the residual range R_T, was, together with a suitable choice of β_T, the adjustment of the mass discrimination level in equation 2.2, to accept all particles of charge 1e having a mass greater than 1.3 GeV/c^2.

Selection of the desired particles was carried out by Rutherford fast electronics in a similar mode to Figure 2.8. A coincidence A $\overline{\mathrm{CII}}$ B $\overline{\mathrm{CI}}$ C,D,E,F was demanded with a resolving time of 55 ns. The discrimination levels used, are shown in Table 3.2, in terms of E_s for the scintillation counters and E_c for the Cerenkov counters.

TABLE 3.2

Counter	A	B	C	D	E	F	CII	CI
Discrimination level	0.15	0.15	0.15	0.15	0.15	0.1	0.37	0.32

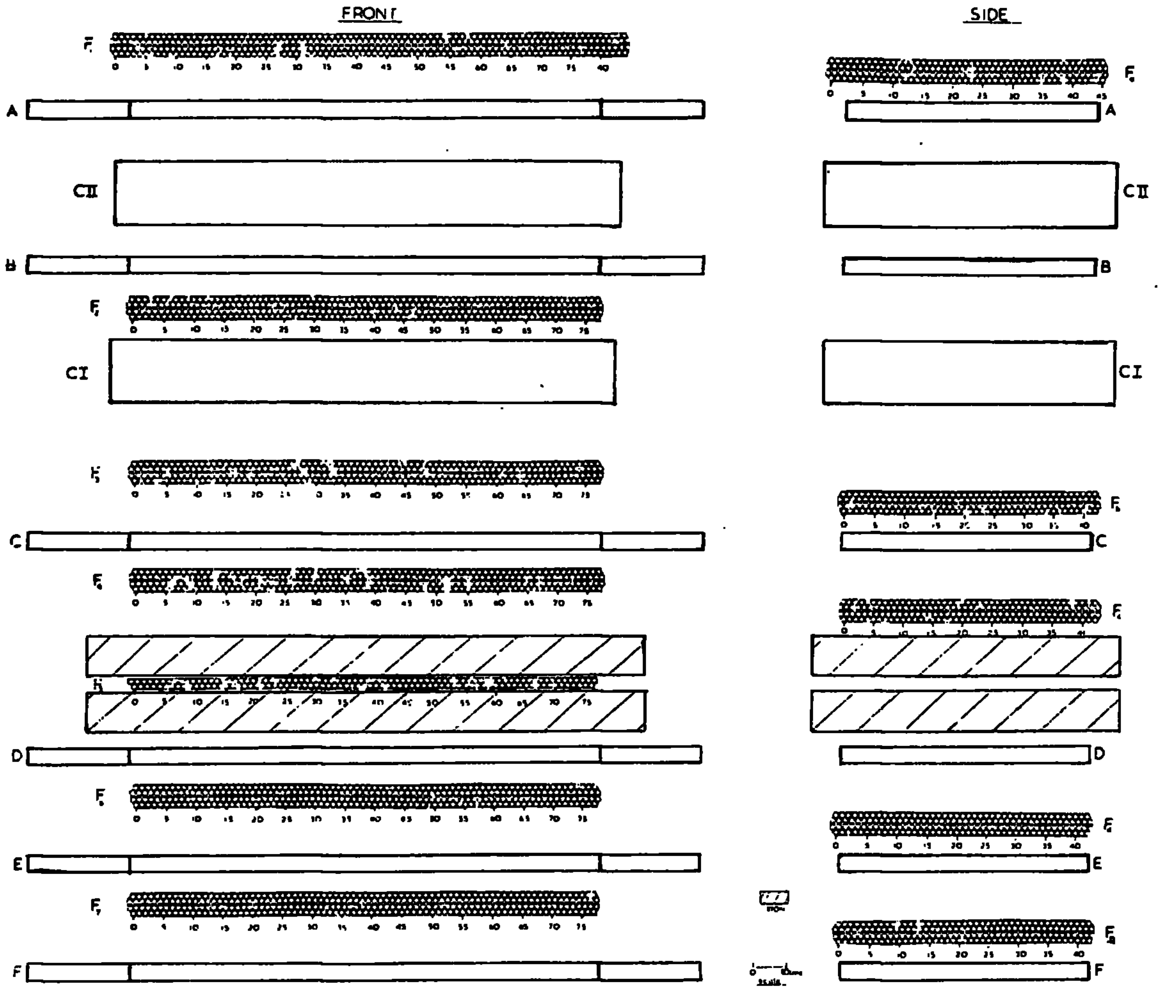

Figure 3.3 The heavy mass telescope. A-F are plastic scintillators(NE102A); CII, CI are water Cerenkov counters; F_1-F_7, F_a-F_e are neon flash tube trays and the hatched area is steel.

The parameters necessary in the mass analysis were measured in the same way as in the preliminary proton experiment.

3.4.2 Basic data

The basic information from this experiment is shown in Table 3.3.

TABLE 3.3

Selection System	ABCDEF $\overline{\mathrm{CII\ CI}}$
Running time, T hours	1040.4
Total number of triggers	2200
Number of angled triggers	1810
Number of weak electron photon showers	359
Number requiring further analysis	31

The angled triggers comprised of tracks traversing the C to F region of the telescope and missing A to CI.

3.4.3 Analysis of the heavy mass candidates

Only two events of the 31 requiring further analysis showed a track through the whole telescope, both of which were scattered. The remaining events had the appearance of being neutrally induced in CI, with the exception of two events which were otherwise accounted for.

The method of mass analysis expounded in Section 2.9 was applied to the two events showing single penetrating trajectories. In conjunction with the velocity comparisons between the scintillators and Cerenkov counters, for different z values, the best fit of charge and mass was assigned to each event. With this approach, the events shown in Figures 3.4 and 3.5 with their relevant R - f(β) plots, were found to be consistent with having charge 1e and least squares fit mass values of 1.89 ± 0.54 GeV/c^2 and 2.49 ± 0.55 GeV/c^2. Fractional electron charges were ruled out in both cases by the large inconsistency between the velocity estimates derived from the scintillators and those derived from the Cerenkov counters, under the assumption of such charges. While it cannot be completely ruled out that these two particles are integrally charged quarks of mass $\sim$ 2 GeV/c^2, a more likely interpretation is that they are both deuterons.

The incident momentum bands accepted by the telescope are defined by the minimum residual range of the telescope, R_T, and the velocity discrimination levels of the Cerenkov counters as discussed in Section 2.2. The limiting incident momentum bands are shown in Figure 3.6 for $z = 1, \frac{2}{3}, \frac{1}{3}$, over a range of mass values. The momenta with which these two 'deuterons' entered the detector were, (2.33 ± 0.04) GeV/c and (2.57 ± 0.08), GeV/c.

A deuteron angular distribution of the form $\cos^8\theta$ would be expected for which, from Figure 2.9, the acceptance aperture is 1.25 x 10^3 cm^2 sterad, giving an intensity of detected deuterons, $(1.3^{+1.7}_{-0.8})10^{-12}$ cm^{-2} sec^{-1} sterad^{-1} (MeV/c)$^{-1}$ at a mean incident momentum of 2.45 GeV/c. The running time was taken as 3.74 x 10^6 seconds and the accepted incident momentum band as 2.28 - 2.61 GeV/c.

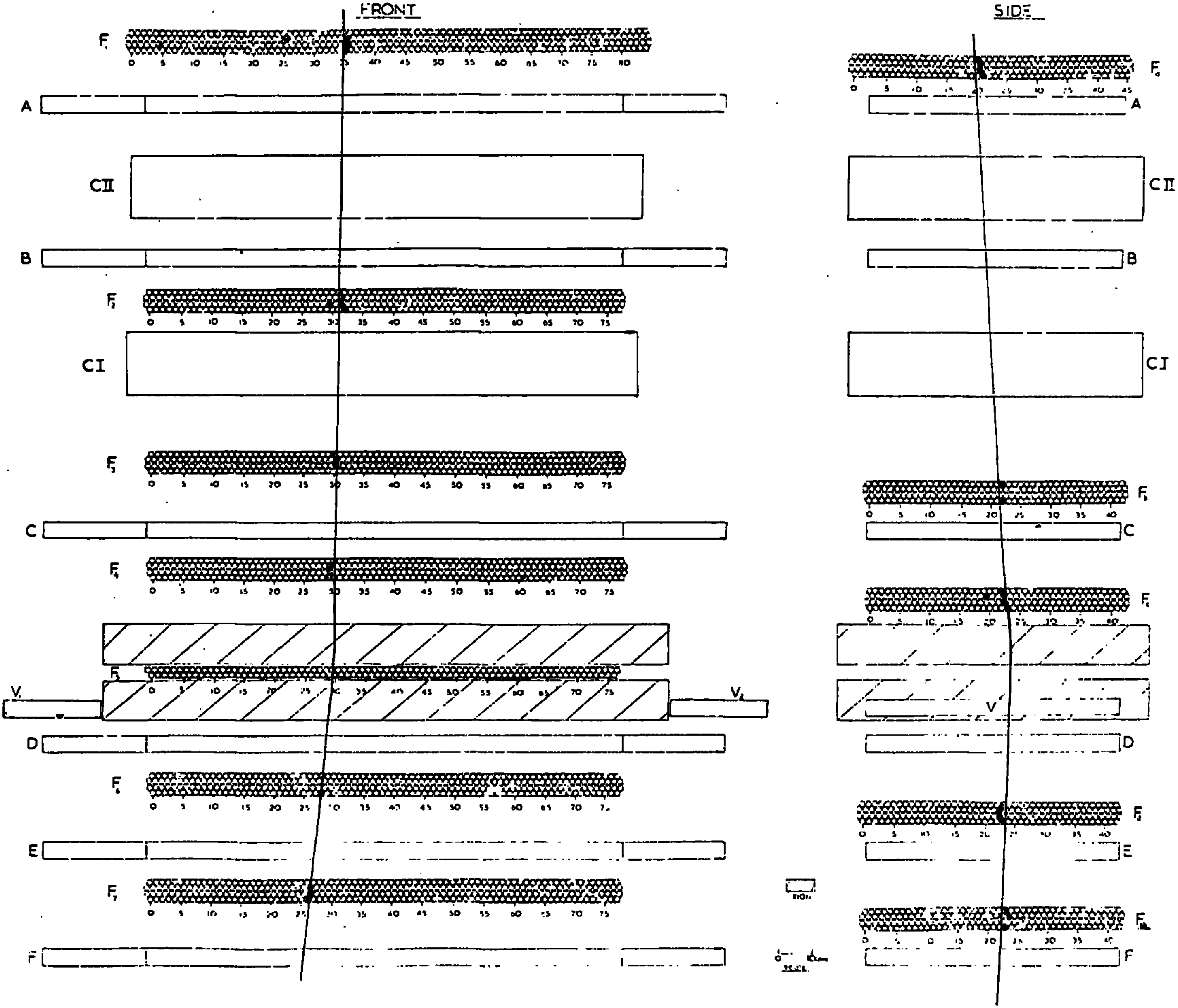
FRONT
SIDE
F1
A
CII
B
F2
CI
F3
C
F4
F5
V1
V2
V
D
F6
E
F7
F
F8
F9
F10
F11
F12
0 5 10 15 20 25 30 35 40 45 50 55 60 65 70 75 80
0 5 10 15 20 25 30 35 40 45

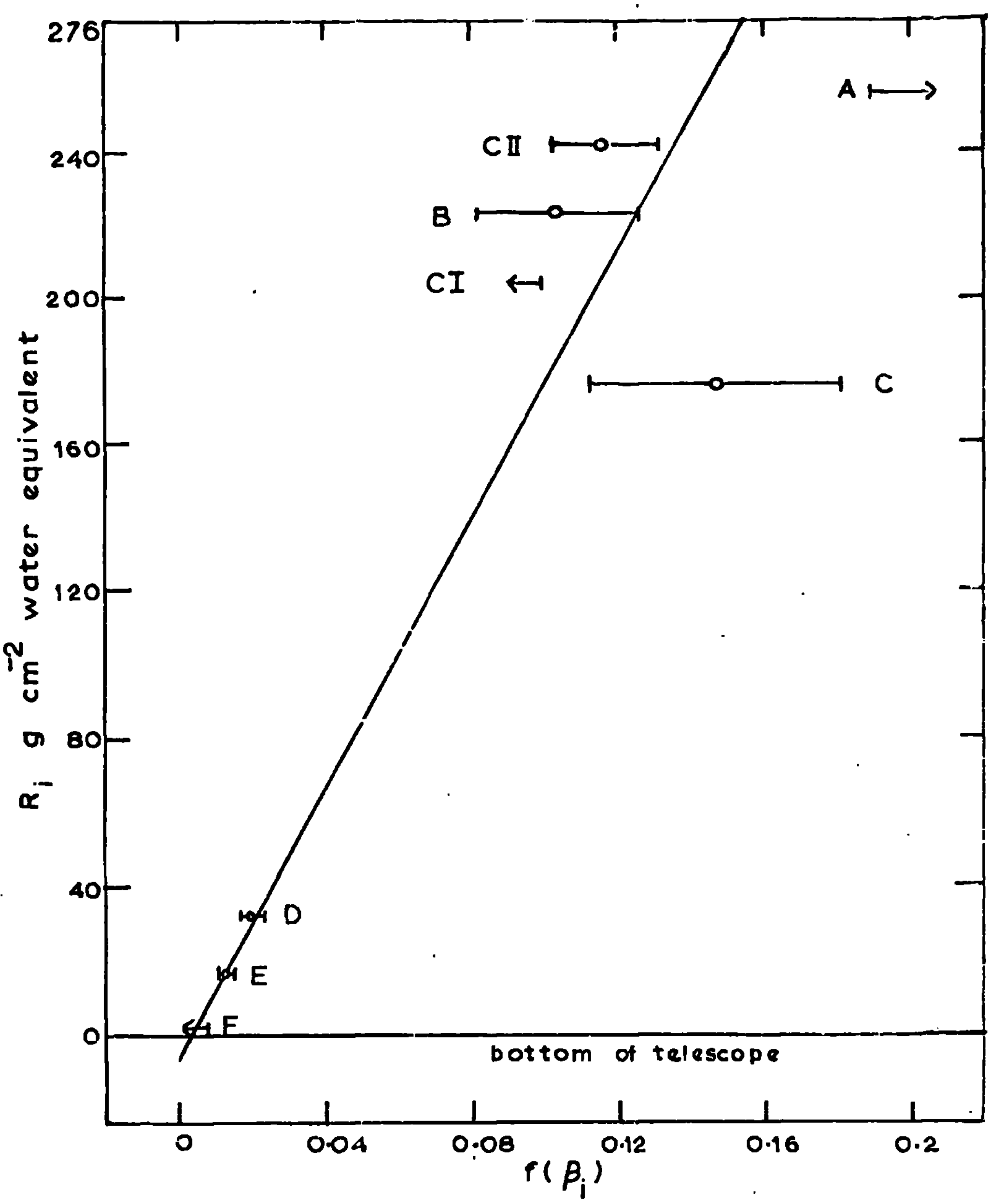

counter	A	C II	B	C I	C	D	E	F
V_N	1·25	0·17	1·61	0	1·45	2·88	3·43	>4·26
β	0·85	0·75	0·74	<0·72	0·78	0·53	0·48	<0·42

Figure 3.4 The trajectory of the particle is shown opposite. The pulse heights and the corresponding β values, assuming unit charge, are given above. The R–f(β) plot is given above and the resulting mass estimate is 1.89 ± 0.5 GeV/c^2.

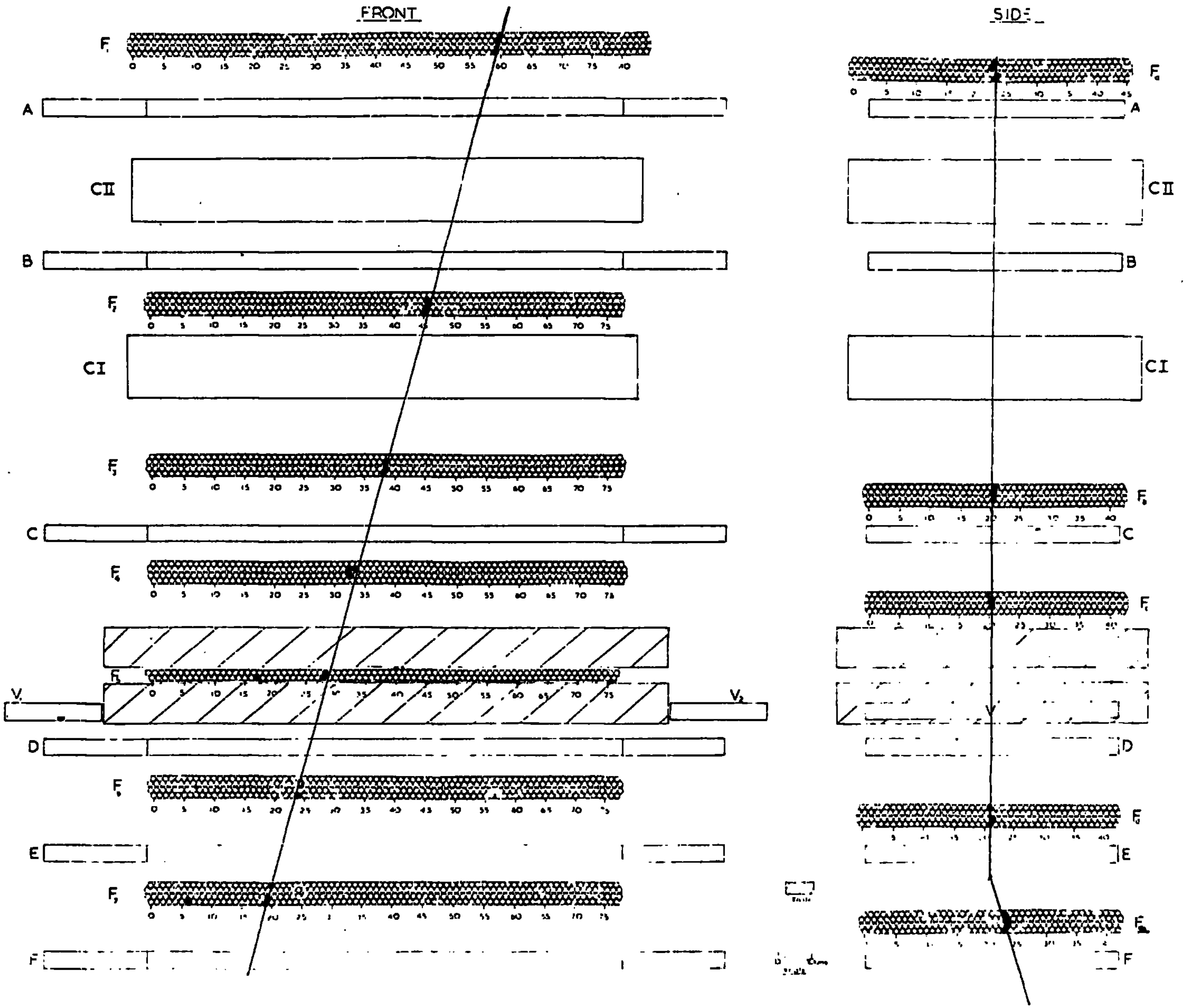
FRONT
SIDE
A
B
C
D
E
F
CII
CI
V1
V2

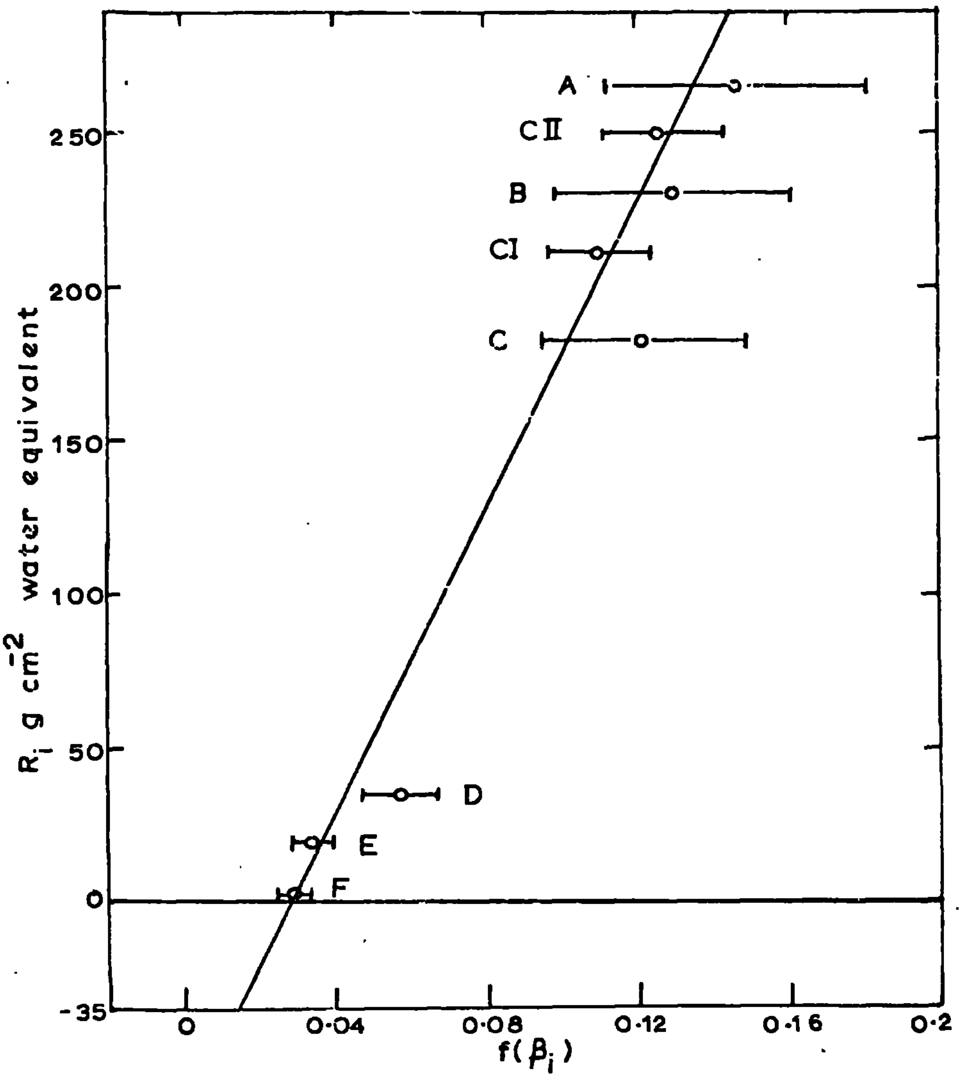

counter	A	C II	B	C I	C	D	E	F
V_N	1·45	0·20	1·51	0·13	1·54	1·95	2·34	2·50
β	0·78	0·76	0·76	0·74	0·75	0·66	0·59	0·57

Figure 3.5 The trajectory of the particle through the telescope is shown opposite and the pulse height recorded by each counter and the corresponding β values, assuming unit charge, are given in the table. The R–f(β) plot is shown above and the resulting mass estimate gives 2.49 ± 0.5 GeV/c^2.

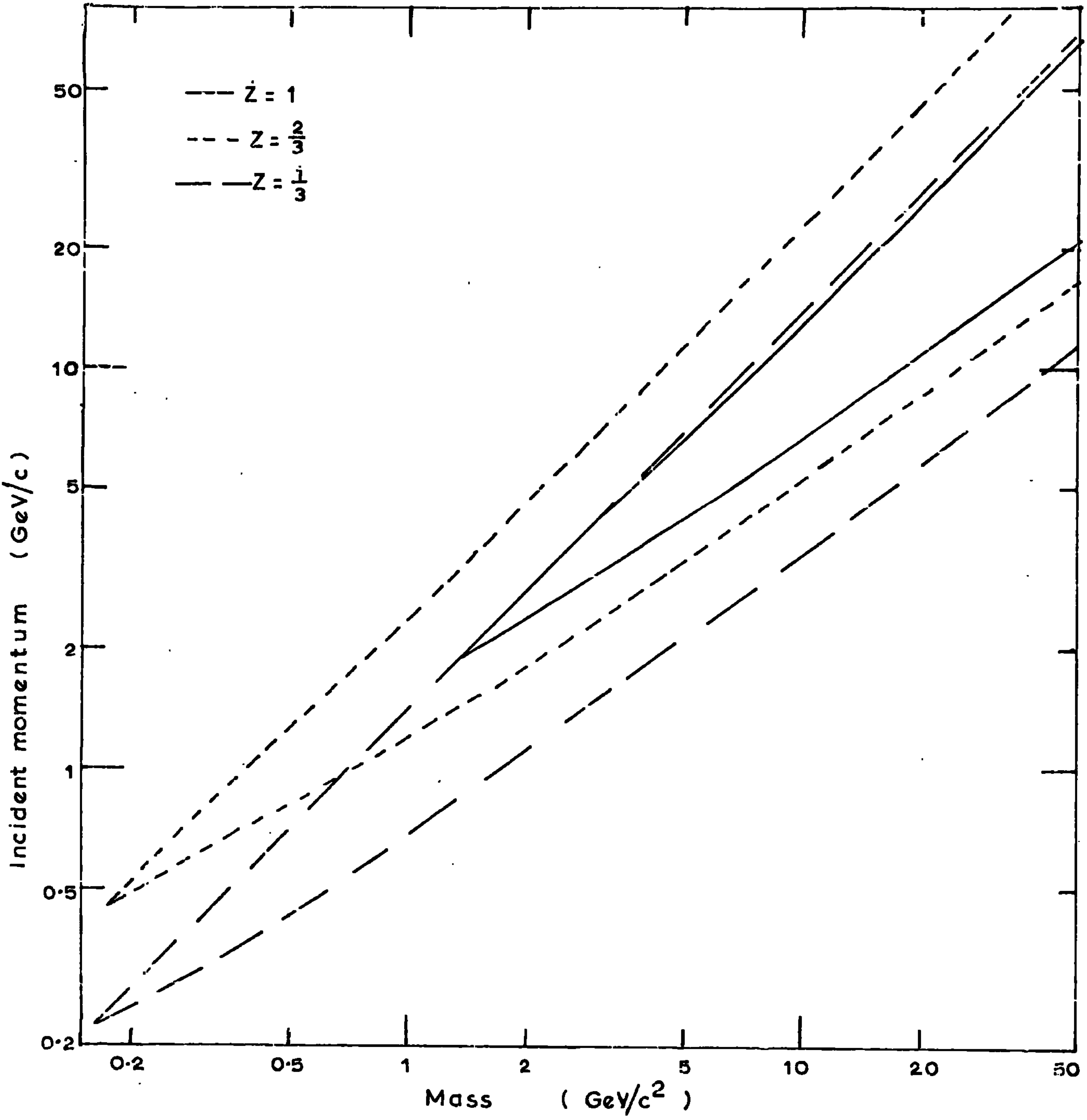

Figure 3.6 The incident momentum bands, as a function of the particle mass, accepted by the telescope for charges of e, $\frac{1}{3}$e and $\frac{2}{3}$e.

Correction for the inelastic interactions of deuterons in the telescope (see Section 3.3) gives the number of deuteron inelastic interaction lengths in the modified telescope as 5.64. In deriving the true incident deuteron intensity, consideration is also taken of the velocity selection efficiency of the Cerenkov counters as a function of incident momentum, which combined with the correction for interaction loss gives a true incident intensity of deuterons, $(4.8^{+6.8}_{-3.3})10^{-10}\mathrm{cm}^{-2}\mathrm{sec}^{-1}\mathrm{sterad}^{-1}(\mathrm{MeV/c})^{-1}$ at a mean momentum of 2.45 GeV/c. The statistical error has been broadened to include a 5% error on the number of inelastic interaction lengths and also a 1.5% error on the correction factor calculated to allow for the velocity selection efficiency of the Cerenkov counters as a function of momentum.

The d/p ratio is $3.4^{+4.8}_{-2.4}$ % at a momentum of 2.45 GeV/c, where the sea level, proton spectrum due to Brooke and Wolfendale (1964) has been used as a comparison.

3.5 The low energy, deuteron, sea level spectrum

3.5.1 The measured, low energy, deuteron, sea level spectrum

The observed, sea level intensities of deuterons, identified using an ionisation, residual range technique in two versions of the scintillator range telescope each defining different accepted momentum bands, are shown in Figure 3.7, with the sea level, proton spectrum of Brooke and Wolfendale.

3.5.2 Comparison with other workers

No other measurements on the deuteron intensity at sea level have apparently

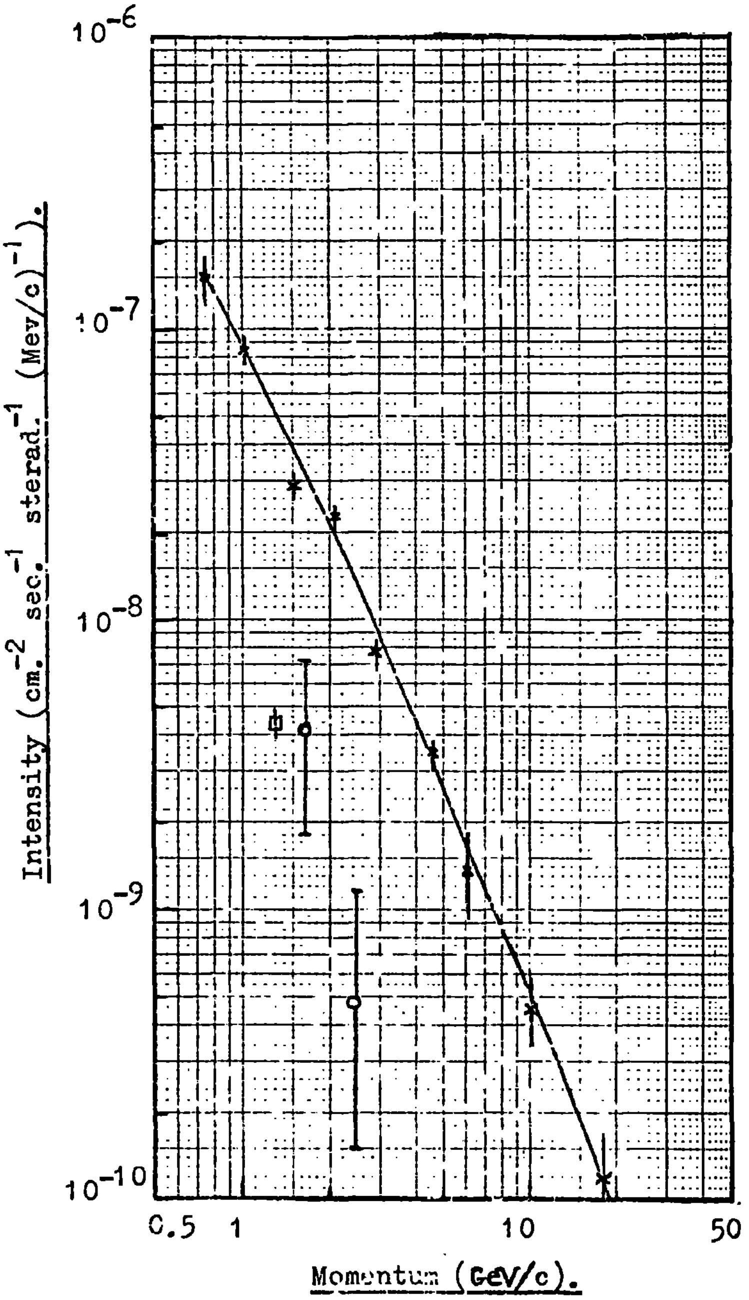

Figure 3.7 The measured sea level deuteron intensities (open circles) compared with the proton spectrum due to Brooke and Wolfendale (1964), (crosses). The measurement due to Badalian (1959), (full square) is included for completeness and was derived assuming the same d/p ratio to pertain at sea level as at 3200m. above sea level, the location of the latter measurement.

been made. However, measurements made by Badalian (1959) at 3200 metres above sea level yielded a d/p ratio of 8.6 ± 1.0% at a mean momentum of 1.3 GeV/c.

In the momentum region concerned, the d/p ratio is insensitive to atmospheric depth (concluded from the results on the nucleon momentum spectrum as a function of atmospheric depth by Schopper, 1967) and consequently the result of Badalian is directly compared to the sea level results in Figure 3.7. The d/p ratios are not found to be inconsistent. Further, the observed fall off with increasing momentum, plotted in Figure 3.8, is found to be consistent with the momentum dependence of the d/p ratio as calculated by Badalian (1959). Badalian predicted a d/p variance of $p^{-0.64 \pm 0.44}$ from a consideration of deuteron production by indirect and direct 'pick up' processes. In Figure 3.8 this d/p variation has been normalised to the measurement of Badalian at 1.3 GeV/c, for comparison with the measured d/p variation.

In a detailed consideration by Ashton et al. (1969a), it was concluded that the measured intensities of deuterons are a factor of ten greater than those expected from deuteron production processes in reactions such as,

$$N + N \rightarrow d + \pi.$$

This conclusion and apparent agreement between the d/p variations in Figure 3.8, not only substantiates the assumption that the heavy mass particles, observed in both experiments using the range telescope, are indeed deuterons, but further suggests that their production was via locally occurring 'pick up' processes.

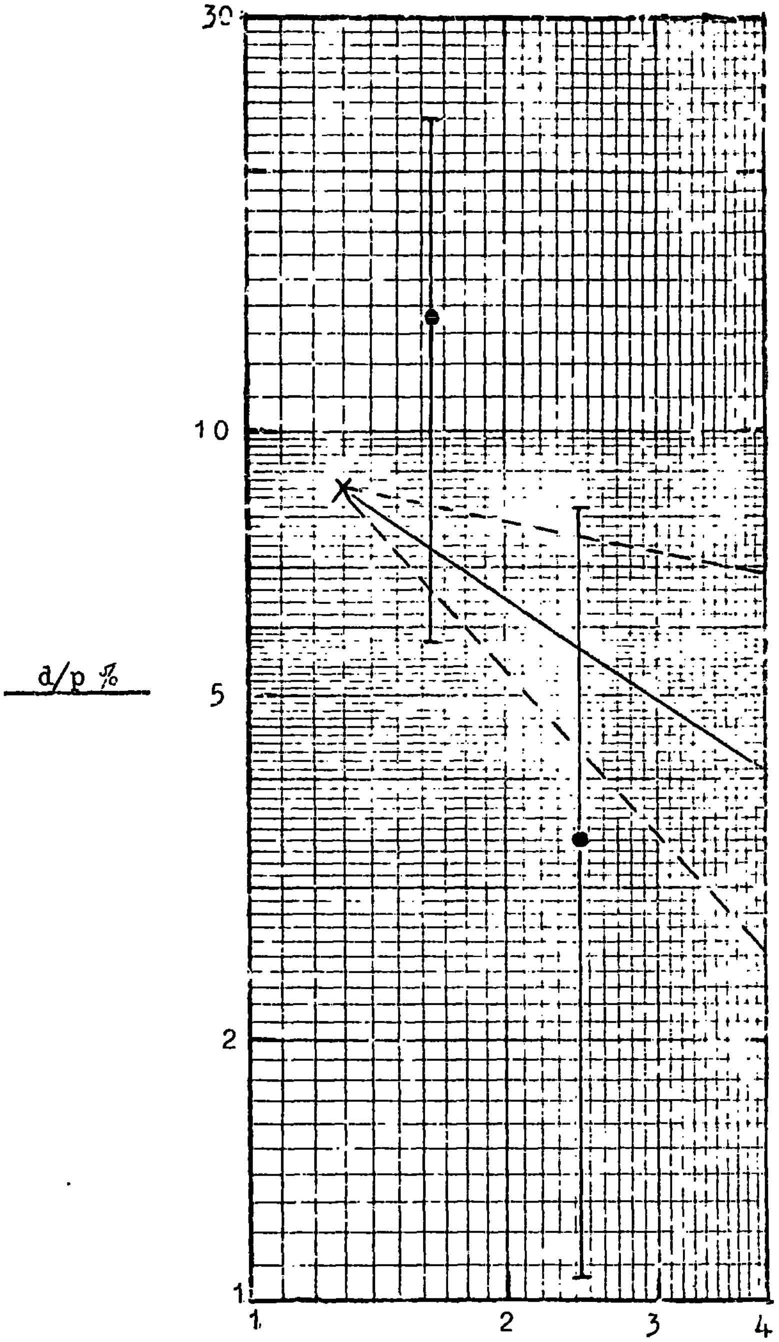

Figure 3.8 The measured d/p ratio compared with its calculated momentum dependence (Badalian, 1959). The d/p variation has been normalised to the measurement of Badalian at 1.3 GeV/c and the predicted momentum dependence varies as $p^{-0.64\pm0.44}$.

3.6 The Glashow U particle

3.6.1 Origin

Recent results on the angular distribution of cosmic rays underground by Bergeson et al. (1967), in the energy range 10^3 - 10^4 GeV, have led Callan and Glashow (1968) to propose the existence of a previously unknown U particle in the cosmic radiation. The U particles are suggested to be: stable, massive ($\gtrsim$ 4 GeV/c^2), singly charged, weakly interacting, and to be present to the extent of 10^{-3} of the normal primary component. Further it was suggested by Callan and Glashow that this ratio should be virtually energy independent.

3.6.2 Limits on the intensity of low energy U particles

Consideration, by Ashton et al. (1968a), on the mass distribution of low energy particles observed in the preliminary proton experiment, (Section 3.2), has placed an upper limit (with a 90% confidence) to the intensity of these U particles, with mass $\geqslant$ 3 GeV/c^2, of 1.5×10^{-10} cm^{-2}sec^{-1}sterad^{-1}MeV^{-1} in the near vertical direction at sea level and in the region of 700 MeV kinetic energies. Transforming to the top of the atmosphere, allowing for ionisation loss and comparing with the accepted primary proton intensity, gave an upper limit, to the fraction of U particles (mass $\geqslant$ 3 GeV/c^2) at 3 GeV kinetic energy, of 10^{-5}.

Similarly no evidence of the U particle manifesting the proposed properties has been revealed in the observed mass distribution obtained while selecting particles of mass > 1.3 GeV/c^2 ($z = 1$) in the heavy mass search (Section 3.4).

An upper limit (at a 90% confidence level) on the sea level intensity of these particles, for mass values > 1.3 GeV/c^2, is found to be 5.23 x 10^{-10} $cm^{-2}sec^{-1}sterad^{-1}$ assuming an isotropic incident flux. Allowing for ionisation loss through the atmosphere and comparing with the primary proton intensity, the upper limit to the U/p ratio, shown in Figure 3.9, varies from 4 x 10^{-8} to 2 x 10^{-7} for a U particle whose mass varies from 2 GeV/c^2 to 50 GeV/c^2. At a mass of 3 GeV/c^2 the U/p ratio is 3.6 x 10^{-8}. The corresponding momentum bands are shown in Figure 3.10.

The results from both experiments are inconsistent with a U/p ratio of 10^{-3} as proposed by Callan and Glashow. It is concluded that U particles, exhibiting the properties suggested initially, are not present in the cosmic radiation at the level suggested by Callan and Glashow.

Although this does not rule out the existence of these particles at higher energies, evidence by Ashton et al. (1968a) suggests that U particles do not exist up to sea level energies of 10^4 GeV either.

It is concluded that the explanation of the Utah results seems to be highly unlikely in terms of a massive, singly charged particle having no strong interaction with matter.

3.7 Limits on the intensity of low energy quarks

An upper limit to the intensity of quarks in the sea level cosmic radiation can be calculated from the results of the heavy mass search using a scintillator range telescope for mass determinations of low energy, cosmic ray particles with mass values > 1.3 GeV/c^2 (z=1). The velocity range over which quarks would

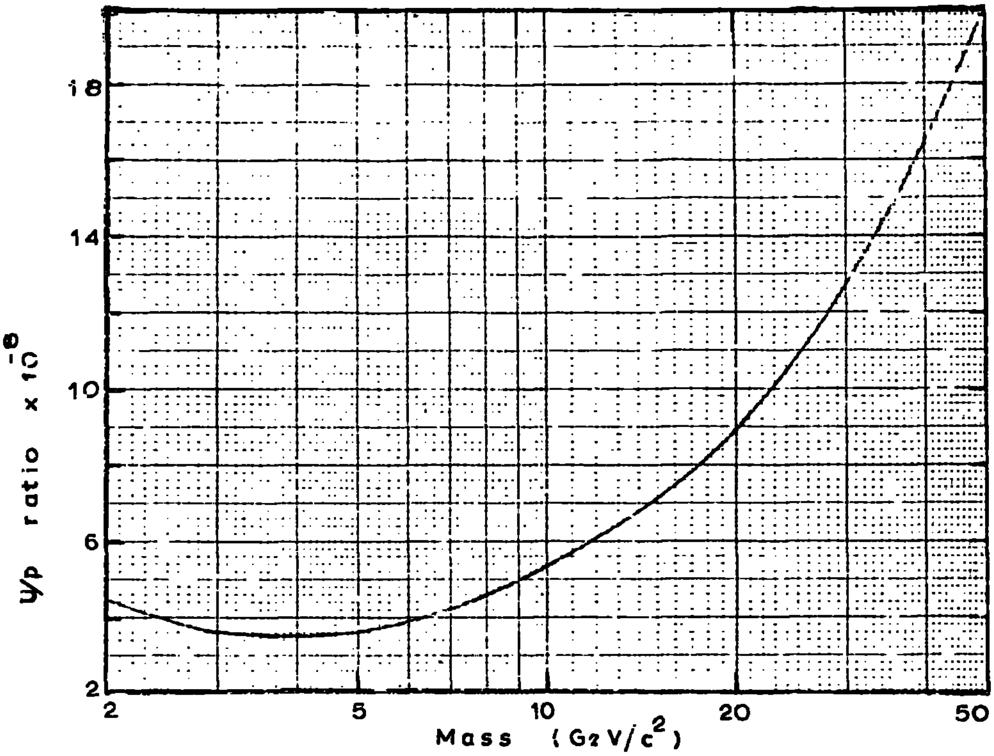

Figure 3.9 The limits at the 90% confidence level on the U/p ratio pertaining at the top of the atmosphere, in the momentum bands given below, as a function of the U particle mass.

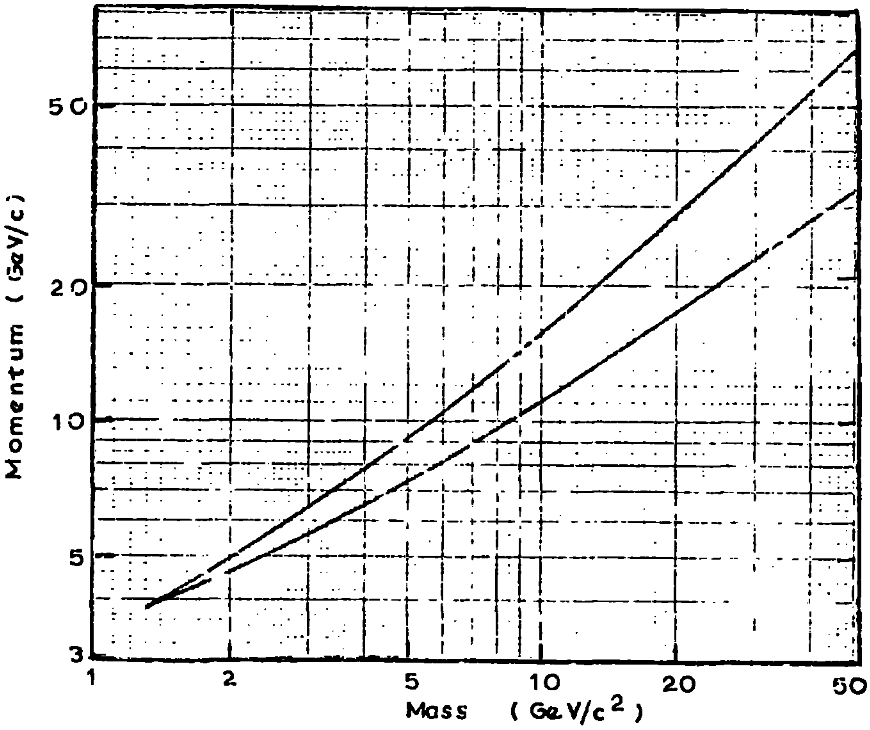

Figure 3.10 The momentum bands for unit charged particles, as a function of their mass, at the top of the atmosphere that would be accepted at sea level by the heavy mass telescope (assuming energy losses in the atmosphere due only to ionisation).

be detected in this experiment, are shown as a function of quark mass in Figure 3.11, for charges of e, 2e/3 and e/3.

Assuming that both particles detected are deuterons, the upper limit to the intensity of quarks, at a 90% confidence level, is 4.9 x 10^{-10}cm^{-2}sec^{-1} sterad^{-1}, over the velocity bands shown in Figure 3.11. If account is taken of quark inelastic interactions in the telescope, by assuming the quark-nuclei interaction to be identical to the nucleon-nuclei interaction and that all interacting quarks are lost, then the upper limit should be raised by a factor of ∿ 17, the total material in the telescope corresponding to 2.82 nucleon inelastic interaction lengths.

3.8 Conclusion

The search for low energy, heavy mass particles in the cosmic radiation by means of a large aperture, scintillator range telescope, although only setting upper limits on the intensity of quarks and U particles, has given definite information on the low energy, deuteron, sea level spectrum.

1. The upper intensity limits on the low energy U particles was placed at a level of ∿ 10^{-7} of the proton flux, in the range 2 - 50 GeV/c^2 of mass values. This was considered either insufficient to explain the observations of Bergeson et al. or to be indicative of a discontinuous spectrum of U particles.

2. An upper limit of 4.9 x 10^{-10}cm^{-2}sec^{-1}sterad^{-1} was placed on the observed quark intensity at a 90% confidence level and appears to be inconsistent with the intensity of 10^{-7}cm^{-2}sec^{-1}sterad^{-1} for the z=1, relativistic, triplet member as observed by Dardo et al. However, it may be that the present search for low energy, heavy mass particles is not sensitive to the relatively weakly

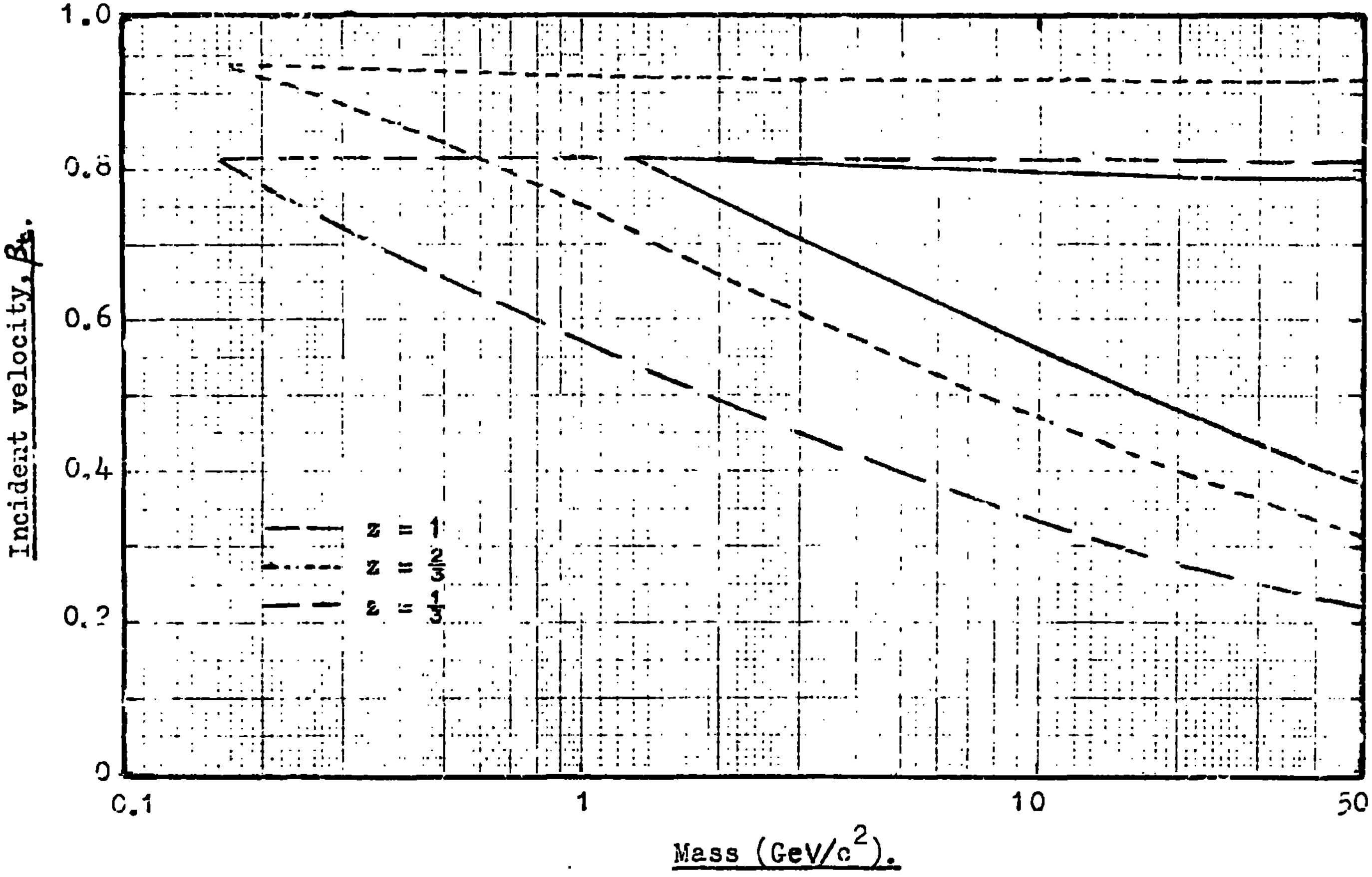

Figure 3.11 The incident velocity bands, as a function of the particle mass, accepted by the telescope for charges of e, $\frac{1}{3}$e and $\frac{2}{3}$e.

interacting, high energy particles observed by Dardo et al.

3. Deuteron mass and charge characteristics have been revealed by 6 events in the preliminary experiment and 2 events in the subsequent heavy mass search using a modified telescope. Their interpretation as deuterons is substantiated from the low energy, sea level, intensity agreements with other measurements in the same energy region. Further, the fall off in the observed deuteron spectrum with momentum is somewhat steeper than that of the proton spectrum and is consistent with that expected for deuteron production via 'pick up' processes.

Although the observed, heavy mass particles were assumed to be deuterons, it has recently been suggested by Friedländer (1970) that a reasonable mass estimate for the hypothetical triplet particles observed by Dardo et al. is of the same order as the deuteron mass. Friedländer concluded that, if the mass resolution of the particle detector was insufficient to distinguish them from sea level deuterons, then another method must be found to detect them.

With this in mind, it was thought that a technique which not only enabled determinations of the mass and charge but also the sign of charge, would allow the sea level deuterons to be distinguished from the stable members of the antitriplets, produced in high energy interactions of the type

$$N + N \rightarrow N + N + T + \overline{T} + nB \quad ,$$

which have subsequently slowed down to sufficiently low energies at sea level to enter the sensitive energy region of the detector.

(nB represent n number of bosons and T,$\overline{T}$ are the triplet and antitriplet).

Such a technique involving an air gap magnetic spectrometer and scintillators for momentum measurements, ionisation loss and time of flight measurements, is proposed in Chapter 4. The actual spectrometer and time of flight system used, is described in Chapter 5, with conclusions in Chapter 8 as to its expected performance in accepting and accurately identifying some familiar low energy, heavy mass particles in the cosmic radiation.

CHAPTER 4

DESIGN OF A PROTOTYPE MAGNETIC SPECTROMETER FOR THE MASS MEASUREMENT OF COSMIC RAY PARTICLES

4.1 Introduction

A technique was described in Chapter 2 for the mass and charge determination of cosmic ray particles slowing down in a scintillator range telescope. The main advantage of this technique is the very large aperture that can be employed, but it has the following disadvantages:

1. There is no information on the charge sign of the particle. This information is needed to enable the resolution of antiprotons. The extra parameter would also provide further evidence in the identification of the particles with mass $\sim$ 2 GeV/c^2 observed in the heavy mass search (Chapter 3). Doubt has recently been cast on their interpretation as deuterons, from a proposal by Friedländer (1970), that, if the heavy mass, delayed particles of integral charge observed by Dardo et al. (1968) are indeed the stable members of the fundamental triplet and anti-triplet, then a reasonable estimate of their mass is around 2 GeV/c^2.
2. The sizeable quantity of material ($\sim$ 2.82 nucleon inelastic interaction lengths in the heavy mass search) needed to slow down particles of mass > 1.3 GeV/c^2 (Z=1) before sufficient accuracy is obtained on the mass determination, accordingly: reduces the accepted rate of cosmic ray particles through the scintillator telescope if they are nuclear active, and increases the minimum value of the incident velocity needed by particles to traverse the telescope material (typically β = 0.5 for a

mass of 10 GeV/c^2, $Z = 2/3$). Because of the mode of mass determination, inaccurate mass estimates are obtained for nuclear active particles which have inelastically interacted in the telescope (but have continued on through the remaining scintillators), and for particles which have suffered a charge exchange in their observed stopping region. To eliminate the former spurious events, visual detectors, in the form of flash tubes are necessarily used throughout the telescope. The use of the range telescope is then much more suited to detecting weakly interacting particles.

To specify the properties of cosmic ray particles completely one should measure both the magnitude and sign of their charge, and also their mass. In principle this can be achieved from simultaneous measurement of their charge ze, their angular deflection ϕ in traversing a magnetic field and their velocity β. For a particle of velocity β, charge ze and momentum p, the rest mass is given by

$$m = \frac{p}{\gamma\beta C} \qquad 4.1$$

where

$$p = \frac{300z}{\phi} \int B\, d\ell \qquad 4.2$$

A further advantage of this technique is that beam material can be reduced to very small amounts, a factor of considerable importance if the particles under study are nuclear active, and thus allows a search for heavy mass particles (irrespective of their charge) in a velocity region not yet explored. For well known reasons velocity measurements become progressively more difficult with increasing particle energy and differing techniques are suitable for the various energy ranges.

For the particles of $\beta \approx 1$, velocity measurements will be inaccurate and some method must be found to measure their Lorentz factor $\gamma = \frac{1}{\sqrt{1-\beta^2}}$ directly. One such method is to use the increase in the most probable energy loss of charged particles with increasing Lorentz factor, in a gas.

For the experimentally most amenable energy range, that involving particles of low energy, time of flight measurements are suitable for velocity determinations. With these considerations in mind a prototype magnetic mass spectrometer has been constructed in which the initial experimental programme has been to concentrate on the study of low energy particles in which accurate velocity measurements can be made by time of flight measurements and charge estimations can be deduced from the measured ionisation losses in scintillation counters.

4.2 Error in the mass determination from momentum and time of flight measurements

An assessment of the error in mass determination is found by adding the errors due to momentum and time of flight measurements, in quadrature.

From equation 4.1

$$p = \gamma m v = \gamma m \beta c \qquad \text{where} \quad \gamma = \frac{1}{\sqrt{1-\beta^2}}$$

$$m = \frac{p}{\beta c} \sqrt{1 - \beta^2} \tag{4.3}$$

From equation 4.3

$$\frac{\partial m}{\partial \beta} = -\frac{p}{c} \frac{1}{\beta^2} \sqrt{\frac{1}{1 - \beta^2}}$$

$$\frac{\partial m}{m} = \frac{-1}{(1-\beta^2)} \frac{\partial \beta}{\beta} \tag{4.4}$$

also from 4.3

$$\frac{\partial m}{\partial p} = \frac{1}{\beta c} \sqrt{1 - \beta^2}$$

$$\frac{\partial m}{m} = \frac{\partial p}{p} \qquad 4.5$$

Adding 4.4 and 4.5 in quadrature gives

$$\frac{\delta m}{m} \doteq \left[\left(\frac{\delta p}{p} \right)^2 + \frac{1}{(1-\beta^2)^2} \left(\frac{\delta \beta}{\beta} \right)^2 \right]^{\frac{1}{2}} \qquad 4.6$$

As $\frac{\delta\beta}{\beta} = \frac{-\delta t}{t}$ where t is the measured time of flight over a specified distance

$$\frac{\delta m}{m} = \left[\left(\frac{\delta p}{p} \right)^2 + \frac{1}{(1-\beta^2)^2} \left(\frac{\delta t}{t} \right)^2 \right]^{\frac{1}{2}} \qquad 4.7$$

From equation 4.7 it can be seen that the factor $\frac{1}{(1-\beta^2)^2}$ limits the maximum value of β on which precise mass estimates can be obtained. The precision with which momentum can be measured, for a magnet of given $\int B d\ell$, is determined by the magnitude of multiple scattering produced by the finite amount of material in the region where the magnetic bending is measured. The $\int B d\ell$ attainable with the available magnet is considered in the following section.

4.3 Properties of the available air gap magnet

The available air gap magnet consists of a U shaped magnetic circuit, the pole faces being 45 x 45 cm square and their separation adjustable. The coils of the magnet are air cooled, the air being taken in from outside the building and redeposited there after passing over the magnet coils. As large an aperture as possible was required for the instrument, so the pole face separation was set to its maximum value of 38.1 cm.

For this gap of 38.1 cm, measurements were made of the magnetic induction B along a vertical line AY (see Figure 4.1), through the centre of the gap, for different values of magnet excitation current. The result is shown in Figure 4.2. All magnetic induction measurements were deduced from the fluxmeter deflection readings caused by the change in magnetic flux through a calibrated search coil. The value of $\int B d\ell$ was evaluated from Figure 4.2 for each magnet current and the results are plotted in Figure 4.3.

To determine whether a correction to the line integral of the magnetic induction was necessary for different positions of particle paths through the magnet gap, calibration of this integral was made for different intersection points of the vertical trajectory with AA', BB' and CC' (Figure 4.1). The results, shown in Figure 4.4, were taken with a magnet exciting current of 34.5 amp. The magnetic induction was found to be reasonably symmetrical about the line AX, but symmetry of the magnetic induction was assumed for positions about AA', as the construction of the magnet hampered any measurements of $\int B d\ell$ values in this area. As particle positions through the magnet gap were only recorded in the deflection plane, average values of $\int B d\ell$ were taken across the lengths AA', BB' and CC'. The result as a function of the distance along AX is shown in Figure 4.5, for a current of 34.5 amp.

A maximum error of $\sim$ 4% in $\int B d\ell$ is produced by taking a mean value of the line integral, equal to 2.51×10^5 gauss cm, for all three positions along

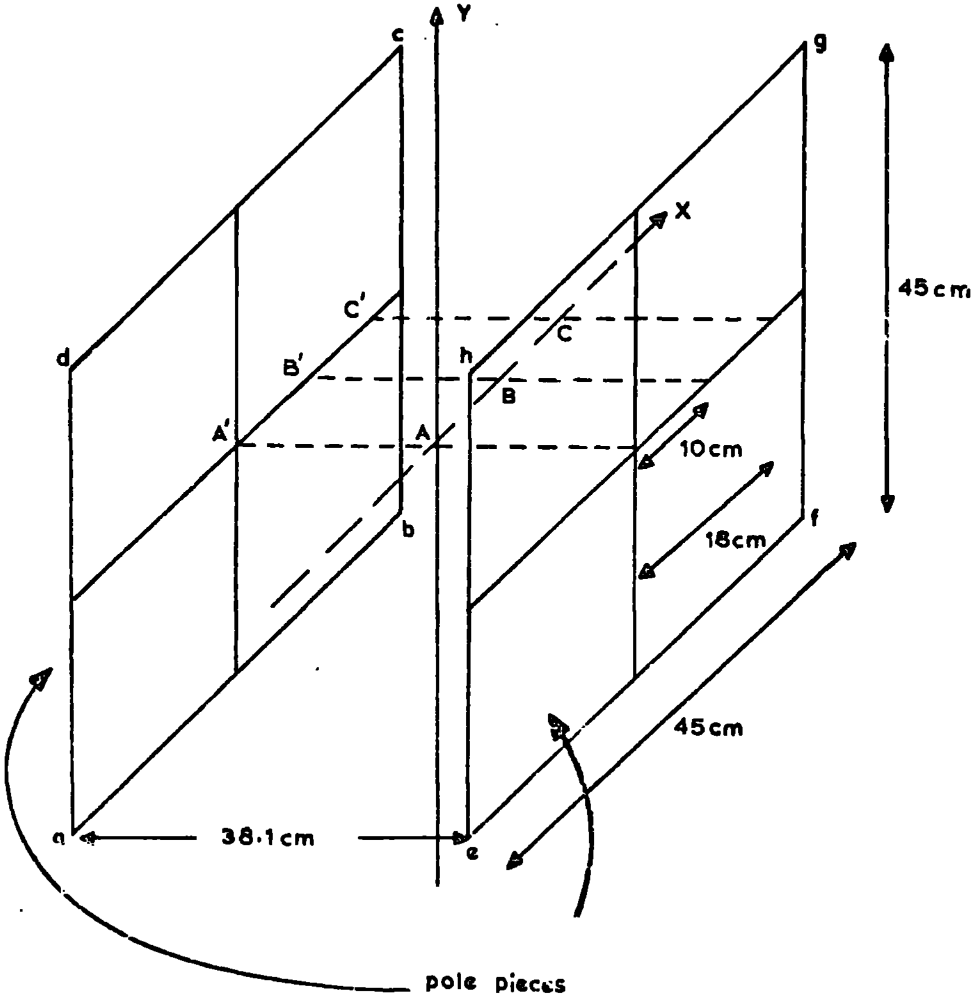

Figure 4.1 Diagram to illustrate the magnetic field calibration, where abcd and efgh are the pole faces of the air gap magnet.

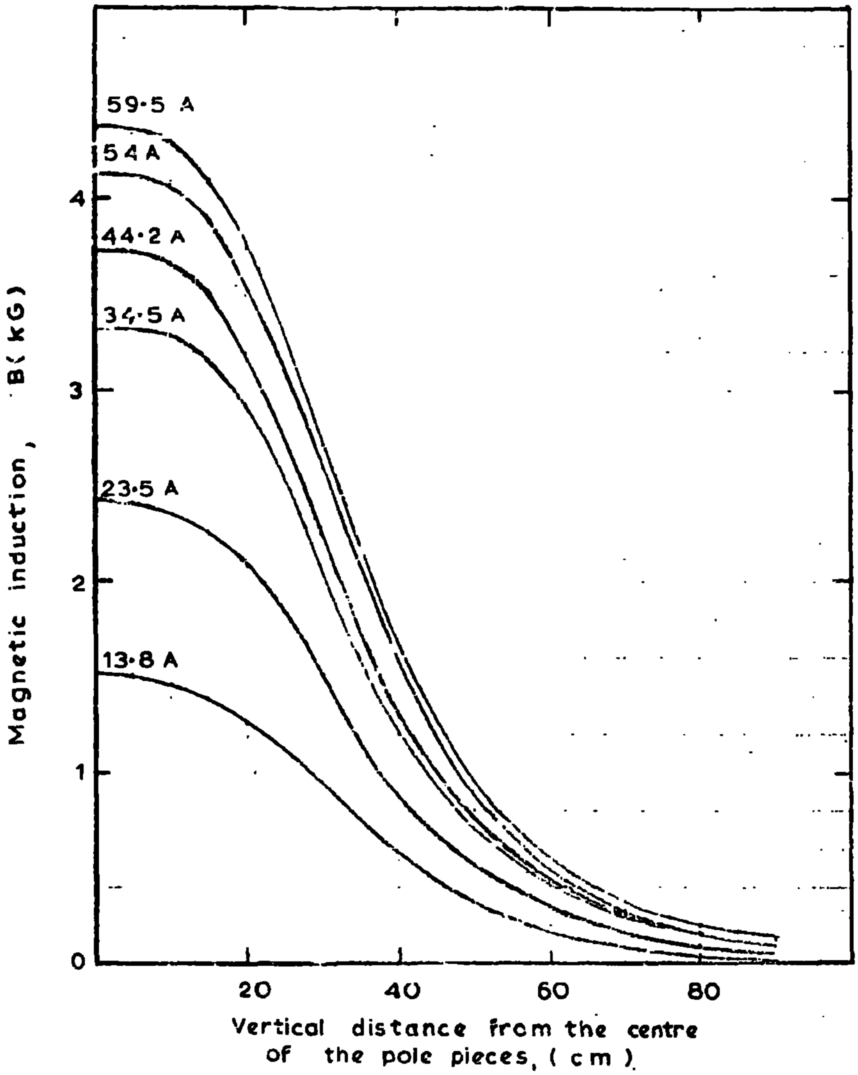

Figure 4.2 Measurements of the magnetic induction along a vertical line through the centre of the magnet gap, for various current values.

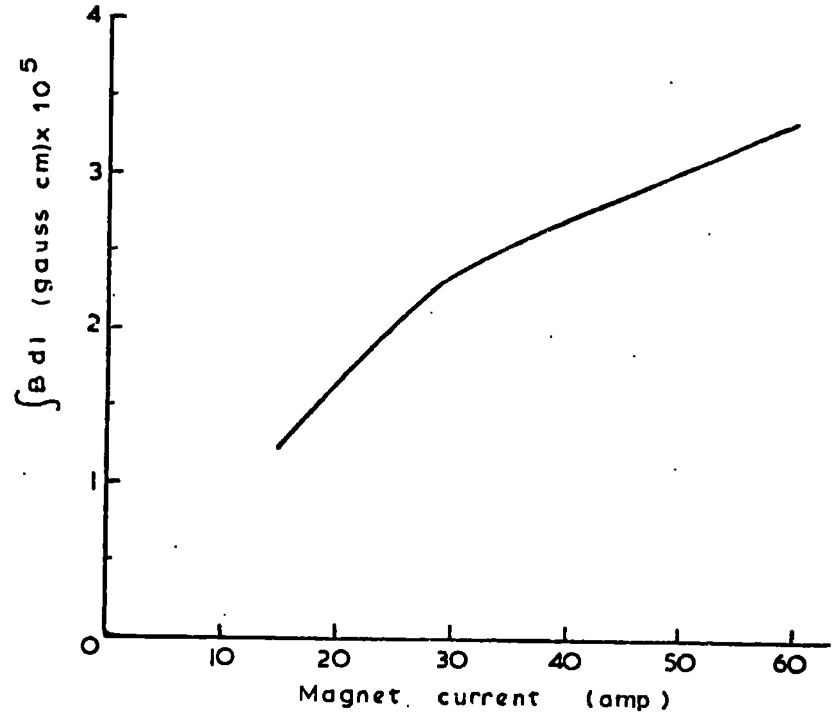

Figure 4.3 Variation of $\int$ Bdl with magnet current

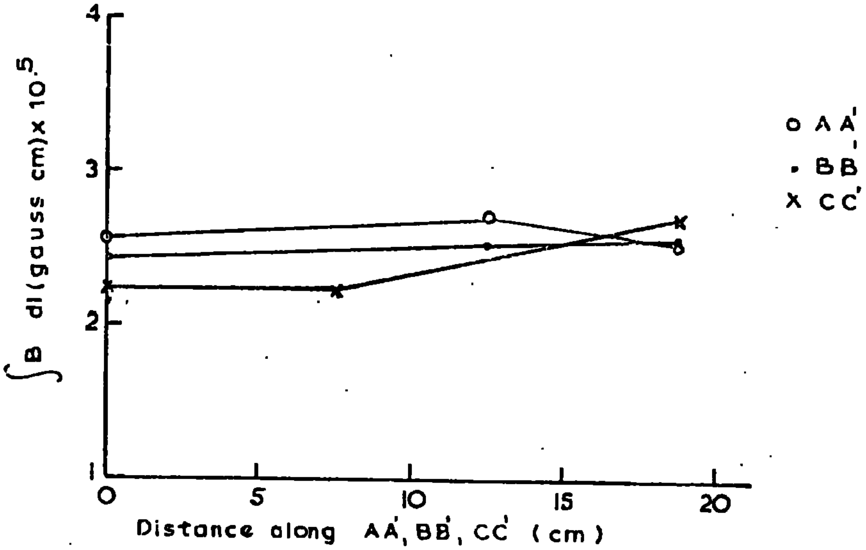

Figure 4.4 Variation of $\int$Bdl with position in the magnet field (I = 34.5 A).

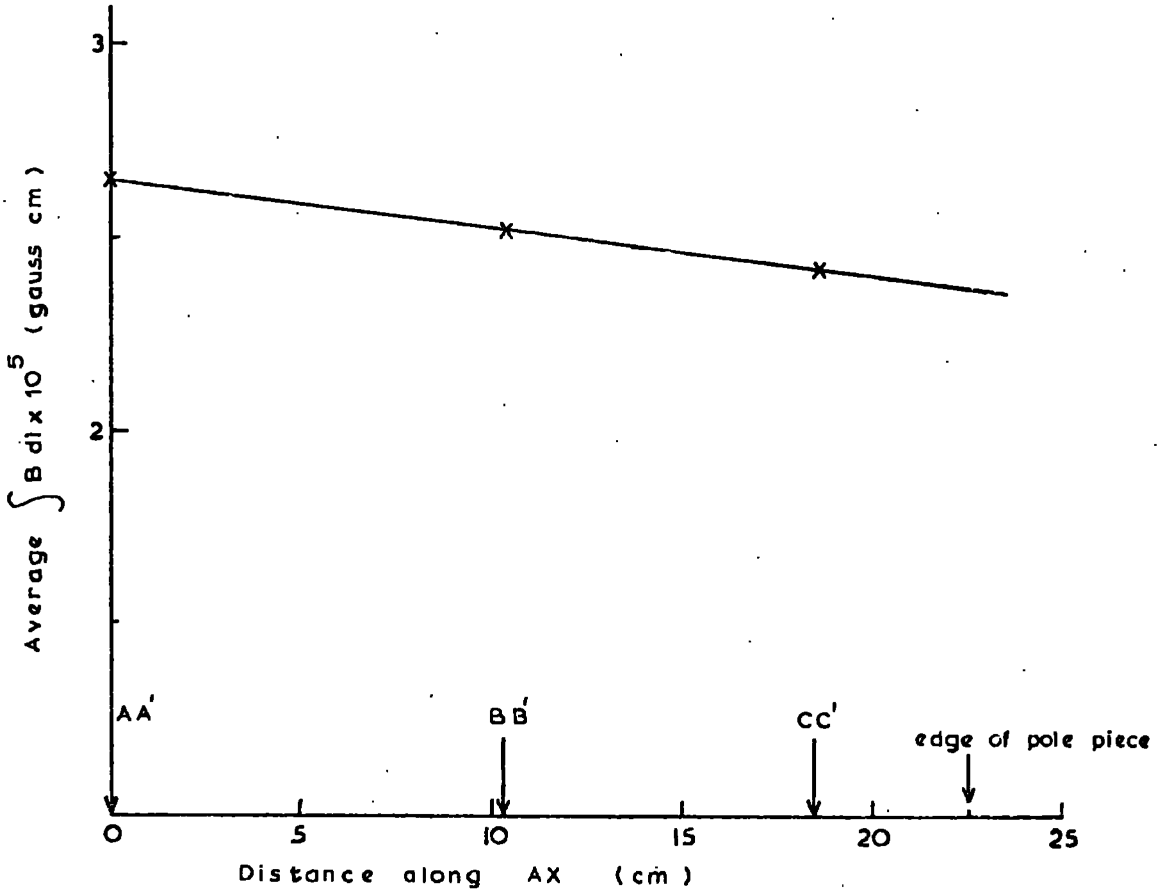

Figure 4.5 Variation of average $\int$Bdl along the magnet gap.

AX. Application of a correction factor to the momentum, for the various positions of trajectory intersections along AX, was considered unnecessary compared to the inaccuracies of the momentum determination caused by the multiple scattering (see section 5.11). The mean value of $\int B d\ell$ taken over the magnet area, is only 1.6% less than the value of 2.55×10^5 gauss cm (Figure 4.3) found for a vertical trajectory passing through the exact centre of the magnet gap. Finally, a graph of the average $\int B d\ell$ versus magnet current, for trajectories traversing any point in the magnet gap, is shown in Figure 4.6.

For the optimum momentum precision attainable for a particle with a certain momentum, the magnet field strength is set at the maximum value possible. Temperature recordings set an upper limit on the magnet current at an average I = 36 amp, for which the temperature of the cooling air after passing over the magnet coils was $\sim 37^{\circ}$C. For larger currents a burning smell was detected in the cooling air, due presumably to charring of the magnet coil insulation. For the same transformer tappings, at the maximum current setting, an average magnet current, I = 36.0 ± 0.2 amp, was found.

4.4 Limit on the amount of scattering material in the region where the magnetic deflection is measured

For a particle of momentum p and charge ze, its angular deflection on traversing a magnetic field is given by

$$\phi = \frac{300\, z \int B d\ell}{p} \quad \text{radians}$$

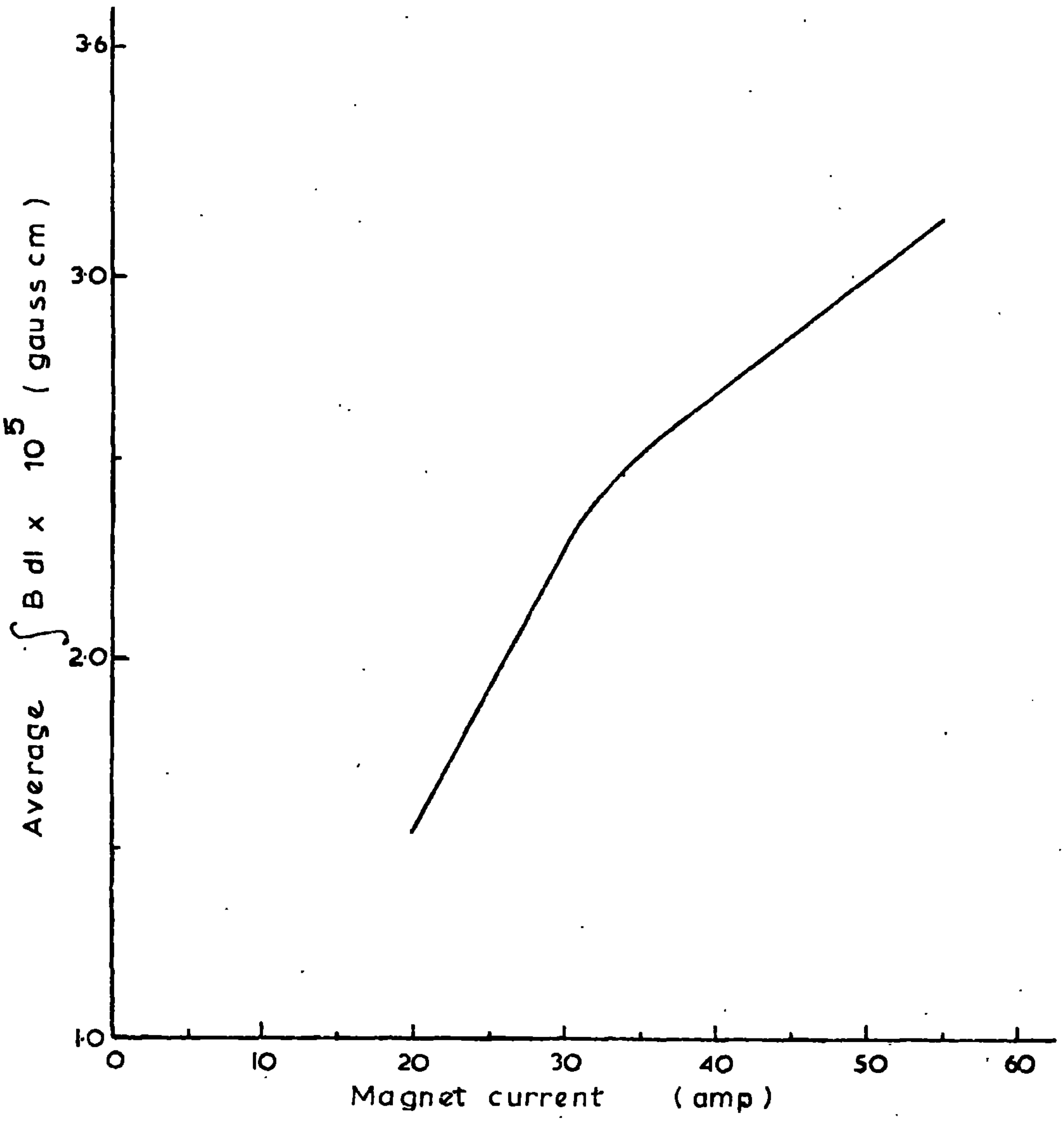

Figure 4.6 Variation of the average $\int$ Bdl with current, where the $\int$ Bdl is an average value taken from points over the magnet area.

where $\int B d\ell$ is in gauss cm and p in eV/c. For I = 36 amp from Figure 4.6, $\int B d\ell = 2.57 \times 10^5$ gauss cm.

Then

$$\phi = \frac{z \times 7.71 \times 10^7}{p} \text{ radians} \qquad 4.8$$

If the detectors used to measure the angular deflection of the particle produce a r.m.s. angle of scattering $<\theta>$, then

$$<\theta> = \frac{z \times 1.48 \times 10^7 \times t^{\frac{1}{2}}}{p\ \beta} \text{ radians} \qquad 4.9$$

where t is the thickness of the scatterer in radiation lengths and p is in eV/c. From equations 4.8 and 4.9

$$\frac{<\theta>}{\phi} = \frac{0.19\ t^{\frac{1}{2}}}{\beta}$$

If the position detectors locate the particle trajectory with negligible location error then

$$\frac{\delta p}{p} = \frac{<\theta>}{\phi} = \frac{0.19\ t^{\frac{1}{2}}}{\beta}$$

Then for $\frac{\delta p}{p} = 0.1$

$$t = 0.276\ \beta^2$$

$$t = 0.276 \qquad \text{for } \beta \approx 1$$

Thus to measure the momentum of a low energy particle, with $\beta \approx 1$, to a precision of $\leqslant 10\%$ with a magnet of $\int B d\ell = 2.57 \times 10^5$ gauss cm, the detectors producing the scattering, $<\theta>$, should contain material of thickness $\leqslant 0.276$ radiation lengths. As a 5 cm thick plastic scintillator is equivalent to 0.144 radiation lengths, it is seen that this condition could best be met using a single 5 cm thick, plastic scintillator in conjunction with spark chambers, utilising thin foil electrodes of negligible thickness (in radiation lengths), to perform the tasks of selecting the particles that pass through the magnet gap and locating their trajectories.

4.5 Abstract of the constructed mass spectrometer

With the above considerations in mind the mass spectrometer shown in Plate I and Figure 5.1 was constructed. Rather than measure the angular deflection of a particle in traversing the magnet, it was decided to measure the magnetic displacement, D (Figure 5.8), as this only required the flash tube trays $F2_a$, $F3_a$, and $F4_a$ to contain very accurately located tubes.

As nearly all penetrating cosmic rays at sea level are muons, with a mixture of ∿ 1% protons, ∿ 0.1% deuterons, and a probable lower composition of other particles, some method of mass selection needs to be incorporated into the spectrometer. This is accomplished using the Cerenkov counter C.T. (Figure 5.1), as described in Chapter 2. The time of flight counters A and D, are separated by 530.38 cm. With a timing precision of ± 1ns the expected error in velocity determination for particles of $\beta \approx 1$ is ± 5.7%.

A more complete description of the mass spectrometer and the actual precision of mass determination attainable is given in the next chapter.

CHAPTER 5

THE CONSTRUCTED MASS SPECTROMETER AND RESULTS OF THE ZERO FIELD RUN

5.1 Introduction

To specify the properties of low energy, cosmic ray particles completely, a different technique from that using a scintillator range telescope (as discussed in Chapter 2) incorporates the simultaneous measurement of particle momentum, ionisation loss and velocity, for the determination of mass, sign and magnitude of charge, of particles traversing an air gap magnetic spectrometer.

The mass spectrometer, shown in Plate I, was thus constructed to detect such particles and so to determine their associated properties. The momentum, sign of charge and magnitude of charge are derived from the observed deflection in the magnetic field and the measured ionisation loss in each scintillation counter (where momentum and charge are related according to equation 5.6). The velocity ensues from the time measured for a particle to travel 530.38 cm between scintillators A and D, (see Figure 5.1).

Calibration of the magnetic spectrometer and time of flight system, and calculation of the geometrical constants, was accomplished from the acceptance of relativistic muons (i.e. $Z = 1$) through the spectrometer in the zero field run (Chapter 5) and from the experimental measurement of the low energy muon spectrum (Chapter 6).

The limitations of the technique in its ability to accept and subsequently resolve low energy, massive (> 244 MeV/c^2) particles, with particular reference to the familiar particles of unit electron charge, are finally compared

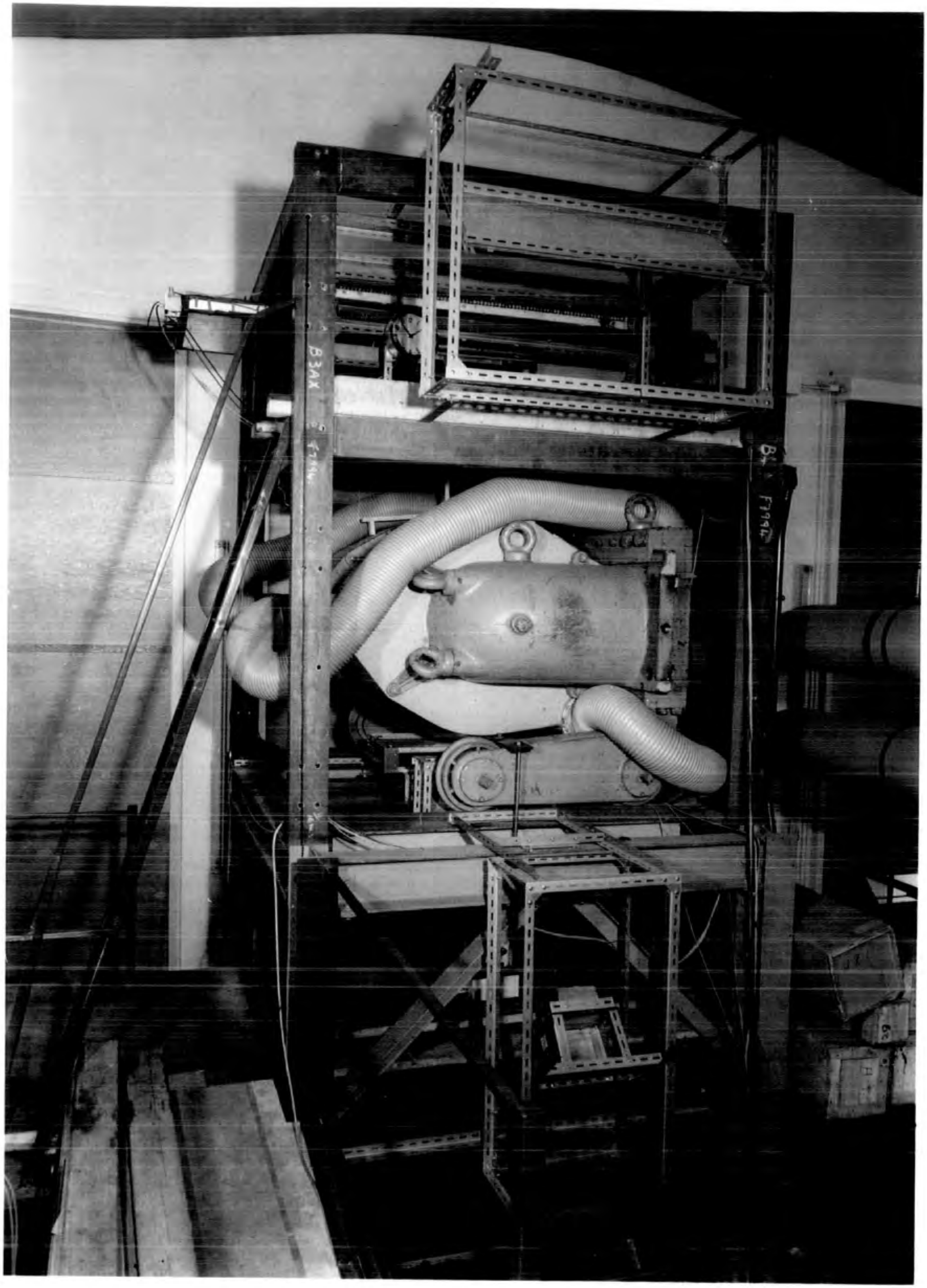

Plate I The mass spectrometer

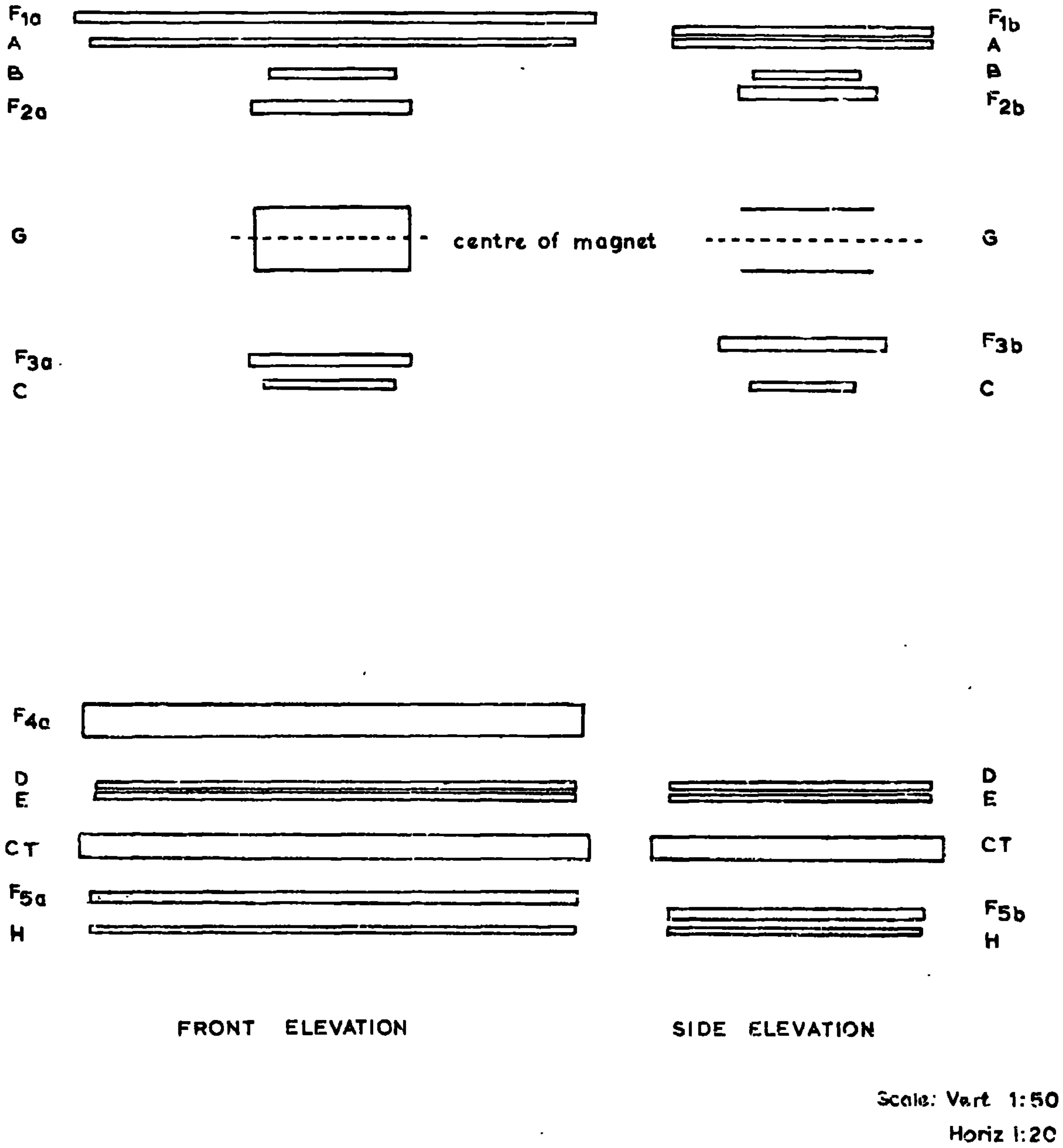

Figure 5.1 Scale diagram of the mass spectrometer.

(in Chapter 8) to the limitations exposed in the experiment using an ionisation, residual range technique (in Chapter 2).

5.2 General features

The mass spectrometer, shown in Figure 5.1, consists of a Blackett type, air gap electromagnet (as discussed in Section 4.3), with NE 102A scintillation counters at the levels A,B,C,D,E,H, a Cerenkov counter CT and nine neon flash tube trays, F1a, F1b, F2a, F2b, F3a, F3b, F4a, F5a, F5b.

The voltage pulse heights from the scintillation counters indicate the particle ionisation loss through the spectrometer. The output pulses from B,C,H are also used in coincidence to accept only penetrating particles, while the Cerenkov counter is employed as a velocity discriminator on these particles, in a similar role to that used in Section 2.2. The time of flight for each particle is derived from the difference in the arrival times of the pulses from scintillation counters A and D, separated by 530.38 cm. The incident and emergent trajectories are located at the three accurate measuring levels, F2a, F3a, F4a, where a refers to the (front) deflection plane. Background effects are in theory identified by the misalignment of the trajectory located by F1a and F2a coordinates, projected to the centre of the magnet, G, with the trajectory through F3a, F4a. Similarly F1b, F2b, F3b, F5b, side plane arrays are intended for a future use as an independent check on background effects, but are not operated in the experiment to be described.

5.3 Basic detectors

5.3.1 Scintillation counters

Essentially scintillation counters A,D,E and H are identical to those used in the scintillator range telescope, described in Chapter 2 , with their accompanying photomultipliers and resistance chains. The viewing positions of the photomultipliers on the scintillation counters A,D,E, and H, are shown in Figure 5.2a. The design and properties of these scintillation counters has been considered by Ashton et al. (1968). The negative output pulses from the anodes of the photomultipliers, at either end of the scintillation counters, are fed into an emitter follower. The outputs from the two emitter followers, at either end of each counter, are subsequently added.

The Mullard 56 AVP photomultipliers, viewing A and D scintillation counters, are used in the time of flight measurements (Figure 5.2a). Only small contributions to the output pulse widths arise from the 0.5 ns time spread of the 56 AVP photomultiplier. The photomultiplier also has the advantages of a high peak gain and a maximum spectral sensitivity of 4250 Å. The pulses of approximately 10 ns width are fed directly from the anode of the 56 AVP photomultipliers, in Figure 5.2b, into the Rutherford fast electronic units.

The small scintillation counters B and C are used in coincidence with scintillation counter H, and essentially restrict the paths of the particles to travel from B to H, through the magnet area (see Figure 5.1). The plan dimensions of the 5 cm thick counters, are shown in Figure 5.3. The Mullard 53 AVP photomultiplier viewing one end of each scintillation counter, B and C, is supplied with a positive supply voltage in a similar way to the

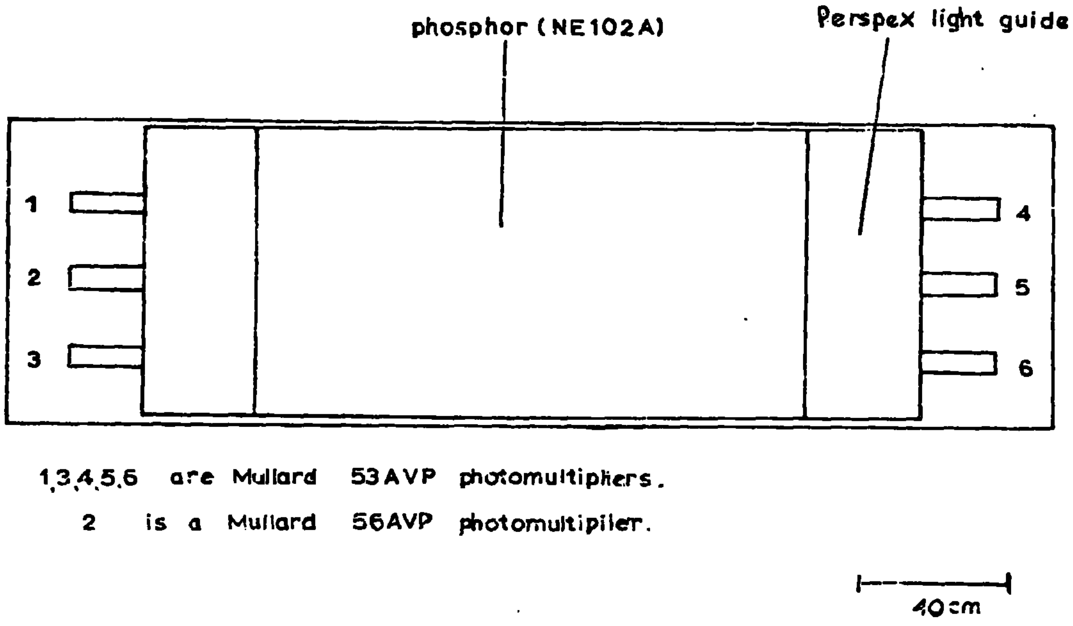

1,3,4,5,6 are Mullard 53AVP photomultipliers.
2 is a Mullard 56AVP photomultipiler.

Figure 5.2a Top view of a scintillation counter (A,D,E,H) showing the viewing positions of the photomultipliers.

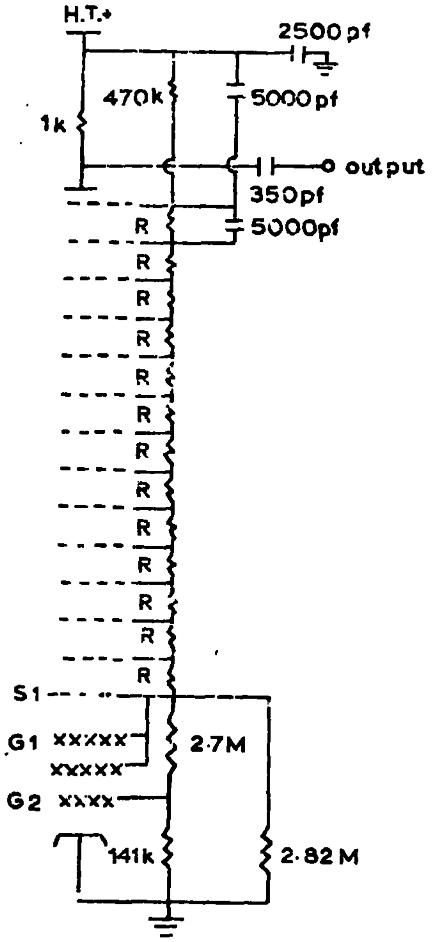

Figure 5.2b The resistance chain of the Mullard 56 AVP photomultiplier.

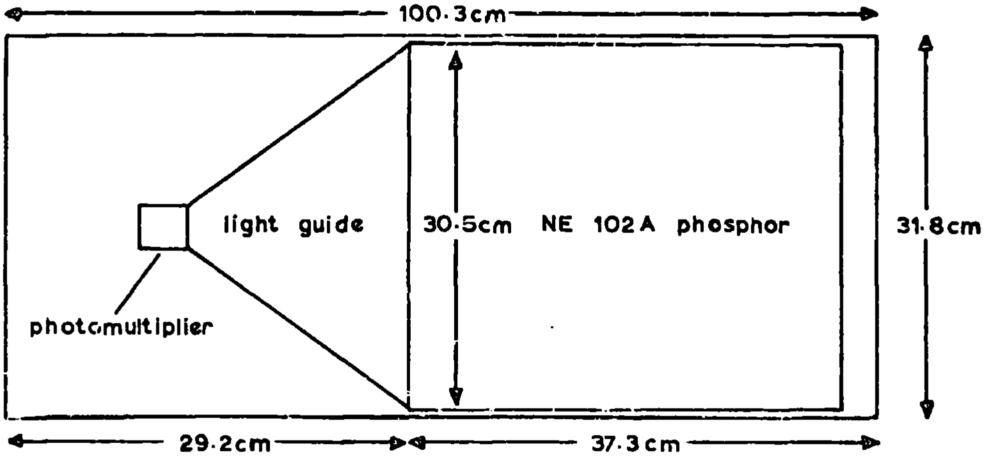

Figure 5.3 Plan view of the scintillation counters B and C. (not to scale).

counters A,D,E and H. Four sheets of 16 swg steel shielding cover the photomultipliers of B and C scintillation counters in an attempt to minimise the effect of the magnetic field on the multiplication process of the photomultipliers.

A positive supply voltage was assigned to each photomultiplier such that they all had the same gain.

As it was known that the majority of particles accepted through the spectrometer in the calibration experiment, were to be the familiar particles of unit electron charge ($Z = 1$) (e.g. muons, protons), it was considered unnecessary to measure the scintillator output pulse heights, for charge determinations, in this preliminary experiment.

5.3.2 Cerenkov counter

The roles of the Cerenkov counter in searching for low intensity, low energy, heavy mass particles in the cosmic radiation are two fold. Firstly, in providing an efficient means of discriminating against any unwanted, lower mass particles (e.g. muons, as described in Section 2.2). Secondly in providing an upper limit on the precision in the mass determinations. These aspects are more fully discussed in Sections 5.19 and 8.2. The design and properties of the Cerenkov counter have been reported by Ashton and Kelly, (1969).

In the calibration of the spectrometer with relativistic muons (in the zero field run and in the experiment to measure the low energy, muon spectrum, Section 5.4 to Section 7.13) the Cerenkov counter's velocity discrimination level was not operated.

5.3.3. Flash tube trays

The use of neon flash tubes in the recording of particle deflections in a magnetic spectrometer requires certain characteristics to be fulfilled for accuracy of operation. The essential qualities required are well known to be high efficiency, high spatial resolution, high time resolution, low spurious flashing and a large acceptance area coupled with low cost.

To achieve high accuracy of track location eight layers of tubes, staggered in the optimum arrangement as suggested by Kisdnasamy (1958) (Figure 5.4a) are used at the measuring trays F2a, F3a, F4a (Figure 5.1). The arrays, F2a, F3a, hold flash tubes of internal and external diameters, 0.59 cm and 0.77 cm, respectively. The design of the tubes (in F2a and F3a) to give maximum efficiency was considered by Coxell et al. (1960), and the flash tube array by Brooke (1964). The vertical distance between layers is 1.16 cm and the horizontal separation of the tubes, 0.799 cm. The original flash tube trays F2a, F3a, were modified by Dr. D. Alexander to achieve uniform brightness over all the eight layers of tubes. A brightener electrode was placed in between the layers of tubes to act as an extension of the original electrodes. The application of the high voltage pulse over the last few centimetres of tube was considered important in continuing the electron-photon discharge process and thus resulted in brightening the light output from the viewing end. It has been shown by Coxell et al. (1960) that high efficiency for trays F2a, F3a results from short time delays, of approximately 10μsec between the passage of the particle and the application of the high voltage pulse, and rise times of 0.5μsec. According to Coxell et al. the flash tubes could be operated on the plateau of efficiency with the application of electric

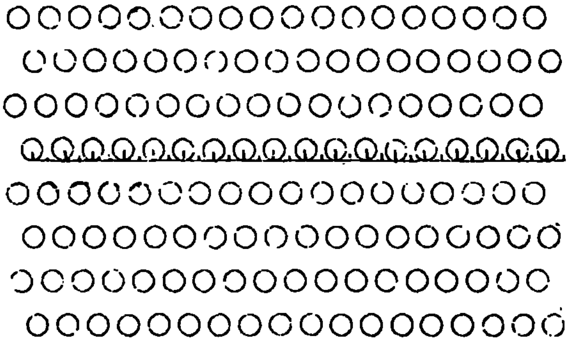

Figure 5.4a The optimum arrangement of the measuring tray flash tubes. (Kisdnasamy 1958).

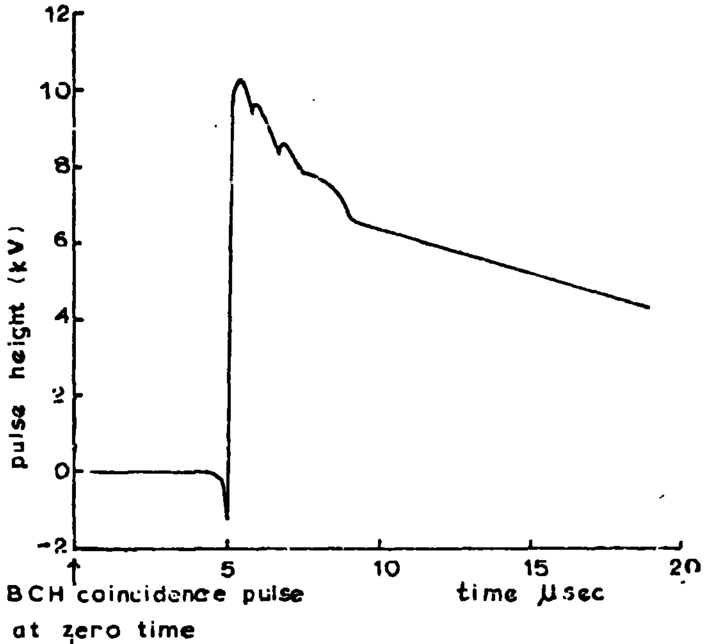

Figure 5.4b. F2a, F3a, high voltage tray pulse.

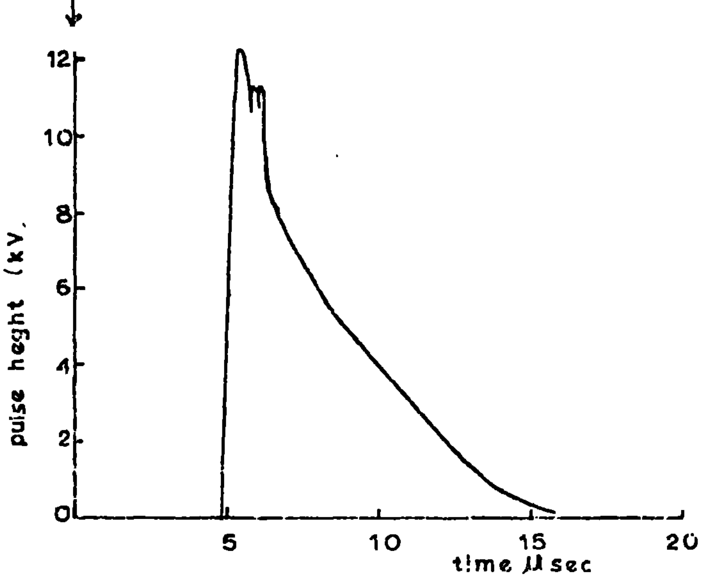

Figure 5.4c. F4a high voltage tray pulse.

fields such that 6 kV/cm was maintained for at least 2μsec. Excessive ripple on the high voltage tray pulse was found to cause breakdown across the brightener electrodes together with a decrease in internal efficiency. The requirements for high efficiency and hence small location errors are thus met sufficiently with the tray pulse shown in Figure 5.4b at a time delay of ∿ 5μsec. The resulting internal efficiencies of F2a, F3a were observed to be 85% and 80%, respectively.

The flash tube array F4a (Figure 5.1) also supports eight layers of staggered flash tubes. The tube supports are constructed such that the tubes resting in the tufnol slots are parallel to the side of the supporting frame and the position of each tube is known to 0.1 mm. The tubes are of average internal diameter, 1.55 cm, and encase 60 cm mercury pressure of commercial grade neon. The horizontal and vertical separations between the tubes are 1.91 cm and 2.79 cm, respectively. An internal efficiency of 96% resulted from the tray pulse shown in Figure 5.4c being applied to the electrodes of F4a, at a time delay of ∿ 5μsec.

The flash tube trays F1a, F5a (Figure 5.1) only support four layers of flash tubes. These trays were used in the scintillation counter telescope described in Chapter 2, and their properties and design have been considered by Ashton et al. (1968). If the F1a coordinate was also used to locate the particle trajectory, then the advantage of an increased accuracy in determining the deflection of a trajectory from four measuring levels, would be overwhelmed by the larger positional uncertainty in the location of a particle trajectory in the flash tube tray, F1a. A discrepancy measurement (see Section 6.7) at the centre of the magnet, G, in Figure 5.1, however provides information about the contribution of background accompanyment, (i.e. 'separate track' events). A best internal efficiency of 30% and 77% for F1a and F5a, respectively, however, in practice, limited their use in discrepancy cut off evaluations. The flash tube tray F1a was not operated in the zero field run but was in subsequent experiments.

5.3.4 The flash tube pulsing circuits

High voltage pulses of short time delays and rise times, are applied across the electrodes of the flash tube arrays via the circuits shown in Figures 5.5, 5.6 and 5.7. The low voltage trigger unit comprises a valve monostable and a BTY87 thyristor circuit. The output pulse from the thyristor anode is then transformed to trigger the high voltage spark gap pulsing unit. Since each type of tray requires different high voltage pulse heights, four spark gaps are used to supply the flash tube electrodes. The resistance R_j in series with the output of each spark gap, is designed to act as a compromise in satisfying the conditions of short rise times and low ripple contribution on the rising edge of the pulse, especially important for F2a and F3a. The values used for the series resistances, and the approximate high voltage pulse height for each tray, are shown in the table accompanying Figure 5.7.

5.4 The zero field run

To obtain the mass and the associated mass precision of an accepted particle, it is necessary to ascertain the precisions attainable in the observed displacement and time of flight values. The relativistic muon flux was employed to determine these precisions and the geometrical constants of the spectrometer, in a zero field run.

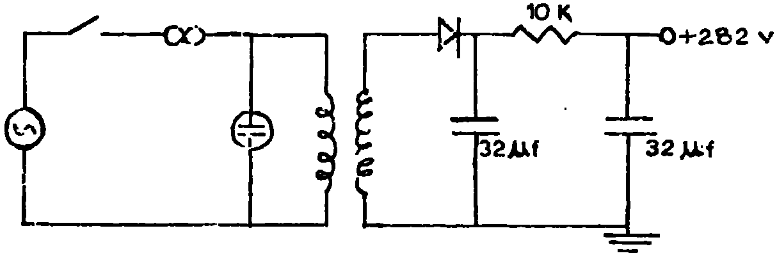

power supply to monostable

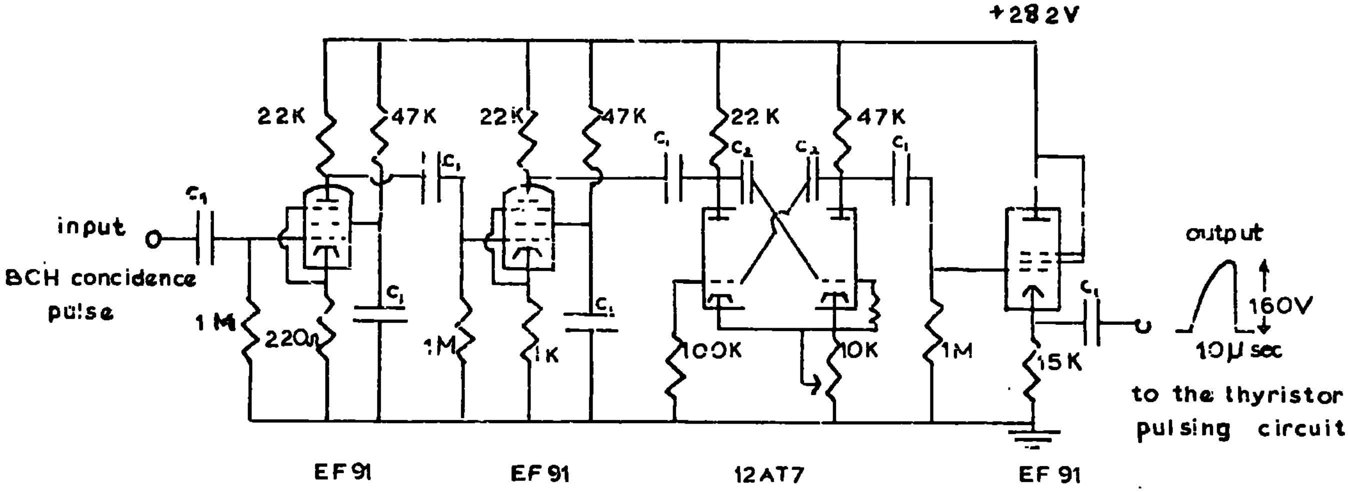

$c_1 = 0.1\ \mu f$

$c_2 = 100 pf$

Figure 5.5 Valve monostable.

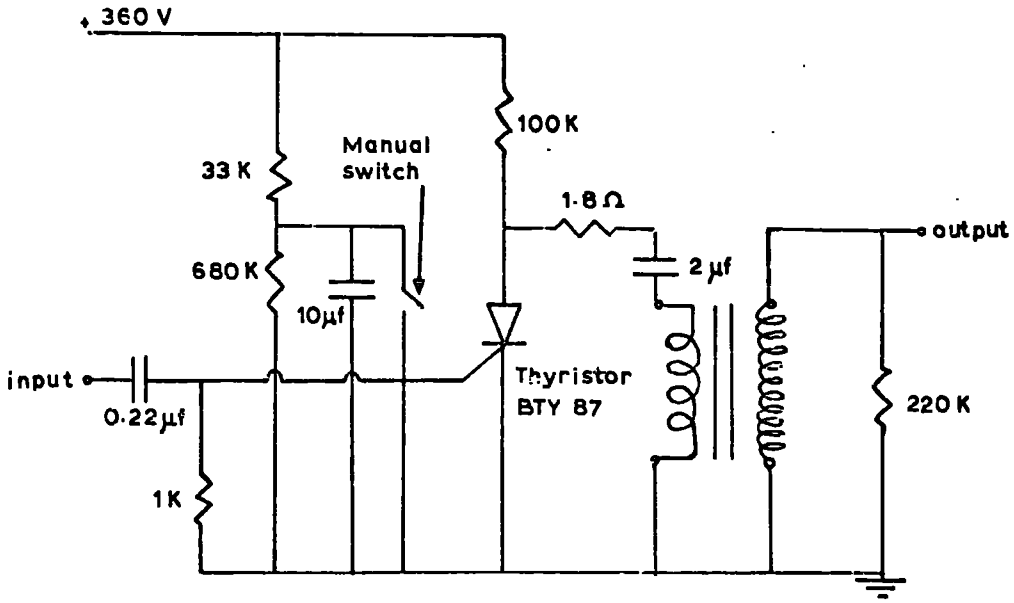

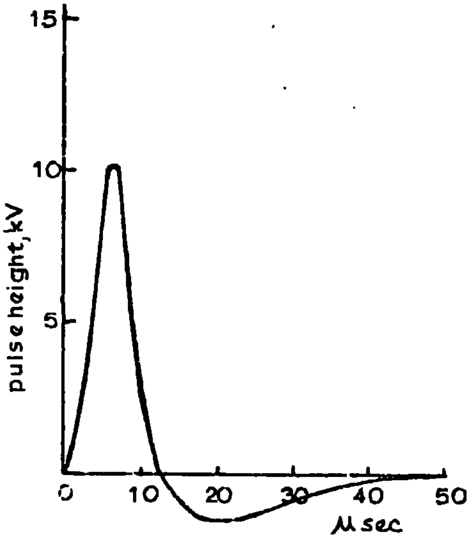

Output pulse profile from the thyristor pulsing circuit which subsequently triggers the spark gaps shown in Figure 5.7

Figure 5.6 Thyristor pulsing circuit.

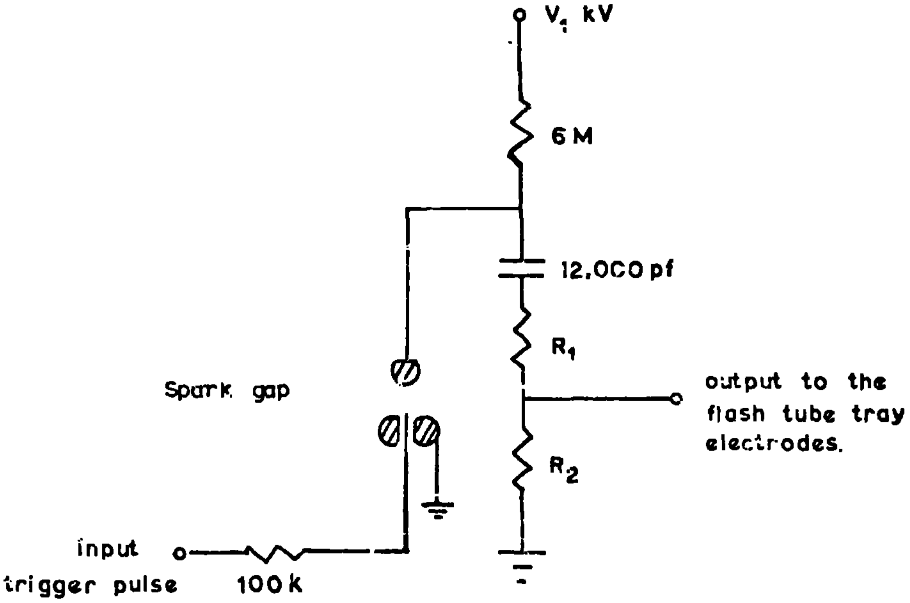

Table of component values used in the above circuit for each of the flash tube trays F1a, F2a, F3a, F4a, F5a.

Flash tube tray	High tension voltage, V_1 kV.	R_1	R_2	Tray voltage pulse height, $+V_2$ kV.
F1a	-14·0	—	500Ω	∼ 13
F2a	-17·4	141Ω	3·45 k	∼ 10
F3a	-17·4	141Ω	3·45 k	∼ 10
F4a	-14·0	47Ω	1 k	∼ 12
F5a	-14·0	—	500Ω	∼ 13

Figure 5.7 Spark gap high voltage pulsing unit.

For precise measurements of the displacement it is necessary both to align all the flash tubes in the three measuring trays to be parallel and to determine a quantity Δ_o accurately. Δ_o is a constant dependent on the relative horizontal displacements of the measuring trays. Acceptance of muons, satisfying a BCH coincidence requirement (Figure 5.8), through the spectrometer in a zero field run was used as a check on the value of Δ_o obtained from direct measurements of the lengths involved.

5.5 Momentum determination

Referring to Figure 5.8, the quantity required for the determination of the particle momentum is the displacement, D. The relation between the displacement D in cm and the angular deflection, ϕ radians, for small incident angles to the vertical, is given by

$$\phi = \frac{D}{\ell_1} \qquad 5.1$$

assuming that all the deflection takes place at the centre of the magnet and where ℓ_1 is the separation between F2a and the magnet centre, G. If a_2, a_3, a_4 are the distances from tube zero in the flash tube trays, F2a, F3a, F4a to a fixed reference line, and x_2, x_3, x_4 are the corresponding intersection coordinates of the trajectory, also measured with respect to tube zero. Then according to the geometry depicted in Figure 5.8

$$\theta_2 = \frac{a_3+x_3-x_4-a_4}{\ell_3}$$

and $$a_2+x_2+D = a_4+x_4 + (\ell_1+\ell_2+\ell_3)\theta_2$$

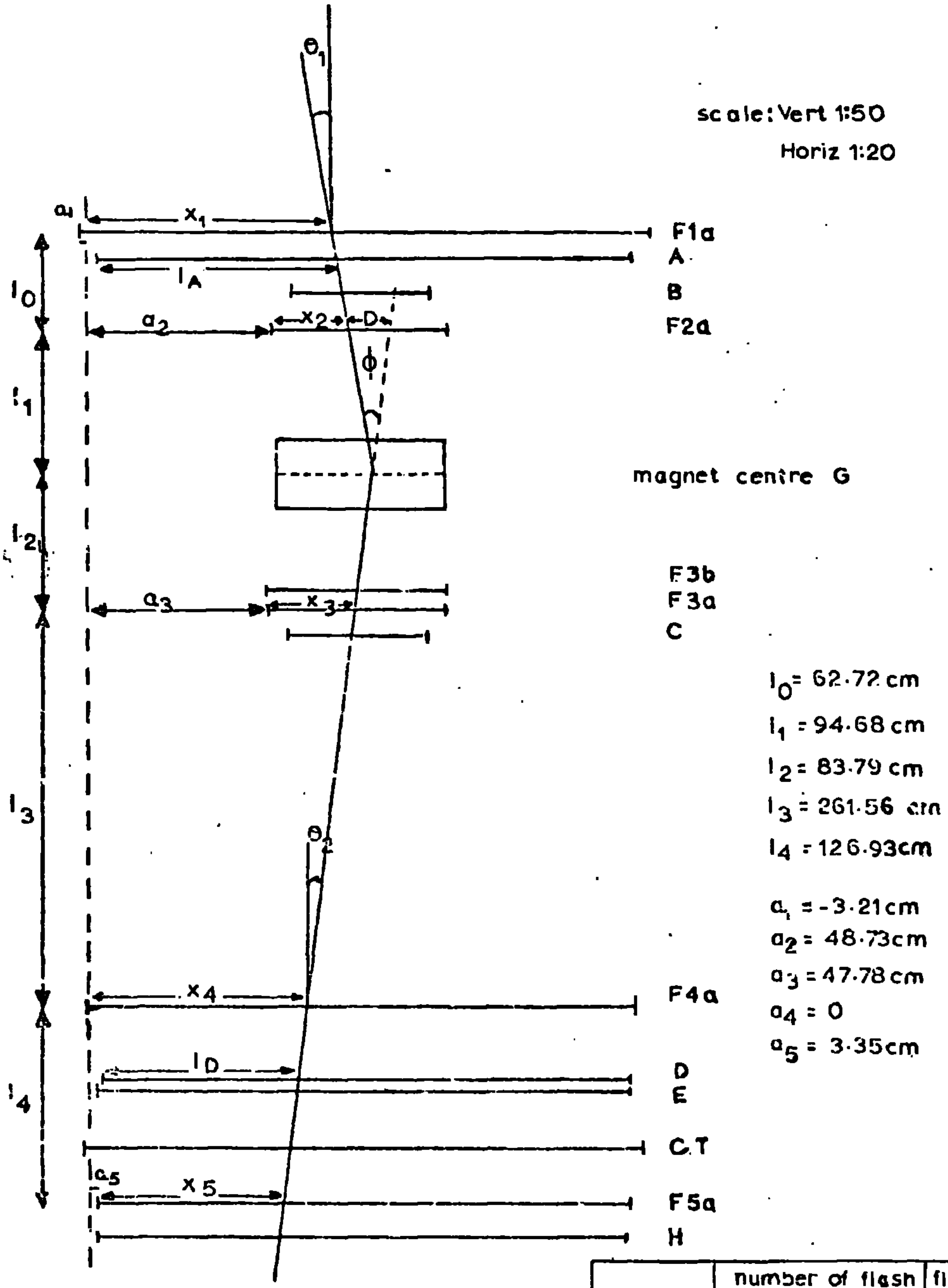

l_0 = 62·72 cm
l_1 = 94·68 cm
l_2 = 83·79 cm
l_3 = 261·56 cm
l_4 = 126·93cm

a_1 = -3·21cm
a_2 = 48·73cm
a_3 = 47·78cm
a_4 = 0
a_5 = 3·35cm

tray	number of flash tubes per layer	flash tube separation
F1a	85	1·80cm
F2a	60	·799cm
F3a	61	·799cm
F4a	77	1·905cm
F5a	79	1·80cm

Figure 5.8 The spectrometer dimensions.

From the above two equations

$$D = (x_4-x_2) + \frac{\ell_1+\ell_2+\ell_3}{\ell_3}(x_3-x_4) + (a_4-a_2) + \left(\frac{\ell_1+\ell_2+\ell_3}{\ell_3}\right)(a_3-a_4) . \qquad 5.2$$

Substitution of the appropriate dimensions from Figure 5.8 gives

$$D = x_4-x_2 + 1.682\ (x_3-x_4) + (1.682\ a_3)-a_2 \qquad 5.3$$

or $$D = \Delta + \Delta_o \qquad 5.4$$

where $\Delta = 1.682x_3-x_2-0.682x_4$ and $\Delta_o = (1.682\ a_3)-a_2$

and x_2, x_3, x_4, a_2, a_3 are in cm.

In measuring x_2, x_3, x_4 from the photographic film it is convenient to measure x_2, x_3 in units of 0.799 cm (flash tube spacings) and x_4 in units of 1.905 cm. In this case

$$D = 1.344\ x_3 - 0.799\ x_2 - 1.299\ x_4 + \Delta_o \text{ cm} \qquad 5.5$$

where x_2, x_3, x_4 are expressed in tube separations.

For a particle of momentum p in GeV/c and charge ze, its angular deflection ϕ, on traversing a magnetic field is given by

$$\phi = \frac{300 \times 10^{-9} \times z \times \int B d\ell}{p} \text{ radians} \qquad 5.6$$

where $\int B d\ell$ is in gauss cm. Substitution of equation 5.1, then enables the momentum to be determined from the observed displacement D

$$p = \frac{2.84 \times 10^{-5} \times z \times \int B d\ell}{D} \text{ GeV/c} \qquad 5.7$$

where D is in cm and $\int B d\ell$ in gauss cm.

The following conclusions are to be drawn from the distribution in delta values of muons accepted in the zero field run:

(1) The mean of the measured distribution in Δ values (equation 5.4) obtained for relativistic muons satisfying the coincidence and selection criteria of the zero field run (Sections 5.7, 5.8.2) provides a value of Δ_o for comparison with that from direct measurement.

(2) As the width of the Δ distribution (Section 5.11) is composed of contributions from multiple scattering in the spectrometer and location precisions of measurements at each level, a calculation of the former contribution and observation of the total width, enables an estimation of the location precision at each measuring level. This subsequently allows the precision of the momentum determination as a function of particle momentum to be calculated.

5.6 Alignment and direct measurement of Δ_o

The distances involved in Δ_o (i.e. the spectrometer dimensions in Figure 5.8) were each measured directly on the spectrometer, to an accuracy of 0.1mm. This was a by-product of the alignment of the instrument, during which the flash tubes were made parallel to each other. The detectors were positioned symmetrically with respect to the magnet area, with the aid of four corner plumb bobs. All the vertical distances in Figure 5.8 are measured from:

(1) the bottom of the fourth row of flash tubes for F2a,F3a and F4a.

(2) the bottom of the second row of flash tubes for F1a, F5a.

(3) the phosphor surfaces of the scintillation counters.

(4) the water surfaces of the Cerenkov counter.

The horizontal distances take the centre of the tube zero in F4a as a common reference line to similar reference points in the different flash tube trays.

Mean values of the above distances gave a value,

$$\Delta_o = 31.62 \pm 0.17 \text{ cm from direct measurement} \qquad 5.8$$

The mean flash tube separations are shown in the table with Figure 5.8, measured to an accuracy of 0.01 mm with the exception of Fla and F5a which are quoted to an accuracy of 0.1 mm.

5.7 Electronics and recording system of the zero field run

Relativistic muons were selected by the Rutherford fast electronic equipment. The logic shown in Figure 5.9a demands a BCH coincidence with a resolving time of 55 ns. There is no offsetting of B, C or H channel pulses at the first coincidence, for transit times of relativistic particles. The discrimination levels of B, C, H were all set at $0.2E_s$, where E_s is the most probable pulse height produced by a relativistic muon in a G calibration of the spectrometer (see Section 2.5).

The three fold coincidence pulse was then used to trigger: (Figure 5.9a)

(1) the time base of the time of flight Tektronix 519 oscilloscope.

(2) a 200 ms pulse generator, which was used as a veto in the BCH coincidence and was designed to cover the time delay before the paralysis of the cycling system began to operate.

(3) the monostable to the flash tube high voltage pulsing unit.

(4) the cycling system trigger (Figure 5.9b) and hence the cycling system motor. The cycling system operated:

    (a) a paralysis for the coincidence input.
    (b) the illumination of the fiducial crosses on the end of the flash tube trays.

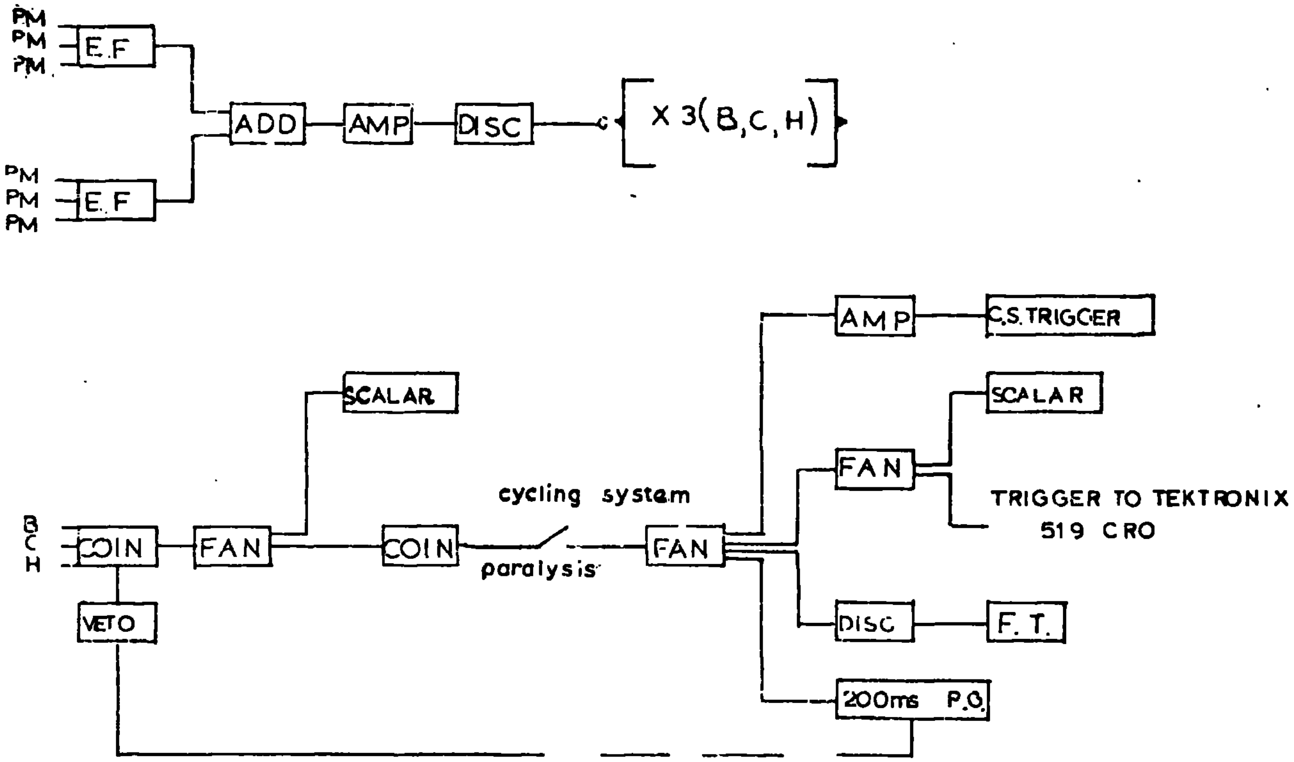

Figure 5.9a Electronic logic used in the zero field run.

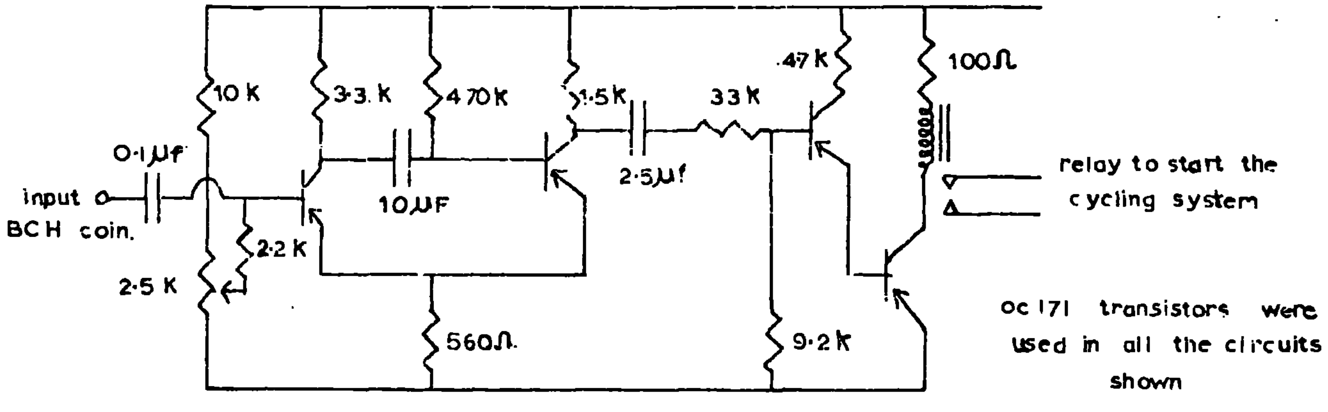

oc 171 transistors were used in all the circuits shown

Figure 5.9b Cycling system trigger.

(c) the illumination of the clock for time correlation purposes.
(d) the camera d.c. motors, to wind on the film in two cameras and await the next event.

The illuminated flash tubes, produced by the ionisation trail of a charged particle, were photographed in the dark by means of a camera viewing the front elevation via the reflecting mirrors shown in Figure 5.10.

5.8 Location of particle trajectories in the magnetic spectrometer

5.8.1 Projection method

To determine the displacement of each accepted event, the projection method was used to locate the particle trajectory in the magnetic spectrometer.

The photographs of the illuminated tubes and fiducial crosses were projected through a mirror system onto a scanning board, on which the location of every tube had been accurately drawn. The positions were obtained by photographing all the flash tubes in the presence of a gamma-ray source and at the same time applying a succession of high voltage pulses. The projected images of the flashes were aligned on the board by means of the reference crosses. The coordinates of the trajectory were located from the scales immediately below the fourth layer of flash tubes in the three measuring trays. The best estimate of a track was obtained by taking the mean of all possible track positions such that a cursor passed through all the flashed tubes and either missed or passed as near to the edge as possible, all unflashed tubes.

5.8.2 Criteria employed to select muon events for the determination of their delta values, in the zero field run

Rejection of events, satisfying the BCH coincidence, occurred for the following reasons:

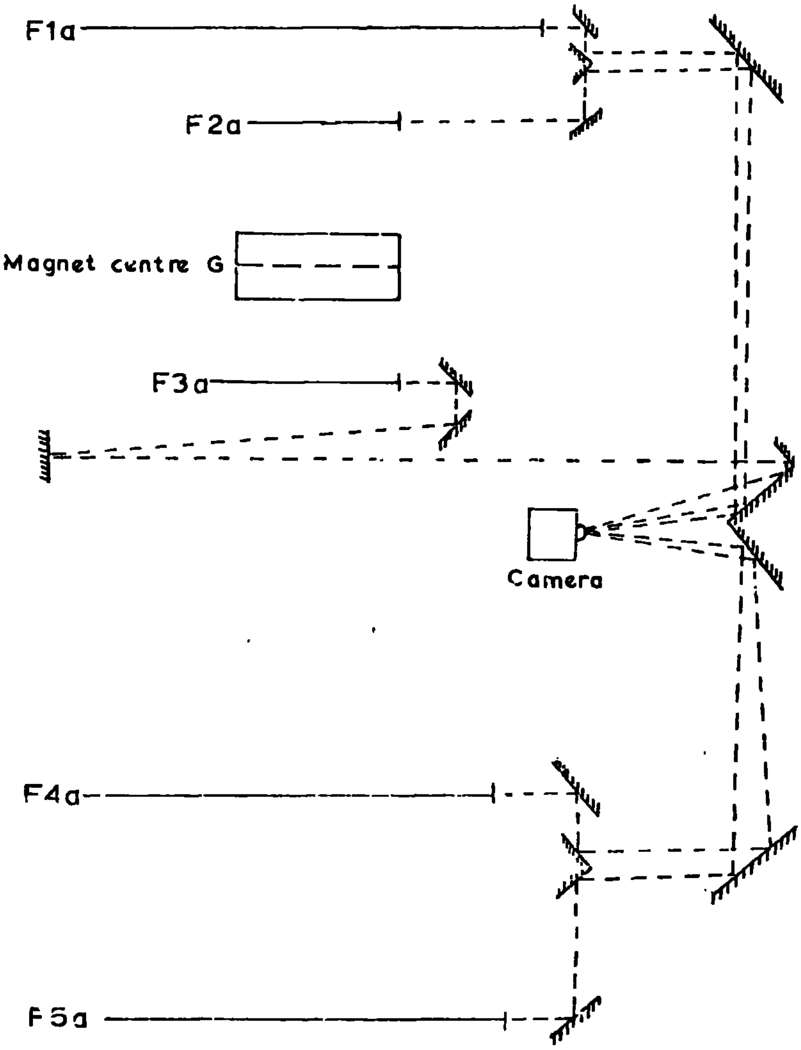

Figure 5.10 Optical system for photographing the front of the flash tube trays, shown from the side elevation.

(a) A track was termed out of geometry if B, C, H or the magnet centre, were not intercepted.

(b) As flash tube tray F1a was not operated in the zero field run, the inability to check the alignment of double track events in F2a, lead to their rejection.

(c) If two or more tracks were observed in each of two or more arrays of flash tubes.

(d) If two tracks or a knock-on electron occurred in one tray such that the trajectory and the accompanyment were considered indistinguishable.

(e) To distinguish background 'separate track' events, all the trajectories were examined for overall alignment of the track in the flash tube trays. These background events arose from the traversal of separate angled particles through the detectors above and below the magnet, and also from separate particles through BC and through H, such that the front projection simulated a trajectory. As such events were more likely to yield large displacement values compared to those typical of muons in a zero field, especial attention was paid to all events exhibiting large deflections.

(f) If the frame was spurious, where the expected spurious rate was $\sim 9 \times 10^{-7}$ min^{-1}

5.8.3 Contributions to the location precision at each measuring level

Contributions to the location precision at each measuring level arise from several sources. For the 'projection method' these are:

(a) an inherent error contribution of locating a track through eight layers of flash tubes, dependent on, the geometrical arrangement of the flash tubes, varying separations and thicknesses etc.

(b) poor layer efficiencies.

(c) undetectable knock-on electron contamination.

(d) measurement errors in taking only one reading of the co-ordinates x_2, x_3, x_4. Narrowing of the delta distribution can be achieved by taking the mean of several coordinate readings for each event. However, the measurement error on one reading is representative of the contribution to the location precision when determining the momentum of a particle from its displacement in the magnetic field.

(e) a more precise location of trajectories at each measuring level can be achieved if consideration is given to the trajectory as a whole through the spectrometer. The projection method of coordinate determination however considers each flash tube tray separately and therefore does not allow such an improvement.

5.8.4 The maximum detectable momentum

The maximum detectable momentum (m.d.m.) is defined as the momentum at which the magnetic displacement, D, is equal to the r.m.s. error in measuring D and is calculated, for the magnetic spectrometer, in Section 5.11.5. The m.d.m. is dependent on the accuracy with which particle trajectories can be located at the measuring levels and also the separation of these levels. The m.d.m. is hence lowered by a factor of approximately 2.5, an effect of the particle trajectory only being located at three accurate levels as opposed to four accurate levels, and is also dependent on the method used for the coordinate determination. The projection method is considered accurate enough in this experiment, as particles of momenta far below the m.d.m. are being studied.

5.9 Basic data of the zero field run

Total running time	36 minutes
BCH, coincidence rate	11.2 ± 1.5 events/minute
Cycling system dead time	4.13 ± 0.01 seconds
Effective running time	1238.5 seconds
Total number of events	223
Showers and spurious	33
Out of geometry	7
Indistinguishable tracks	21
Identified 'separate tracks'	9
Accepted events	153

5.10 Zero field delta distribution

The distribution of muon delta values, Δ, obtained from the zero field run is shown in Figure 5.11. The mean value of this distribution, Δ_o, is shown in Table 5.1 for comparison with the value of Δ_o calculated from direct measurements.

TABLE 5.1

	Δ_o
Calculated from direct measurements (equation 5.8)	31.62 ± 0.17 cm
Determined from the mean of the Δ distribution in Figure 5.11	32.01 ± 0.14 cm

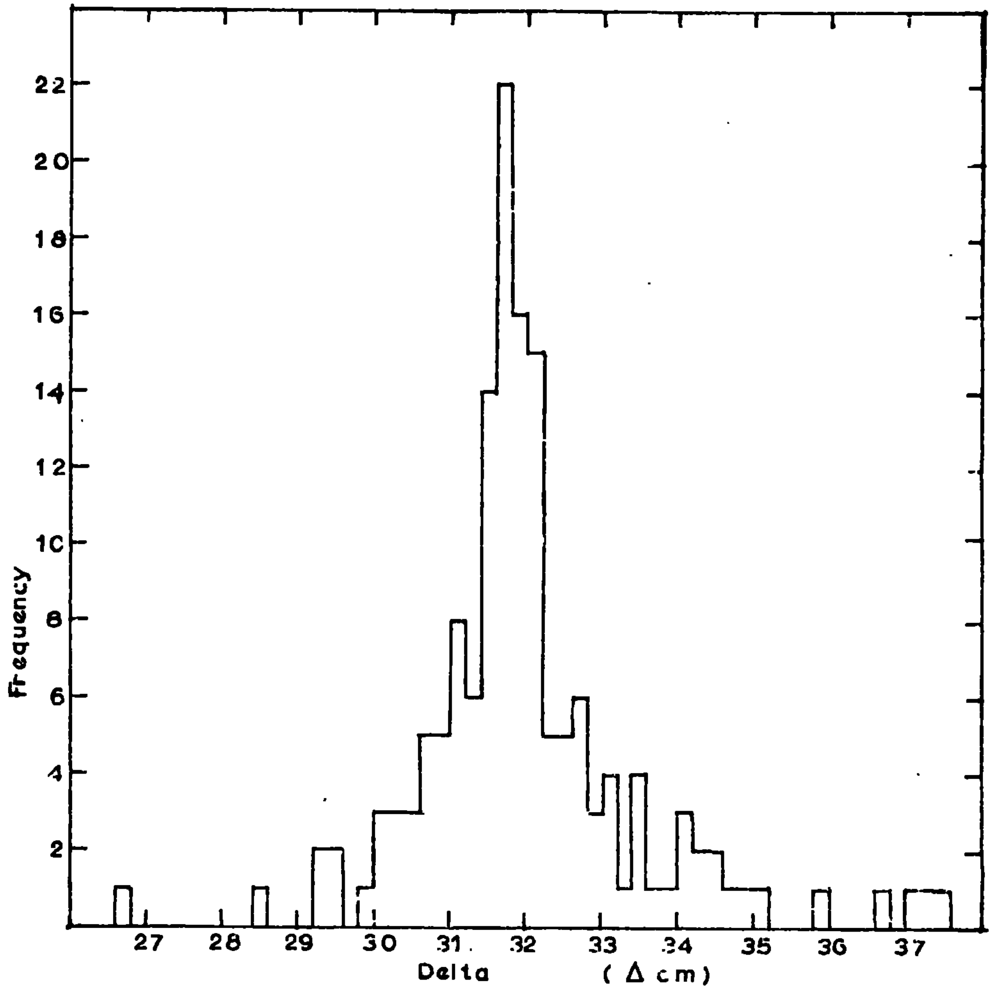

mean of the delta distribution = 32.01 ± 0.14 cm

standard deviation = 1.781 cm

Figure 5.11 Distribution of muon delta values obtained from the zero field run.

The consistency between the Δ_o values obtained from direct measurement and the zero field run, gave confidence in the accuracy of the displacement equation 5.5.

The value of $\Delta_o = 31.62 \pm 0.17$ cm was adopted for use in all calculations as the delta distribution needed a much larger number of events to give a more precise value of Δ_o, rendering it preferable for use in the displacement equation.

5.11 Analysis of the zero field delta distribution

5.11.1 Contributions to the width of the delta distribution

Contributions to the total width come from the following:

(1) The finite location precision of the particle trajectory at the measuring levels F2a, F3a, F4a, contributions to which arise from the sources given in Section 5.8.3.

(2) Multiple scattering of particles in F3a, F3b, and C.

If $\delta\Delta$ is the r.m.s. value of the measured delta distribution, $\delta\Delta_\ell$ the contribution from location precision and $\bar{\delta}\Delta_s$ from multiple scattering then,

$$\delta\Delta^2 = \delta\Delta_\ell^2 + \bar{\delta}\Delta_s^2 \qquad 5.9$$

The contribution from the location error, $\delta\Delta_\ell$, is resolved from the resultant width, $\delta\Delta = 1.781$ cm (Figure 5.11), of the Δ distribution, and the calculated width due to the scattering component, $\bar{\delta}\Delta_s$.

5.11.2 Determination of $\delta\Delta_\ell$

From equation 5.4

$\Delta = 1.682\ x_3 - x_2 - 0.682\ x_4$ cm where x_2, x_3, x_4 are in cm.

Assuming the location errors of x_2, x_3, x_4 are the same and equal to $\delta\Delta_o$ then,

$$\delta\Delta_\ell^2 = (1.682\ \delta\Delta_o)^2 + (\delta\Delta_o)^2 + (0.682\ \delta\Delta_o)^2$$

$$\delta\Delta_\ell^2 = 4.295\ \delta\Delta_o^{\ 2}\ \text{cm}^2 \qquad 5.10$$

where $\delta\Delta_o$ is in cm.

5.11.3 Determination of $\bar{\delta}\Delta_s$

In the absence of multiple scattering a particle would traverse the spectrometer along a straight line trajectory DEF, shown in Figure 5.12. Scattering at each detector level causes an error in the determined value of Δ (where, for the zero field run, the true value of $\Delta = -\Delta_o$). The effect on the value of Δ due to scattering at any level is the same as the effect on the displacement D, measured at the level F2a (this is evident from equation 5.4).

With reference to Figure 5.12, if a particle is scattered through an angle θ_1 in F3b, this will give an error in the displacement, δD_{F3b}, at the level F2a, given by,

$$\delta D_{F3b} = (\ell_1+\ell_2+\ell_3 - y_3)\theta_1 \quad \text{where } \ell_3 = y_2 .$$

Similarly a scattering angle of θ_2 in F3a when projected onto the level F2a, gives an error in the displacement, δD_{F3a}, given by

$$\delta D_{F3a} = (\ell_1+\ell_2)\ \theta_2 .$$

A scattering angle of θ_3 in C, according to the notation in Figure 5.12, causes a displacement in the location of the trajectory at the level F4a,

$$H_3H_2 = y_1\theta_3$$

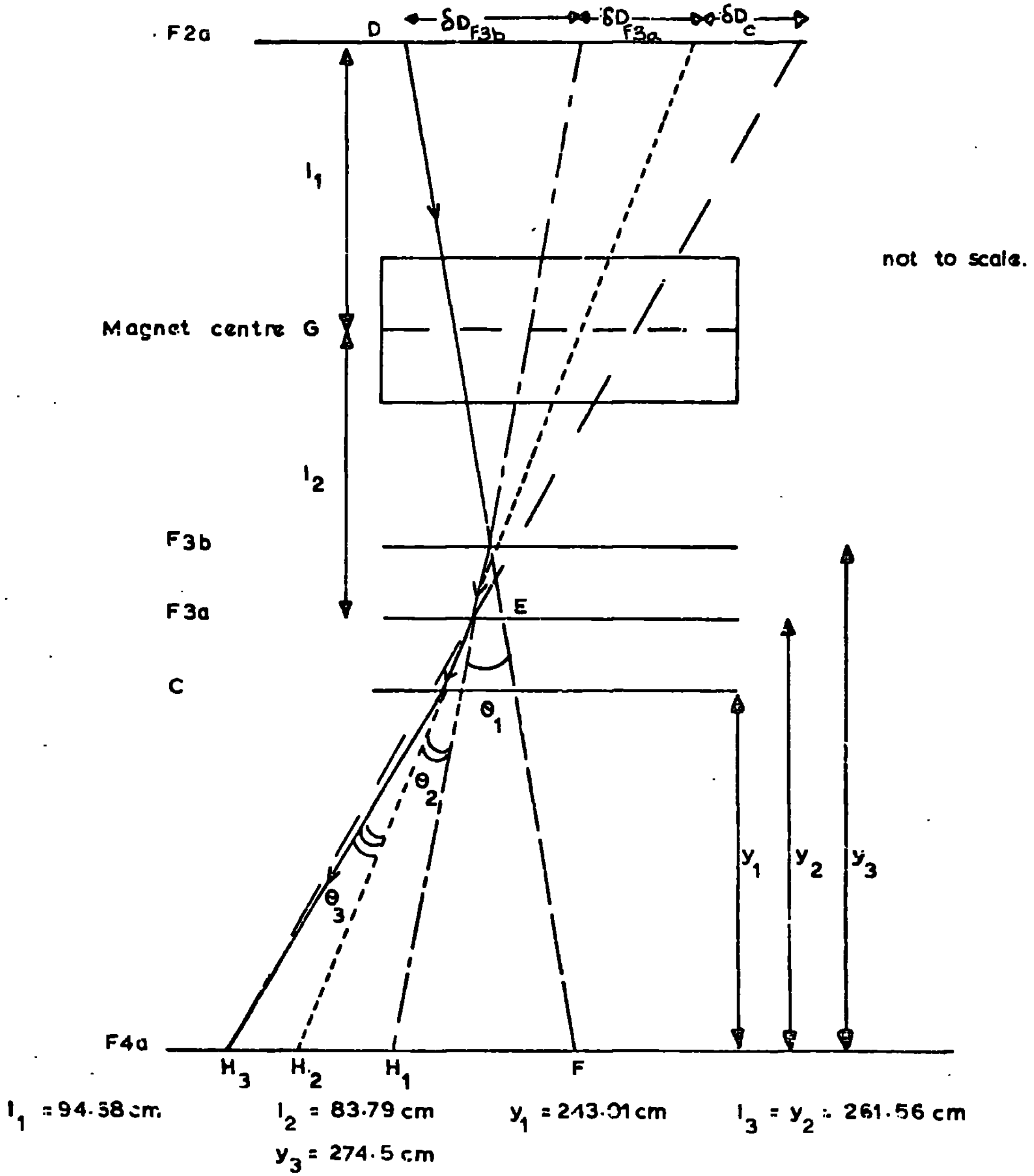

Figure 5.12 Diagram showing the error produced in the displacement value of a particle track, DEF, by the scattering angles θ_1, θ_2, θ_3 at F3b, F3a and C respectively.

From equation 5.2 the error in D, δD_c, due to scattering at this level is then given by

$$\delta D_c = -\left(\frac{\ell_1+\ell_2}{\ell_3}\right) y_1\theta_3$$

Reference to equation 5.4 shows that the error in the displacement value caused by scattering at each level is equal to the error in the delta value from the scattering at each level,

then

$$\delta\Delta_{F3b} = (\ell_1+\ell_2+\ell_3-y_3)\theta_1$$

$$\delta\Delta_{F3a} = (\ell_1+\ell_2)\theta_2$$

$$\delta\Delta_c = -\left(\frac{\ell_1+\ell_2}{\ell_3}\right) y_1\theta_3$$

where $y_2 = \ell_3$.

If $<\theta_1>$, $<\theta_2>$ and $<\theta_3>$ are the r.m.s. projected angles of scattering in the flash tube trays F3b, F3a and in the scintillator C, respectively, then the total r.m.s. error in Δ from the scattering contributions is given, from an addition in quadrature of the separate contributions, to be

$$\delta\Delta_s^{\,2} = \delta\Delta_{F3b}^{\,2} + \delta\Delta_{F3a}^{\,2} + \delta\Delta_c^{\,2}$$

$$\delta\Delta_s^{\,2} = \left[(\ell_1+\ell_2+\ell_3 - y_3)<\theta_1>\right]^2 + \left[(\ell_1+\ell_2)<\theta_2>\right]^2 + \left[\left(\frac{\ell_1+\ell_2}{\ell_3}\right) y_1<\theta_3>\right]^2 \qquad 5.12$$

Contributions to the multiple scattering are only important from detectors F3a, F3b and C. Scattering above (and below) the reference scales in F2a (and F4a) only alter the incident (and emergent) angle of the trajectory i.e. above F2a (and below F4a). The scattering contributions from the remaining halves of F2a and F4a are negligible.

The radiation lengths, X_o, for the individual materials were calculated from the following expression,

$$\frac{1}{X_o} = \sum_i \frac{4}{137} \frac{N}{\rho_i} \left[\sum_i \frac{\rho_i}{A_i} Z_i(Z_i+1) \log (183\ Z_i^{-1/3}) \right] g^{-1} cm^2 \qquad 5.13$$

where N = Avogadro's number and ρ_i refers to the density of the ith atom.

The radiation lengths calculated for the various materials are shown in Table 5.2.

TABLE 5.2

Material	$\bar{Z}$	$\bar{A}$	X_o g cm^{-2}
Glass	10.61	21.33	28.86
NE 102A	3.65	6.83	47.66
Aluminium	13.00	26.98	24.40 *

* from Rossi (1952).

The r.m.s. projected angle of scattering, $\langle\theta\rangle$, in a material of t radiation lengths, ignoring energy loss in the medium, was calculated by Rossi (1952) to be given by

$$\langle\theta\rangle = \frac{1.482 \times 10^{-2} \times t^{\frac{1}{2}}}{p\beta} \text{ radians} \qquad 5.14$$

for a particle of charge 1e,

where p is the momentum in GeV/c and β the velocity in terms of c.

The r.m.s. projected angle of scatter, $\langle\theta\rangle$ radians, for a particle travelling through t radiation lengths in each detector is shown in Table 5.3.

TABLE 5.3

Detector	Glass (gcm^{-2})	Aluminium (gcm^{-2})	Phosphor (gcm^{-2})	Total radiation lengths (r.l.)	rms projected angle of scatter in radians, p in GeV/c
F3b	3.376	1.098	-	0.162 r.l.	$\langle\theta_1\rangle = \frac{5.96\times10^{-3}}{p\beta}$
F3a	4.16	1.976	-	0.225 r.l.	$\langle\theta_2\rangle = \frac{7.03\times10^{-3}}{p\beta}$
C	-	0.878	5.16	0.144 r.l.	$\langle\theta_3\rangle = \frac{5.63\times10^{-3}}{p\beta}$

Substitution of the r.m.s. projected angles of scatter from Table 5.3 and the appropriate lengths from Figure 5.12 into equation 5.12, yields the scattering contribution of particles with momentum p to the width of the Δ distribution.

$$\delta\Delta_s^{\;2} = \frac{1}{p^2\beta^2}\left[(178.47\times7.03\times10^{-3})^2 + (165.6\times5.96\times10^{-3})^2 + (165.81\times5.63\times10^{-3})^2\right]$$

$$\delta\Delta_s^{\;2} = \frac{3.420}{p^2\beta^2}\ \text{cm}^2 \qquad \text{with p in GeV/c}$$

$$\delta\Delta_s = \frac{1.849}{p\beta}\ \text{cm} \qquad 5.15$$

In the zero field run, muons of momentum > 329 MeV/c (Figure 5.24) were selected, so that the contribution to the width of the delta distribution due to multiple scattering is given by

$$\bar{\delta}\Delta_s^{\ 2} = \frac{\int_{329}^{\infty} \delta\Delta_s^{\ 2}\, N(p)dp}{\int_{329}^{\infty} N(p)\, dp} \qquad 5.16$$

where a combination of muon spectra from Taylor (1961) and Hayman and Wolfendale (1962) contributed the value

$$\int_{329}^{\infty} N(p)dp = 7.69 \times 10^{-3}\ \mathrm{cm}^{-2}\ \mathrm{sec}^{-1}\ \mathrm{sterad}^{-1}.$$

Evaluating equation 5.16 gives

$$\bar{\delta}\Delta_s = 1.741\ \mathrm{cm}.$$

5.11.4 Determination of the location error $\delta\Delta_o$

The contribution of location errors at the measuring levels to the width of the delta distribution can now be evaluated.

From equation 5.9

$$\delta\Delta^2 = \delta\Delta_\ell^2 + \bar{\delta}\Delta_s^{\ 2}$$

Substituting $\delta\Delta = 1.781$ cm and $\delta\bar{\Delta}_s = 1.741$ cm as determined, gives

$$\delta\Delta_\ell^{\ 2} = \delta\Delta^2 - \delta\bar{\Delta}_s^{\ 2}$$

$$\delta\Delta_\ell^{\ 2} = 0.0985\ \mathrm{cm}^2$$

$$\delta\Delta_\ell = 0.314\ \mathrm{cm}$$

As the location error, $\delta\Delta_o$, at each measuring level is given by

$$\delta\Delta_\ell^{\ 2} = 4.295\ \delta\Delta_o^{\ 2}\ \mathrm{cm}^2 \qquad 5.17$$

$\delta\Delta_o$ can now be found. i.e. $\delta\Delta_o = 1.51$ mm.

The location error at each measuring level, $\delta\Delta_o$, is then found to be 1.5 mm.

5.11.5 The m.d.m. of the magnetic spectrometer

From equation 5.7, the relation between momentum p in GeV/c, displacement D cm and $\int Bd\ell$ in gauss cm, for a particle of charge 1e, (Z=1), is

$$p = \frac{2.84 \times 10^{-5} \times \int Bd\ell}{D} \quad \text{GeV/c} \qquad 5.18$$

For a mean exciting current, I = 36 amp (Section 4.3), $\int Bd\ell = 2.57\times10^{5}$ gauss cm

then $pD = 7.3$ GeV/c cm 5.19

The m.d.m. is defined in Section 5.8.4, as that momentum at which the magnetic displacement, D, is equal to the r.m.s. error in measuring D. From equation 5.4

$$D = 1.682\, x_3 - x_2 - 0.682\, x_4 + \Delta_o \text{ cm} \quad \text{with } x_2, x_3, x_4 \text{ in cm and}$$

$$\Delta_o = 31.62 \pm 0.17 \text{ cm.}$$

Then

$$\delta D^2 = (1.682\, \delta x_3)^2 + (\delta x_2)^2 + (0.682\, \delta x_4)^2 + (\delta\bar{\Delta}_o)^2 \qquad 5.20$$

where $\delta\bar{\Delta}_o$ is the error in Δ_o, and assuming

$\delta\Delta_o = \delta x_2 = \delta x_3 = \delta x_4 = 1.51$ mm as found previously, then

$$\delta D^2 = (0.151)^2 \left[(1.682)^2 + 1^2 + (0.682)^2 \right] + (0.17)^2$$

$$\delta D^2 = 0.1270 \text{ cm}^2$$

$$\delta D = 0.36 \text{ cm} \qquad 5.21$$

The m.d.m. is thus given by $p = \frac{7.3}{0.36}$ GeV/c = 20.2 GeV/c.

5.11.6 Precision of momentum determination as a function of momentum

At low momenta the uncertainty in the measured momentum is mainly produced by multiple scattering in the flash tube trays F3a, F3b, and scintillation counter, C. The r.m.s. error, δD_s, in the value of D due to this cause has already been given, equation 5.15

$$\delta D_s = \frac{1.849}{p\beta} \qquad 5.22$$

for particles of momenta p GeV/c.

From equation 5.18 and 5.22 the ratio of the r.m.s. scattering to magnetic displacement is given by

$$\frac{\delta D_s}{D} = \frac{6.509 \times 10^4}{\beta \times \int B d\ell} \qquad 5.23$$

For a mean exciting current of 36 amp

$$\frac{\delta D_s}{D} = \frac{0.253}{\beta} \qquad 5.24$$

The total r.m.s. error in D, δD, at a momentum p GeV/c, is obtained from the addition of the error produced by multiple scattering, $\frac{0.253D}{\beta}$, to that produced by the location errors (equation 5.21), 0.36 cm, in quadrature,

$$\delta D^2 = \left(\frac{0.253D}{\beta}\right)^2 + (0.36)^2 .$$

This applies to a particle of unit charge (Z=1).

Thus
$$\left(\frac{\delta D}{D}\right)^2 = \left(\frac{0.253}{\beta}\right)^2 + \left(\frac{0.36p}{7.3}\right)^2$$

As $pD = 7.3$ GeV/c cm then $\frac{\delta D}{D} = \frac{\delta p}{p}$ where δp is the r.m.s. value of the error in p. Then

$$\frac{\delta p}{p} = \left[\left(\frac{0.253}{\beta}\right)^2 + \left(\frac{0.36p}{7.3}\right)^2 \right]^{\frac{1}{2}}$$

$$\frac{\delta p}{p} = \left[\left(\frac{0.253}{\beta}\right)^2 + (0.049p)^2 \right]^{\frac{1}{2}} \text{, for a particle of } Z=1 \qquad 5.25$$

where p is in GeV/c.

In Figure 5.13, $\frac{\delta p}{p_m}$ is shown as a function of measured momentum, p_m, for muons, protons, and deuterons. (The term'measured momentum' and the subscript 'm' subsequently refer to the momentum at the magnet centre.)

5.12 Conclusions

Conclusions of the zero field run are the following:

(1) The value of $\Delta_o = 31.62 \pm 0.17$ cm is adopted for use in all calculations of momenta.

(2) The r.m.s. error in track location at each measuring level F2a, F3a and F4a is 1.5 mm. For a magnet excitation current of 36 amp the maximum detectable momentum is 20.2 GeV/c.

(3) At low momenta, where track location errors are unimportant the fractional error in momentum determination, $\frac{\delta p}{p}$, is $\frac{0.253}{\beta}$. The precise variation of $\frac{\delta p}{p}$ with momentum for muons, protons and deuterons is shown in Figure 5.13.

5.13 Time of flight measurement technique

In cosmic ray experiments searching for low intensity particles, large area counters are required for time of flight measurements on a tolerable rate

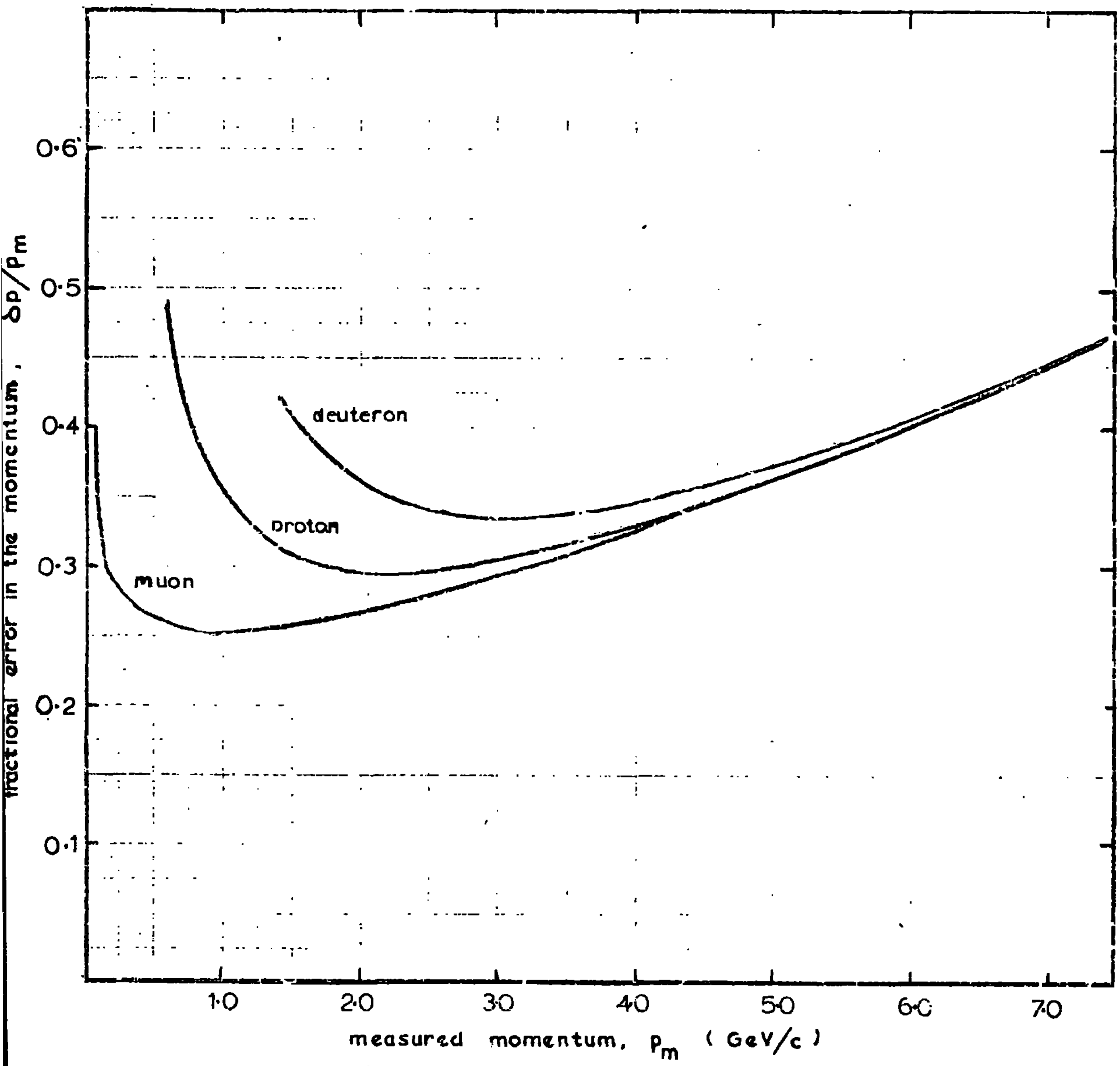

Figure 5.13 Fractional error in the momentum as a function of the momentum, measured at the magnet centre. The curves are calculated for a magnet current of 36 amp.

of events. The time of flight arrangement shown in Figure 5.2a uses two 5 cm thick, $1m^2$ area, scintillation counters, A and D, each viewed edgewise on by single 2" 56 AVP photomultipliers and separated by 530.38 cm in the spectrometer arrangement shown in Figure 5.1. With this system, low velocity particles must be selected by independent means as in Section 5.3.2, whereas with an isochronous counter low velocity particles can be selected by the counters themselves. The simple design in Figure 5.2a was chosen mainly because of the small volume (but large surface area) taken up by the counters and their adaptability in fitting in between other types of detectors, necessary in the basic design of a magnetic spectrometer. With such a system, the r.m.s. error in the time of flight has systematic contributions dependent on the distance travelled by the photons down the phosphor and Gaussian contributions predominately from the statistical variations in the limited numbers of photo-electrons produced at the photomultiplier photocathodes.

However, when a comparison is drawn between the resolution attained by Stefanski et al. (1967) using an isochronous counter (Section 5.17.3), the two methods are found to be equally precise and indeed the former system exhibits many advantages.

To determine the time of flight precision, muon time of flight measurements were taken in conjunction with the delta value determinations of muons accepted in the zero field run.

5.14 Time of flight display electronics.

As described in Section 5.7 cosmic rays were selected by a BCH coincidence with a resolving time of 55 ns, during the zero field run, where the discrimination levels were set at $0.2E_s$ in B, C and H. The BCH coincidence in Figure 5.9a externally triggered the Tektronix 519 oscilloscope, so displaying the time of flight pulses from A and D, for each event. The time of flight information associated with each event was obtained by photographing the pulses, of approximate width 10 ns, from the scintillation counters A and D as displayed on the Tektronix oscilloscope, set at a nominal sweep speed of 10 ns/cm. The display electronics is shown in Figure 5.14a together with the arrangement used for the accurate calibration of the time base and determination of the inherent delay imposed between the pulses. An inherent delay of $T_o$ns was introduced between the pulses, so that a measurable time separation always occurred even for relativistic particles. The time base, set at an accurate value of fns/cm, was calibrated with a 10 ns pulse width followed by its associated reflection from a 20 ns open circuit delay line. (Figure 5.14b). Calibration of fns/cm and $T_o$ns took place before every run, using the circuits shown in Figure 5.14 a,b.

The pulses from the anodes of the two 56 AVP photomultipliers are fed directly into the Rutherford fast electronics, as shown in Figure 5.2b. To ensure no dependence of time delay on voltage pulse heights from the photomultipliers, double times ten amplifiers are shown, in Figure 5.14a, to be inserted before the discriminators. The purpose of the discriminator is to provide a constant output pulse profile independent of the input pulse height from the photomultiplier, such that the constant output pulse height does not saturate the Rutherford electronics adder. Fluctuations in the pulse heights from the photomultipliers are caused mainly by the statistical nature of the production of photoelectrons at the photocathode, fluctuations in the photoelectron multiplication process and non-linearity over the scintillation counter

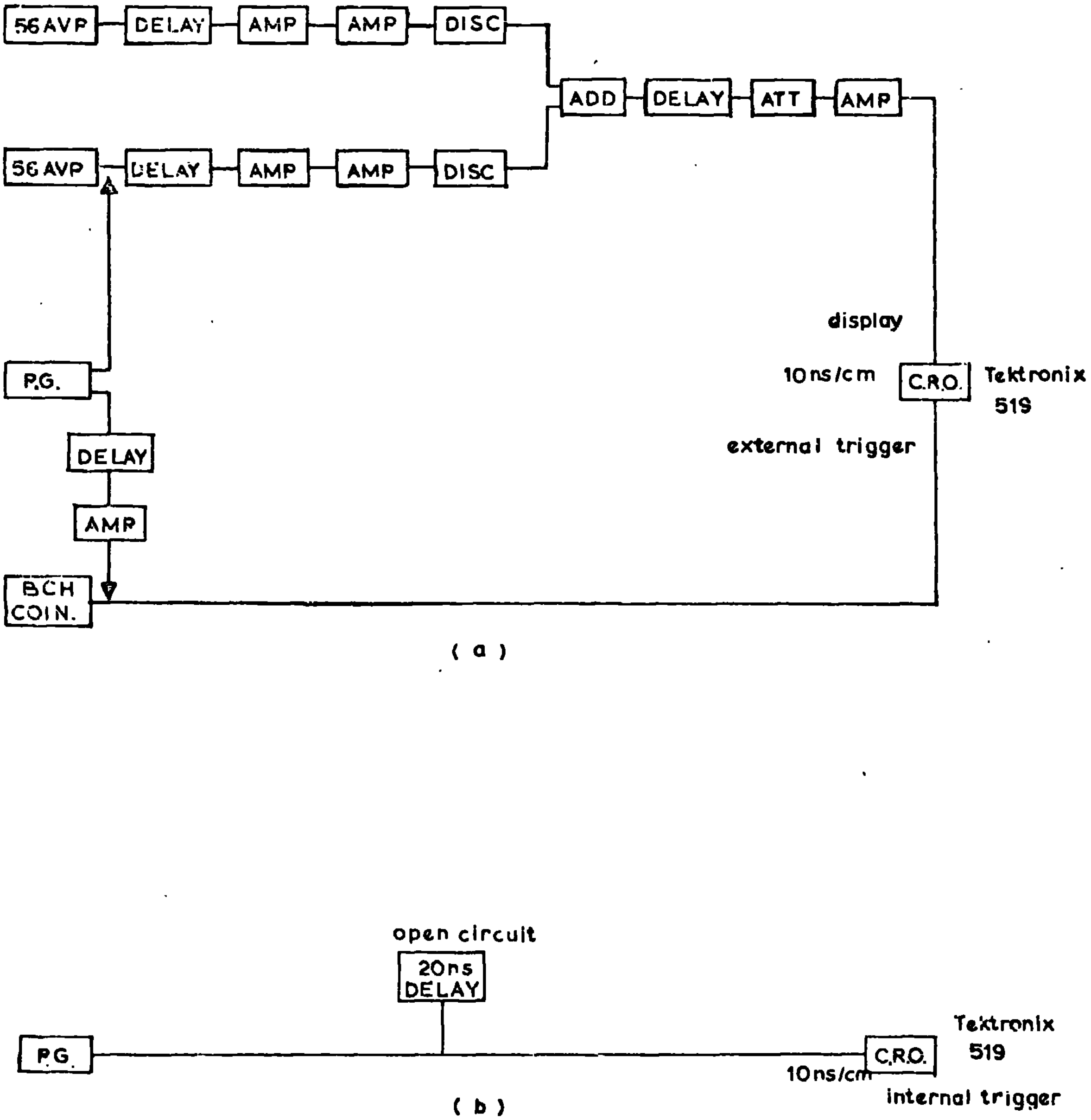

Figure 5.14 Time of flight electronics a) for display of pulses and the determination of the inherent delay b) for calibration of the time base.

length. Smaller contributions to the fluctuations in pulse heights originate from the Landau distribution in energy loss and path length variations of particles traversing the scintillation counter. For the best compromise between low discrimination levels of $\sim 0.02E_s$ and low random pulse rates, the discrimination levels in the channels of A and D were adjusted to a counting rate of 2×10^5 counts per minute. Adjustment of the displayed pulse profile is accomplished with the attenuator and amplifier preceding the oscilloscope, in Figure 5.14a.

5.15 Recording system and the criteria used to select events for time of flight measurements

The photographs of the regulated pulses were projected onto a scanning board, where measurements of their time separations were taken. The time of flisht is derived from the difference between the intercept of the leading edge of each pulse with a scale located half-way down the pulse edge, as shown in Figure 5.15. The inherent delay and the time base calibration are likewise measured. The scanning of regular pulse shapes is found to be the most satisfactory technique for determination of the time of flight.

In addition to the rejection criteria chosen for the determination of muon delta values in the zero field run (Section 5.8.2) rejection of events for time of flight determinations occurred if the pulse information was at all ambiguous or if accompanyment appeared with the track in any of the flash tube trays, F2a, F4a, F5a.

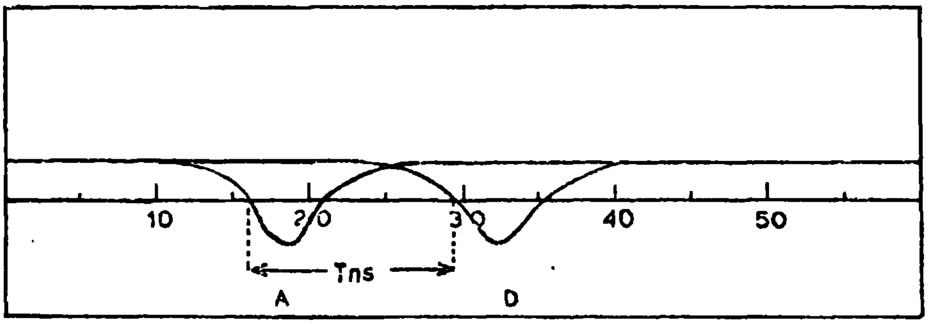

The observed time separation T ns is given by

$$T = T_D - T_A$$

where T_D and T_A are the respective arrival times of the scintillator pulses from D and A, as read on a scale situated half-way down the pulse.

Figure 5.15 Projection of the time of flight pulses.

5.16 Basic data for zero field time of flight measurements

Events selected for the delta distribution of muons	153
Events rejected for time of flight measurements	36
Events selected for time of flight measurements	117
Time base calibration, fns/cm	11.57 ns/cm
Inherent delay, T_o ns	7.17 ns
Running time	20 minutes 38.5 seconds

The inability of the Rutherford scalar to count pulses of 10 ns widths, effected the misconception of the true counting rate. The true counting rate of approximately 10^7/min, corresponding to a discrimination level in channels A and D of < $0.02E_s$, prompted the high spurious rate seen.

5.17 Analysis of the zero field time of flight measurements

5.17.1 Systematic corrections

To obtain the time of flight of the particle, between the points at which it traverses A and D, a correction has to be applied for the time taken by the produced scintillation light to traverse the phosphors and light guides to the detecting photomultipliers on A and D. To calculate this time accurately is difficult, as all the produced light does not traverse the same path length.

Initially, the time distribution in the emission of photoelectrons from the photomultiplier photocathode (which are stimulated by photons arriving at different times via the different reflection stages) should be calculated.

Finally, the additional time taken for the produced voltage pulse height to reach the discrimination level in each counter, yields the correction to be applied to the observed time delay of T_{ns}. Clearly, the calculation of a matrix of such correction times over the area in each scintillation counter, A, D, could only be achieved approximately, as fluctuations in the number of photoelectrons collected are extremely large, e.g. for a typical average number of 37. Accordingly, as a first approximation the flight time for direct light only, has been used as a correction factor.

If ℓ_A and ℓ_D are the phosphor lengths in scintillation counters A and D, as shown in Figure 5.16, and ℓg the light guide lengths, the correction is

$$+\left\{\left(\frac{\ell_A}{c/n_1}+\frac{\ell g}{c/n_2}\right)-\left(\frac{\ell_D}{c/n_1}+\frac{\ell g}{c/n_2}\right)\right\}=+\left(\frac{\ell_A-\ell_D}{c/n_1}\right)\text{ for }\ell_A>\ell_D$$

and

$$-\left\{\left(\frac{\ell_D}{c/n_1}+\frac{\ell g}{c/n_2}\right)-\left(\frac{\ell_A}{c/n_1}+\frac{\ell g}{c/n_2}\right)\right\}=+\left(\frac{\ell_A-\ell_D}{c/n_1}\right)\text{for }\ell_A<\ell_D$$

where n_1 and n_2 are the refractive indices of the phosphor and Perspex, respectively. For the phosphor $n_1 = 1.6$, which is the refractive index of the phosphor at the wavelength of peak emission (4520 Å) of the produced light. The use of c/n, as an approximation for the group velocity, was calculated to be accurate within ∿ 3%.

A further correction must be applied for the time delay difference, T_o, in the electronics associated with scintillator A and D channels. Using a pulse generator it was established, with the circuitry in Figure 5.14 a, that the pulse from A arrives before the pulse from D by T_o = 7.17 ns, in the zero field run.

Thus the time of flight of a particle, between the points at which it

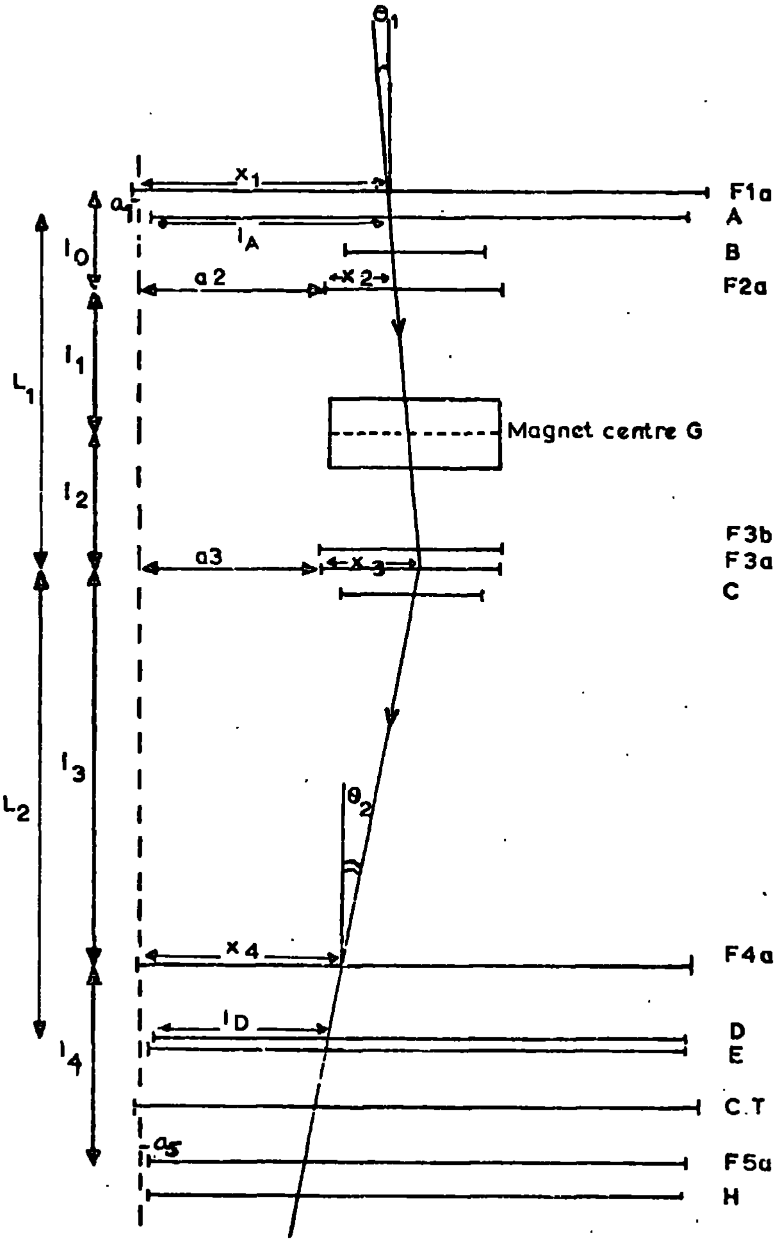

$L_1 = 224{\cdot}79$ cm

$L_2 = 305{\cdot}59$ cm

$l_0 = 62{\cdot}72$ cm

$l_1 = 94{\cdot}68$ cm

$l_2 = 83{\cdot}79$ cm

$l_3 = 261{\cdot}56$ cm

$l_4 = 126{\cdot}93$ cm.

$a_1 = -3{\cdot}21$ cm

$a_2 = 48{\cdot}73$ cm

$a_3 = 47{\cdot}78$ cm

$a_4 = 0$.

$a_5 = 3{\cdot}35$ cm

Scale: Vert 1:50
Horiz 1:20

Figure 5.16 Diagram illustrating the corrections to the measured time of flight, for a particle traversing the spectrometer during the zero field run.

traverses scintillation counters A and D is

$$\left(T + \frac{\ell_A - \ell_D}{c/n_1} - T_Q \right) \text{ ns}$$

In order to determine the precision of velocity measurement, it is convenient to normalise all the measured time of flight values, between A and D, to a standard path length which has been taken to be the perpendicular distance between A and D, i.e. $L_1 + L_2$ from Figure 5.16. Further, the angular deviation experienced by a particle traversing the spectrometer due to multiple scattering has been assumed to take place at the centre of F3a. For the trajectory shown in Figure 5.16 the path length between the vertical centres of A and D is

$$\frac{L_1}{\cos\theta_1} + \frac{L_2}{\cos\theta_2}$$

where $L_1 = 224.79$ cm

and $L_2 = 305.59$ cm.

If the measured time of flight is

$$\left(T + \frac{\ell_A - \ell_D}{c/n_1} - T_o \right) \text{ ns}$$

then the time of flight normalised to a path length L_1+L_2 is

$$t_c = \frac{T + \dfrac{\ell_A - \ell_D}{c/n_1} - T_o}{\dfrac{0.424}{\cos\theta_1} + \dfrac{0.576}{\cos\theta_2}} \qquad 5.26a$$

For a particle deflected by the magnetic field, as shown in Figure 5.8, normalisation to a vertical standard path length involves the assumption that magnetic deflections take place at the magnet centre. Thus for the trajectory shown in Figure 5.8 the path length between A and D is

$$\frac{L_1}{\cos\theta_1} + \frac{L_2}{\cos\theta_2} \quad \text{where} \quad L_1 = 141.00 \text{ cm}, \quad L_2 = 389.38 \text{ cm}$$

and θ_1, θ_2 refer to the angle of the trajectory to the vertical, above and below the magnet centre, respectively. Thus the corrected time of flight normalised to the vertical path length, for a particle deflected by the magnetic field is

$$t_c = \frac{T + \dfrac{\ell_A - \ell_D}{c/n_1} - T_o}{\dfrac{0.266}{\cos\theta_1} + \dfrac{0.734}{\cos\theta_2}} \qquad 5.26.b$$

5.17.2 Zero field time of flight distributions

Figure 5.17 shows the distribution of $T-T_o$, and the distribution of t_c values (calculated using equation 5.26a) for muons selected subject to the criteria stated in Section 5.15, in the zero field run. It is seen that, correcting for the transit times of direct photons up the phosphor in scintillation counters A and D and normalising the resulting time of flight to a standard path length of L_1+L_2, considerably sharpens the distribution. However, the distribution is broad and suggests that the transit time correction of scintillation photons up the phosphor is more complex than the value of $\ell/c/n$ used. As expected the scatter plot of t_c versus ℓ_D shown in Figure 5.18 indicates a systematic increase of t_c with increasing ℓ_D, although the statistics are not accurate enough to establish this magnitude.

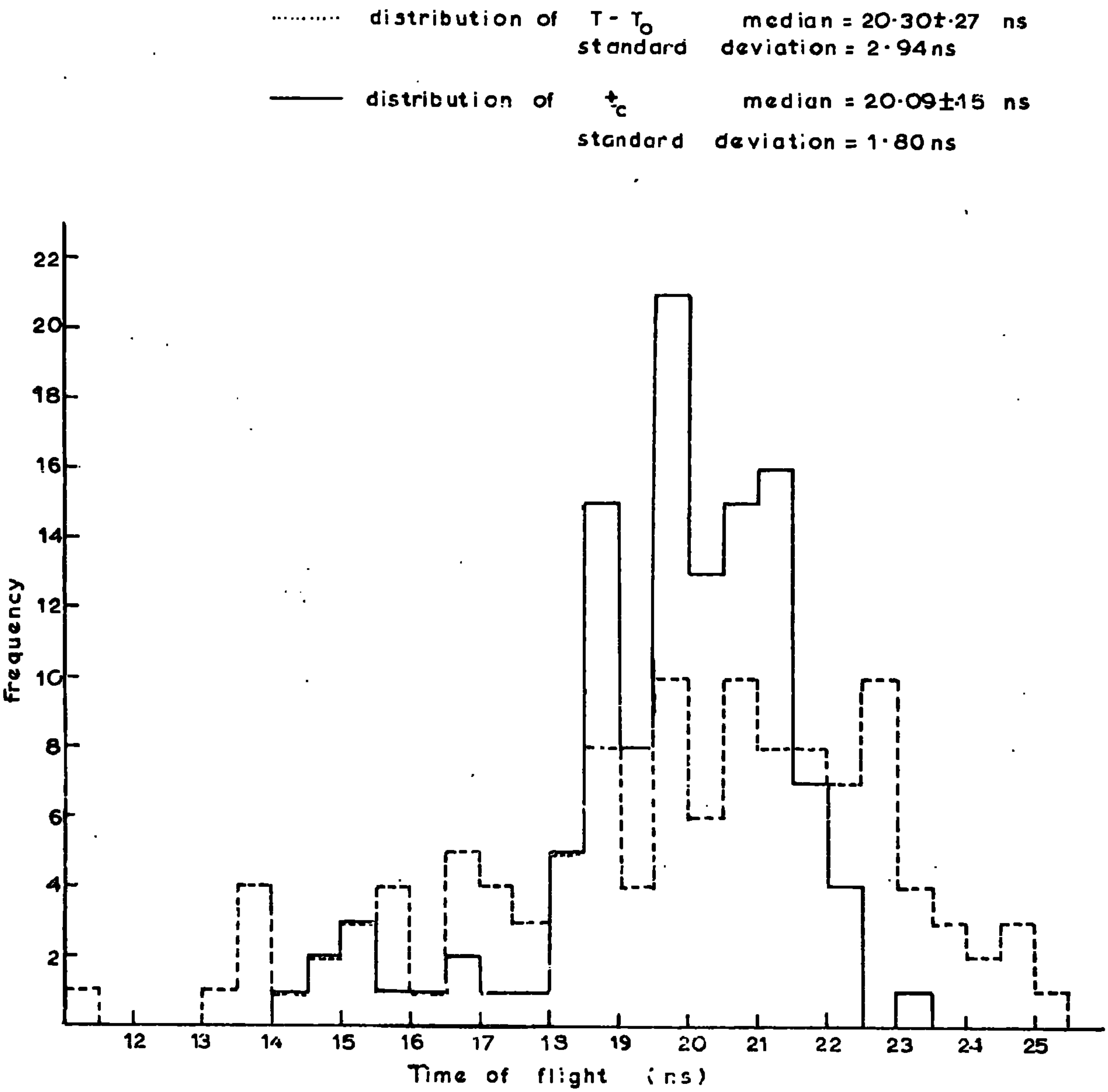

Figure 5.17 Muon time of flight distributions obtained from the zero field run.

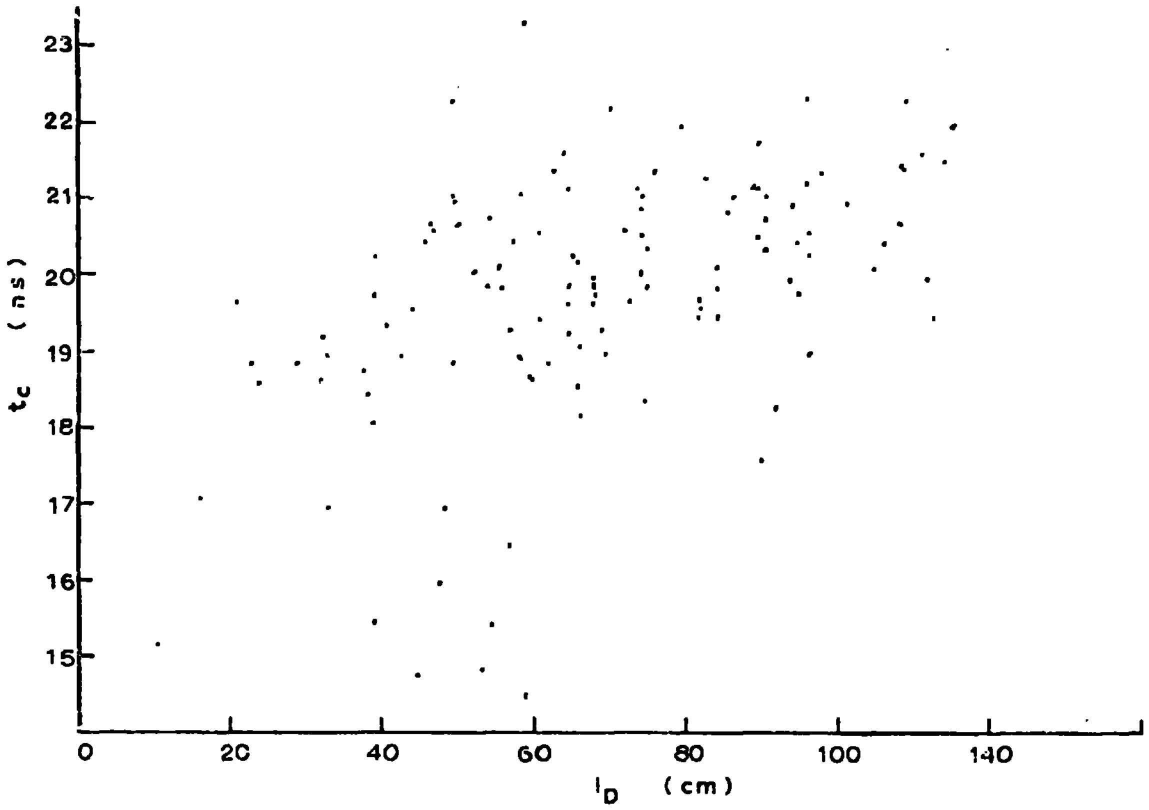

Figure 5.18 Scatter plot of muon t_c values versus the distance l_D, of the trajectory intersection point from the end of the phosphor in counter D.

Subsequent measurements, described in Chapter 6, enabled this systematic effect to be accurately measured. Using the correction factors, t', obtained in Section 6.13.2, Table 6.5, the value of t_c, found for each muon event selected in the zero field run, was corrected for this systematic effect, so that all events were corrected to traverse the centre of scintillator D. The final time of flight values, t, are given by

$$t = t_c + t' \qquad 5.27$$

where t' is dependent on ℓ_D and is given in Table 6.5 for 20 cm cells along the length of ℓ_D.

The median of the final time of flight distribution was then corrected to the value expected for a relativistic muon traversing the centre of scintillation counters A and D, i.e. t = 17.68 ns. The final time of flight distribution obtained for muons in the zero field run is shown in Figure 5.19 and it is seen that this correction considerably sharpens the distribution although there is an excess of short time of flight pulses. This excess of events is considered in Section 7.12 to be mainly of a spurious nature.

Fitting a Gaussian to the body of the distribution, a least squares fitting procedure shows that the best fit is given by the dotted histogram in Figure 5.19 which has a standard deviation, σ, of 1.0 ns. The half width at half height of the observed distribution is 1.25 ns.

The systematic shift of $\sim$ 2.42 ns in the median of the final time of flight distribution (where the final time of flight $t = t_c + t'$) from the value of 17.68 ns expected for a relativistic muon, was thought to be caused by the transit time difference for photoelectrons to travel from the cathode to the anode in each 56 AVP photomultiplier. This interpretation of the time

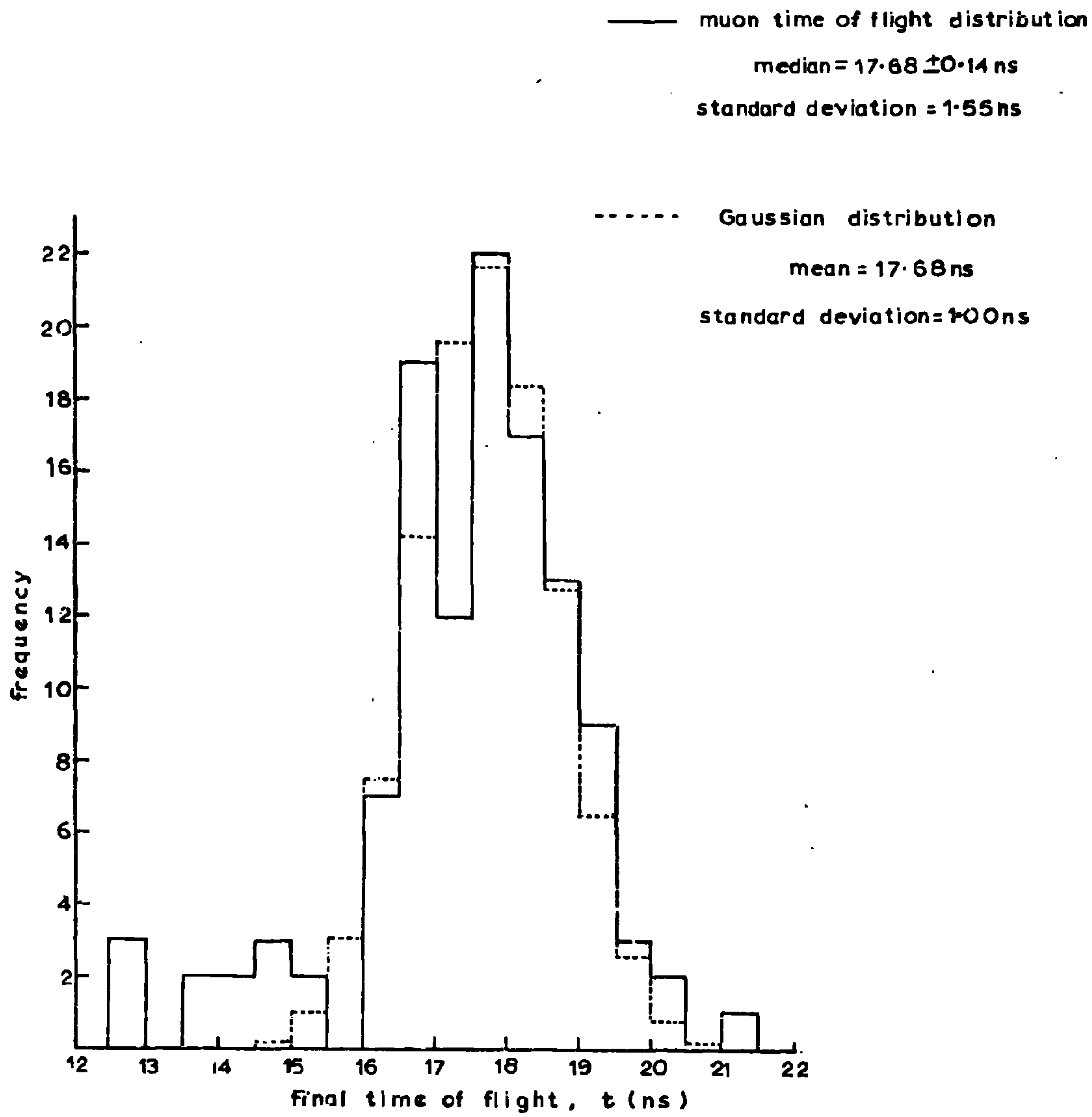

Figure 5.19 Final time of flight distribution for muon events in the zero field run.

of flight shift was calculated to be feasable when suitable differences in the voltages of the first dynode stages were considered. This was conclusively checked in the time of flight measurements taken where the first dynode voltages in the 56 AVP photomultipliers of A and D were matched and is considered in the next Chapter.

5.17.3 Precision of the time of flight determination

Using the large area scintillation counters of the type described, separated by 530.38 cm, the time of flight of a particle, travelling between them, can be established to a precision of ± 1.0 ns. For particles travelling close to the velocity of light this corresponds to a 5.7% error in the velocity and therefore an even greater percentage accuracy for lower velocity particles.

The full width at half height of the distribution in muon time of flight values (Figure 5.19) is 2.5 ns and this can be compared with the value of 3.2 ns found, by Stefanski et al. (1967), for an isochronous counter. The full width at half height obtained with the system shown in Figure 5.2a could be reduced by increasing the number of photomultipliers used on each counter. However, because the design of an isochronous counter only allows single photomultipliers to be used, the resolution of the isochronous counter can only be improved by obtaining a phosphor of increased scintillation efficiency or a photomultiplier of increased quantum efficiency.

The resolution in the time of flight measurements taken with the simple design of counter shown in Figure 5.2a is concluded to be slightly better than that obtained by workers using the more complex isochronous counter,of a similar area. Added attributes of the former system are in its simplicity, large area but small volume and adaptability for use in a scintillation counter, magnetic spectrometer, such as that shown in Figure 5.1.

5.18 Mass determination

From equation 4.3, the mass, m, of a particle travelling with momentum, pGeV/c, at a velocity, β, is given by

$$m = \frac{p}{\beta} (1-\beta^2)^{\frac{1}{2}} \ \mathrm{GeV/c^2} \qquad 5.28$$

The mass of a particle accepted through the spectrometer (described in this chapter) is determined from measurements of:

1. its displacement D (equation 5.5) in the magnetic field. The momentum of the particle measured at the magnet centre, p_m, is subsequently derived from the displacement, D, using equation 5.7, where the charge, Ze, is deduced from the measured ionisation losses in the scintillation counters $\left(\alpha \frac{Z^2}{\beta^2}\right)$. However, in the preliminary calibration of the spectrometer only particles of unit electron charge (Z=1) (e.g. muons, protons) were expected and therefore momentum determinations only involved measurements of the displacement, D.
2. the time, t ns, the particle takes to travel 530.38 cm between counters A and D. The time of flight, t ns, is derived from the observed time delay with the application of the correction factors expressed in equations 5.26.b and 5.27.

The mass, m, is then derived from the momentum, p_m, and time of flight, t, by the relation

$$m = \frac{p_m x t}{17.68} \left[1 - \left(\frac{17.68}{t}\right)^2\right]^{\frac{1}{2}} \text{ GeV/c}^2 \qquad 5.29$$

where p_m is in GeV/c and t in nanoseconds.

Alternatively, expressed in terms of the displacement, D, and $\int B d\ell$

$$m = \frac{t \times z \times \int B d\ell \times 2.84 \times 10^{-5}}{D \times 17.68} \left[1 - \left(\frac{17.68}{t}\right)^2\right]^{\frac{1}{2}} \text{ GeV/c}^2$$

using Equation 5.7, where D is cm and $\int B d\ell$ is gauss cm and t in ns.

For a mean exciting current of 36 amp, it was shown in Section 4.3 that $\int B d\ell = 2.57 \times 10^5$ gauss cm, and therefore substituting in the above equation

$$m = \frac{t \times z \times 7.3}{D \times 17.68} \left[1 - \left(\frac{17.68}{t}\right)^2\right] \text{ GeV/c}^2 \qquad 5.30$$

As the majority of particles accepted through the spectrometer (even when muons are not accepted) are the familiar particles of unit electron charge (Z=1) (e.g. protons, deuterons) then,

$$m = \frac{7.3 \times t}{D \times 17.68} \left[1 - \left(\frac{17.68}{t}\right)^2\right] \text{ GeV/c}^2 \qquad 5.31$$

5.19 Precision of the mass determination

Having established the precision of momentum determination as a function of momentum (equation 5.25) and the precision of the velocity measurement, (Section 5.17.3), an estimate can now be made on the precision of mass determination as a function of momentum, expected for particles, of different mass values, traversing the spectrometer.

From equation 4.6, the fractional error in the mass is given by

$$\frac{\delta m}{m} = \left[\left(\frac{\delta p}{p}\right)^2 + \frac{1}{(1-\beta^2)^2}\left(\frac{\delta\beta}{\beta}\right)^2\right]^{\frac{1}{2}} \qquad 5.32$$

For a particle travelling 530.38 cm between A and D, the fractional error in the mass, $\frac{\delta m}{m}$, is then related to the fractional errors in the displacement, $\frac{\delta D}{D}$, and in the time of flight, $\frac{\delta t}{t}$, by the expression,

$$\frac{\delta m}{m} = \left[\left(\frac{\delta D}{D}\right)^2 + \left(\frac{t\ \delta t}{t^2 - 312.58}\right)^2\right]^{\frac{1}{2}} \qquad 5.33$$

Substitution of $\frac{\delta D}{D}$, from equation 5.25, into equation 5.33, gives, for a mean exciting current of 36 amp,

$$\frac{\delta m}{m} = \left[\left(\frac{0.253}{\beta_m}\right)^2 + \left(0.049\ p_m\right)^2 + \left(\frac{t\ \delta t}{t^2-312.58}\right)^2\right]^{\frac{1}{2}} \qquad 5.34$$

The precision in the mass determination of a unit charged particle, with measured momentum p_m, velocity β_m and time of flight t ns (where δt = 1ns is the precision on the time of flight value) is then calculated from equation 5.34.

To determine the precision expected on the mass values of several known particles, their time of flight values were calculated as a function of momentum, where momentum loss through the spectrometer was also considered. The expected time of flight values for muons, kaons, protons and deuterons, as a function of momentum at the magnet centre, are shown in Figure 5.20. Using Figure 5.13 and Figure 5.20, with δt = 1ns, $\frac{\delta m}{m}$ was calculated from equation 5.33, and is shown as a function of the momentum and velocity (at the magnet centre) for the above mentioned particles in Figures 5.21, 5.22 and 5.23. The variation of $\frac{\delta m}{m}$ shown, is for a mean excitation current of 36 amp.

From these graphs the upper momentum limit, and the corresponding velocity limit, at which the precision of mass determination is 50% can be deduced and the results are shown in Table 5.4.

TABLE 5.4

Particle	Upper measured momentum limit p_m max.	Upper incident momentum limit p_i max.	Upper measured velocity limit β_m max.	Upper incident velocity limit β_i max.
Muon	0.295 GeV/c	0.356 GeV/c	0.94	0.96
Kaon	1.30 GeV/c	1.34 GeV/c	0.94	0.94
Proton	2.4 GeV/c	2.45 GeV/c	0.93	0.93
Deuteron	3.8 GeV/c	3.82 GeV/c	0.90	0.90

Also shown in Table 5.4 are the upper incident, momentum and velocity, limits for which $\frac{\delta m}{m} = 0.5$ (where the term 'incident momentum' and the subscript 'i' subsequently refer to the particle momentum, incident on the spectrometer).

In practice, the lower momentum limit on which mass measurements can be made is determined by the minimum momentum required by a particle to be

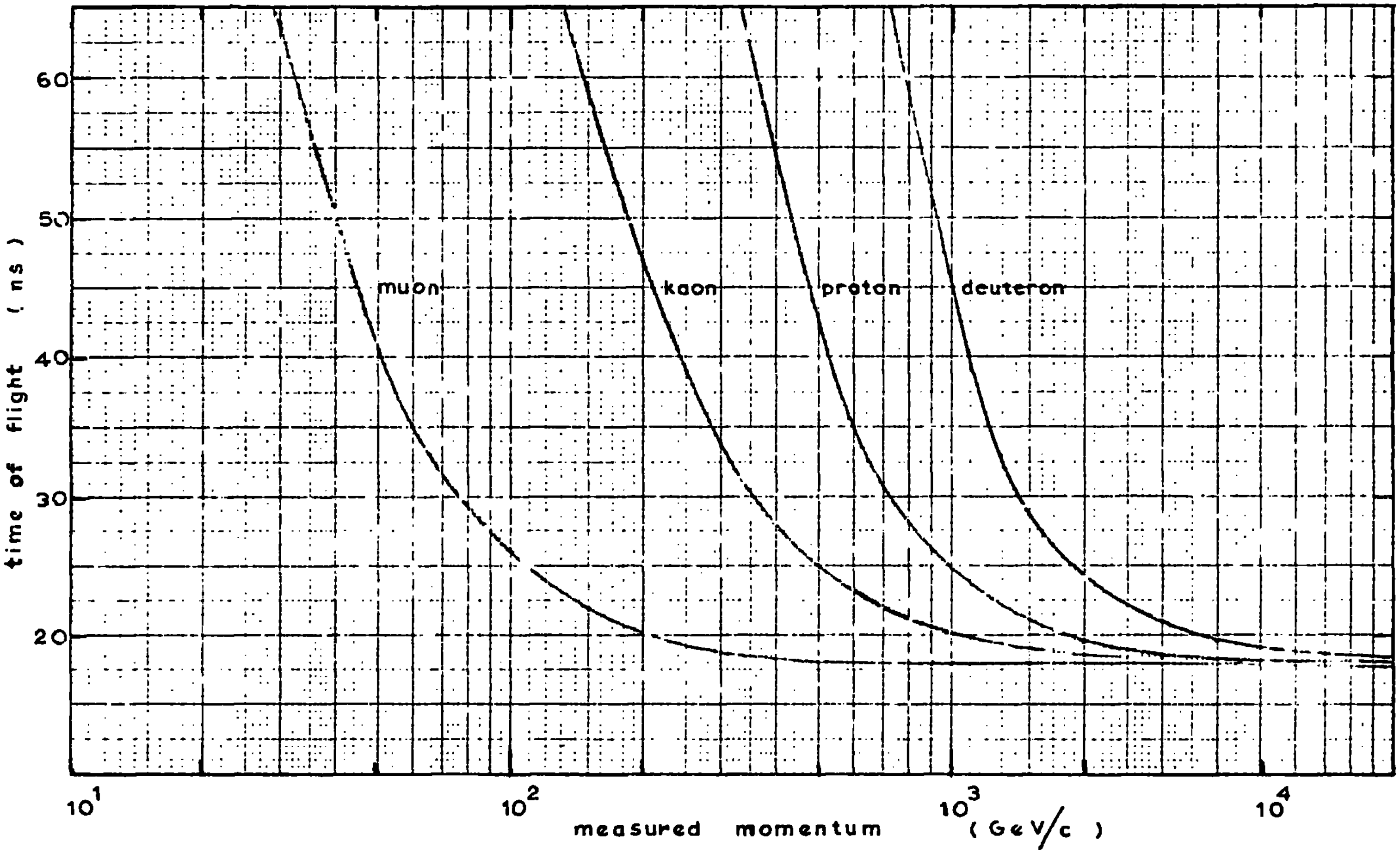

Figure 5.20 Expected time of flight as a function of measured particle momentum, for various particles travelling the vertical distance of 530.38 cm between A and D.

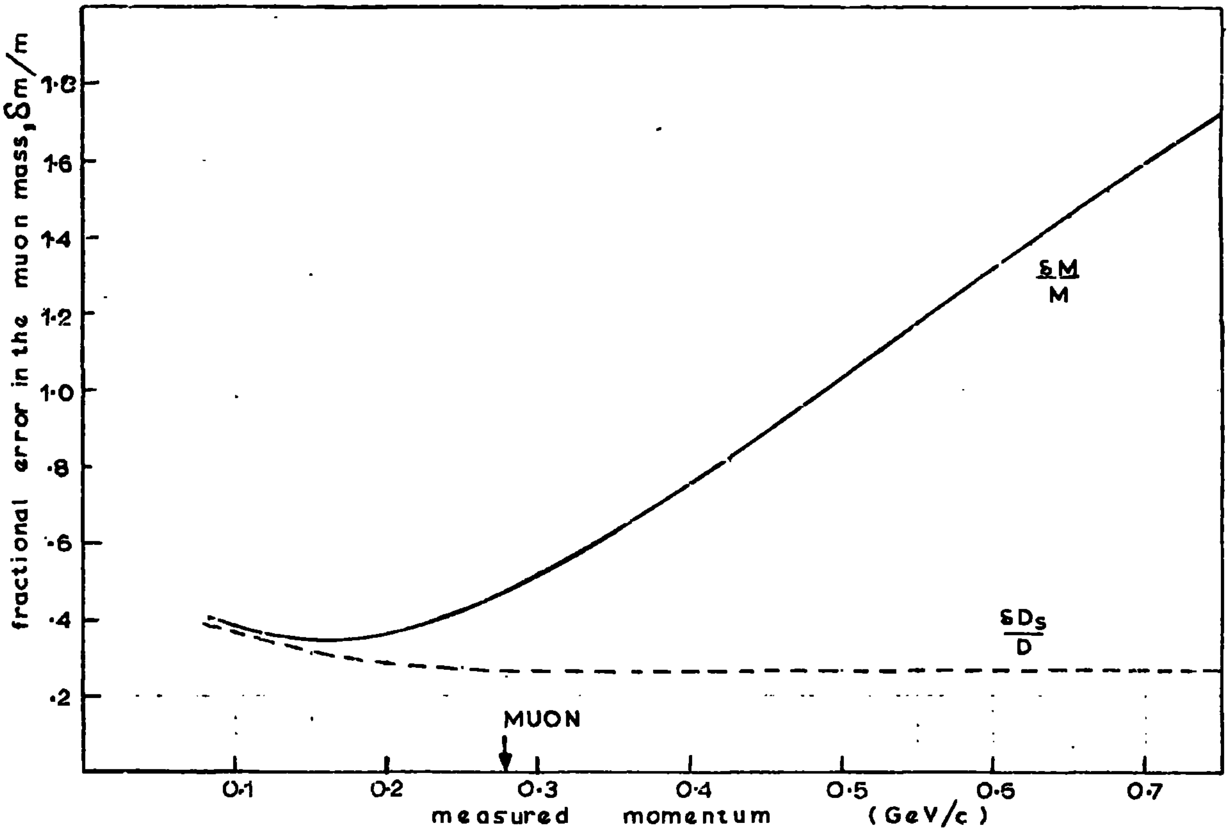

Figure 5.21 Fractional error in the muon mass determination $\delta m/m$, as a function of the momentum measured at the magnet centre, p_m GeV/c. The curves are drawn for a magnet exciting current of 36 amp. Also shown is the contribution to the fractional error from the multiple scattering in the magnet, $\delta D_s/D$. The minimum momentum required by a muon to traverse the spectrometer to H is also indicated.

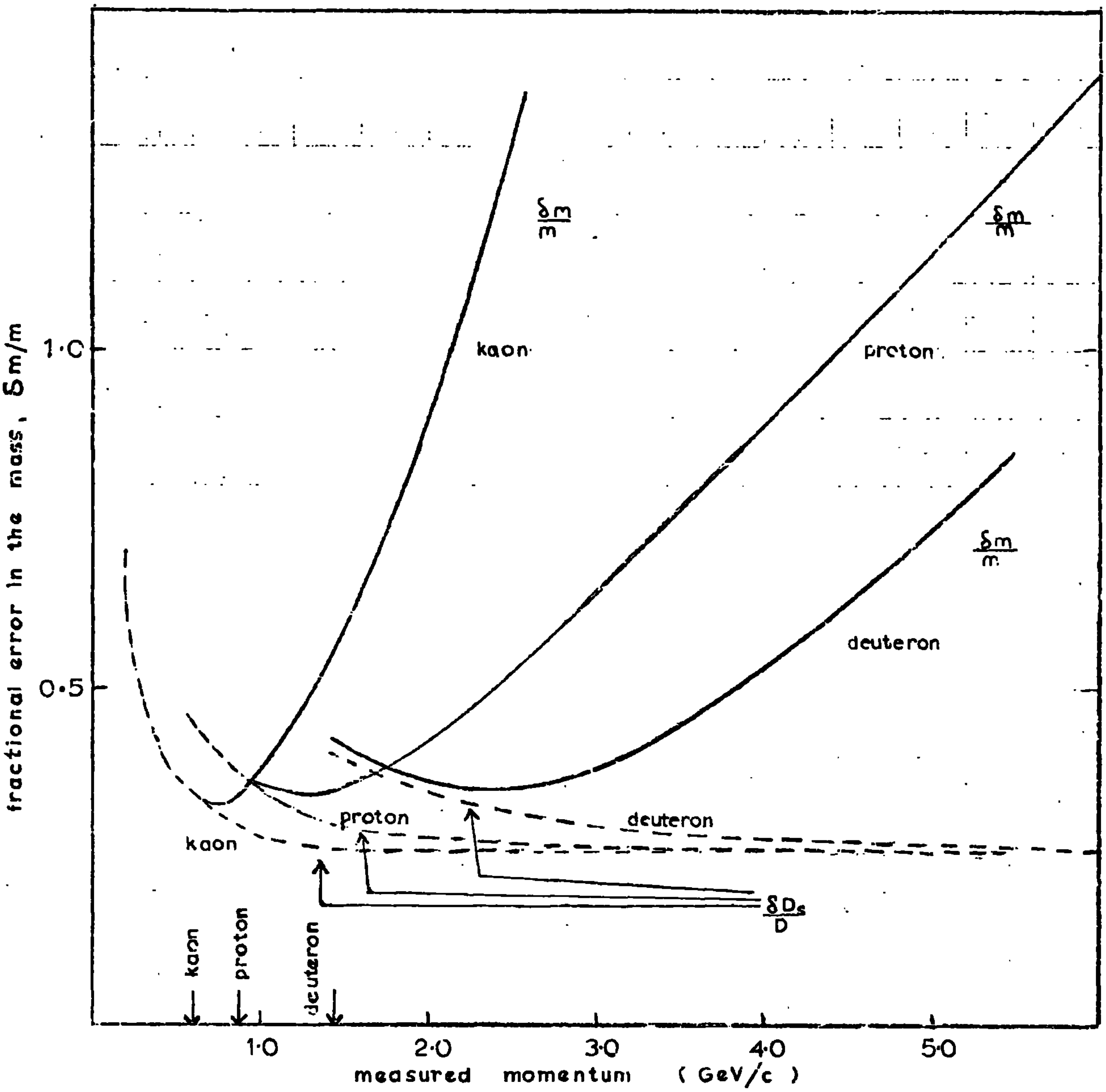

Figure 5.22 Fractional error in the mass determination δm/m, as a function of the momentum measured at the magnet centre, p_m, for kaons, protons and deuterons (magnet current = 36 amp). Also shown is the contribution to the fractional error in the mass from multiple scattering in the spectrometer, $\delta D_s/D$. The momentum limits shown correspond to the minimum momenta required to traverse the magnet to scintillator H.

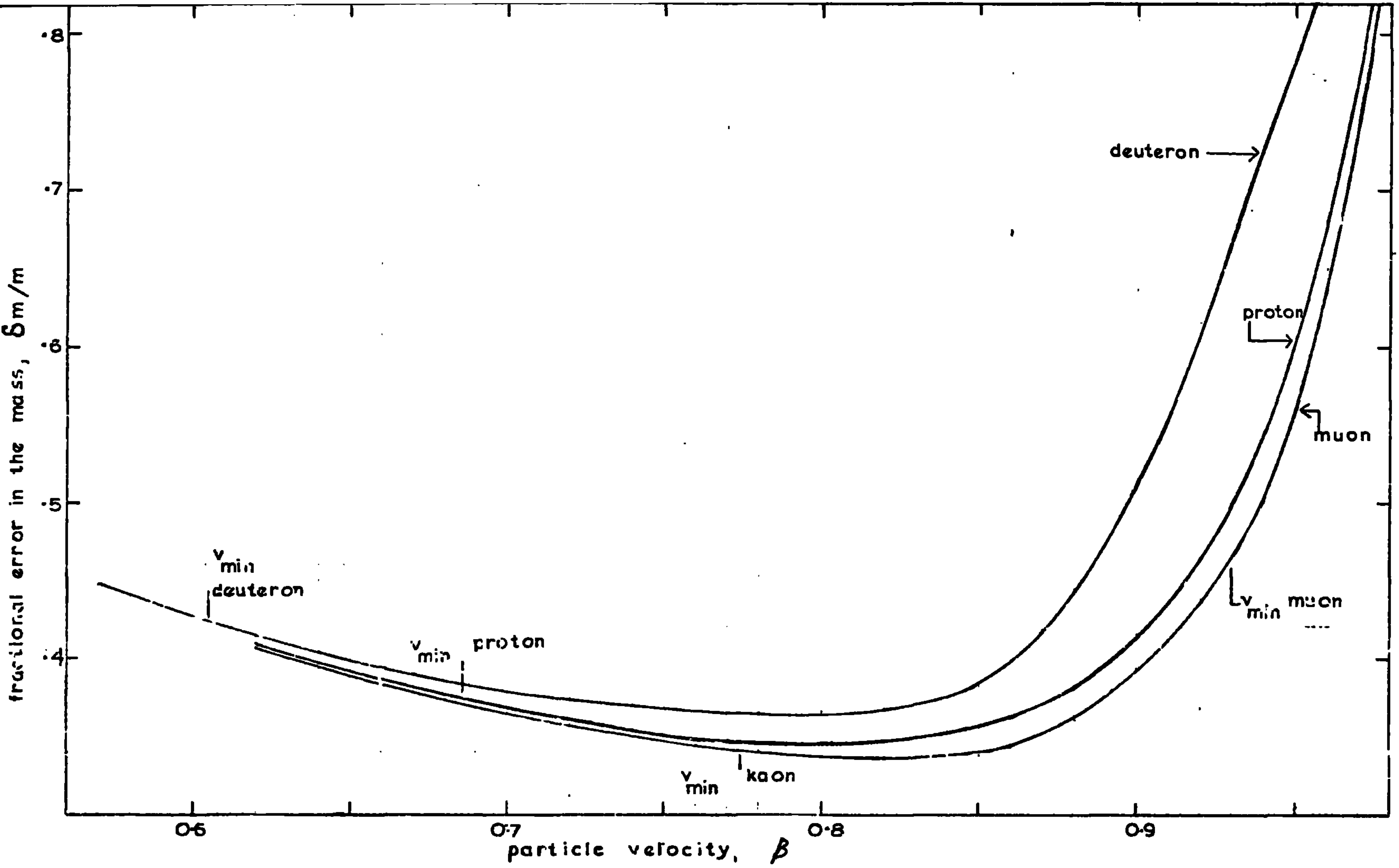

Figure 5.23 Fractional error in the mass, $\delta m/m$, as a function of the particle velocity measured at the magnet centre. The velocity limits v_{min} , shown for each particle correspond to the minimum velocities reqired to traverse the spectrometer to scintillator H.

detected, due to the finite amount of absorber in the spectrometer. The minimum incident momentum required by a particle for selection with a BCH coincidence, in the experimental arrangement shown in Figure 5.1, is plotted in Figure 5.24 as a function of particle rest mass, and for vertical paths through the spectrometer. For muons, kaons, protons and deuterons the minimum incident momenta are 0.33 GeV/c, 0.69 GeV/c, 1.02 GeV/c and 1.59 GeV/c, respectively. To obtain $\frac{\delta m}{m} < 0.5$ for particles of mass in the region of the muon mass, the selection system used would have to be BCD. For muons to penetrate the spectrometer and stop at the centre of D scintillation counter their incident momenta must be 0.23 GeV/c. However, a BCH coincidence would give a reasonable range of incident momenta over which mass measurements could be made, for kaons, protons and deuterons. This is important in that the Cerenkov counter, CT (Figure 5.1), can be used to select protons, kaons and deuterons only, by a BCH $\overline{\text{CT}}$ coincidence.

Suggested selection systems for the mass determination of muons, kaons, protons and deuterons, such that $\frac{\delta m}{m} < 0.5$, are shown in Table 5.5, together with the incident threshold momenta, p_i min, and the maximum incident momenta, $p_i$max, at which $\frac{\delta m}{m} = 0.5$.

TABLE 5.5

Particle	Selection system	Incident, momenta and velocity			
		$p_i$min	$p_i$max	$\beta_i$min	$\beta_i$max
Muon	BCD $\overline{\text{E}}$	0.23 GeV/c	0.36 GeV/c	0.91	0.96
Kaon	BCH $\overline{\text{CT}}$	0.69 GeV/c	1.34 GeV/c	0.82	0.94
Proton	BCH $\overline{\text{CT}}$	1.02 GeV/c	2.45 GeV/c	0.74	0.93
Deuteron	BCH $\overline{\text{CT}}$	1.59 GeV/c	3.82 GeV/c	0.65	0.90

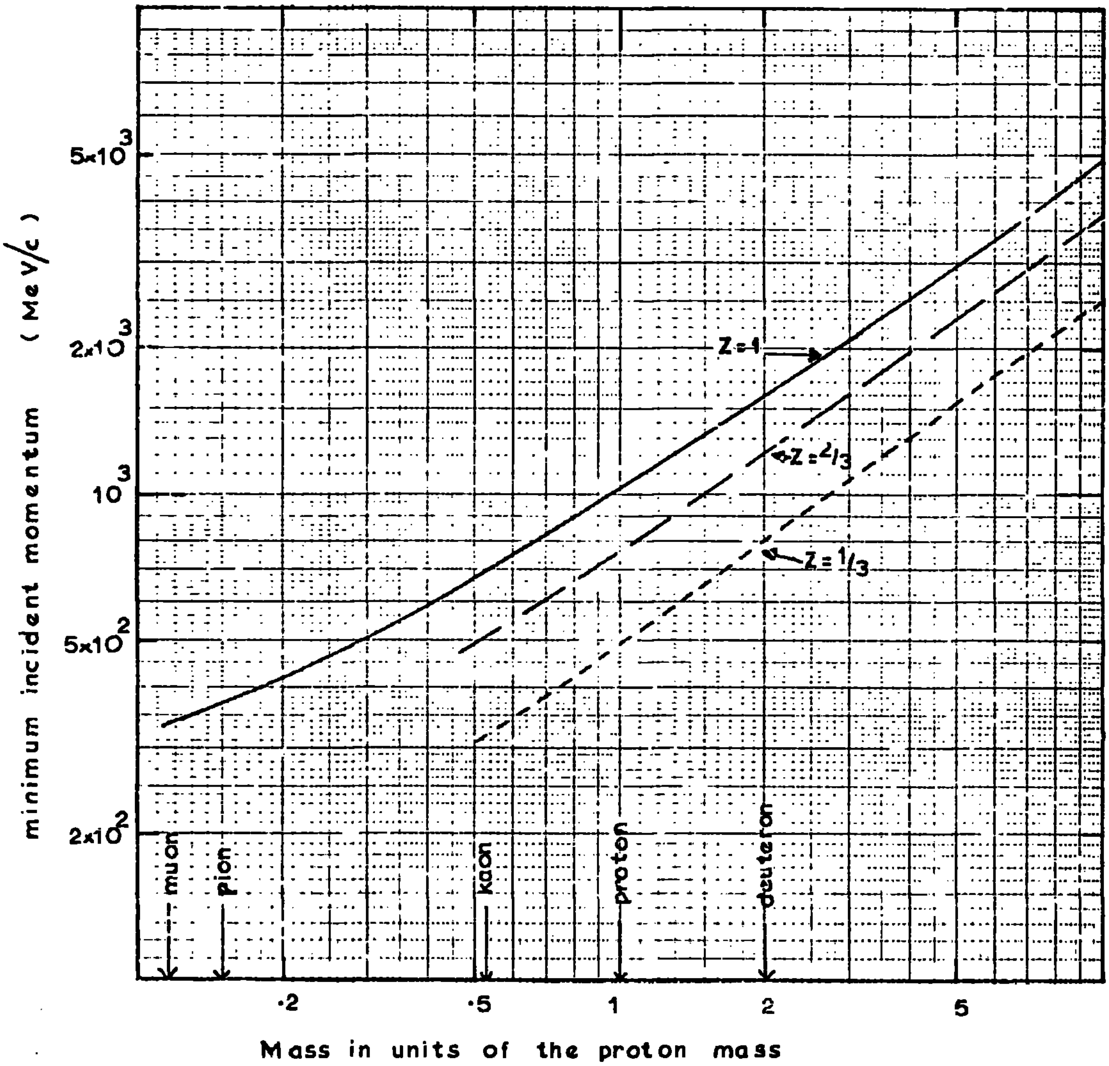

Figure 5.24 The minimum incident particle momentum able to traverse the spectrometer as a function of particle charge and mass.

CHAPTER 6

MEASUREMENT OF THE LOW ENERGY MUON SPECTRUM

6.1 Introduction

Having established the precision of mass determination as a function of momentum and the geometrical constants of the mass spectrometer from the zero field run, it was decided to make measurements on cosmic ray particles selected by a simple BCH coincidence, with the magnet excitation current set at 36 amp. Most BCH coincidences were expected to be muons (at a calculated rate of 513 per hour) with a few per cent proton contamination. By making both momentum and time of flight measurements on ∿ 1,000 events it was intended to:

1. measure the muon spectrum and charge ratio,
2. extend the measurements giving the precision in the time of flight determination, as all muons satisfying a BCH coincidence should have a velocity close to the velocity of light, i.e. $\beta \approx 1.0$.
3. ascertain if low energy protons could be identified at a level of a few per cent, from the momentum and time of flight information,
4. conduct a search for the faster-than-light particles, namely tachyons, whose existence was originally proposed by Bilanuik et al. (1962). Confirmation of these particles' existence ensues from measurements of their time of flight.

The results of aims 1 and 2 are given in this Chapter, the results of 3 and 4 in Chapter 7.

6.2. The spectrometer acceptance function

The three scintillation counters B,C,H, used in the coincidence requirement

(Figure 5.1), and the magnet area, limit the possible incident angles of the accepted particles and also the area through which they pass. Since particles are deflected on passing through the spectrometer, the acceptance aperture is a function of momentum, falling to zero at 'the least detectable momentum'.

Under the geometrical conditions of the experiment in limiting the incident angles and accepting only small angles of deflection, the acceptance function, $A(\phi)$ cm^2 sterad, can be subdivided into an acceptance in the deflection plane, $A_1(\phi)$ radian cm, and a constant acceptance in the back plane, A_2 radian cm. Such that

$$A(\phi) \quad = \quad A_1(\phi) \times A_2 \quad cm^2 \text{ sterad} \qquad 6.1$$

The acceptance $A_1(\phi)$ in the front plane of the spectrometer is given, with reference to Figure 6.1, by

$$A_1(\phi) \quad = \quad \int d\alpha(\phi) \quad dH \text{ radian cm} \qquad 6.2$$

where $d\alpha(\phi)$ is the range of angles for which particles with a deflection ϕ pass through B,C, the magnet centre G and a small length dH on H. For small incident and deflection angles

$$d\alpha(\phi) \quad = \quad \frac{dg(\phi)}{\ell}$$

where $dg(\phi)$ is the limited length on G, (the magnet centre), subtended by the angle $d\alpha$ over the length $\ell = 492.38$ cm.

As the spectrometer is not exactly symmetrical about the magnet centre the acceptances, $A_1(\phi)$ and A_2, were evaluated graphically from a diagram of the apparatus, scaled by 1:10 and 1:5 in the vertical and horizontal directions, respectively. Using a trajectory of a fixed deflection, ϕ degrees, $\frac{dg(\phi)}{\ell}$

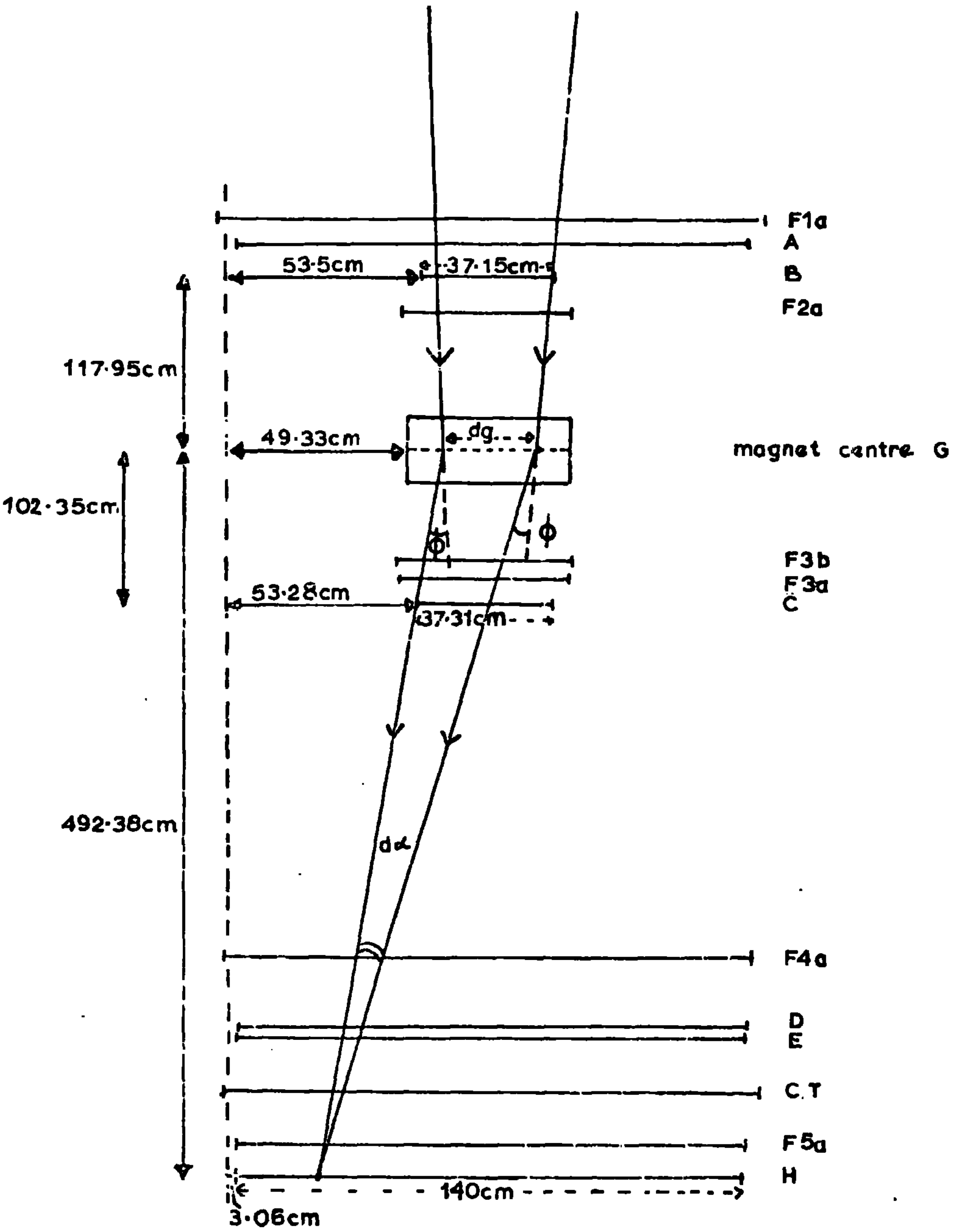

Figure 6.1 Diagram illustrating the measurement of the acceptance function, $A_1(\phi)$, in the front plane of the spectrometer.

was measured for different points on H, under the assumption of isotropic incident radiation. The area under the resultant curve yielded $A_1(\phi)$ in radian cm for each deflection ϕ. The values of $A_1(\phi)$ shown in Figure 6.2, for positive and negative deflections of ϕ, are averages of two independent calculations. A_2 was similarly measured, in terms of radian cm, from a scale diagram of the side plane, as shown in Figure 6.3.

The acceptance function, $A(\phi)$, calculated from equation 6.1 and expressed in cm^2 sterad, is shown in Figure 6.4 as a function of the magnetic deflection, ϕ, and in Figure 6.5 as a function of the momentum measured at the magnet centre, for an excitation current of 36 amp and for incident particles of unit electron charge. The least detectable momentum accepted by the spectrometer is found not to be limited by the acceptance threshold momentum of 0.148 GeV/c (Figure 6.5), but by the threshold momenta required by incident particles to traverse the spectrometer absorbing material to scintillator H. The threshold momenta required by muons, kaons, protons and deuterons to vertically traverse the absorbing material from the magnet centre to scintillation counter H, are indicated by the vertical lines in Figure 6.5.

6.3 Experimental conditions of the spectrometer

For the measurement of the low energy muon spectrum and the muon time of flight values the experimental conditions of the zero field run were repeated, apart from the modifications listed below, designed to overcome the problems encountered in the zero field run:

6.3.1 Modifications to the scintillation counters

To eliminate the systematic shift of the time of flight distribution observed in the zero field run (Section 5.17.2) from that expected for a

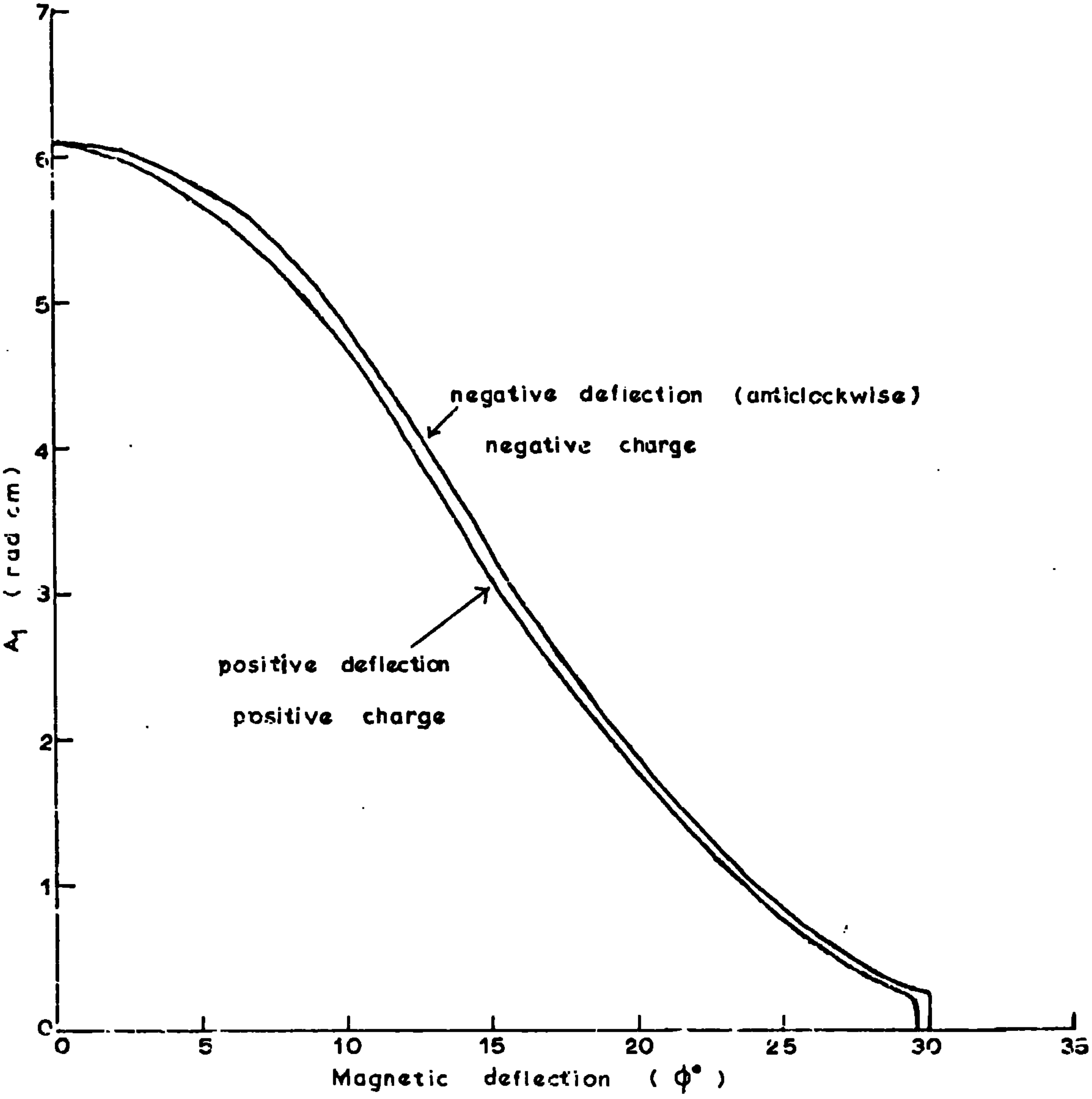

Figure 6.2 The front plane acceptance, $A_1(\phi)$, as a function of the magnetic deflection ϕ .

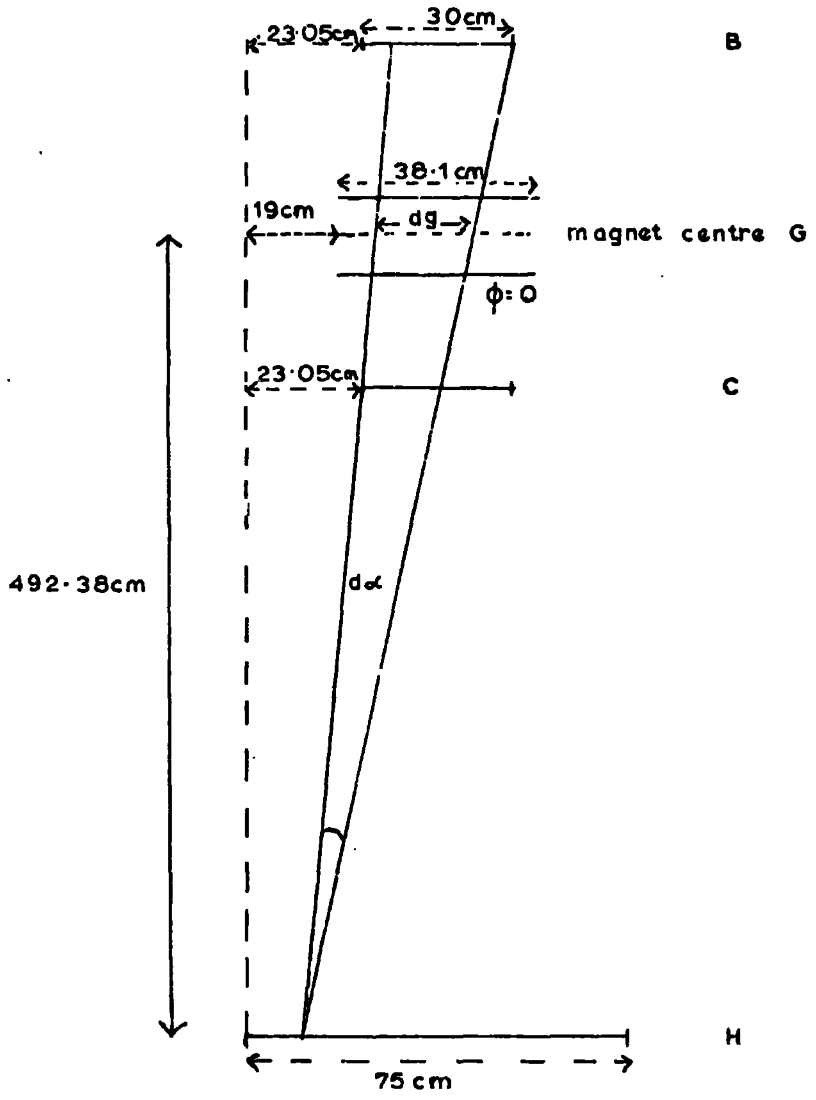

Figure 6.3 Diagram illustrating the measurement of the acceptance, A_2, in the side plane of the spectrometer.

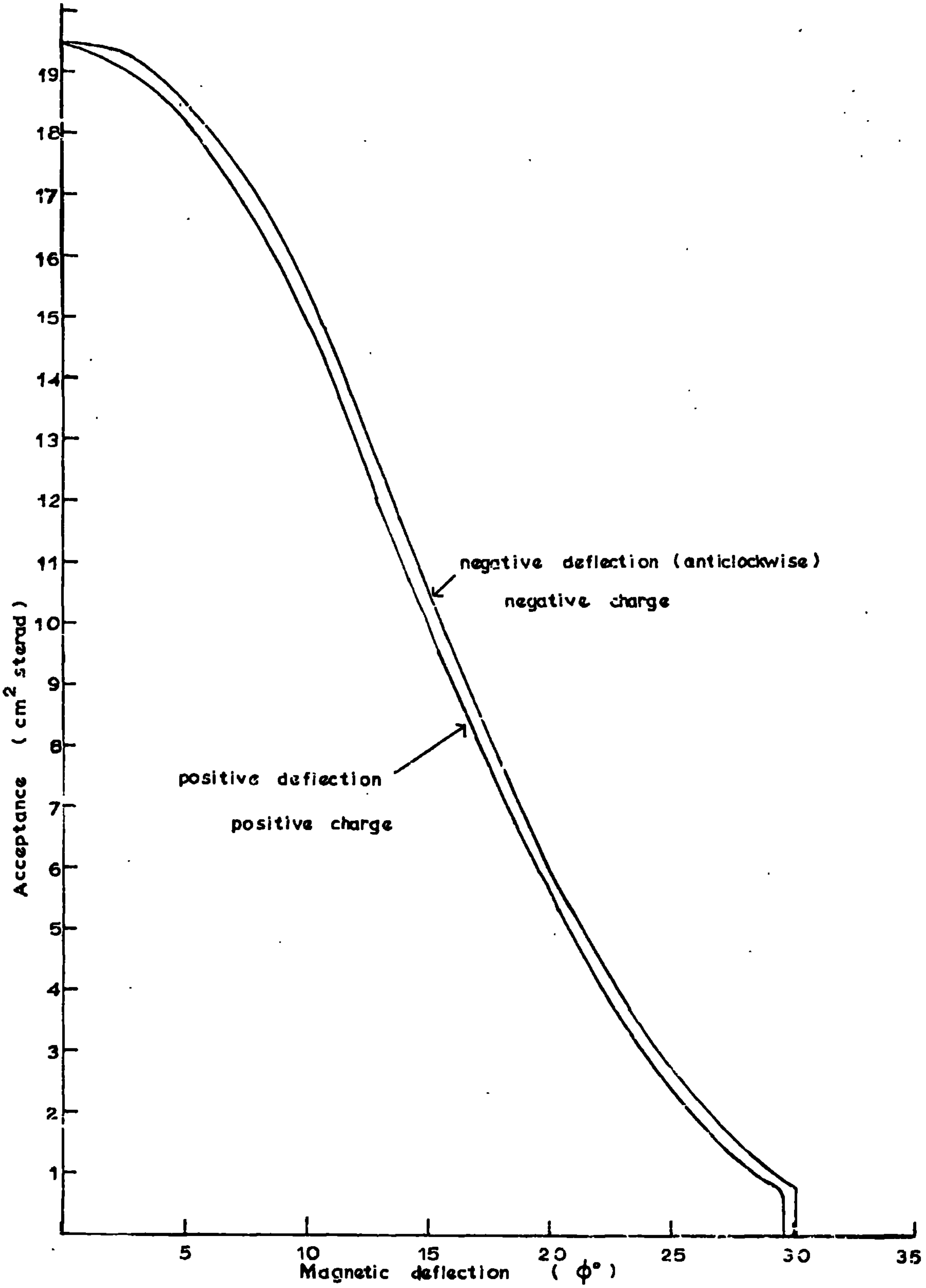

Figure 6.4 Acceptance of the spectrometer as a function of the magnetic deflection, for isotropic radiation.

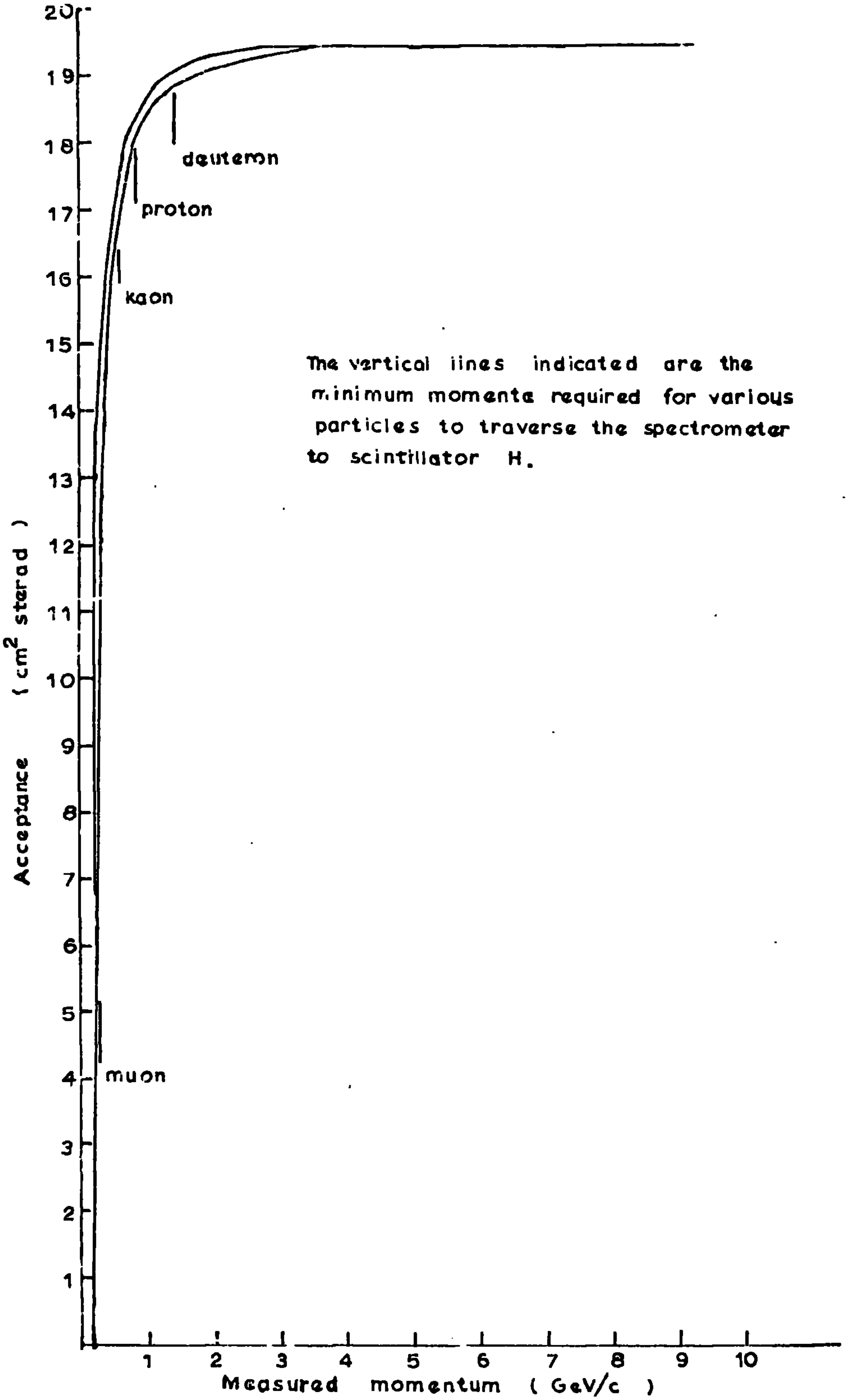

Figure 6.5 Spectrometer acceptance as a function of particle momentum measured at the magnet centre G, for a magnet current of 36 A.

relativistic muon, the voltages of the first dynode in each 56 AVP photomultiplier were matched.

6.3.2 Flash tube tray modifications

To measure the discrepancy values of deflected trajectories in the magnetic spectrometer (see Figure 6.9) the trajectory location in F1a was included with the three accurate locations in F2a, F3a, F4a. For technical reasons the flash tube tray F1a did not always register a track, however, an internal efficiency of 70% was obtained for trajectories displaying two or more flashed tubes in that tray.

6.3.3 Electronics modifications

To allow for the reduction of the scintillator pulse heights in the presence of the magnetic field, double amplifiers were incorporated prior to the discriminators shown in the logic circuitry of Figure 5.9a. The discrimination levels of B,C,H were each reset to $0.2E_s$ (where E_s is defined in Section 2.5) by comparing the smallest pulse height observed to pass through the discriminator channel, to the most probable pulse height, E_s, from the same scintillation counter, under the same electronic conditions. The coincidence, BCH, was demanded to accept muons deflected by the magnetic field, using a resolving time of 55 nanoseconds. The subsequent electronics, triggered by the BCH coincidence pulse, is shown in Figure 5.9a and is identical to that employed in the zero field run.

Consideration of the background 'separate track' events encountered in the zero field run and their associated distribution in time of flight values

(Section 7.11) instigated the modification of the regulated time of flight pulse profiles, so that their channel origin (i.e. either from A or D) could be identified. This not only enabled the recognition of events displaying pulses from the same scintillator photomultiplier (as this was thought to be the cause of the excess in low time of flight events observed in the zero field time of flight distribution, Figure 5.19), but also, the order in which the different channel pulses arrived. The modified pulse profiles are shown in Plate IIb.

As it was found, in the zero field run, that the Rutherford scalars were unable to count on pulses of 10 ns width, the discrimination levels of channels A and D were reset to give a counting rate of 2 x 10^5 /min with the electronic logic shown in Figure 6.6. The scalars thus counted on pulses of 50 ns width. The counting rate was chosen as a compromise between low discrimination levels and low spurious rates, and was calibrated to be discriminating at $\left(0.019^{+0.002}_{-0.001}\right)E_s$ and $\left(0.02^{+0.001}_{-0.001}\right)E_s$ for A and D, respectively, by the method used for counters B, C and H.

6.3.4 Recording system and criteria used to select muon events for determination of their momenta

Information regarding each selected event was obtained by projection of the flash tube photograph and the associated time of flight photograph onto a scanning board, as described in Sections 5.8.1 and 5.15. A typical event is shown in Plate II. The flash tube photograph (Plate IIa) shows a particle track, deflected through a small angle in the magnetic field. The time of flight photograph (Plate IIb) shows the associated time of flight pulses from

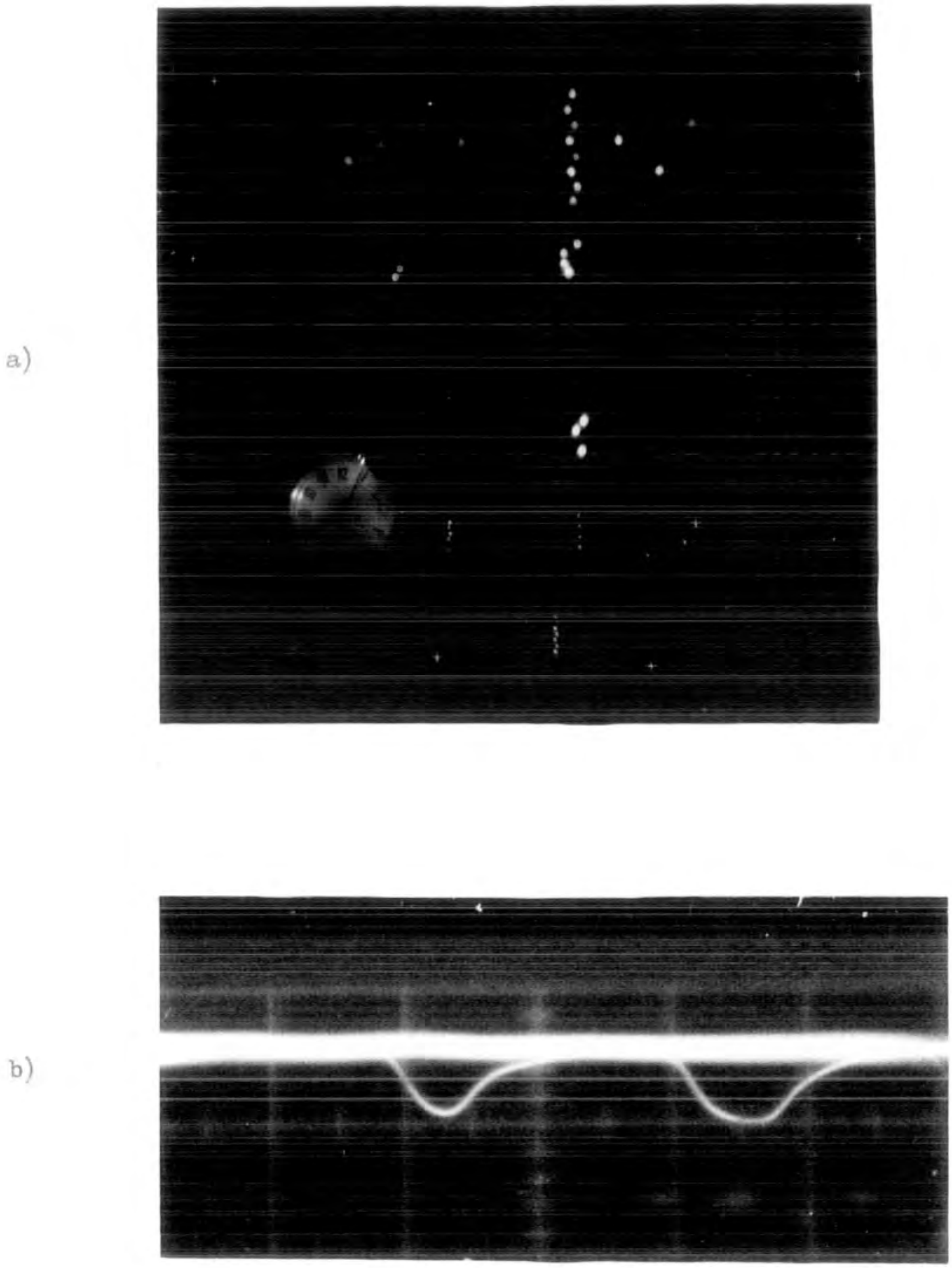

Plate II Photograph information of a typical event accepted through the spectrometer showing,

a) the flash tube photograph used to determine particle momentum,
b) the time of flight pulses from counters A and D used for velocity determination.

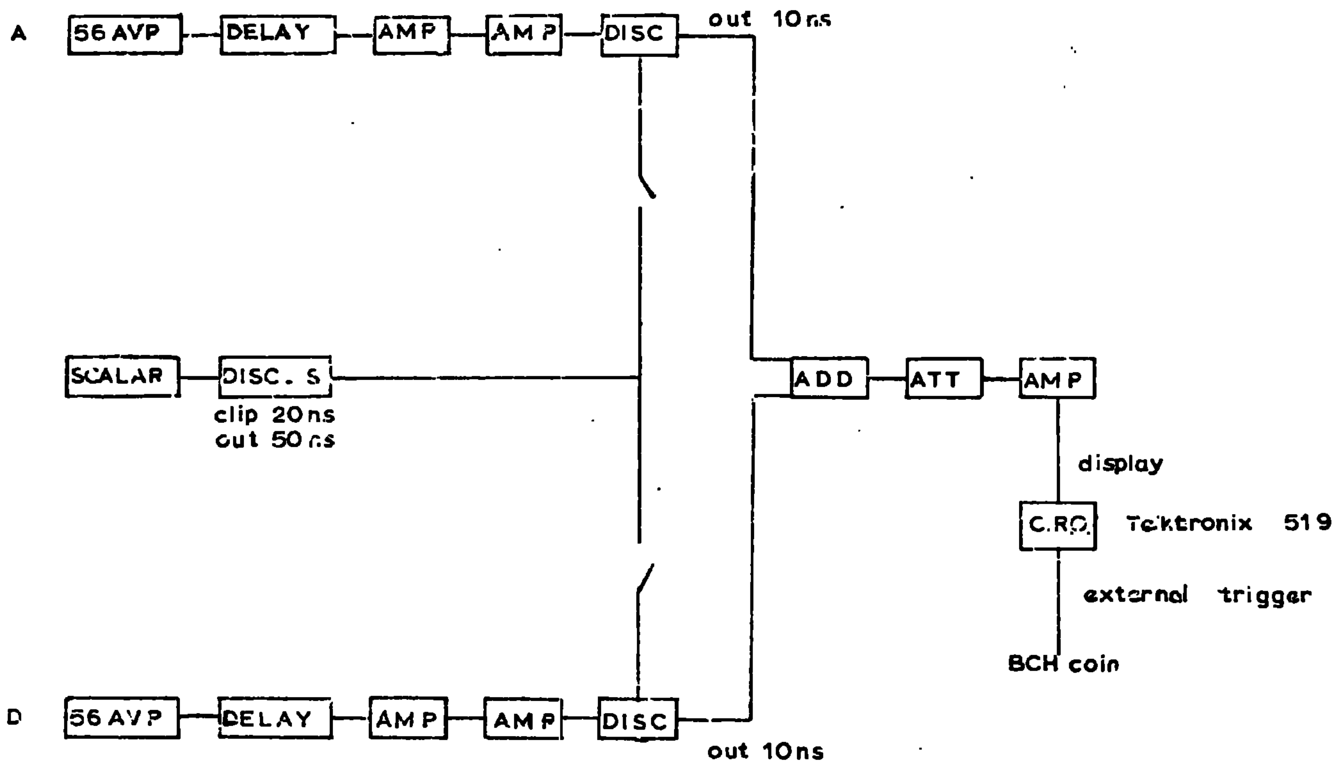

Figure 6.6 Time of flight electronics, illustrating the modified scalar counting system.

counters A and D.

As for technical reasons the flash tube tray F1a was inefficient, the muon events were recorded as either Class I (track in F1a) or Class II (no track in F1a or a track in F1a , i.e. all the accepted muon events), where a track in F1a is defined as two or more flashed tubes in the F1a trajectory.

The same criteria as stated in Section 5.8.2 were used to select muon events for the measurement of the muon momentum spectrum, apart from the following modifications:

1. For Class I events only. Trajectories displaying two or more flashed tubes in F1a were accepted into Class I. The coordinate estimations for this tray were taken from the straight line passing through all the flashed tubes irrespective of the positions of the unflashed tubes. A layer efficiency of only 25% in this tray (for all the muon events) instigated the adoption of this track location method.

2. Events exhibiting distinguishable double tracks in F2a were accepted for Class I events, with the knowledge of the track location in F1a, F3a, and F4a.

6.4 Basic data of the experiment

With the magnet excitation current set at a mean I = 36 ± 0.2 amp events were selected with a BCH coincidence. The basic data obtained during a running time of 1hr 42 min is shown in Table 6.1. The vast majority of the observed triggers were single unaccompanied particles with a small contribution from showers and other background effects.

TABLE 6.1

Selection	BCH
Magnet excitation current	36 amp
Total number of triggers	1,083
Number of showers, blanks and spurious	123
Number out of geometry	21
Total number of tracks showing only single time of flight pulses	110
Number of unmeasurable events, caused by accompanyment	111
Number of Class I events (track in Fla and two time of flight pulses)	198
Number of Class II events (no track in Fla and two time of flight pulses, plus, track in Fla and two time of flight pulses (i.e. plus Class I events))	718

If the 110 events exhibiting single time of flight pulses are not caused by instrumental faults (e.g. intermittent faults in the channels A and D), then the only feasable explanation is that they are triggered by background 'separate track' events of the type described in Section 5.8.2. This explanation is further substantiated in Section 7.11, where it is shown that such background events are able to exhibit single time of flight pulses. The acceptance of a substantial fraction of these events is more reasonable when one considers their alternative source mechanisms. The events are either:

1. associated 'separate particles' produced in interactions above the spectrometer such that one secondary passes through B,C (or just B) and one of the

other secondaries passes through H (or CH), thus satisfying the coincidence requirement and resolving time.

2. unassociated 'separate particles'. Random BCH coincidences can be produced between a particle passing through BC (or B) and an unassociated particle through H (or CH). Due to the geometry of the spectrometer, events in which separate particles pass through B and CH are expected to contribute only a small fraction to the total number of 'separate track' events. The events displaying only single time of flight pulses were thus excluded from the measurements on the muon spectrum under the assumption that they were background, rather than true, muon events.

In principle, with the imposition of an upper discrepancy cut off on the events in Class I, background 'separate track' events (exhibiting two time of flight pulses and in general exhibiting large discrepancy values) can be identified. This familiar method of background disposal has been successfully employed by Hayman and Wolfendale (1962). However, as it will be shown in Section 6.8.3, the large location precision in flash tube tray Fla, in practice, renders the discrepancy values of relativistic muons to be of the same order as the discrepancy values expected for background events. The application of this method for distinguishing background events from muon events, in Class I, was thus inoperative.

6.5 The measured spectra, for Class I and Class II events

The displacement measurements of the accepted muon events from Class I and Class II are shown in Table 6.2, where both positive and negative displacement values are included together, and equations 5.5 and 5.19 were used to determine the displacement and momentum of each event.

TABLE 6.2

Displacement cell in cm	Momentum cell in GeV/c	Class I	Class II
> 26	< 0.28	1	7
14 - 26	0.521 - 0.28	50	53
6 - 14	1.217 - 0.521		162
4 - 6	1.825 - 1.217	29	109
2 - 4	3.65 - 1.825	43	152
1 - 2	7.3 - 3.65	36	130
0.5 - 1	14.6 - 7.3	19	61
0.25 - 0.5	29.2 - 14.6	10	23
0 - 0.25	∞ - 29.2	10	21

The absolute intensities for each displacement cell were calculated from the knowledge of: the acceptance function, $A(D)\,\mathrm{cm}^2$ sterad, as a function of displacement; the useful running time, T seconds; and the momentum band, Δp GeV/c (at the magnet centre), for each cell width. The absolute intensity of muons at a mean momentum p_a GeV/c was calculated from the expression

$$N(p)dp = \frac{N_o}{T.A(D_a)\Delta p}\ \mathrm{cm}^{-2}\mathrm{sec}^{-1}\mathrm{sterad}^{-1}\ (\mathrm{GeV/c})^{-1},$$

where N_o muons were observed in the displacement cell of momentum width Δp GeV/c.

The mean momentum (and the mean acceptance) for each cell is an average of the observed momenta (acceptances) of the events in each cell. The minimum threshold momentum, required by muons to traverse the spectrometer to scintillator H, has been corrected for the increased path length traversed by the muons subject to deflection in the magnetic field.

The muon spectra of Class I and Class II events are shown in Figure 6.7(i) normalised to the differential muon spectrum as detected by Hayman and Wolfendale (1962) at 2.6 GeV/c and 1.5 GeV/c, respectively. The spectrum of the latter workers is shown for comparison. The muon spectra are seen to be consistent with the standard spectrum up to the value of the maximum detectable momentum (∿20 GeV/c). Improvement in this agreement is achieved with the application of a correction for the ionisation loss of muons in traversing 28.3 g cm^{-2} water equivalent to the magnet centre. Such a correction, and corresponding improvement, has been applied to the Class II events shown in Figure 6.7(ii). Further improvement results from the application of corrections for: multiple scattering of muons; proton contamination (few %); the use of mean momenta, more important for large cell widths (typically a decrease of 6.6%, in the momentum, is caused by this approximation at 19 GeV/c); and effects of location precision. However, as measurements on the differential muon spectrum are so well established, and the measurements of the low energy muon spectrum taken with this spectrometer are sufficiently in agreement, the application of these correction factors was not considered worth while.

6.6 The measured muon charge ratio

The elementary summation of the positive and negative muon numbers falling into each displacement cell, is shown in Table 6.3 for Class II events.

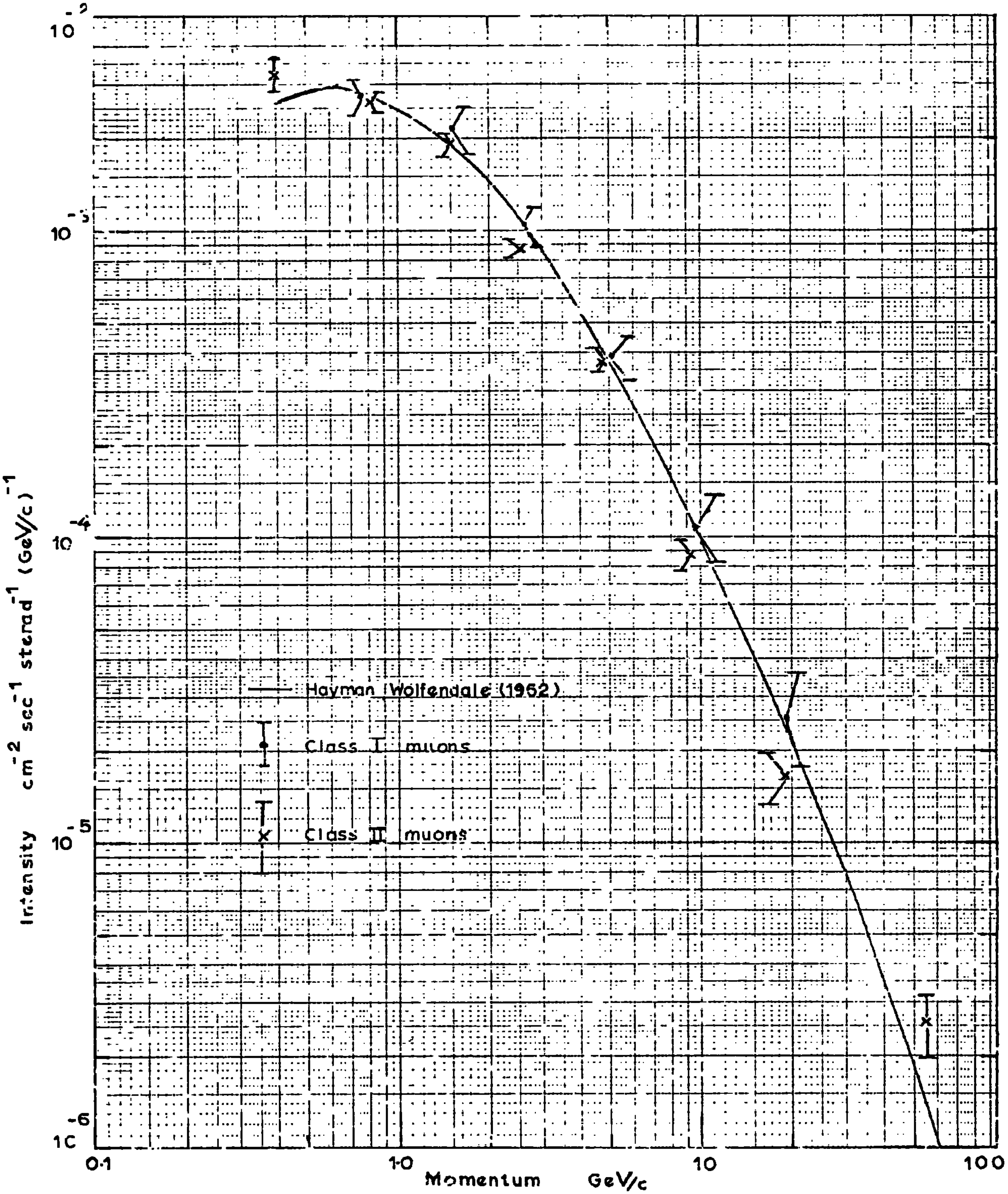

Figure 6.7(i) The measured sea level muon spectrum, for Class I and Class II events, normalised to the muon spectrum due to Hayman and Wolfendale.

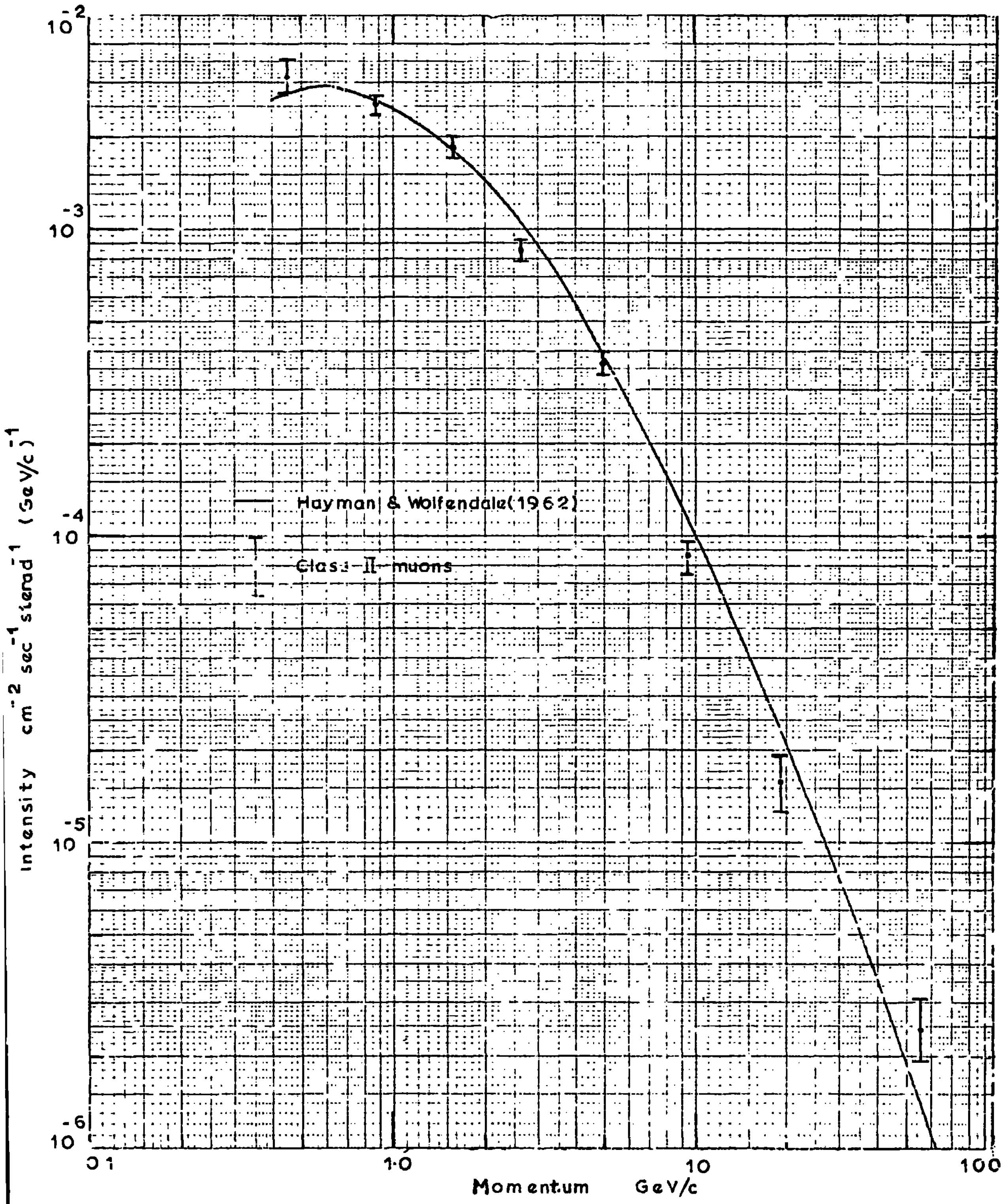

Figure 6.7(ii) The measured muon sea level spectrum (ClassII events) of Figure 6.7(i), corrected for ionisation loss.

TABLE 6.3

Displacement cell in cm	Momentum cell in GeV/c	Class II events	
		Number of positively charged muons	Number of negatively charged muons
> 26	< 0.28	4	3
14 - 26	0.521 - 0.28	28	25
6 - 14	1.217 - 0.521	87	75
4 - 6	1.825 - 1.217	62	47
2 - 4	3.65 - 1.825	82	70
1 - 2	7.3 - 3.65	71	59
0.5 - 1	14.6 - 7.3	35	26
0.25 - 0.5	29.2 - 14.6	14	9
0 - 0.25	∞ - 29.2	15	6

The measured muon charge ratio, for Class II events, as a function of momentum is shown in Figure 6.8, where the original ratios have been corrected for the relative acceptance apertures of positive and negative deflections and the errors are of a statistical nature. As this muon charge ratio is observed to be sufficiently consistent with previous measurements of this ratio, application of further correction factors is considered unnecessary.

6.7 Discrepancy measurements of the Class I events

When the estimated positions of a particle track at the four measuring levels F1a, F2a and F3a, F4a are projected to intersect the level G (Figure 6.9), where the magnetic deflection is assumed to take place, then the discrepancy, X, between the apparent incident trajectory, ADF, and the

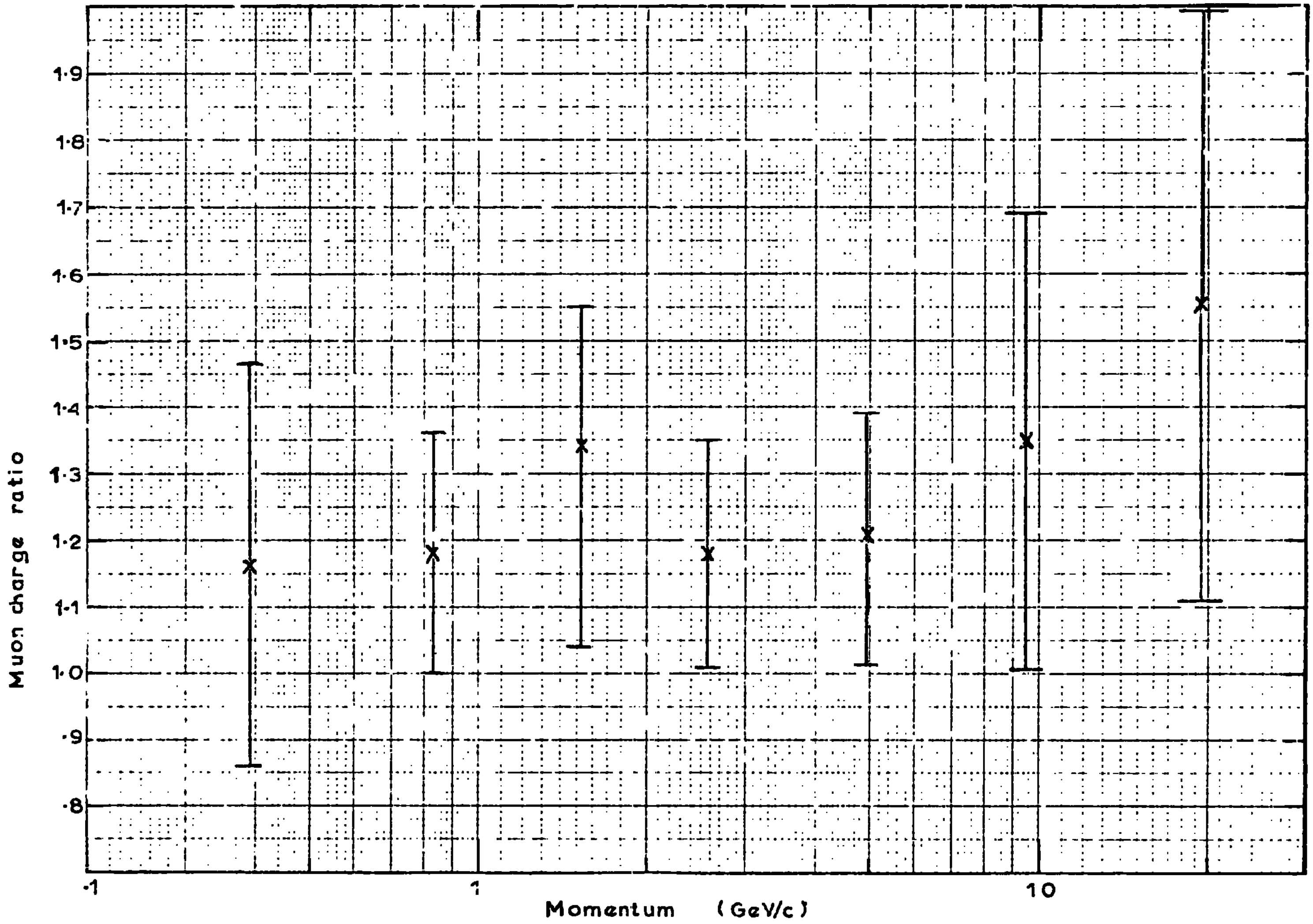

Figure 6.8 The measured sea level muon charge ratio as a function of momentum, corrected for the relativistic acceptance apertures of positive and negative deflections in the spectrometer.

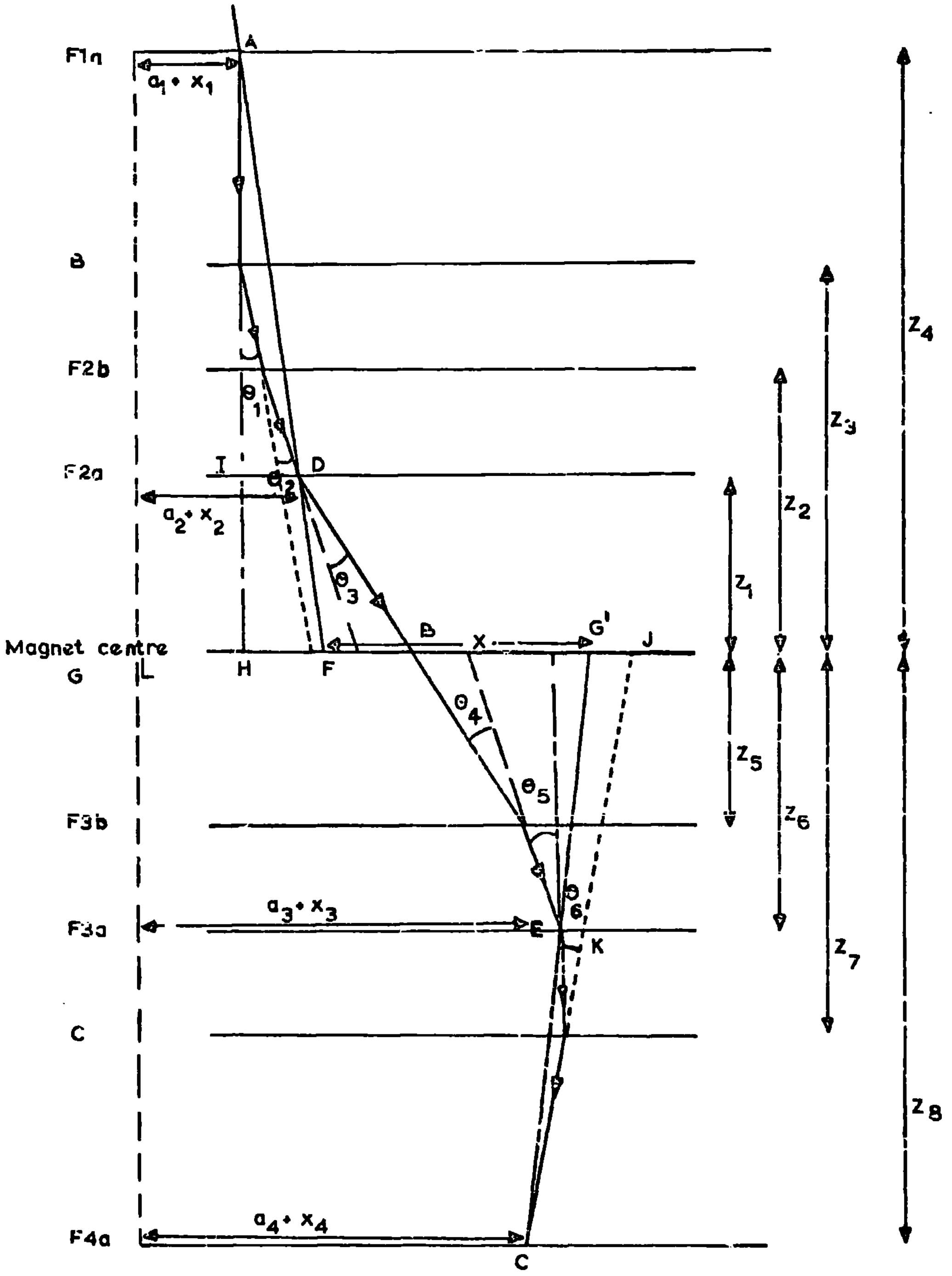

Figure 6.9 Diagram (not to scale) illustrating the effect of multiple scattering at the detector levels B, F2a, F2b, F3a, F3b and C, on the discrepancy measurement, X, of a track subject to zero magnetic deflection.

apparent emergent trajectory, G'KC, is calculated from the geometry to be given by,

$$X = LG' - LF$$

where

$$LG' = (a_4 + x_4) + \left\{(a_3 + x_3) - (a_4 + x_4)\right\} \frac{Z_8}{Z_8 - Z_6}$$

and

$$LF = (a_1 + x_1) + \left\{(a_2 + x_2) - (a_1 + x_1)\right\} \frac{Z_4}{Z_4 - Z_1}$$

Substituting the dimensions from Figure 6.9 where,

$Z_1 = 94.68$ cm

$Z_2 = 107.58$ cm

$Z_3 = 117.95$ cm

$Z_4 = 157.40$ cm

$Z_5 = 70.89$ cm

$Z_6 = 83.79$ cm

$Z_7 = 102.35$ cm

$Z_8 = 345.36$ cm

$a_1 = -3.21$ cm

$a_2 = +48.73$ cm

$a_3 = +47.78$ cm

$a_4 = 0$

this becomes,

$$X = 1.06x_3 + 2.73x_1 - 2.01x_2 - 0.61x_4 - 64.05 \text{ cm} \qquad 6.3$$

where x_1, x_2, x_3, x_4 are expressed in flash tube separations.

From Section 5.11 it was noted that the uncertainties produced in deriving the trajectory of a particle have contributions from multiple scattering and location errors at each measuring level. As these errors also contribute to the discrepancy measurements of a particle, if a distribution in discrepancy (equation 6.3) for particles of a given displacement is measured, then from the observed variation of mean, square discrepancy with square displacement, the location precision of Fla and also the scattering constant of the spectrometer can be found.

6.8 Contributions to the r.m.s. discrepancy, <X>.

6.8.1 Scattering contribution to the r.m.s. discrepancy, $\langle X_s \rangle = \langle FG' \rangle$

As from Figure 6.9 $\qquad FG' = FB + BG'$

then $$\langle FG'^2\rangle = \langle FB^2\rangle + \langle BG'^2\rangle$$

$$FB = HB - HF$$

i.e. $$FB = Z_3\theta_1 + Z_2\theta_2 + Z_1\theta_3 - HF \qquad 6.4$$

As $$\frac{HF}{ID} = \frac{Z_4}{Z_4-Z_1}$$

then $$HF = \frac{Z_4}{Z_4-Z_1}\left\{(Z_3-Z_1)\theta_1 + (Z_2-Z_1)\theta_2\right\}$$

Hence from equation 6.4

$$FB = Z_3\theta_1 + Z_2\theta_2 + Z_1\theta_3 - \frac{Z_4}{Z_4-Z_1}\left\{(Z_3-Z_1)\theta_1 + (Z_2-Z_1)\theta_2\right\}$$

Substituting the dimensions

$$FB = 91.95\theta_1 + 75.38\theta_2 + 94.68\theta_3$$

therefore

$$\langle (FB)^2\rangle = (91.95)^2\langle\theta_1{}^2\rangle + (75.38)^2\langle\theta_2{}^2\rangle + (94.68)^2\langle\theta_3{}^2\rangle \qquad 6.5$$

Substituting the values of the r.m.s. projected angles of scatter from Table 5.3,

$$\langle\theta_1\rangle = \frac{5.63 \times 10^{-3}}{p\beta} \quad \text{radians} \qquad p \text{ in GeV/c}$$

$$\langle\theta_2\rangle = \frac{5.96 \times 10^{-3}}{p\beta} \quad \text{radians}$$

$$\langle\theta_3\rangle = \frac{7.03 \times 10^{-3}}{p\beta} \quad \text{radians}$$

Equation 6.5 can be written

$$\langle (FB)^2\rangle = \frac{0.902}{p^2\beta^2} \ \text{cm}^2 \qquad \text{with } p \text{ in GeV/c} \qquad 6.6$$

$$BG' = BJ - G'J$$

i.e. $$BG' = Z_5\theta_4 + Z_6\theta_5 + Z_7\theta_6 - G'J \qquad 6.7$$

As $$\frac{G'J}{EK} = \frac{Z_8}{Z_8-Z_6}$$

then $$G'J = \frac{Z_8}{Z_8-Z_6}\left\{(Z_7 - Z_6)\theta_6\right\}$$

Hence from equation 6.7

$$BG' = Z_5\theta_4 + Z_6\theta_5 + Z_7\theta_6 - \frac{Z_8}{Z_8-Z_6}\left\{(Z_7-Z_6)\theta_6\right\}$$

Substituting the dimensions

$$BG' = 70.89\ \theta_4 + 83.79\ \theta_5 + 77.85\ \theta_6$$

therefore

$$<(BG')^2> = (70.89)^2<\theta_4>^2 + (83.79)^2<\theta_5{}^2> + (77.85)^2<\theta_6{}^2> \qquad 6.8$$

Substituting the values of the r.m.s. projected angles of scatter from Table 5.3 where

$$<\theta_1> = <\theta_6> = \frac{5.63 \times 10^{-3}}{p\beta} \quad \text{radians}$$

$$<\theta_3> = <\theta_5> = \frac{7.03 \times 10^{-3}}{p\beta} \quad \text{radians}$$

$$<\theta_2> = <\theta_4> = \frac{5.96 \times 10^{-3}}{p\beta} \quad \text{radians}$$

Equation 6.8 can be written

$$<(BG')^2> = \frac{0.72}{p^2\beta^2} \ \text{cm}^2 \ \text{with p in GeV/c} \qquad 6.9$$

As $$<(FG')^2> = <(FB)^2> + <(BG')^2>$$

from equations 6.6 and 6.9

$$<(FG')^2> = \frac{1.622}{p^2\beta^2} \text{ cm}^2 \text{ with p in GeV/c} \qquad 6.10$$

For a magnet current of 36 amp, pD = 7.3 GeV/c cm

then equation 6.10 can be written as

$$<X_s^2> = <(FG')^2> = \frac{0.031D^2}{\beta^2} \quad \text{with D in cm} \qquad 6.11$$

6.8.2 Location error contribution to the r.m.s. discrepancy, $<X_\ell> = <FG'>$

From equation 6.3 the discrepancy, X, is given by

$$X = 1.5x_1 + 1.32x_3 - 2.5x_2 - 0.32x_4 - 64.05 \text{ cm} \qquad 6.12$$

where x_1, x_2, x_3, x_4 are now expressed in cm.

It was concluded in the zero field run that the r.m.s. error in track location, $\delta\Delta_o$, at the accurate measuring levels F2a, F3a, F4a was equal to 1.5 mm

$$\text{i.e.} \quad \delta\Delta_o = 1.5 \text{ mm} \qquad 6.13$$

From equation 6.12

$$<(FG')^2> = (1.5\ \delta F1a)^2 + (2.5\ \delta\Delta_o)^2 + (1.32\ \delta\Delta_o)^2 + (0.32\ \delta\Delta_o)^2 \qquad 6.14$$

where δF1a is the location precision of flash tube tray, F1a.

From equations 6.13 and 6.14

$$<X_\ell^2> = <(FG')^2> = 2.25(\delta F1a)^2 + 0.183 \text{ cm}^2 \qquad 6.15$$

6.8.3 The r.m.s. discrepancy, <X>, as a function of displacement

Adding the scattering (equation 6.11) and location error (equation 6.15) contributions to FG', in quadrature, gives

$$<X^2> \quad = \quad <X_\ell^2> + <X_s^2>$$

$$<X^2> \quad = \quad 2.25(\delta Fla)^2 + 0.183 + \frac{0.031D^2}{\beta^2} \ \text{cm}^2 \qquad 6.16$$

with δFla and D in cm.

Thus a plot of $<X^2>$ versus D^2 should be a straight line of slope, 0.031, and intercept, $2.25(\delta Fla)^2 + 0.183$, for particles with $\beta \approx 1$ (and $Z=1$).

From the experimental measurements of the muon discrepancy values, for Class I events only, the slope of the $<X^2>$ versus D^2 plot, shown in Figure 6.10, is 0.025 ± 0.003 and the intercept is 1.25 cm^2. The slope is in reasonable agreement with expectation and the location precision of flash tube tray Fla, can be found. It was found that

$$\delta Fla \quad = \quad 0.69 \ \text{cm}$$

6.9 Summary

1. The muon spectrum and charge ratio have been measured up to 20 GeV/c. Both these measurements are consistent with previous measurements of these quantities.
2. The r.m.s. discrepancy, at the centre of the magnet, as a function of magnetic displacement, D, has been evaluated, with the result shown in Figure 6.10. This result, in principle, can be used to recognise background 'separate track' events of the type, where a single particle traverses the top half of the spectrometer and a separate particle traverses the bottom half, within the resolving time of the electronics. However, in practice, this method of distinguishing background events was found to be limited by the large location

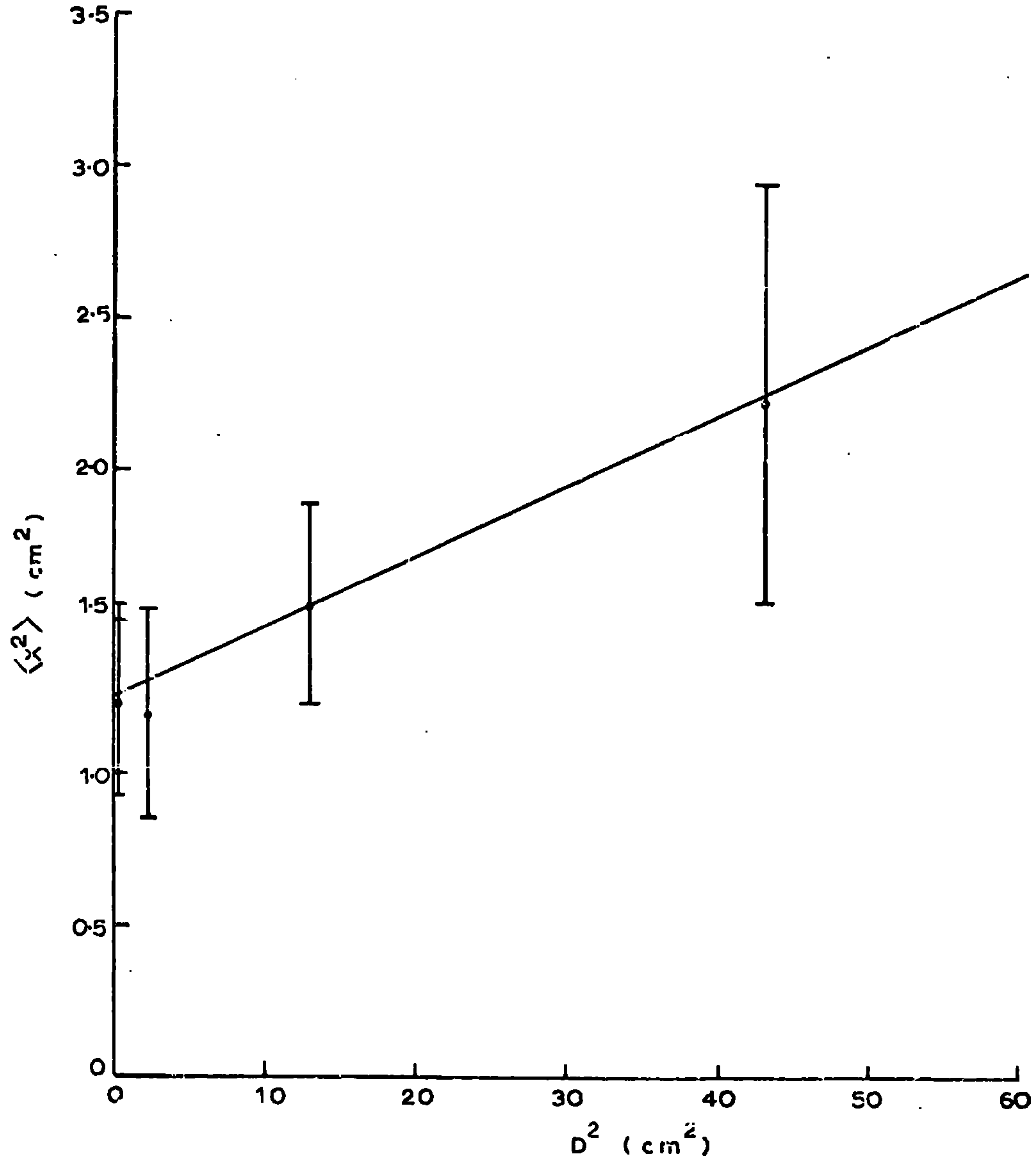

Figure 6.10 The measured variation of the mean square discrepancy $\langle \chi^2 \rangle$, with square displacement D^2, for Class I muon events only.

precision of flash tube tray F1a. Although measurements of the muon spectrum and charge ratio are evidently sufficiently insensitive to this background, for measurements at low intensity levels in the cosmic radiation (e.g. low energy proton and deuteron spectra), an alternative method of eliminating the background events must be found. Such an alternative method is proposed in Chapter 8, to enable a search for low energy, heavy mass particles in a'separate track'free background.

3. The location precision of flash tube tray F1a, where 4 layers of flash tubes, of external diameter 1.7 cm, are close packed and not located in accurately machined slots, has been found to be 0.69 cm. This precision is to be compared with the value of 1.5 mm found for F2a, F3a, and F4a, where 8 layers of tubes are accurately located in machined slots.

6.10 Time of flight measurements

Time of flight values were recorded for the muon events, (in Class I and Class II), which were accepted for the measurement of the muon spectrum, with the intention of extending the measurements giving the time of flight precision, as all muons giving a BCH coincidence were expected to have $\beta \sim 1.0$. With a sufficient statistical accuracy from $\sim$ 700 muon events, the systematic increase of t_c with ℓ_D, that was observed originally in the results of the zero field run (Section 5.17.2), could be measured accurately.

6.11 Display electronics, recording system and selection criteria for time of flight measurements

The display electronics (apart from the modifications given in Section 6.3.3) and the recording system were identical to those of the zero field run

(Sections 5.14 and 5.15). The regulated pulse profiles, from the Mullard 56 AVP photomultipliers of counters A and D, are shown in Plate IIb. The additional selection criteria imposed on the muon events (in Class I and Class II) already accepted for displacement measurements were similar to those stated in Section 5.15.

6.12 Basic data for muon time of flight measurements

The basic data obtained, during a running time of 1 hour 29.2 minutes, for the time of flight measurements of muon events deflected in the magnetic field and subject to the above selection criteria, are shown in Table 6.4.

TABLE 6.4

Total number of muons selected for Class II displacement evaluations	718
Class I muon events selected for time of flight measurements	144
Class II muon events selected for time of flight measurements	542
Time base calibration, fns/cm	11.53
Inherent delay, T_o ns	5.42

The depletion in the number of events accepted for time of flight measurements, from 718 to 542, is caused partially by the additional restrictions imposed in the selection of events for time of flight measurements and partially by the shorter running time of the time of flight film with respect to the flash tube film, by 12.8 minutes.

6.13 Systematic corrections of the time of flight values

6.13.1 Correction for the flight time of direct photons down the phosphor to the detecting photomultipliers on A and D

From the observed time separation, Tns, of each selected event, the corrected time of flight, normalised to the vertical path length between scintillation counters A and D, was calculated from equation 5.26.b.

t_c was calculated from the following expression,

$$t_c = \frac{T + \dfrac{\ell_A - \ell_D}{c/n_1} - T_o}{\dfrac{0.266}{\cos\theta_1} + \dfrac{0.734}{\cos\theta_2}} \quad \text{ns} \qquad 6.17$$

where: Tns is the observed time delay between the pulses from A and D, on the film.

$T_o$ns is the inherent time delay imposed between the pulses from A and D.

$n_1 = 1.6$ is the refractive index of the phosphor.

θ_1, θ_2 are the inclinations to the vertical of the incident and emergent trajectories, in the front elevation, as shown in Figure 5.8. The trajectory is assumed to be deflected at the magnet centre, G, by the magnetic field.

ℓ_A, ℓ_D are the phosphor lengths of the trajectory intersection point in scintillation counters A and D, respectively, as shown in Figure 5.8.

The improvement in the time resolution under the application of the correction for the flight time of direct photons, via equation 6.17, is illustrated in Figures 6.11 and 6.12 for Class I and Class II muon events, respectively. The distributions of $T-T_o$ and t_c are shown for comparison.

6.13.2 Correction for the flight time of indirect photons down the phosphor to the detecting photomultipliers on A and D

The scatter plot of t_c versus ℓ_D, for the muon events in the zero field run, indicated a systematic increase of t_c with ℓ_D. This implied that correction for the flight time of direct photons down the phosphor was in fact a simplification of the true picture. A similar variation is shown in the scatter plot of Figure 6.13, where the corrected time of flight values, t_c, of the Class II muon events are plotted as a function of ℓ_D. The possible reason for the observed variation of t_c with ℓ_D (discussed fully in Section 7.10.1) is that light is collected from scintillators A and D by total internal reflection and there is an increasing tendency for the first photoelectron from the detecting photomultipliers to be produced by other than direct light, with increasing ℓ_D.

Median corrected time of flight values, $\bar{t}_c$, of the Class II events, were calculated for 20 cm cell widths over the distance ℓ_D in scintillation counter D. The variation of the median values, $\bar{t}_c$, over the distance ℓ_D is shown in Figure 6.14, where an increase of 16% over the range ℓ_D=0 to ℓ_D = 140 cm is indicated. The systematic correction factor, t', used to correct each value of t_c to the equivalent value at the centre of scintillation counter D, is shown, in Table 6.5, for the ℓ_D cell widths over which each correction factor is applicable. Thus the final time of flight value, t, of each event is given by,

$$t = t_c + t' \qquad 6.18$$

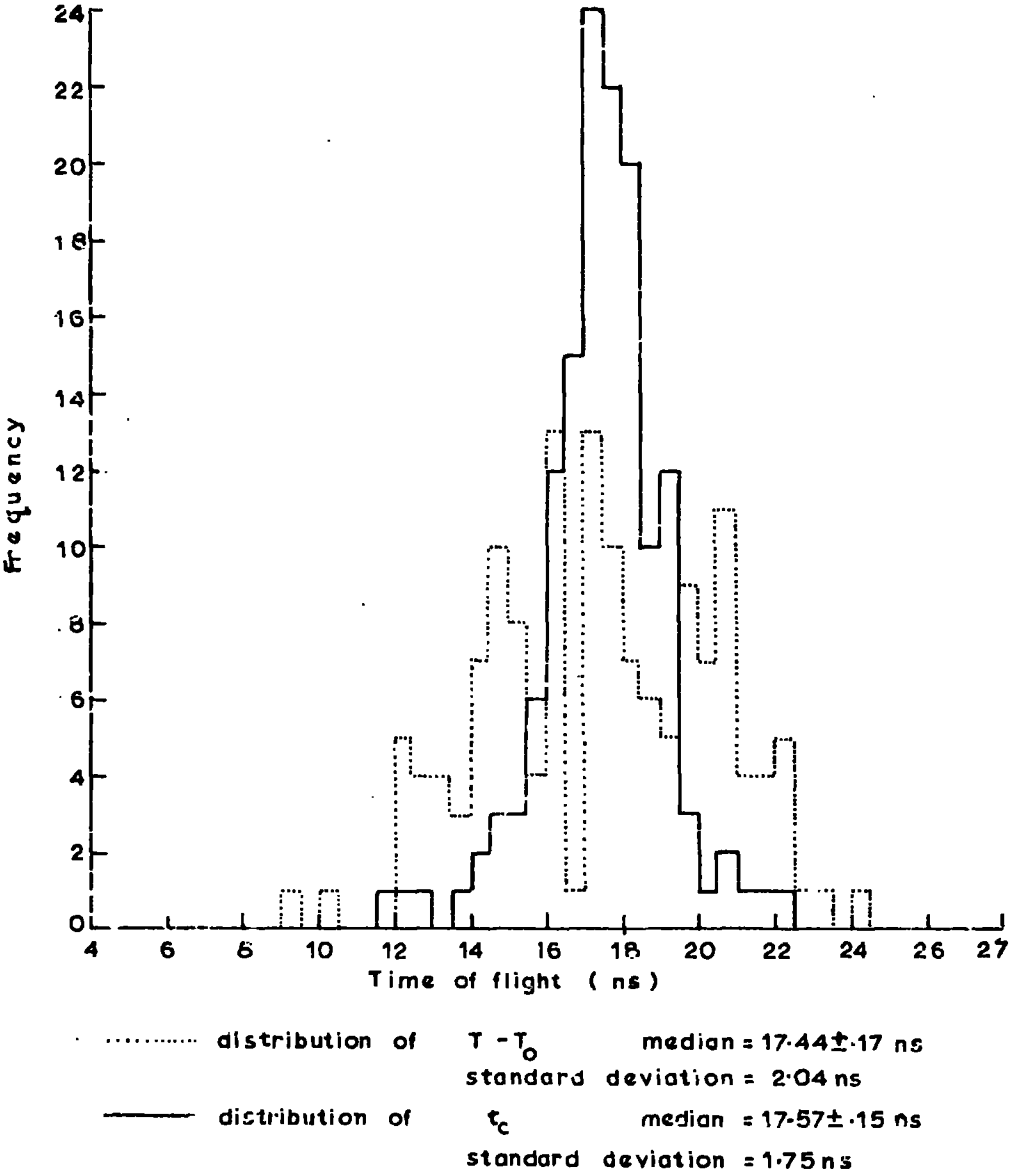

Figure 6.11 Relativistic muon time of flight distributions obtained for Class I events, showing the improvement in the time resolution from the observed $T-T_o$ distribution to the t_c distribution, after correcting for the flight time of direct photons down the phosphor.

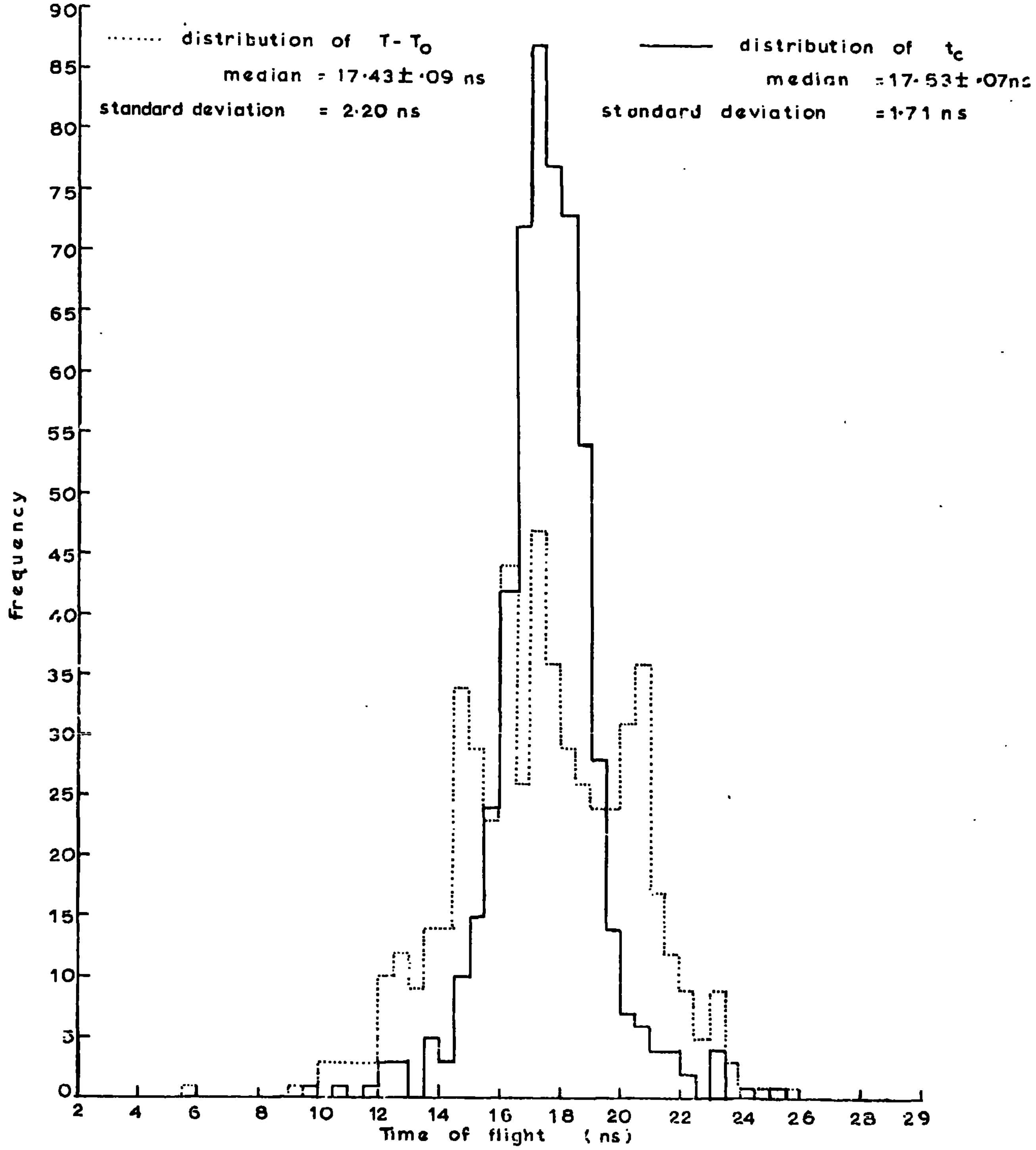

Figure 6.12 Comparison of the T-T_o and t_c time of flight distributions observed for Class II relativistic muon events.

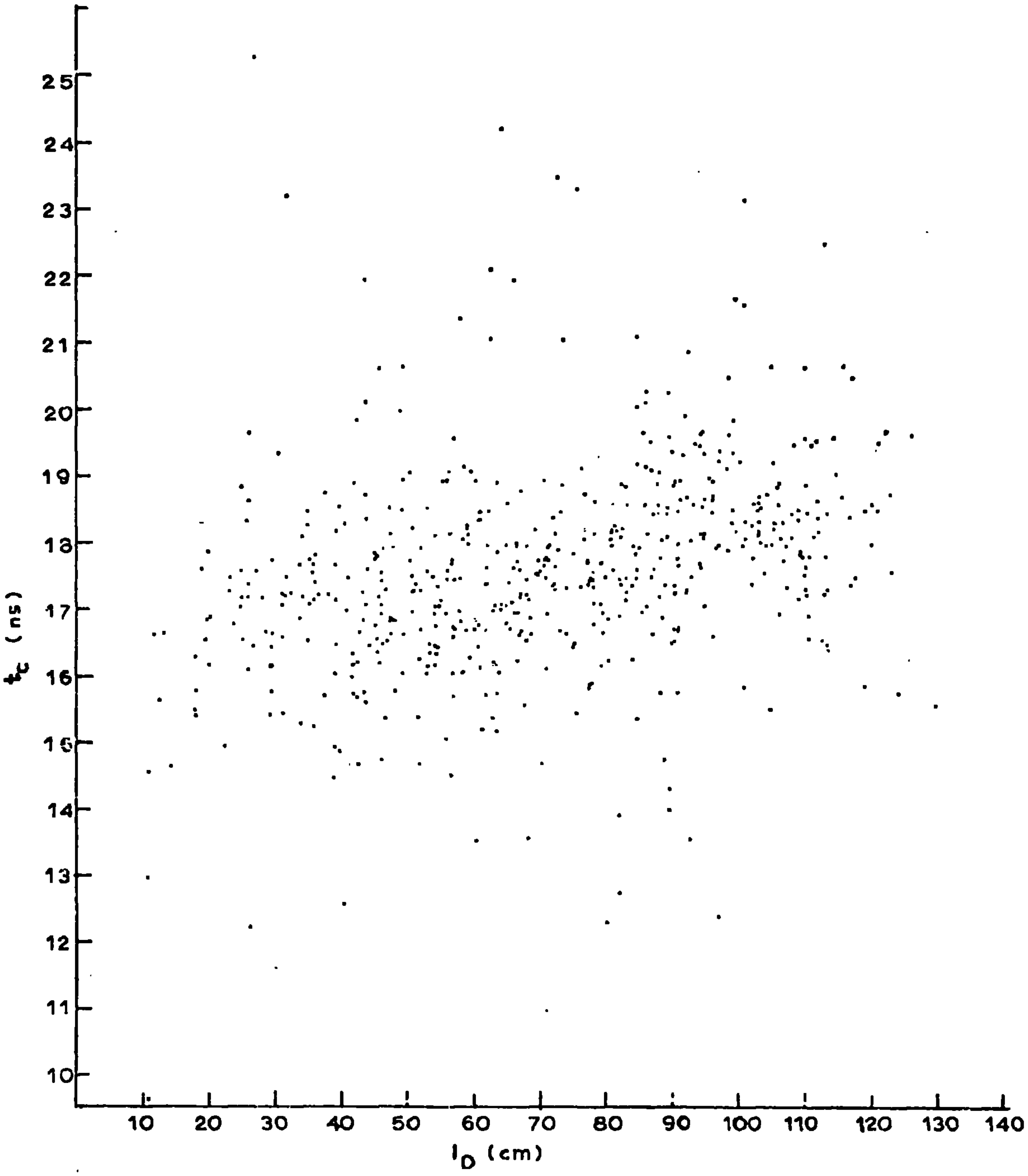

Figure 6.13 Scatter plot of muon t_c values versus the distance, l_D, of the trajectory intersection point from the end of the phosphor in counter D.

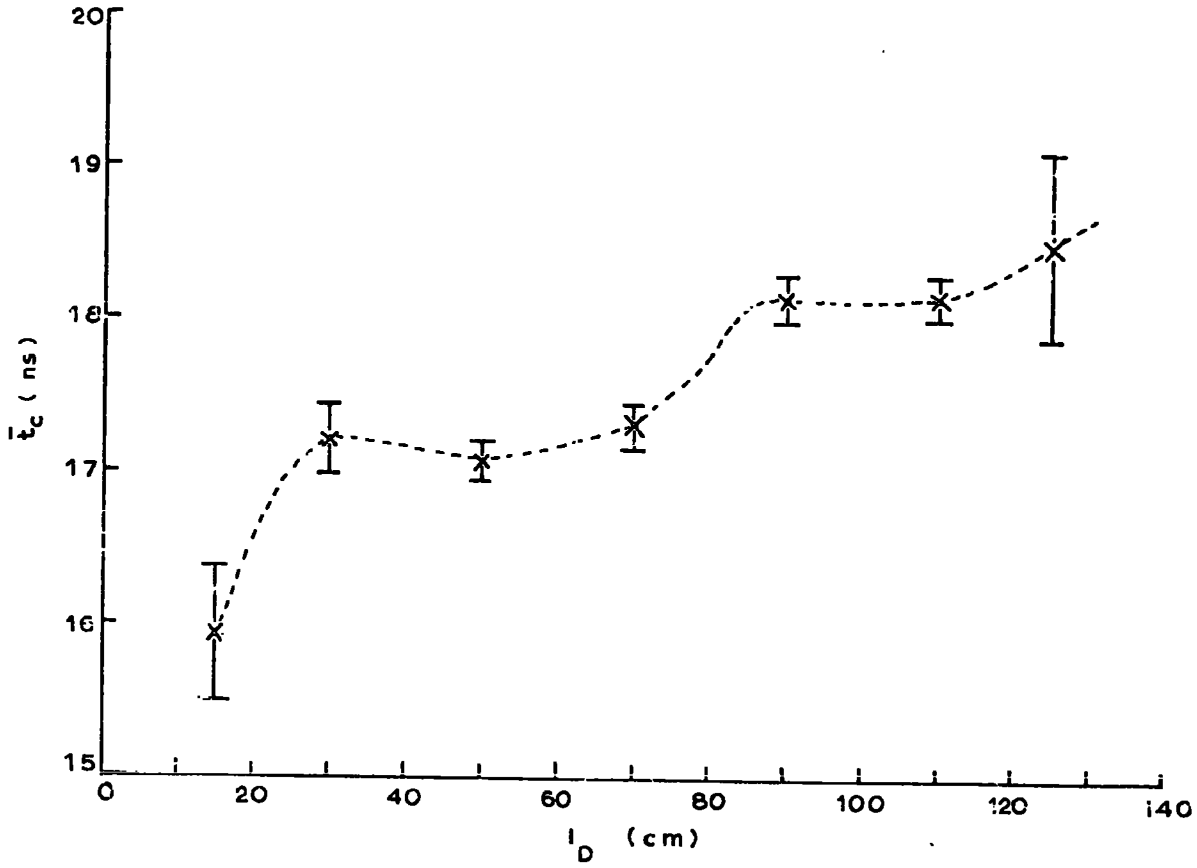

Figure 6.14 Variation of the median, $\bar{t}_c$, over the distance l_D.

where t' is dependent on the ℓ_D value of each event.

TABLE 6.5

ℓ_D cell,cm	$\bar{t}_c$ ns	t' ns
10 - 20	15.94 ± 0.43	+ (1.37 ± 0.45)
20 - 40	17.21 ± 0.23	+ (0.1 ± 0.25)
40 - 60	17.08 ± 0.13	+ (0.23 ± 0.17)
60 - 80	17.31 ± 0.15	0 ± 0.15
80 - 100	18.15 ± 0.15	- (0.84 ± 0.21)
100 - 120	18.16 ± 0.14	- (0.85 ± 0.19)
120 - 140	18.50 ± 0.61	- (1.19 ± 0.62)

The correction of each value of t_c to its equivalent value at the centre of scintillation counter D is justified to some extent, as the trajectories traversing scintillation counter A occur over a limited range of ℓ_A, due to the BCH coincidence selection. Therefore, the dependence of t_c on the position in scintillator A is expected to be only small.

6.14 Final time of flight distributions

The final time of flight distributions, obtained from equations 6.17 and 6.18, are shown in Figures 6.15 and 6.16 for Class I and Class II events, respectively. The media of these time of flight distributions have been corrected to the expected time of flight value for a $\beta = 1$ particle (i.e. 17.68 ns). A systematic correction of + 0.37 ns was applied to all the t

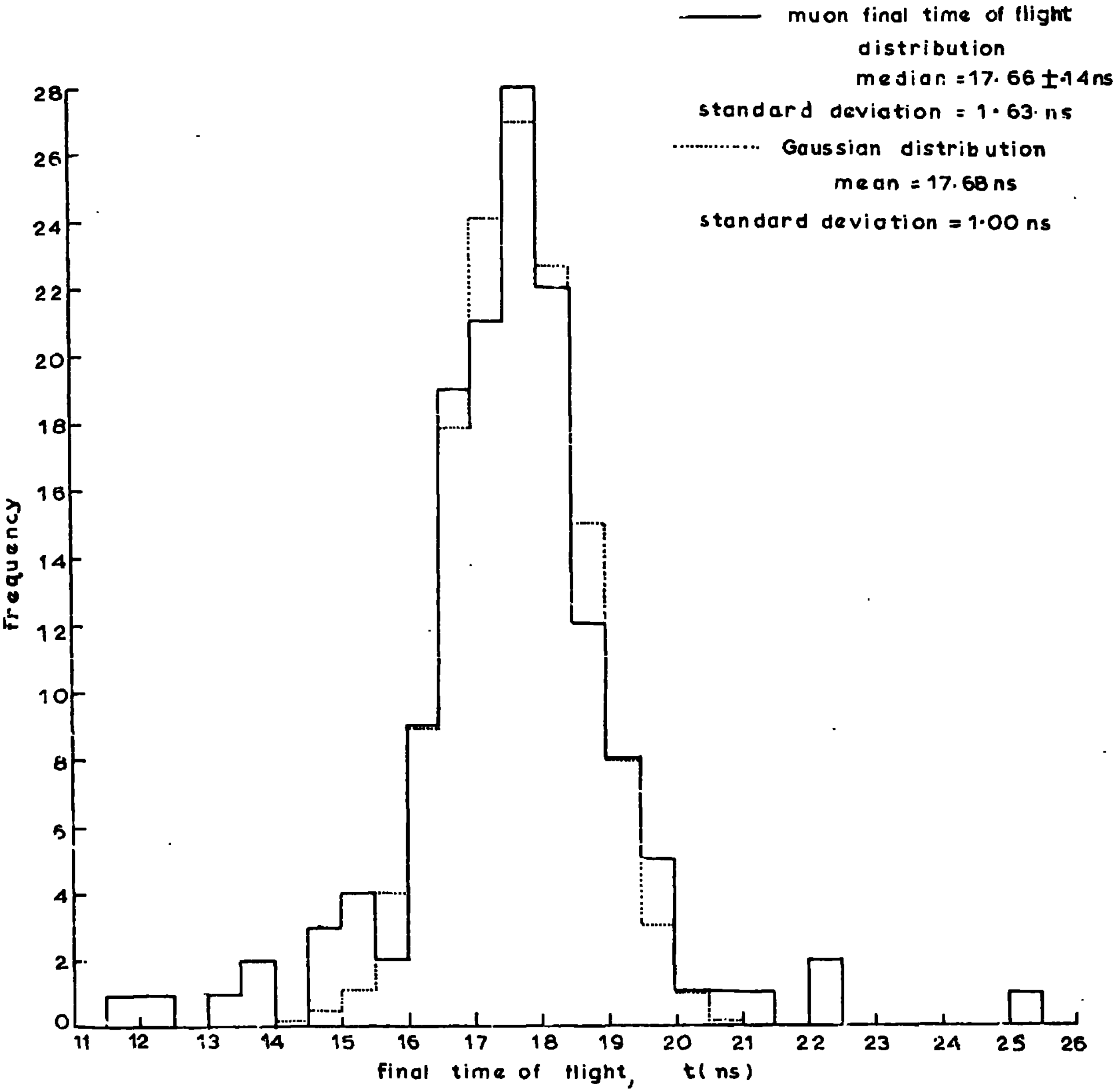

Figure 6.15 Final time of flight distributions for Class I relativistic muons.

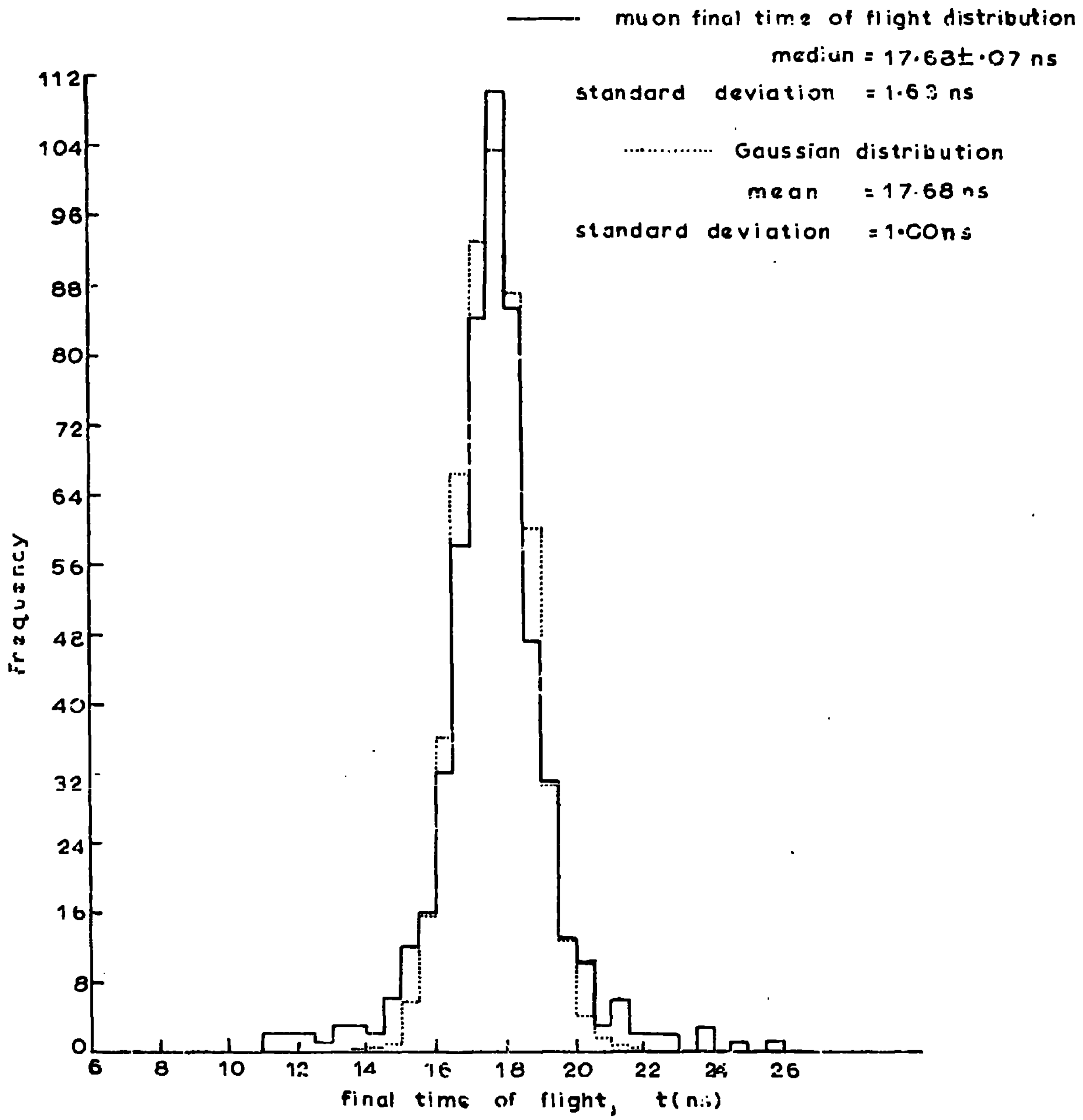

Figure 6.16 Final time of flight distribution for Class II relativistic muons.

values. It is evident that the shift of +2.42 ns, observed in the median value of the zero field time of flight distribution, was caused by the different voltages of the first dynode stages in the Mullard 56 AVP photomultipliers. The shift of - 0.37 ns, in the median of the final time of flight distribution for Class II and Class I events, is within the expected error from using the approximation of c/n_1 as the group velocity of photons in the phosphor.

6.15 Precision of the time of flight determination

It is apparent, from Figure 6.15 and 6.16, that the final time of flight distributions obtained for Class I and Class II events are not of a Gaussian form. However, a least squares fitting procedure shows that the best fit to the body of the distribution is a Gaussian of standard deviation, $\sigma = 1.0$ ns, and a mean of 17.68 ns, given by the dotted histogram in Figures 6.15 and 6.16. The standard deviation of all the Class II events (Figure 6.16) about a median 17.68 ns is, however, calculated to be 1.63 ns.

The full width at half height of the final time of flight distributions, in Figures 6.15 and 6.16, are both observed to be 2.0 ns. This result is comparatively superior to the value of 3.2 ns, found for an isochronous counter by Stefanski et al., (1967).

6.16 Contributions to the time of flight precision

The standard deviation, 1.63 ns, of the Class II time of flight distribution (Figure 6.16) has contributional widths from the following errors:

1. Measurement errors.
2. Errors on the correction factor t' and in t_c.

3. As the fluctuations in the observed time of flight values are also a consequence of the variation in the number of photoelectrons at the photocathodes about a mean, then the standard deviation 1.63 ns has contributions from:

   (a) The statistical fluctuations about a mean number of photoelectrons at the photocathode, where the mean number (and therefore the contributional width) is expected to be dependent on ℓ_D, and also, to a much lesser extend, on ℓ_A and the incident zenith angle to the vertical.

   (b) The Landau distribution in energy loss.

4. Fluctuations in the transit times of the photoelectron multiplication process.

As the average number of photoelectrons collected by the photomultiplier for a $\beta = 1$ particle are only ~ 37 for the experimental set up shown in Figure 5.2a, then contribution, (a), is expected to be far more significant than (b).

Unsymmetrical biasing of the muon time of flight distribution, also contributing to the total width of 1.63 ns, is expected from the following:

1. Background particles of β values other than 1.0, e.g. low energy protons.
2. 'Separate track' events, although small in number, are expected to simulate events with low values of t (discussed in Section 7.11).

Although the cause of the tails on the distributions in Figures 6.15 and 6.16 are not fully understood, under the extreme assumption that all the events are relativistic muons, the most unfavourable precision is only ± 1.63 ns, and under the assumption that the tail events are not members of the muon time of flight distribution, the precision attained is ± 1ns.

The exact value of the precision in the time of flight determination, from the range 1.0 - 1.63 ns, for low energy particles (such as those considered in Chapter 8, i.e. protons and deuterons of $\beta \lesssim 0.8$) is subject to some doubt. However, taking a value of ± 1.0 ns seems reasonable in that not only is this value the same as the precision observed in the zero field run and the half width at half height of the muon distribution in Figure 6.16, but that such a choice between 1 and 1.63 ns does not affect the precision in the mass determination by > 5%, for low energy particles. Multiple scattering of particles in the spectrometer is seen, from Figure 5.22, to have the most substantial contribution to the mass precision, at momenta just above the minimum momenta required by particles to traverse the spectrometer to scintillator H. Hence the assumption that, the time of flight precision, is independent of β, ℓ_D, ℓ_A, of Z, does not significantly affect the mass precision for such values of momenta expected for protons, deuterons etc., through the spectrometer.

6.17 Conclusion

1. The time of flight precision is deduced to be of the same order as the value ± 1ns, obtained from the zero field time of flight distribution. The half width at half height of the muon final time of flight distribution is observed to be 1.0 ns.

2. A contribution of tail events to the muon time of flight distribution is evident in Figure 6.16. Proton contamination of $\sim$ 2% is identified

(Section 7.3) in the high time of flight tail, from mass estimations on events at greater than three standard deviations (> 3ns) away from the median of the distribution. The possible causes of the remaining tail events of the time of flight distribution in Figure 6.16, is considered, in the next chapter, in terms of:

(a) Statistical fluctuations in the muon time of flight value, associated with the relatively small number of photoelectrons produced at each timing photomultiplier.

(b) Background 'separate track' events.

(c) The observation of faster-than-light particles namely, tachyons, (Feinberg, 1967).

CHAPTER 7

ANALYSIS OF THE TIME OF FLIGHT MEASUREMENTS

7.1 Introduction

From the time of flight distributions, shown in Figures 6.15 and 6.16, obtained for relativistic muons, which were restricted to travel through the magnetic field by a simple BCH coincidence, the objectives were to:

1. establish the cause of the observed tail events.
2. resolve a proton flux from the low velocity tail.
3. ascertain the possible contribution of a tachyon flux in the high velocity tail.

7.2 Mass analysis of the low velocity tail events

It was found that a Gaussian form did not fit all the data in the distribution of Figure 6.16 due to the presence of both a high and low time of flight tail. However, a Gaussian was best fit to the body of the distribution about a mean value of 17.68 ns, when the standard deviation $\sigma=\pm 1$ns. The number of events with deviations $>3\sigma$ (i.e.>3 ns) from the median of the Class II time of flight distribution (i.e. from 17.68 ns), amounts to 18 on the high time of flight side and 15 on the low time of flight side.

The masses of the 18 low velocity events have been calculated using their measured momentum, p_m, and time of flight determination, t, in equation 5.29. The mass, m, is given by

$$m = \frac{p_m \times t}{17.68} \left[1 - \left(\frac{17.68}{t} \right)^2 \right]^{\frac{1}{2}} \quad \text{GeV/c}^2 \qquad 7.1$$

where p_m is in GeV/c, t in nanoseconds and where Z is assumed to be unity.

The precisions in these mass determinations were deduced from the relation (equation 5.34)

$$\frac{\delta m}{m} = \left[\left(\frac{0.253}{\beta m} \right)^2 + (0.049\ p_m)^2 + \left(\frac{t \delta t}{t^2 - 312.58} \right)^2 \right]^{\frac{1}{2}}$$

where p_m is in GeV/c, t in nanoseconds and $\delta t = \pm$ 1ns is the precision on the time of flight determination. Only events with time of flight values greater than three standard deviations away from the median are considered in this analysis, because relativistic muons simulate very high mass values above this velocity limit. As muons with time of flight values > 19.0 ns have momenta less than the threshold momentum required by muons to penetrate the spectrometer, no precise muon mass estimates are expected in the low velocity tail events. Muons with fluctuations greater than three standard deviations away from the median will, however, simulate high mass values in the tail.

7.3 Proton identification in the low velocity tail events

The mass determinations of the events in the low velocity tail, together with other relevant parameters, are listed in Table 7.1. As Class I events, by definition in Section 6.3.4, are constituents of Class II, discrepancy values are only given for Class I events. The velocity of each event (written as a β value) is compared to the velocity of light, for which the time of flight t = 17.68 ns.

TABLE 7.1

Class II (including Class I) events with final time of flight values > 20.68 ns

Event No.	Corrected time of flight, t_c ns	Final time of flight, t ns	β	Dcm	p_m GeV/c	Mass ± δm GeV/c^2	Discrepancy Xcm	ℓ_A cm	ℓ_D cm
1	20.10	20.70	0.853	+8.55	+0.854	0.52±0.18		86.9	43.8
2	21.54	21.06	0.839	+2.70	+2.707	1.78±0.65P		64.8	101.0
3	21.63	21.16	0.836	-4.68	-1.561	1.02±0.36		56.2	99.0
4	20.57	21.17	0.836	+5.85	+1.248	0.82±0.28P		53.1	45.5
5	20.58	21.18	0.836	+10.52	+0.694	0.45±0.15	-1.83	87.0	49.1
6	21.01	21.38	0.828	+5.72	+1.276	0.86±0.30P		69.8	62.8
7	21.05	21.42	0.825	+3.67	+1.991	1.34±0.47P		83.1	73.4
8	22.42	21.94	0.806	-12.11	-0.603	0.44±0.15		56.1	112.8
9	21.36	21.96	0.805	+2.30	+3.171	2.32±0.86P		87.1	57.9
10	21.90	22.27	0.794	-11.41	-0.640	0.50±0.17		74.8	66.0
11	22.09	22.46	0.787	+4.43	+1.648	1.29±0.45P	-0.28	84.0	62.8
12	21.94	22.54	0.785	+4.12	+1.772	1.42±0.50P	+0.72	61.2	43.9
13	23.10	22.62	0.780	-10.78	-0.677	0.54±0.19		81.5	101.5
14	23.26	23.63	0.747	+3.85	+1.894	1.67±0.61P		78.8	75.2
15	23.19	23.66	0.746	-2.57	-2.838	2.50±0.95		61.6	32.0
16	23.47	23.84	0.740	+1.11	+6.565	0.60±0.22P		74.1	72.6
17	24.21	24.58	0.720	+7.11	+1.026	0.99±0.36P		77.4	64.2
18	25.25	25.72	0.688	+32.29	+0.226	0.24±0.09	-4.92	50.2	27.0

Events are identified as protons if their mass, m, and mass precision, δm, satisfy the relation $\frac{0.938-m}{\delta m} < 2$, and also if their displacement sign is positive (positive charge). Mass determinations of the events in Table 7.1 are plotted in Figure 7.1 against their individual momentum values. The 10 events labelled as 'P' in Figure 7.1 (and subsequent diagrams) and Table 7.1 are observed to satisfy the above conditions. The remaining 8 events are to be compared with the 15 observed in the high velocity tail, whose parameters are listed in Table 7.2.

TABLE 7.2

Class II (including Class I) events with final time of flight values < 14.68ns

Event No.	Corrected time of flight t_c ns	Final time of flight t ns	β	Dcm	p_m GeV/c	Discrepancy X cm	ℓ_A cm	ℓ_D cm
1	10.91	11.28	1.57	-5.04	-1.449		81.0	71.0
2	9.62	11.36	1.56	-1.91	-3.814		85.0	10.9
3	12.25	11.78	1.50	+0.49	+14.959	+0.22	67.8	80.1
4	12.38	11.91	1.48	-9.71	-0.752		57.0	96.8
5	11.68	12.08	1.46	-1.11	-6.559	+0.52	73.0	30.0
6	12.71	12.24	1.44	-1.36	-5.368		82.5	82.0
7	12.24	12.71	1.39	+9.41	+0.778		59.1	26.0
8	13.53	13.06	1.35	+8.99	+0.812		59.0	92.5
9	12.52	13.12	1.35	+9.38	+0.778	+0.27	88.1	40.4
10	13.9	13.43	1.32	-3.21	-2.273		57.9	82.3
11	14.0	13.53	1.31	-6.15	-1.187		50.9	89.5
12	14.3	13.83	1.28	-0.28	-26.160	+1.42	53.6	89.5
13	13.59	13.96	1.27	+2.74	+2.666	-0.18	57.2	68.4
14	13.52	14.12	1.25	-25.38	-0.287		86.1	60.0
15	14.75	14.28	1.24	-21.20	-0.344		73.0	89.0

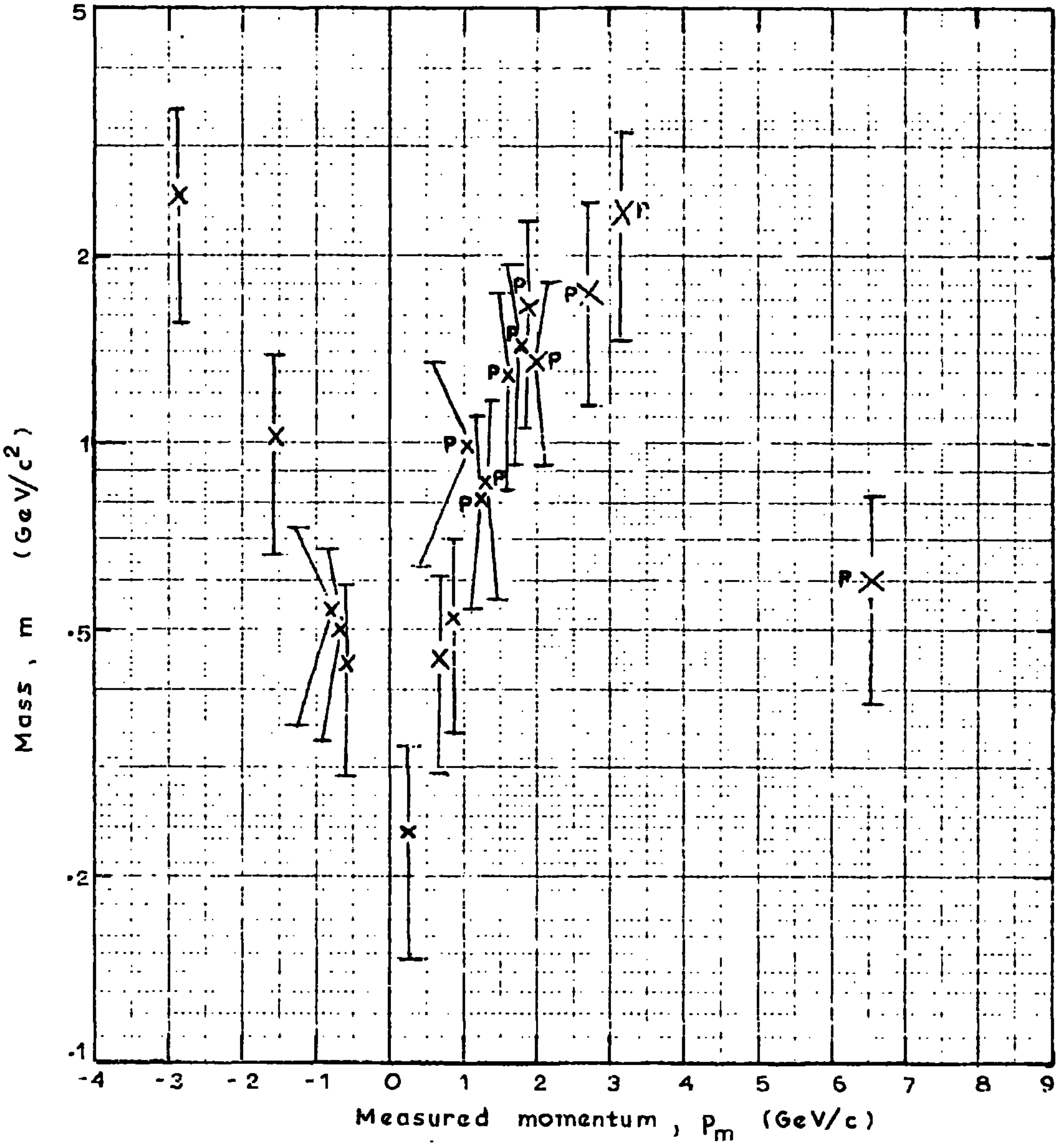

Figure 7.1 Mass determination of 18 events with a final time of flight t> 20.68 ns, as a function of their momentum, p_m , measured at the magnet centre.

The observation of a high velocity tail in the muon time of flight distribution, in agreement with the expected behaviour of tachyons, necessitates a closer examination of the following:

1. The remaining 8 events in the high time of flight tail.
2. The 15 events in the low time of flight tail.
3. Other possible causes of these tail events (besides the effect of a tachyon flux).

From this examination it is intended to establish the existence, or otherwise, of a tachyon signal.

Before continuing with a discussion on the likely causes of the non-Gaussian form of the distribution, it seems relevant, here, to discuss the proposed theories, to date, on the properties of tachyons and the experiments already conducted to search for them. So to establish if this time of flight technique is, in fact, sensitive to tachyons and therefore if the evidence of such a tachyon signal, in the low time of flight tail, is feasable.

7.4 History of the tachyon

The existence of particles travelling at velocities greater than the speed of light has been overruled, in the past, on the grounds that these particles would contravene the special theory of relativity (Einstein, 1905) and the causality principle. The suggestion of the existence of faster-than-light particles arose from the considerations of symmetry with the conventional particles travelling less than and equal to the velocity of light. Since the development of relativistic quantum mechanics with its characteristic discontinuous creation of particles, Bilaniuk et al. (1962) and Feinberg (1967) have shown that it is possible to describe faster-than-light particles consistently within the special theory of relativity. Bilaniuk et al. originally discussed the possible existence of faster than light particles in terms of the classical theory of relativity. Feinberg extended this idea by showing that the formalism of relativistic quantum theory could also include such particles, which he called tachyons.

7.5 Properties of tachyons

The proposed properties of tachyons and their subsequent agreement with Einstein's relativistic laws, are summarised below.

1. If tachyons are created, already and always travelling faster than light, then no contradiction with the special theory of relativity, in the need for an infinite source of energy to accelerate particles through the light barrier, results.

2. The energy E and momentum p, of a tachyon of mass m, was originally suggested by Bilaniuk et al. to be given by,

$$E = \frac{\mu c^2}{\left(\frac{u^2}{c^2} - 1\right)^{\frac{1}{2}}} \qquad 7.3$$

$$|p| = \frac{\mu u}{\left(\frac{u^2}{c^2} - 1\right)^{\frac{1}{2}}} \qquad 7.4$$

$$E^2 - p^2c^2 = -\mu^2c^4 \qquad 7.5$$

where $m = i\mu$ and u is the velocity of the tachyon. As tachyons can never be brought to rest, their rest mass, $m = i\mu$, is not directly measurable and therefore is not compelled to be a real quantity. From equations 7.3 and 7.4, the limits on the energy and momentum of a tachyon are,

$$0 < E < \infty$$

$$\mu c < p < \infty$$

$$\infty < u < c$$

Thus a tachyon losing energy by radiation or interaction would speed up until, at infinite speed, its total energy, E, is zero. The condition of infinite, or indeed any, speed is not invariant but dependent on the observer's relative velocity.

3. From equation 7.5 $|pc| > E$, and hence an ordinary Lorentz transformation could change the sign of the energy. The occurrence of this not only contradicts the known stability of ordinary matter, but also the relativistic theory, that in any frame of reference the energy of a particle must be positive. Another inference of the particles travelling faster than light, is the possibility of a particle being detected before it is emitted, an obvious violation of the causality principle. An interpretation by Bilaniuk et al. however, shows that a time reversal always accompanies the propagation of negative energy particles. The consequence of Lorentz transformations is therefore to relate the rates of emission and absorption, rather than to require the introduction of negative energy states and therefore a closer connection is implied between the two processes than for ordinary particles.

4. A consequence of the above characteristic of tachyons, is its disagreement with the particle theory which demands the Lorentz invariance of the number of particles in a given state. Feinberg concludes, 'the fact that a Lorentz transformation links states with different numbers of tachyons is a new feature

of these particles, but does not imply non-invariance of the normal particle theory. A result of this peculiarity of tachyons is that they cannot be used to send reliable signals either backward or forward in time, in the sense that the production of tachyons is uncontrollable'.

5. Feinberg also solves the Klein Gordon equation for a scalar c, number field $\phi(x)$ with an imaginary mass $m = i\mu$, and for a wave function of a particle with real energy. The wave numbers of the solutions are found to be restricted and this incompleteness has several consequences, the most important of which implies that the wave function describing a tachyon cannot be localised in space. Because of the impossibility of localising the wave function, the velocity of the tachyon is concluded, by Feinberg, to be somewhat loosely defined and therefore any method of detection relying on a velocity measurement might be unsuccessful for this reason.

7.6 Production processes of tachyons

As tachyons are proposed to be able to exist with zero total energy, creation can be achieved spontaneously, with zero energy input, and independently of their rest mass. Feinberg (1967) however suggests that if tachyons are fermions of zero spin, then restrictions might occur on their production, in that the number of tachyons modulo two is conserved, and the available free energy states are limited by Fermi statistics.

Little is known about the production processes of tachyons but two interactions have been investigated.

1. Experiments have been performed by Alväger et al. (1968) on the photo production of charged tachyons.

2. Neutral tachyons have been looked for in the secondaries of the interactions,

$$\left.\begin{aligned} k^- + p &\rightarrow \Lambda^o + X^o \\ \bar{p} + p &\rightarrow X^o + n(\pi^+) + n(\pi^-) \end{aligned}\right\} \quad 7.6$$

(where X^o was usually a π^o) by Feinberg et al. (1970).

7.7 Interactions of tachyons

Feinberg (1967) describes the spinless non-interacting tachyons in terms of the relativistic quantum field theory, but as yet, has not extended the theory to the case of interacting particles. The experiments which have relied on the interactions of tachyons, for detection purposes, have therefore lacked confirmation from the field of quantum theory.

1. However, elastic decay of tachyons has been proposed for many years by Sommerfeld et al. (1904) in the form of Cerenkov radiation. Alvåger et al.(1968) calculated that tachyon emission of Cerenkov radiation was considerable and thus only short distances would be travelled by tachyons, before losing almost all their energy.

2. Feinberg (1967) also considers the elastic decay of these particles, with the emission of a particle mass, m_o. The threshold energy, E_T, required by the tachyon is deduced to be,

$$E_T^2 = m_o^2 + \frac{m_o^4}{4\mu^2}$$

3. Further, Feinberg suggests that, as it is always energetically possible for tachyons to decay into several such particles, if their self interaction is strong, then rapid decay of the energetic tachyons into less energetic members is possible.

4. Alväger et al. (1968) consider the possible capture of charged tachyons by a nucleus or an electron. A simple approach to the problem yields a capture cross section $\sigma \approx 3 \times 10^{-30} \mathrm{cm}^2$ for a tachyon energy of 0.5 MeV, real mass $\mu c^2 = 10$ MeV and $Z = 1$. They conclude that only for very small mass values, μ, does the capture cross section become significant.

7.8 Detection of tachyons

Since the proposal of the tachyon by Bilaniuk et al. (1962), only three experiments have been performed to establish their existence.

Alväger et al. (1968), used gamma rays to produce tachyons in a lead shield, from which they were subsequently detected by the Cerenkov radiation. An ingenious method of supplying energy to the tachyons while passing through an electric field ensured the continued radiation of photons in the visible wavelength region, without which, the rapid energy loss by Cerenkov radiation would cause photons to be emitted in the infra red wavelength region. This search for tachyons placed an upper limit on the photoproduction of such particles in lead, of 3μb (at a 90% confidence level), for incident photon energies of 0.8 MeV. This limit applied to particles having charges in the range 0.1e to 2e and held for any value of rest mass, μ.

A similar experiment was repeated by Davis et al. (1969), who only succeeded in reducing the upper limit to 2 nb, for incident photon energies of 1.2 MeV and a tachyon charge range of 0.5e to 1.9e.

Because of the general uncertainty connected with the interactions of tachyons, a search was carried out by Feinberg et al. (1970), which was independent of their interaction characteristics. The missing mass squared of the neutral particles X^o, produced in the interaction equations 7.6, were analysed. A negative value of the missing mass squared would indicate single tachyon production, whereas a broad distribution over both positive and negative values of mass squared would indicate pair production of tachyons. No such indications were found.

The reasons for the negative results of these two experiments has been suggested, by Alväger et al. (1968) and Feinberg (1970), as being caused either by:

1. the strict selection rules on the production of tachyons, discussed in Section 7.6.
2. a very weak photoproduction because of a tachyon fractional charge, or
3. a value of mass squared close to zero.

A possibility finally proposed by Feinberg (1970) is, 'tachyons interact with ordinary particles and can exchange energy with them, but cannot be produced from them. Hence the validity of such a hypothesis can be tested by searching for tachyons in natural phenomena, such as cosmic rays'.

7.9 A search for tachyons in the cosmic rays at sea level

The above suggestion by Feinberg was sufficient to initiate a search for tachyons in the cosmic radiation, using a method which measured the time for a particle to travel between two points of a known separation. Such time of flight measurements were made on a majority of muons accepted through the spectrometer, as described in Chapter 6. The muon time of flight distribution obtained from these measurements is shown in Figure 6.16.

Although this detection technique does not rely on any production processes or any assumptions associated with Cerenkov radiation, for the technique to be sensitive to an incident tachyon flux, the following assumptions have to be made on the properties of tachyons:

1. Velocity measurements are possible for a particle described by an unlocalised wave function (Section 7.5.5).
2. Ionisation loss in the scintillation counters is sufficient to give a pulse height > 1.8 MeV.
3. Other forms of energy loss (Section 7.7) do not prevent tachyons from travelling the spectrometer length.

The cosmic ray tachyon flux is then expected to produce asymmetries in the muon time of flight distribution, by displaying values of t between 0 and 17.68 ns. They are also expected (although this is a subsidiary observation) to have discrepancy values similar to muons and momenta between, 0 and μc, eV/c, assuming their interaction with the magnetic field is similar to ordinary particles.

Although the asymmetry observed in the muon time of flight distribution indicates the possible existence of a tachyon signal, a discussion of other more likely causes of the tail events in terms of:

1. relativistic muons (at greater than three standard deviations away from the median of the distribution),
2. background 'separate track' events,

is presented before a conclusion is drawn as to the existence of such a tachyon signal.

7.10 Fluctuations in the relativistic muon time of flight

7.10.1 Corrections for the flight time of indirect photons down the phosphor

It is possible to explain the observed variation of the median corrected time of flight, $\bar{t}_c$, over the scintillator length, ℓ_D (shown in Figure 6.14) in terms of two effects. The sum of which ultimately gives an increasing tendency for the first photoelectron from the detecting photomultipliers to be produced by other than direct light, with increasing ℓ_D.

The first, and considered to be the most important effect, is concerned basically with the statistical production process of photoelectrons. According to Kasha and Stefanski (1968), the probability, P(T), that the leading edge of a pulse from the cathode of the timing photomultiplier will arrive Tns after the light from the scintillation counter strikes the surface of the tube, depends on the width of the distribution in the number of photoelectrons, about a mean $\bar{n}$, and the decay time of the scintillator, $t_D$ns. It was concluded in Section 6.16 that the width of the distribution is mainly determined by the statistical nature of the photoelectron production at the photocathode. Thus the probability, P(T), is given approximately (by Kasha and Stefanski, 1968) to be,

$$P(T) = \sum_{n=1}^{\infty} \frac{(\bar{n})^n}{n!} e^{-\left(\bar{n} + \frac{nT}{t_D}\right)}$$

for each scintillation counter A and D, where for NE 102A plastic scintillators, the decay time t_D = 3ns. Consideration of the two probability distributions, $P(T)_A$, $P(T)_D$, from the scintillation counters A and D, respectively, yields a distribution in time of flight values about a mean , for a particle of β= 1.

The processes involved in the collection of light by one photomultiplier, from the path of a particle traversing the scintillation counter (A or D) at a distance ℓcm away, have been considered by Simpson, (1967). The curve in Figure 7.3 shows the theoretical response of a photomultiplier as a function of ℓ and it is seen to be consistent with the measured response. The response was calculated from a consideration of the separate contributions from the different reflection stages. That is, the mean number of photoelectrons, $\bar{n}(\ell)$, at the photocathode, due to a particle traversing the counter at distance ℓ away, can be subdivided into contributions, $\bar{n}_o(\ell)$, $\bar{n}_R(\ell)$ from the direct and reflected light, respectively. The systematic increase of $\bar{t}_c$ with ℓ_D is then caused by the relative degrees of the probability distributions, $P(T)_{Dx}$ (where $x = 0, R$,) between the direct and reflected light. At some distance ℓ_1 in D, the average number of photoelectrons, $\bar{n}_o(\ell_1)$, from the direct light (where $\bar{n}_o(\ell_1) << \bar{n}_R(\ell_1)$) are such that these photoelectrons in the leading edge of the pulse most probably arrive later than the photoelectrons from the reflected light. The further increase of $\bar{t}_c$ with ℓ_D is probably caused by similar processes happening between the higher and lower order reflection stages. Because of the small length along scintillator A through which particle trajectories are confined to pass, the effect of ℓ_A on $\bar{t}_c$ is expected to be small.

The second additory effect contributing to the observed variation of $\bar{t}_c$ with ℓ_D, is the time taken for the output pulse profile from the photomultipliers to reach the imposed discrimination level in each channel. As the discrimination levels imposed are only 0.02 E_s this effect is also thought to be comparatively small.

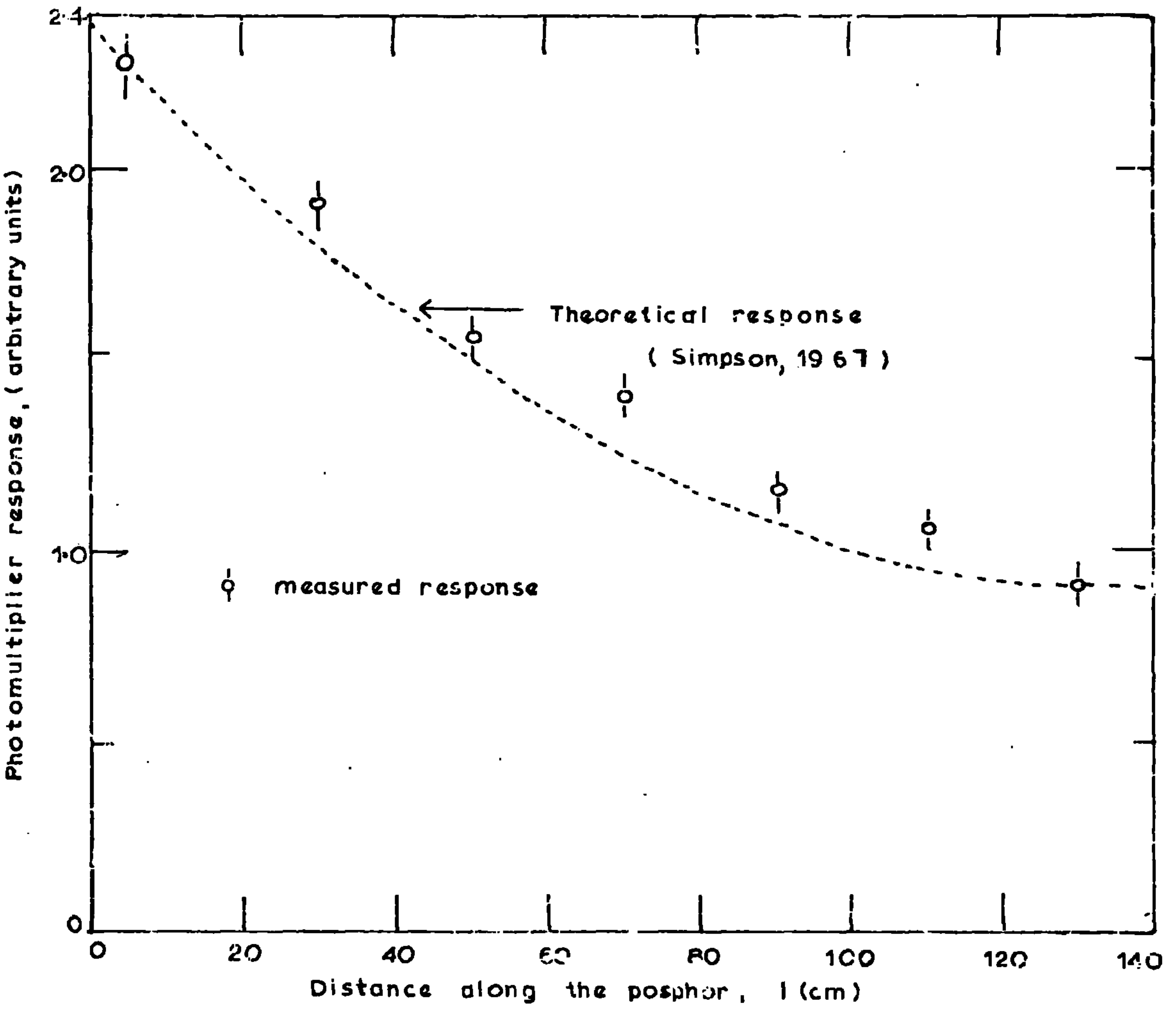

Figure 7.3 Response of a photomultiplier viewing one end of the scintillator (A, D), as a function of the position of the incident particle along the centre line.

7.10.2 Statistical fluctuations in the relativistic muon time of flight, as a function of ℓ_D

The mean photoelectron numbers, $\bar{n}_x(\ell)$, collected from the photocathode for each reflection stage x = 0, R_1, R_2 etc. decrease with increase in ℓ, the total varying according to Figure 7.3. As $P(T)_D$ is dependent on the relative degrees of the probability distributions $P(T)_{Dx}$ and as these are each functions of $\bar{n}_x(\ell)$ and the fluctuations about these means (fractional width $\propto \frac{1}{\sqrt{\bar{n}_x(\ell)}}$), then the resolution of the resulting time of flight distribution is expected to degenerate with increasing ℓ_D. However, the variation of this resolution with ℓ_D is not necessarily expected to be smooth. After correcting for systematic effects, the resultant time of flight distribution would then be the sum of distributions, with different widths, centred about the same mode, the tails of the distribution being caused by events with larger ℓ_D values.

7.11 Distribution in time of flight values expected for background 'separate track' events

The external triggering system of the Tektronix 519 oscilloscope on which the pulses from A and D are displayed, is such that the sweep triggers off a coincidence pulse from BCH. The time of arrival of this external trigger is governed by the last pulse to pass through B or C or H. In normal conditions, for a muon vertically traversing the BCH coincidence system, the timing of the displayed pulses from A and D, on the oscilloscope trace, is shown in Figure 7.4(ii). The pulses appear at an average of 17.83 ns and 41.22 ns, respectively, from the initial sweep point.

For background 'separate track' events, of the type described in Section 6.4, the positions of these time of flight pulses on the oscilloscope trace,

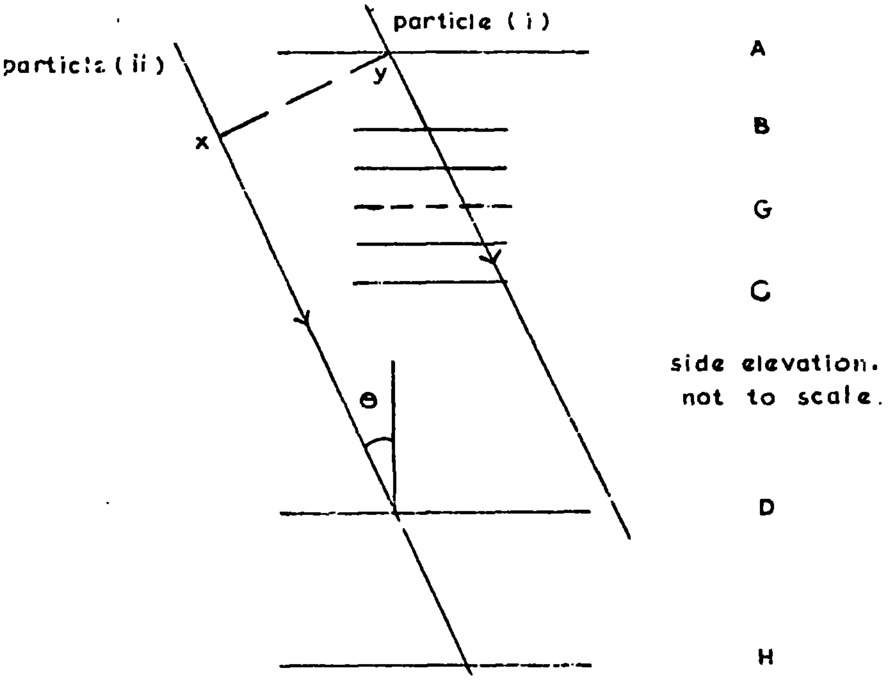

Figure 7.4(i) Representation of a background 'separate track' event through the spectrometer. The arrival time difference, Δt ns, between the track (i) and (ii), is measured at the wavefront xy.

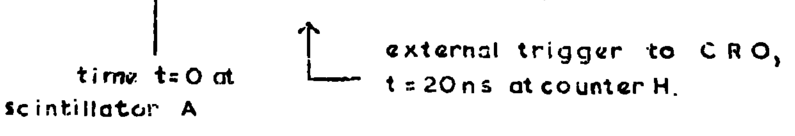

Figure 7.4(ii) The pulse profiles from A and D, illustrating the timing of a normal muon event on the time of flight oscilloscope.

varies. If Δt ns is the time delay between two particles (i) and (ii) on the wave front at A, where particle (i) traverses the top half of the spectrometer (i.e. A, B, C) and particle (ii) traverses the bottom half (i.e. D,H), as shown in Figure 7.4(i). Then Δt is positive when (ii) precedes (i), or negative when (i) precedes (ii). For $\Delta t \leqslant -17.83$ ns (e.g. $\Delta t = -20$ ns) and $\theta = 0$, the triggering pulse from H arrives after the display pulse from A, and only the pulse from D is displayed. Similarly, for $\Delta t \geqslant +53.19$ ns, the triggering pulse from C arrives after the display pulse from D, and only the pulse from A is displayed. The only feasable explanation of the events displaying one time of flight pulse (as observed in the experiment described in Chapter 6), is in terms of the 'separate track' events. The muon momentum limit to display such a pulse, < 59 MeV/c, will not penetrate the spectrometer. It also seems highly improbable that these events are the result of an intermittent connection fault, as both A and D channels would have to suffer from this defect.

The results of an analysis on the time of flight distributions expected for background 'separate track' events, over a wide range of time delays Δt, for various incident angles, θ, of particle (ii) to the vertical, is shown in Figure 7.5(i). An assumed delayed particle spectrum of the form shown in Figure 7.5(ii), for associated particles, was then used to determine the form of the distribution in time of flight values exhibited by these events. The expected distribution is shown in Figure 7.5(iii). The resultant distribution summed over all values of θ is observed to be asymmetrically biased towards the lower time of flight values. The contribution of associated 'separate track' events with a delayed spectrum of the form shown, is expected to exhibit time of flight values mainly over the region 12.5 - 20 ns. Similarly, unassociated

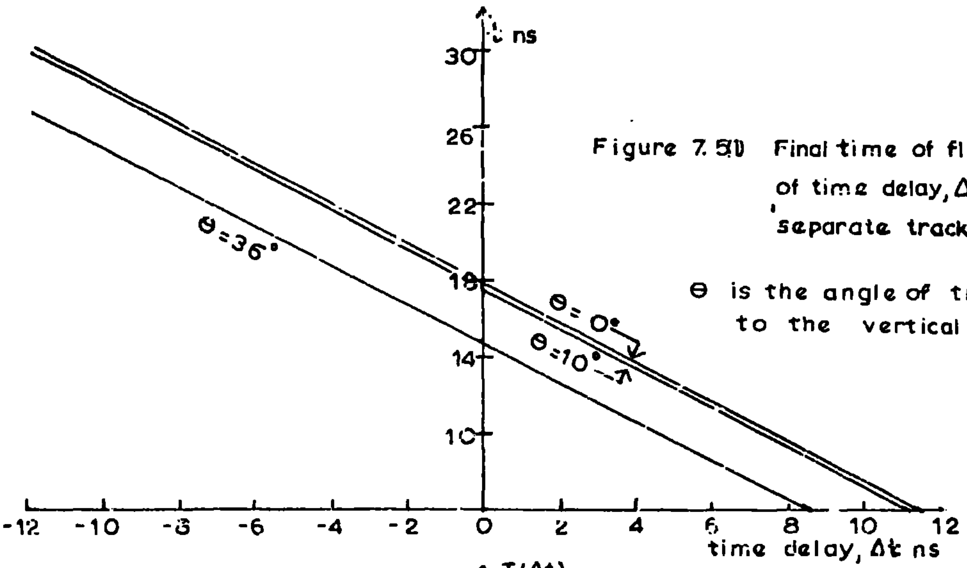

Figure 7.5(i) Final time of flight, t ns, as a function of time delay, Δt ns between the 'separate tracks'.

θ is the angle of track (ii) to the vertical

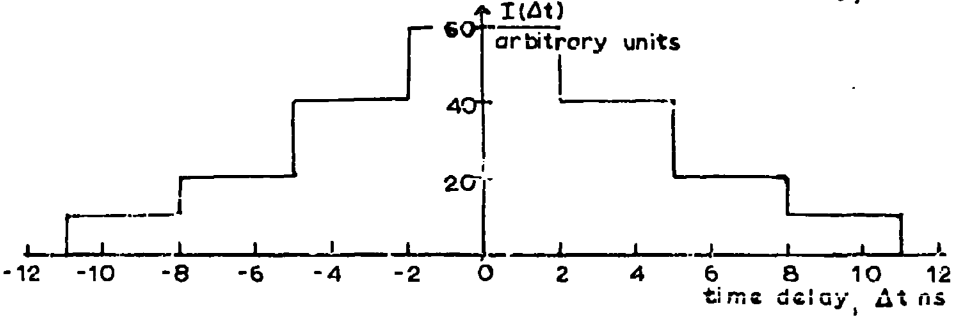

Figure 7.5(ii) The assumed delayed particle spectrum, I(Δt).

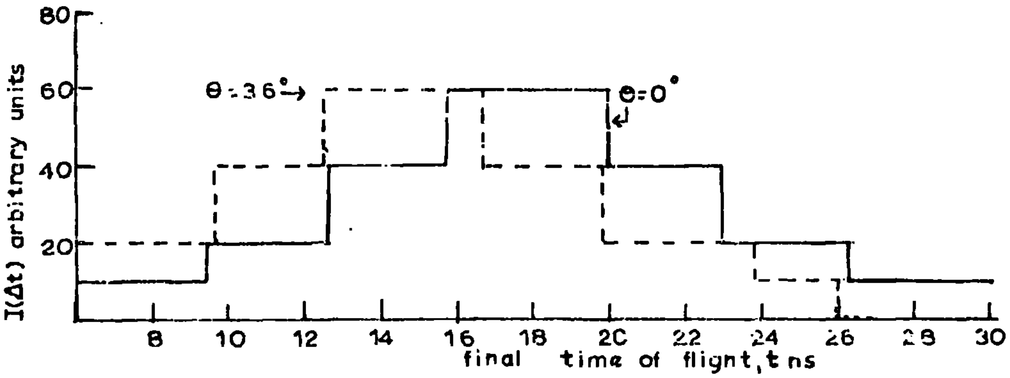

Figure 7.5(iii) The expected form of the final time of flight distribution for 'separate track' events.

'separate track' events display an asymmetry in time of flight values. The discrepancy and displacement values of these background events are most likely to be large.

7.12 Identification of the tail events

A scatter plot of displacement versus final time of flight values of the Class II events, shown in Figure 7.6, reveals a predominance of negative displacement values in the tail events (not including the 10 proton events). This relationship implies the tail events to be mainly negatively charged muons, the majority of which are thus deflected to pass through large ℓ_D values. Evidence of muon contribution in the tail events, is also enforced from the observed variation of R with t, where $R = \dfrac{\text{number of events, } \ell_D > 80 \text{ cm}}{\text{number of events, } \ell_D < 80 \text{ cm}}$, as shown in Table 7.3. In Section 7.10 it was concluded that the time of flight resolution would be expected to degenerate with increasing ℓ_D, thus yielding a muon contribution, with large ℓ_D values, in the tail events of the final time of flight distribution. However, a steady increase in the standard deviation on the median time of flight values, $\bar{t}_c$, is not revealed in Figure 7.7 for the Class II muon events, but more a peak at $\ell_D = 90$ cm. Individual observation of the events in Tables 7.1 and 7.2 and their ℓ_D values, shows that the majority of these tail events do exhibit ℓ_D values > 70 cm and mainly in the region 80-100 cm. Of the remaining tail events with $\ell_D < 70$cm the majority seem to exhibit ℓ_A values in the region 80-100 cm, suggesting a small reflection of the width variation, $P(T)_A$, with ℓ_A, into the observed time of flight distributions.

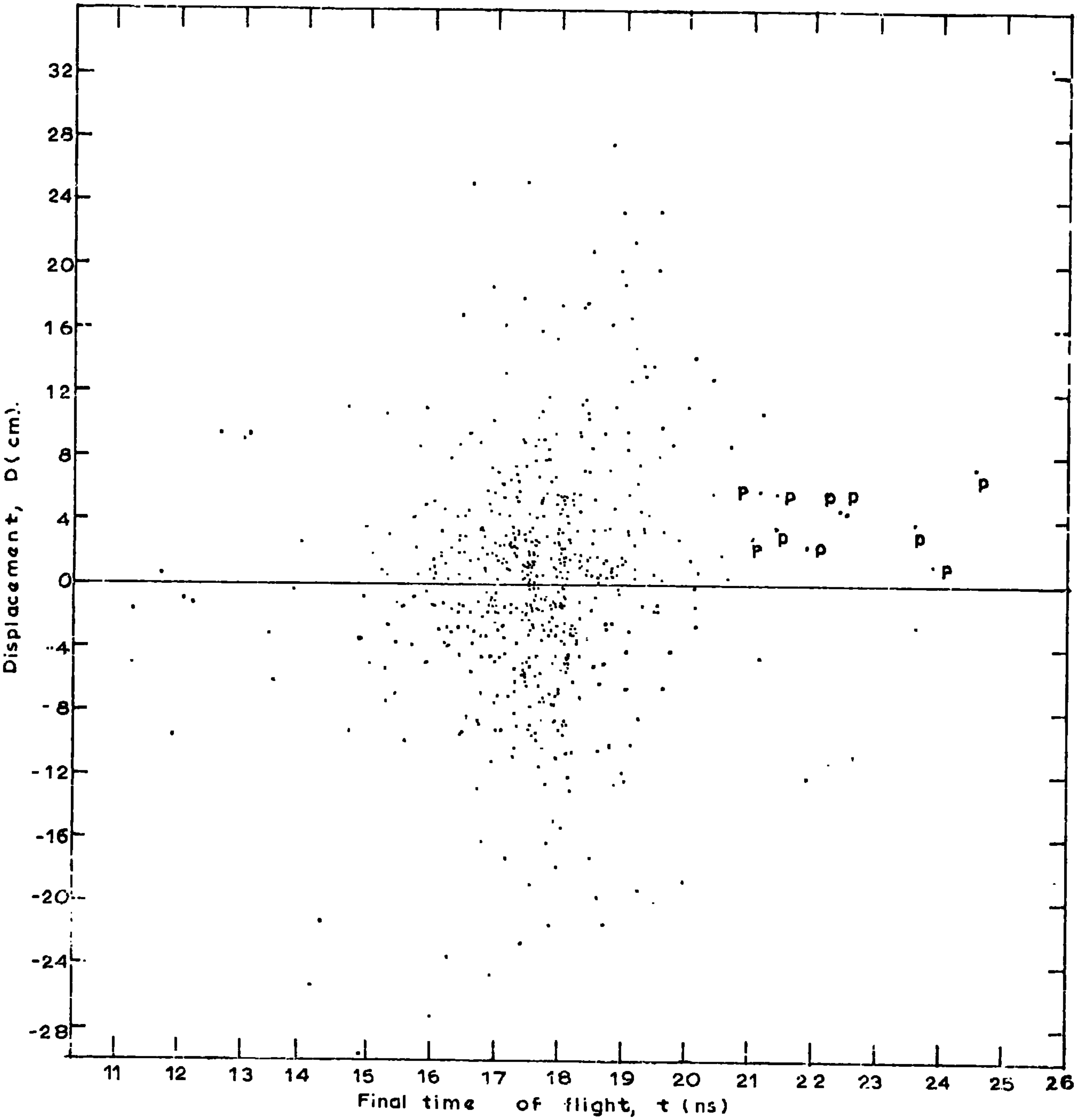

Figure 7.6 Scatter plot of displacement versus final time of flight, for Class II events.

Table 7.3

Final time of flight cells (ns)	R, for Class II muons
<14.3	$1.14^{+.82}_{-.60}$
14.3 — 15	$0.88^{+.63}_{-.41}$
15 — 16	$0.52^{+.22}_{-.19}$
16 — 17	$0.64 \pm .11$
17 — 18	$0.71 \pm .10$
18 — 19	$0.82 \pm .17$
19 — 20.3	$0.80^{+.41}_{-.34}$
>20.3	$0.60^{+.63}_{-.40}$

10 proton events not included

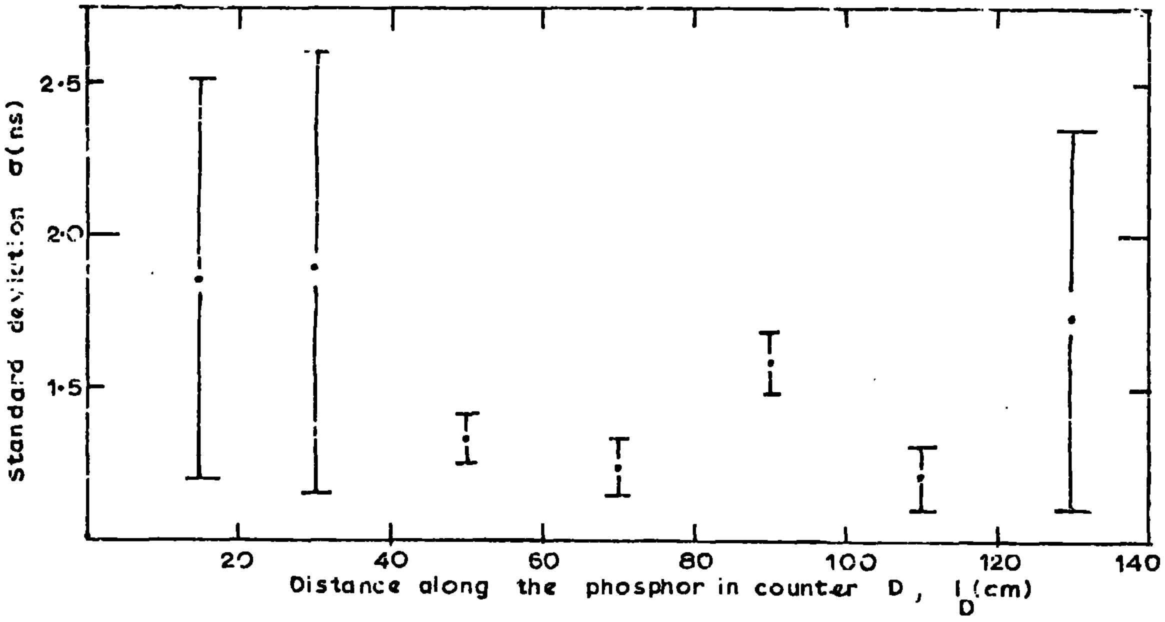

Figure 7.7 The standard deviation, σ, on the median corrected time of flight, $\bar{t}_c$, as a function of distance along the phosphor, l_D.

Tachyons are expected to disclose low discrepancy values and although the observed discrepancy values of the Class I tail events (plotted as moduli in Figure 7.8) are seen to be low, the possibility of a muonic origin is considered more likely, especially in the light of the evidence presented previously.

As background 'separate track' events are expected to exhibit large discrepancies and displacements, the scatter plot of events from the Class I time of flight distribution, shown in Figure 7.9 (as moduli) is, with the exception of one event, again indicative of muonic origins.

If the final muon time of flight distribution is assumed to be symmetrical about the median and the 8 remaining events in the high time of flight tail are muons, then the 7 events unaccounted for in the opposite tail (although statistically insignificant anyway) can quite easily be explained in terms of background 'separate track' events.

The 7 events unaccounted for in the low time of flight tail of the zero field final time of flight distribution are considered to be mainly spurious events caused by, the inability to distinguish the pulses from A and D coupled with the extremely high counting rate of $\sim 10^7$/min in these counters.

7.13 Conclusion

1. The most likely explanation of the tail events observed in the Class II (which includes Class I) muon final time of flight distribution is considered to be a relativistic muon contribution with the possible addition of an asymmetrical background 'separate track' contribution.

2. 10 protons have been identified in a total of 542 events, giving a proton to muon ratio of 1.8%.

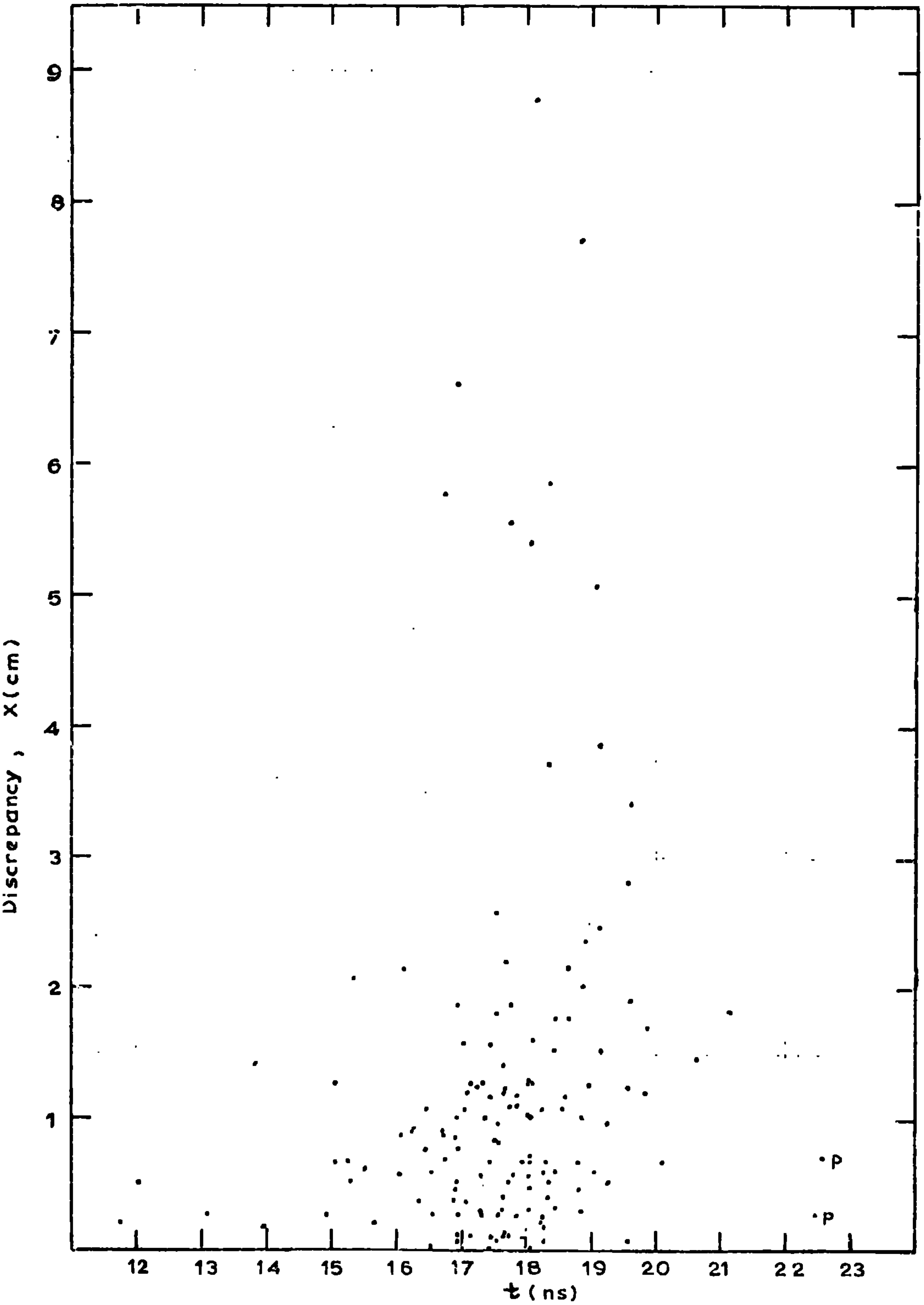

Figure 7.8 Scatter plot of discrepancy, X, as a function of final time of flight, t, for Class I events.

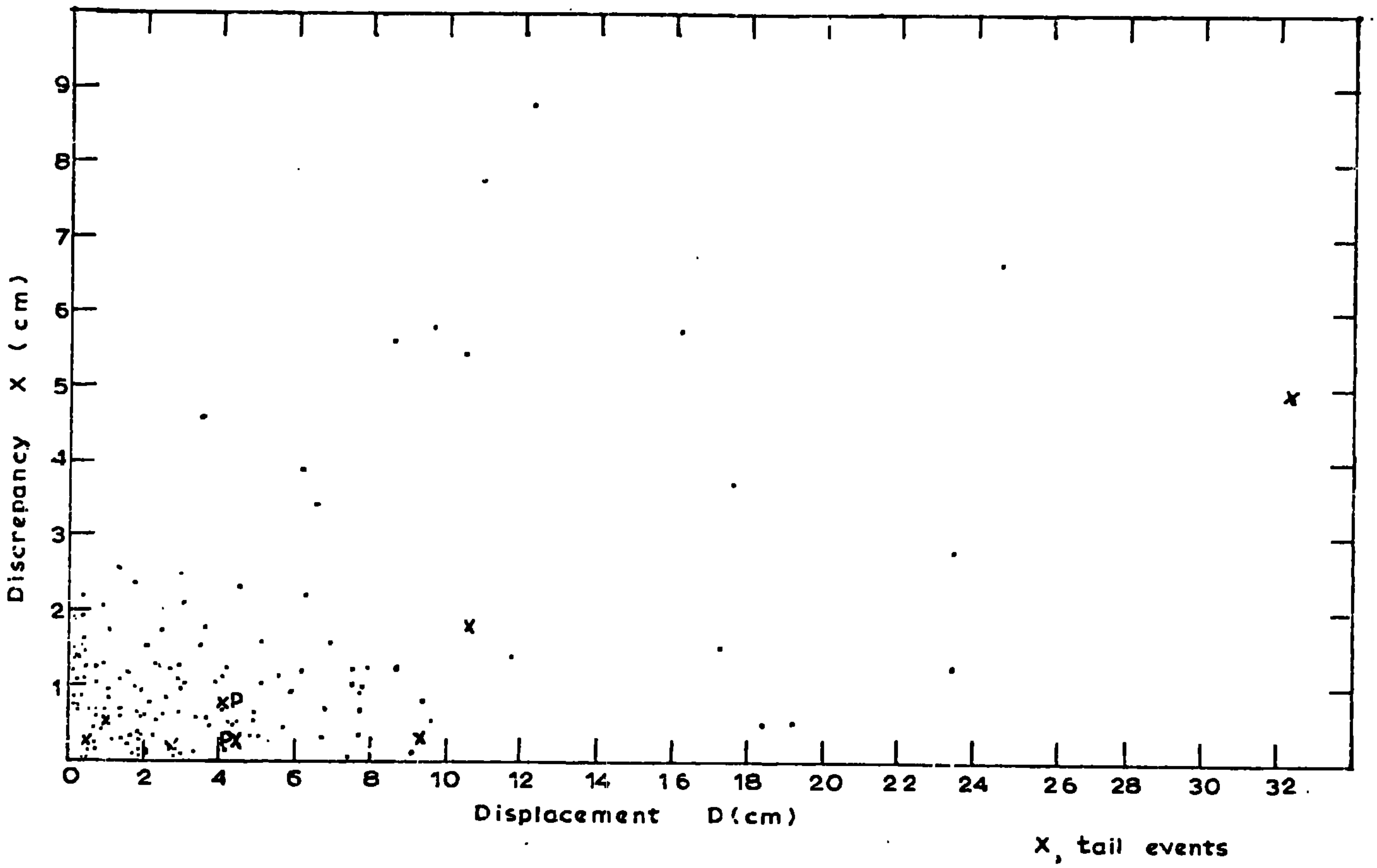

Figure 7.9 Scatter plot of discrepancy, X, as a function of displacement for Class I events.

3. Although the high velocity tail of the time of flight distribution is not fully understood, it is believed to be instrumental (conclusion 1 above) rather than due to tachyons. As no events were observed in the time of flight interval 0 to 11 ns, an upper limit of $< 2.2 \times 10^{-5} \mathrm{cm}^{-2} \mathrm{sec}^{-1} \mathrm{sterad}^{-1}$, at a 90% confidence level, can be placed on tachyons moving with velocities $> 1.6c$ in cosmic rays at sea level. This limit refers to tachyons able to penetrate the spectrometer and deposit > 1.8 MeV in the scintillation counters B,C and H.

CHAPTER 8

EXPECTED PERFORMANCE OF THE MASS SPECTROMETER

8.1 Introduction

An ideal experiment designed to conclusively identify low energy particles traversing a magnetic spectrometer, from estimations of their mass, charge and sign of charge, was proposed in Chapter 4.

The mass spectrometer, shown in Figure 5.1, was thus constructed to detect such particles and so to determine their identity from measurements of particle momentum, ionisation loss and time of flight. The properties of this spectrometer have been established in Chapters 5 and 6, and the expected precision on the mass values of protons, kaons and deuterons has been determined as a function of momentum in Figure 5.22. The dependence of the mass precision on the experimental conditions of the spectrometer is investigated in this chapter, with particular reference to the familiar particles of unit charge namely, protons, kaons and deuterons.

The properties and limitations of the mass spectrometer and the scintillator range telescope (Chapter 2) are compared with respect to their ability to assign a reliable mass estimate to any low energy, cosmic ray particles accepted under the selection criteria of each experiment. The two methods are also compared with respect to their powers of conclusive identification and acceptance rates of low energy particles.

8.2 Mass spectrometer study of low energy, massive particles in a muon free background

To enable particles and antiparticles of low intensity levels to be studied in a muon free background, as in the scintillator telescope experiment described in Chapter 2, an upper velocity threshold coupled with a threshold range momentum is imposed on the incident particles traversing the magnetic spectrometer. The upper velocity threshold is chosen such that, a mass discrimination level of 244 MeV/c^2 satisfies the condition in equation 2.2, and the mass precision $\frac{\delta m}{m} < 0.5$.

The upper velocity threshold is a consequence of the discrimination level imposed on the output pulse heights from the Cerenkov counter, labelled CT in Figure 5.1. The velocity response of this Cerenkov counter, in the threshold region of the response curve, has been well established from the agreement between the expected and measured responses of low energy protons, accepted through the scintillation counter telescope (Chapter 2), and has been fully reported by Ashton and Kelly (1969). A discrimination level of 0.37 E_c (where E_c is defined in Section 2.5) imposed on the Cerenkov pulses thus corresponds to an upper velocity threshold of 0.8C, from Figure 8.1.

The lower limits of momentum, imposed on incident particles, are determined by the amount of material in the spectrometer (Figure 5.24), and are such that particles of that momentum can just penetrate into scintillation counter H. The limiting incident momentum bands have been evaluated for the above conditions as a function of the mass, for particles of unit electron charge (Z=1), at normal incidence, and are shown in Figure 8.2.

8.3 Expected rates of some familiar cosmic ray particles through the mass spectrometer

The relevant data used to calculate the rates of protons, kaons and deuterons, expected through the spectrometer are shown in Table 8.1.

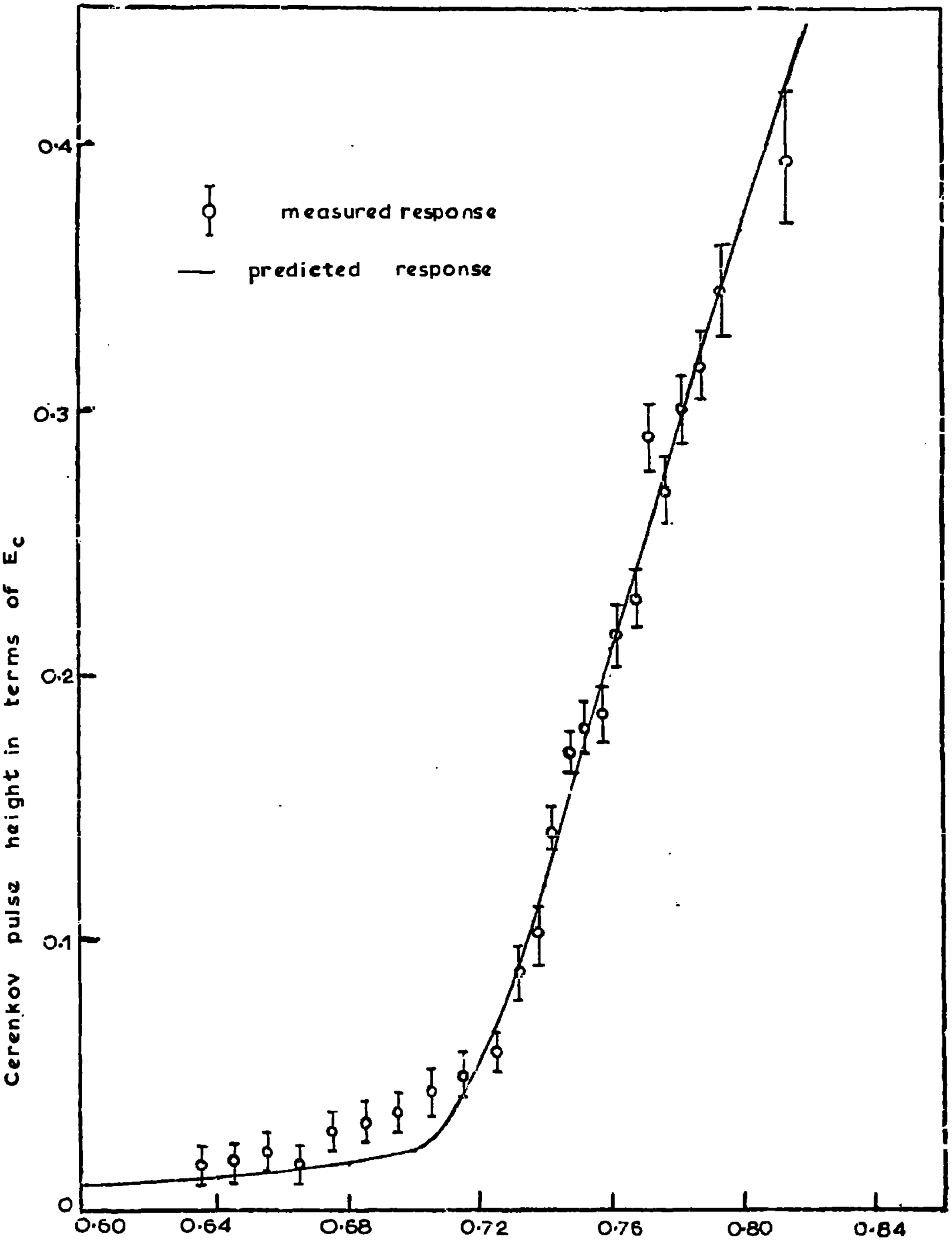

Figure 8.1 The measured Cerenkov response as a function of proton velocity, compared with the theoretical response derived from the consideration of the contributions from water, Perspex and knock-on electrons. E_c is the response at $\beta = 1$.

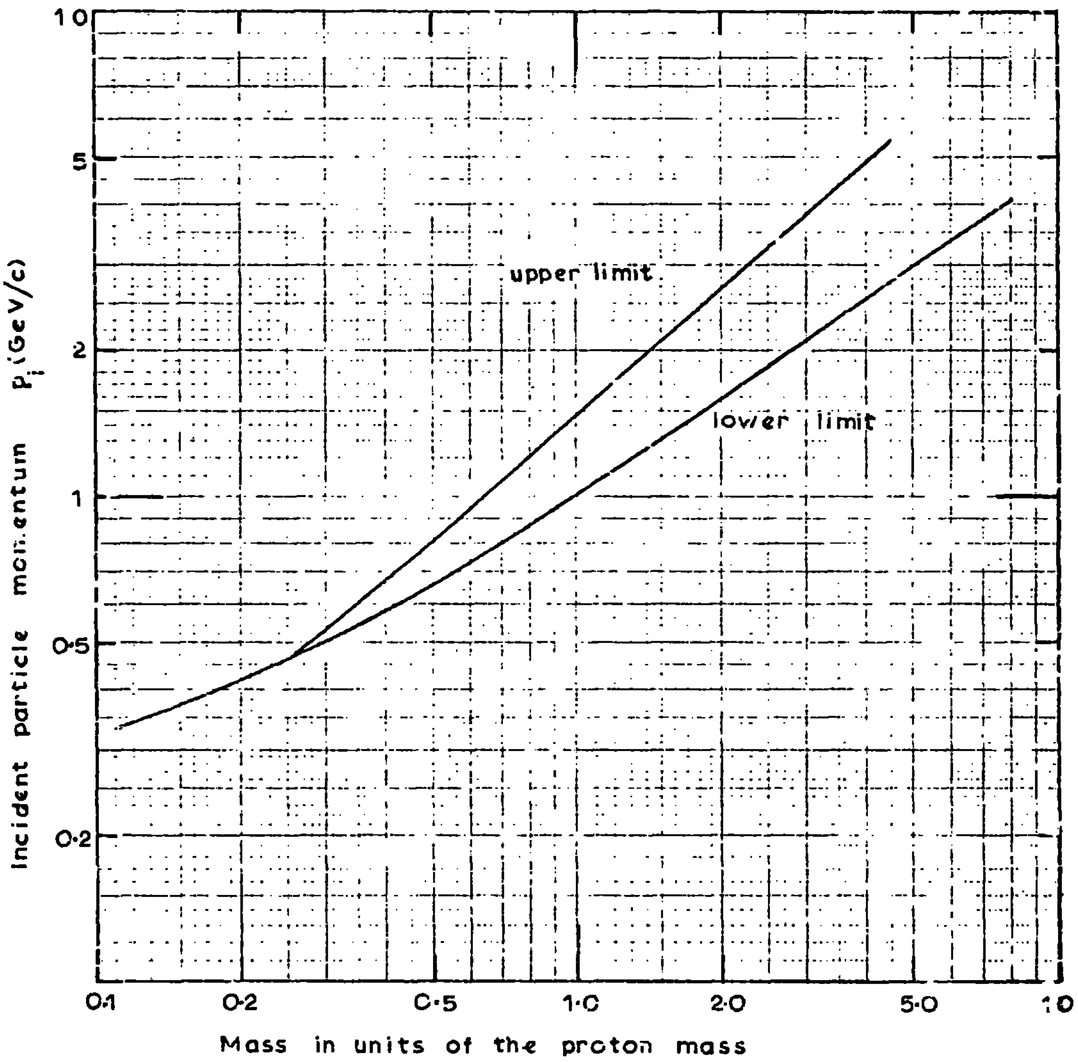

Figure 8.2 The limiting incident momentum bands for particles of different mass values accepted through the spectrometer.

TABLE 8.1

	Proton	Deuteron	Kaon
Incident momentum range accepted, $p_{i.1} - p_{i.2}$, GeV/c	1.021 - 1.463	1.591 - 2.706	0.693 - 0.862
Mean incident momentum, $p_{i.a}$ GeV/c	1.213	2.001	0.780
Measured momentum range accepted, $p_{m.1} - p_{m.2}$, GeV/c	0.875 - 1.385	1.430 - 2.630	0.601 - 0.790
Mean measured momentum, $p_{m.a}$ GeV/c (Corresponding to $p_{i.a}$)	1.115	1.880	0.699
Incident momentum band, Δp_i GeV/c	0.442	1.115	0.169
Acceptance, $A(p_a)$, at the mean momentum, cm^2 sterad.	18.74	19.18	17.65
Assumed incident differential spectrum, $N(p_i)dp_i$	$\alpha p^{-2.1}dp$	$\alpha p^{-3.14}dp$	$\alpha p^{-2}\ dp$
	Brooke and Wolfendale (1964)	Badalian (1959)	assumed in the absence of any definite information

The mean incident momentum, $p_{i.a}$, over the associated momentum band, was derived for each particle from the following data,

$$p_{i.a} = \frac{\int_{p_{i.1}}^{p_{i.2}} p_i \times N(p_i)dp_i}{\int_{p_{i.1}}^{p_{i.2}} N(p_i)dp_i}$$

where:

subscripts, i and m, refer to the incident momentum and momentum measured at the magnet centre, respectively,

a, refers to the mean momentum of the momentum band,

1 and 2 refer to the lower and upper momentum limits, respectively,

N(p)dp is the assumed particle spectrum.

The relation between the incident and measured momentum (at the magnet centre, G) for each particle type is shown in Figure 8.3. Essentially the ionisation loss of each particle in travelling through 28.3 g cm^{-2} water equivalent to the magnet centre was determined for varying incident momenta.

The acceptance value at the mean momentum, for each of the particles in Table 8.1, was deduced from Figure 6.5. The differential proton spectrum of Brooke and Wolfendale (1964), shown in Figure 8.4, was used to calculate the intensity of protons over the incident momentum range.

$$\int_{1.021}^{1.463} N(p_i)dp_i = 2.58 \times 10^{-5} cm^{-2} sec^{-1} sterad^{-1}$$

The expected rate, R_p, of protons through the spectrometer, ignoring losses due to interactions, is then given by

$$R_p = 2.58 \times 10^{-5} \times 18.74 = 1.74 \ hr^{-1}$$

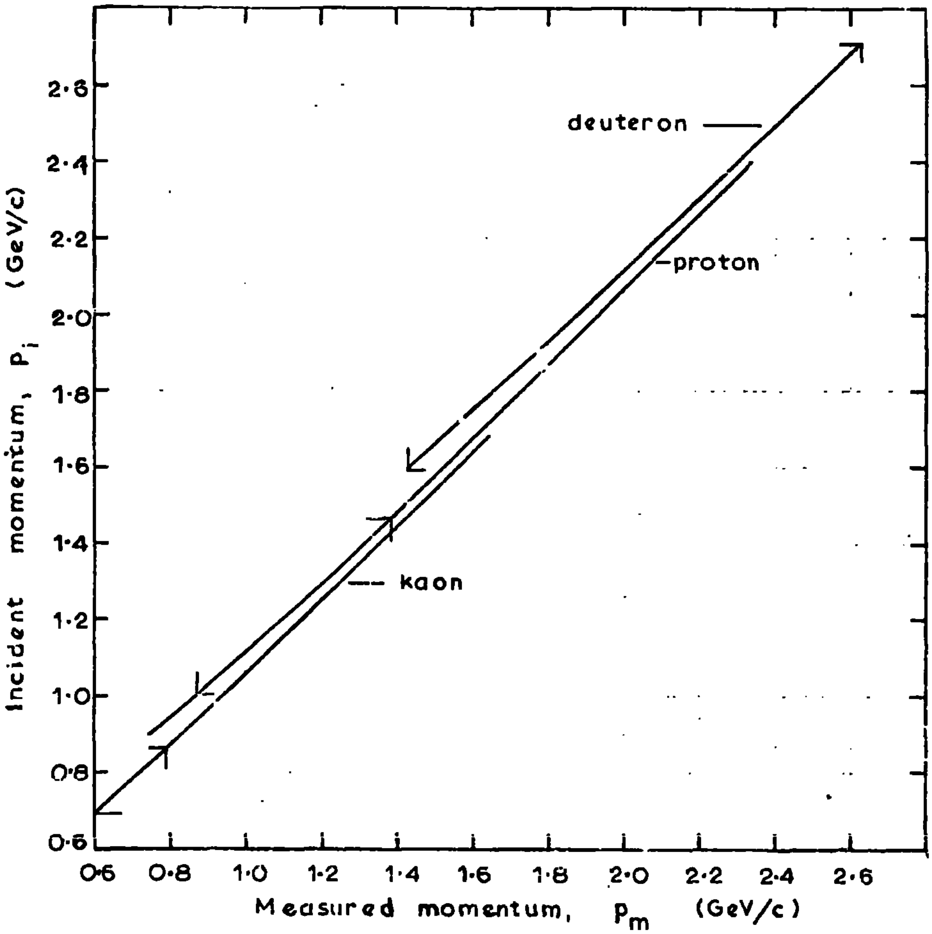

Figure 8.3 The incident momentum, p_i , as a function of the measured momentum, p_m , at the magnet centre, for kaons, protons and deuterons. The vertical and horizontal lines shown on each curve are the limits to the measured and incident accepted momentum bands respectively.

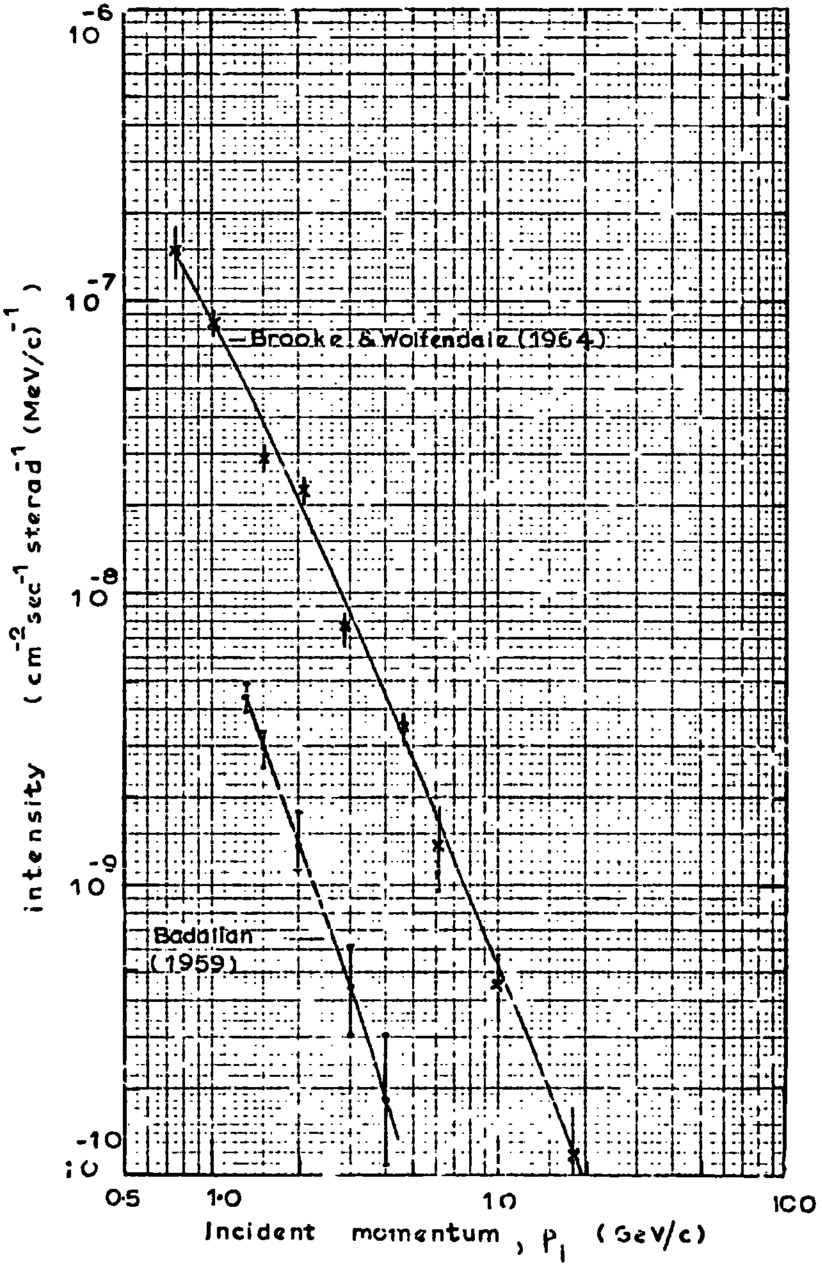

Figure 8.4 The sea level deuteron spectrum predicted by Badalian (1959), compared with the proton spectrum due to Brooke and Wolfendale (1964). The predicted momentum dependence of the deuteron spectrum of the form $N_d(p)dp \propto p^{-3.14\pm.44}dp$, has been normalised to the measurement of Badalian at 1.3 GeV/c.

The deuteron sea level momentum spectrum of the form $N(p)\,dp \propto p^{(-3.14\pm.44)}dp$ as derived by Badalian (1959) (Section 3.5.2) was used to calculate the intensity of deuterons over the incident momentum range. The sea level deuteron momentum spectrum, shown in Figure 8.4, was derived by normalising the deuteron spectral form to a deuteron measurement by Badalian at 1.3 GeV/c (see Section 3.5.2). Thus from Figure 8.4 the intensity of deuterons over the incident momentum band is

$$\int_{1.591}^{2.706} N(p_i)\,dp_i = 1.316 \times 10^{-6}\,\mathrm{cm}^{-2}\,\mathrm{sec}^{-1}\,\mathrm{sterad}^{-1}$$

The expected rate of deuterons, R_d, through the spectrometer, ignoring losses due to interactions, is given by

$$\begin{aligned} R_d &= 1.316 \times 10^{-6} \times 19.18 \ \ \mathrm{sec}^{-1} \\ &= 2.2 \ \mathrm{day}^{-1} \end{aligned}$$

8.4 Correction for interaction losses in the spectrometer

Due to the strongly interacting nature of protons and deuterons, the measured rate of particles will not comprise totally of particles incident in the defined momentum band. Contributions to the rate will come from particles, incident with momenta greater than the upper momentum limit imposed by the Cerenkov discrimination level, but which lose a certain fraction of their energy in interactions before they reach the Cerenkov counter CT, in Figure 5.1. A much smaller contribution to the proton rate will come from the selection of the emitted proton from a deuteron interaction. Losses will occur from particles incident within the accepted momentum limits, but which interact so that their remaining energy is too small to satisfy the coincidence requirement, BCH. Applying a correction for such effects is complicated. However, under an additional selection criteria that rejects all interacting particles, on the grounds that the accuracy of the mass analysis is severely affected by such an interaction, the calculation of the rates from the assumption that all interacting particles are lost, is only in error by the inefficiency of visually detecting an interaction in the spectrometer.

For calculation of the interaction lengths in the spectrometer, the same procedure as in Section 3.3 was adopted. Using the nucleon inelastic interaction lengths as a function of atomic weight (as shown in Figure 3.1 measured by Chen et al. (1955)) the number of inelastic interaction lengths in each of the various detecting elements in the spectrometer were evaluated. The results are given in Table 8.2.

TABLE 8.2

Detector	Number of inelastic interaction lengths, λin
Flash tubes, F1a, F1b	0.085
Scintillation counters, A, B, C, D, E, H	0.069
Flash tubes, F2a, F3a	0.053
Flash tubes, F2b, F3b	0.039
Flash tubes, F4a	0.072
Cerenkov tank, CT	0.316
Flash tubes, F5a, F5b	0.094
	Total 1.16 λin

The spectrometer contains 1.16 nucleon inelastic interaction lengths and an error of 5% is estimated on this value. Assuming the total loss of all interacting particles, the expected proton rate through the spectrometer is,

$$R_p = 1.74\ e^{-1.16}$$
$$= 0.55\ \text{hr}^{-1}$$

In the absence of any definite knowledge of the spectral form for kaons at such low energies, the accepted rate of kaons, R_k, is assumed to be ≈ 1% of the accepted proton rate.

$$R_k = 5.5 \times 10^{-3}\text{hr}^{-1}$$

A summary of nucleon-nucleon and nucleon-deuterium cross sections has been given by Longo (1968) to evaluate the Glauber shadow correction, $\delta\sigma$, for nucleon-deuterium interactions, over the nucleon momentum range 3 - 27 GeV/c. Further values of $\delta\sigma$ have been evaluated by Kelly (1969), at lower momenta values, from the nucleon-nucleon and nucleon-deuterium cross sections as measured by Marshall et al. (1953) and Nedzel (1954). The Glauber shadow correction, as reviewed by the above workers, is shown in Figure 8.5 as a function of nucleon momentum. At a mean incident deuteron momentum of 2.149 GeV/c (which is equivalent to protons of momentum 1.07 GeV/c incident upon deuterium) reference to Figure 8.5 shows that at this momentum $\delta\sigma \approx 0$. Hence from equation 8.1

$$\sigma_{pd} \approx \sigma_{np} + \sigma_{pp} \text{ to within the order of } 2\%$$

The total spectrometer thus contains 2.32 ± 0.12 deuteron inelastic interaction lengths. The expected deuteron rate through the spectrometer

$$R_d = 2.2 \times e^{-2.32}\ \text{day}^{-1}$$
$$= 0.22\ \text{day}^{-1}$$

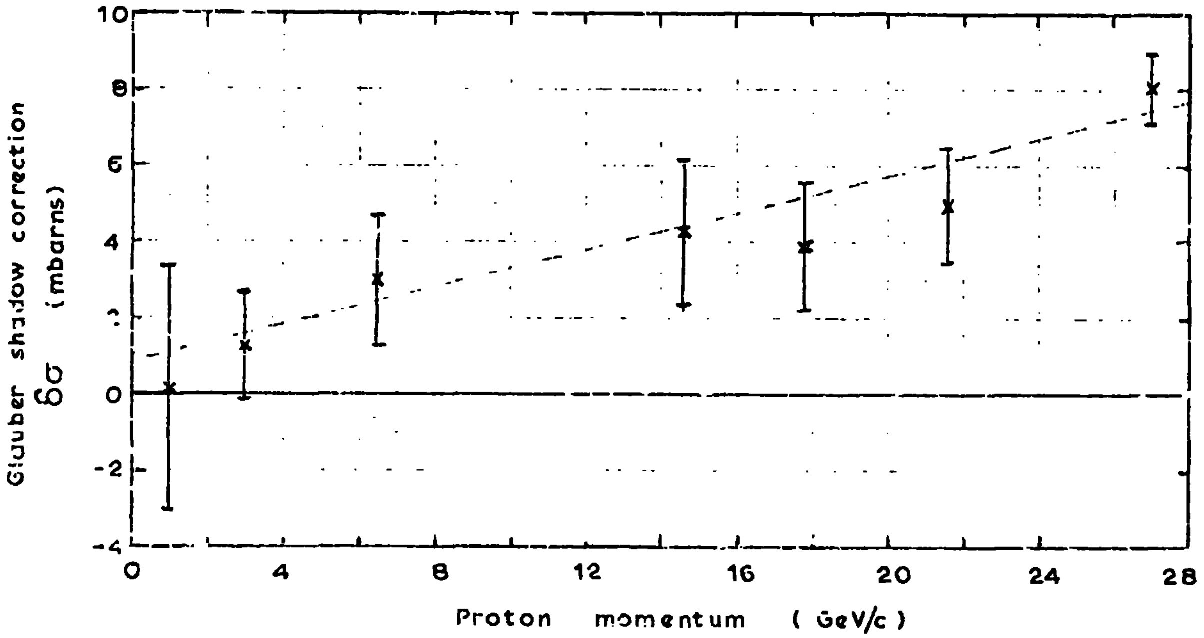

Figure 8.5 The Glauber shadow correction as a function of the incident nucleon momentum where

$$\delta\sigma = \sigma_{pp} + \sigma_{np} - \left\{ \begin{array}{l} \sigma_{nd} \\ \text{or} \\ \sigma_{pd} \end{array} \right. \qquad 8.1$$

$\left.\begin{array}{l}\sigma_{pp}\\ \sigma_{np}\end{array}\right\}$ are the nucleon-nucleon cross sections.

$\left.\begin{array}{l}\sigma_{nd}\\ \sigma_{pd}\end{array}\right\}$ are the nucleon-deuterium cross sections.

8.5 Mass spectrometer study of low energy, massive particles in a 'separate track' free background

The contribution of background 'separate track' events, in the mass spectrometer study of low energy particles, is expected to be substantially decreased in numbers by the imposition of a Cerenkov velocity discrimination level. Biasing, however, is expected to occur to the acceptance of 'separate track' events that arrive at angles such that the particle ii in Figure 7.4(i) misses the Cerenkov counter. To search confidently for heavy mass particles in the cosmic radiation, of expected rates as low as 0.22 day^{-1}, it is necessary to eliminate this background. This can be achieved with either the inclusion of a side flash tube view in the spectrometer or by the simple but subtle method which includes scintillation counter E (in Figure 5.1) into the BCEH $\overline{CT}$ coincidence requirement. The effectiveness of the latter method can be understood from the following conditions: If the selection of 'separate track' events is caused by a coincident random pulse through H (i.e. by the unassociated events, discussed in Section 6.4) the inclusion of a further scintillation counter above the Cerenkov counter will reduce such triggers by $1.5N\tau$, where N is the total counting rate from the scintillation counter and τ the resolving time of the coincidence circuitry, the reduction being $\sim 10^{-5}$. If the effect is due to an accompanying particle (i.e. associated events discussed in Section 6.4) then this particle has now to traverse the Cerenkov counter and such events will be rejected, except for sub-relativistic accompanying particles. The latter method of background elimination is only effective when run in conjunction with the velocity discrimination level imposed by the Cerenkov counter.

8.6 Particle identification

For the charge determination of low energy, massive particles selected for analysis, the scintillator pulse heights also need to be recorded and measured.

The mass of each event is then determined from the measurements of displacement, charge and time of flight, according to Section 5.18 and equation 5.30. The mass precision of a particle of charge, ze, is given by

$$\frac{\delta m}{m} = \left[\left(\frac{0.253}{\beta_m}\right)^2 + \left(\frac{0.049}{z}\,p_m\right)^2 + \left(\frac{t\delta t}{t^2-312.58}\right)^2\right]^{\frac{1}{2}}$$

where $\delta t = \pm 1\text{ns}$. In fact, the term including z does not have a substantial effect on the mass precision till much higher momenta values than those being studied.

The sign of charge for each event follows from the sign of the trajectory deflection in the magnetic field.

8.7 Expected mass distributions, obtained from the selection of low energy, massive particles through the mass spectrometer

The frequency distribution in mass values, $N(\bar{m}-m)dm$, observed for a particle of true rest mass $\bar{m}$, is a consequence of the Gaussian error distributions in the displacement and time of flight measurements, about respective true means $\bar{D}$ and $\bar{t}$. The observed mass distribution for a particle of mass $\bar{m}$ and single electron charge (Z=1), under the experimental conditions of the spectrometer, can be calculated from the following relation,

$$N(\bar{m}-m)dm = \int_{p_i}\int_{D}\int_{t} N(\bar{p}_i)dp_i \times T \times \eta \times f(\bar{p}_i) \times P(\bar{D}-D)dD \times A(D) \times P(\bar{t}-t)dt \qquad 8.2$$

such that the observed events in the mass cell m to m+dm have contributions from a range of combinations of the variables $\bar{p}_i$, D, t, related according to equation 5.31, where:

1. $N(\bar{p}_i)dp_i$ is the assumed incident differential spectrum of particles with mass $\bar{m}$, corrected for interaction losses in the spectrometer and the atmospheric pressure conditions during the experiment. The incident spectrum is integrated from the lower incident momentum limit (shown in Table 8.1 for protons, kaons, and deuterons) to an upper limit of infinity, but which is essentially defined by the probability, $f(\bar{p}_i)$, of an incident particle of momentum $\bar{p}_i$ being accepted by the Cerenkov counter (Figure 8.8). The finite width of the Cerenkov pulse height distribution causes fluctuations in the upper momentum limits (shown in Figure 8.2), imposed by the Cerenkov velocity discrimination level.

2. $(1-\eta)$ is the detection inefficiency caused by the selection of only single (unaccompanied) particle tracks. This is expected to be negligible, compared to statistical errors.

3. T is the running time.

4. $P(\bar{D}-D)dD$ is the Gaussian probability distribution in displacement values with standard deviation δD, about a mean $\bar{D}$ (corresponding to a true momentum, $\bar{p}_m$, where $p_m D = 7.3$ GeV/c cm and where $\bar{p}_m$ and $\bar{p}_i$ are related according to Figure 8.3)

5. A(D) is the acceptance value at each displacement D.

6. $\mathbf{P}(\bar{t}-t)dt$ is the Gaussian probability distribution in time of flight values about a mean $\bar{t}$ (which corresponds to the true measured momentum $\bar{p}_m$ of the particle with mass $\bar{m}$, where $\bar{t}$ and $\bar{p}_m$ are related according to Figure 5.20) with a standard deviation $\delta t = \pm 1$ns.

a range of combinations of the variables $\bar{p}_i$, D, t, related according to equation 5.31, where:

1. $N(\bar{p}_i)dp_i$ is the assumed incident differential spectrum of particles with mass $\bar{m}$, corrected for interaction losses in the spectrometer and the atmospheric pressure conditions during the experiment. The incident spectrum is integrated from the lower incident momentum limit (shown in Table 8.1 for protons, kaons, and deuterons) to an upper limit of infinity, but which is essentially defined by the probability, $f(\bar{p}_i)$, of an incident particle of momentum $\bar{p}_i$ being accepted by the Cerenkov counter (Figure 8.8). The finite width of the Cerenkov pulse height distribution causes fluctuations in the upper momentum limits (shown in Figure 8.2), imposed by the Cerenkov velocity discrimination level.

2. $(1-\eta)$ is the detection inefficiency caused by the selection of only single (unaccompanied) particle tracks. This is expected to be negligible, compared to statistical errors.

3. T is the running time.

4. $P(\bar{D}-D)dD$ is the Gaussian probability distribution in displacement values with standard deviation δD, about a mean $\bar{D}$ (corresponding to a true momentum, $\bar{p}_m$, where $p_m D = 7.3$ GeV/c cm and where $\bar{p}_m$ and $\bar{p}_i$ are related according to Figure 8.3)

5. A(D) is the acceptance value at each displacement D.

6. $\mathcal{P}(\bar{t}-t)dt$ is the Gaussian probability distribution in time of flight values about a mean $\bar{t}$ (which corresponds to the true measured momentum $\bar{p}_m$ of the particle with mass $\bar{m}$, where $\bar{t}$ and $\bar{p}_m$ are related according to Figure 5.20) with a standard deviation $\delta t = \pm 1$ns.

8.8 Approximate calculation of the expected mass distribution for protons, deuterons and kaons

For an idea of the form of the mass distributions expected from momenta and time of flight measurements on protons, deuterons and kaons, subject to the limiting conditions in Table 8.1, the frequency distribution in mass values (equation 8.2) can be approximated to,

$$\frac{N(\bar{m} - m)dm}{T} = P(D_a - D)dD \times \left[\int_{p_{i.1}}^{p_{i.2}} N(\bar{p}_i)dp_i \times A(D_a) \right] \qquad 8.3$$

where D_a is the displacement corresponding to the mean incident momentum $p_{i.a}$ (see Table 8.1) and $\int_{p_{i.1}}^{p_{i.2}} N(\bar{p}_i)dp_i A(D_a) = R$ is the expected rate of particles (corrected for interaction losses) accepted by the spectrometer. R is calculated for protons, deuterons and kaons in Section 8.4. Thus $P(D_a-D)dD$ expressed in terms of the mass, is the probability of obtaining the mass of a particle with true mass $\bar{m}$ between m and m + dm, i.e.

$$f(\bar{m}-m)dm \equiv P(D_a-D)dD.$$

That this is a reasonable approximation can be seen from Figure 5.22, where the contributions to the precision in the mass determinations of protons, deuterons and kaons, are predominately from the scattering errors, over the momentum regions accepted. The Gaussian probability distribution in displacement values, $P(D_a-D)dD$, about a mean D_a, accordingly gives a probability distribution in mass values, $f(\bar{m} - m)dm$, given by

$$f(\bar{m}-m)dm \equiv P(D_a-D)dD = \frac{1}{\delta D_s\sqrt{2\pi}} \, e^{-\frac{(D-D_a)^2}{2\delta D_s^2}} \, dD \qquad 8.4$$

where δD_s is the r.m.s. scattering displacement at D_a.

Substitution into equation 8.4 with equation 5.31 written in the form

$$m = \frac{B}{D} \quad \text{where B is a constant}$$

and hence also with $\frac{dm}{m} = \frac{dD}{D}$

gives, in equation 8.3, where the probability distributions have been scaled to allow for the different accepted particle rates (Section 8.4) compared to the proton rate, R_p,

$$\frac{N(\bar{m}-m)\,dm}{R_p \times T} = f(\bar{m}-m)\,dm \times \frac{R}{R_p} = \frac{1}{\delta D_s\sqrt{2\pi}}\,\frac{B}{m^2}\,e^{\left[-\frac{(B/m-D_a)^2}{2\,\delta D_s^2}\right]}\,dm \times \frac{R}{R_p} \qquad 8.5$$

The quantities used in the evaluation of equation 8.5, for protons, deuterons and kaons, are shown in Table 8.3, where for convenience a value approximately equal to D_a was used, with its corresponding precision, δD_s, evaluated from equation 5.22.

TABLE 8.3

Values used for	Proton	Deuteron	Kaon
D_a cm	6.78	4.17	11.0
δD_s cm	2.12	1.44	3.24
Constant B MeV/c^2 cm	6.36×10^3	7.82×10^3	5.43×10^3
Mass m, MeV/c^2	938	1876	493.8
Rate R hr^{-1}	0.55	0.0091	0.0055

8.9 Mass distributions

8.9.1 Random errors

The mass distributions evaluated from equation 8.5 for protons, deuterons and kaons are shown in Figure 8.6. The mass resolutions of these calculated distributions are observed to be a full width at half height of, 56% in the proton distribution, 63% in the deuteron distribution and 55% in the kaon distribution. The calculated mass distributions are seen to be asymmetrical, due to the inverse relationship between the mass distribution and the Gaussian displacement distribution.

8.9.2 Systematic errors

The calculated mass distributions in Figure 8.6 are each systematically shifted to lower mass values, the peaks appearing at 450 MeV/c^2, 800 MeV/c^2 and 1550 MeV/c^2 for the kaon, proton and deuteron distributions, respectively.

Such a systematic shift in mass values is observed in Figure 8.7 with the substitution of the expected time of flight values (corrected for momentum loss) and the measured momenta from Figure 5.20 into the equation for the mass determination,

$$m = \frac{\bar{p}_m \times \bar{t}}{17.68} \left[1 - \left(\frac{17.68}{t}\right)^2\right]^{\frac{1}{2}} \text{ GeV}/c^2$$

The systematic shift is caused by the deviation in the average velocity of a particle over the distance A to D (as obtained from the measured time of flight) from the velocity at the magnet centre. The increase in the ionisation loss at low momenta for these particles, accordingly increases this deviation. However, the maximum systematic error of $\simeq$ 5%, from this source, is small compared to the half width at half height of each mass distribution.

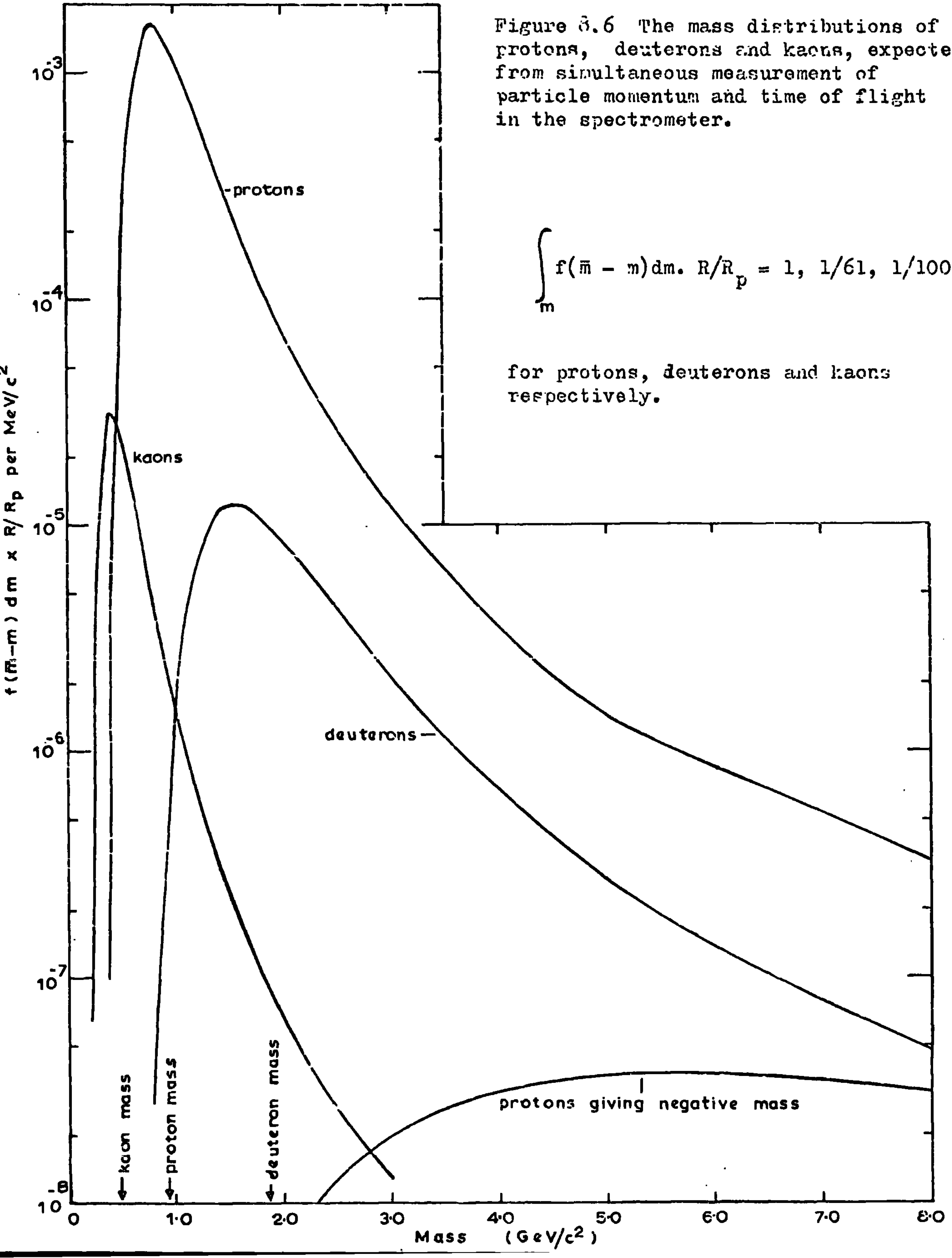

Figure 8.6 The mass distributions of protons, deuterons and kaons, expected from simultaneous measurement of particle momentum and time of flight in the spectrometer.

$$\int_m f(\bar{m} - m)\,dm. \quad R/R_p = 1,\ 1/61,\ 1/100$$

for protons, deuterons and kaons respectively.

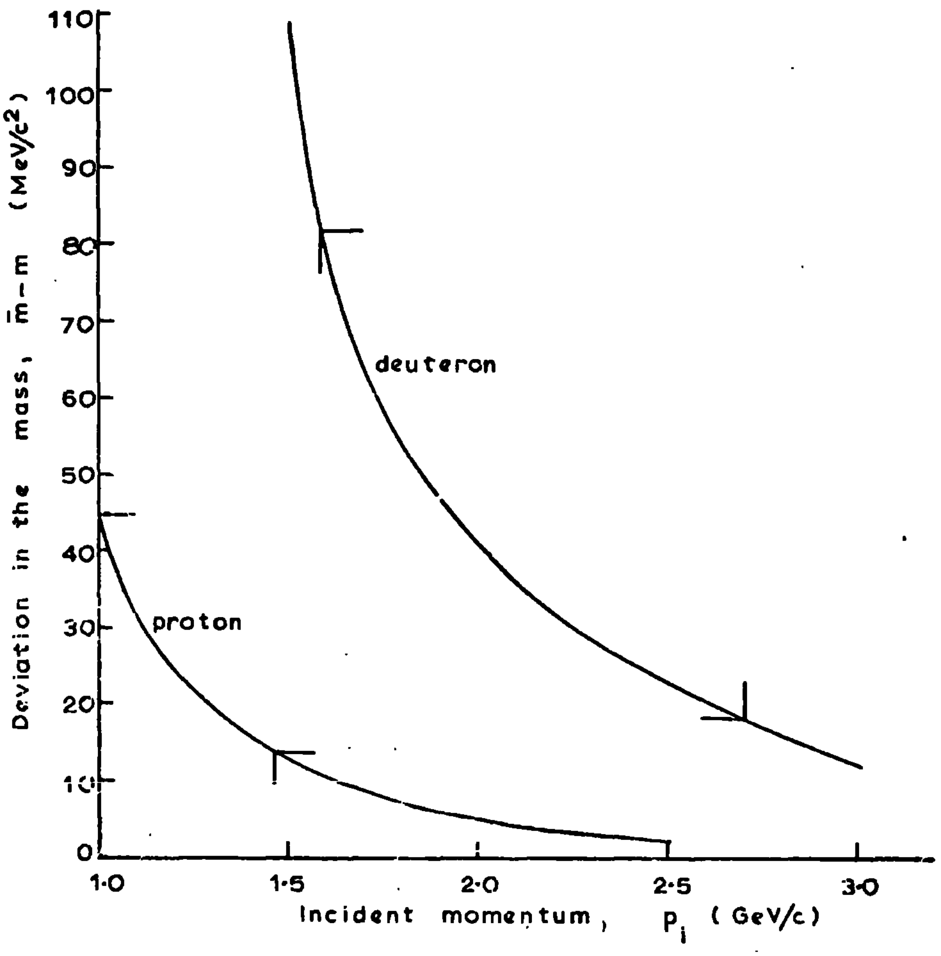

Figure 8.7 Systematic error in the mass of protons and deuterons, over the incident momentum bands. The accepted momentum limits are denoted by the vertical lines.

8.10 Proposed measurement of the deuteron (and kaon) intensity in the cosmic radiation at sea level

The problem of separating the observed mass distribution, obtained while selecting low energy, heavy mass particles through the spectrometer, into the individual distributions of protons and deuterons (and kaons) involves the extraction of the very small numbers of deuterons (and an even smaller number of kaons) from the predominating proton distribution in mass values.

Typically after 3260 hours running time, a total of 1793 protons and 29 deuterons are accepted. In the mass cell 2 - 2.5 GeV/c^2, according to Figure 8.6, the expected numbers of protons are 35.9^{+6}_{-7} and of deuterons $5.7^{+3.3}_{-2.2}$. As the statistical error on the total number of accepted particles in this cell is of the same order as the expected deuteron contribution, extraction of the observed deuteron contribution is impossible for this running time.

The measured distributions in mass values will, in fact, be broader than those shown in Figure 8.6, because of the approximations made (in Section 8.8) in the accurate expected mass distribution of equation 8.2.

For resolution of the observed mass distribution into the known constituents of protons, deuterons (and kaons), where the proton mass distribution is calculated from equation 8.2 (using the incident proton differential spectrum of Brooke and Wolfendale (1964)), the running time is chosen such that the statistical errors, on the total observed numbers of particles in each mass cell, are small compared to the expected number of deuterons (and kaons). The observed deuteron (kaon) rate is then resolved by subtraction of the expected proton mass distribution (calculated from equation 8.2) from the observed mass distribution. The observed rate is thus subject to the subtraction of, the errors involved with the accuracy of the former calculation, from, the statistical errors of the latter.

8.11 Corrections to the observed intensity

The true incident intensity of deuterons (and kaons, if the statistics are adequate), at a mean momentum $p_{i.a} = 1.88$ GeV/c, is evaluated after correcting the observed intensity for the following: (a) Interaction losses. (b) Multiple scattering effects. (c) Fluctuations in the upper momentum limit, $p_{i.2}$, due to the finite width of the Cerenkov pulse height distribution. (d) Detection efficiencies, η. (e) Efficiency of extraction. Caused by the acceptance of deuterons only over the mass range in which they are resolvable from the proton contribution.

As the precision of the deuteron (or kaon) intensity estimate depends mainly on the errors of the initial number extracted from the observed mass distribution, the accuracy of this estimate will be vastly improved when the proton contribution in the deuteron (or kaon) mass range is decreased.

8.12 Proposed intensity measurement of negative particles (< 1.5 GeV/c^2) in the cosmic radiation at sea level

Consideration of the extraction of negative particles, from Figure 8.6, shows that proton background is negligible ($\sim 5.7 \times 10^{-12}$/(MeV/c^2)) for negative mass values < 1.5 GeV/c^2.

For an assumed antiproton rate of $\simeq 7$ year^{-1} through the spectrometer, a total of 2.7 antiprotons will be accepted in a running time of 3260 hours. Of these, approximately 1.4 will appear in the region 0.75 - 1.25 GeV/c^2 (assuming the same mass distribution form as for protons).

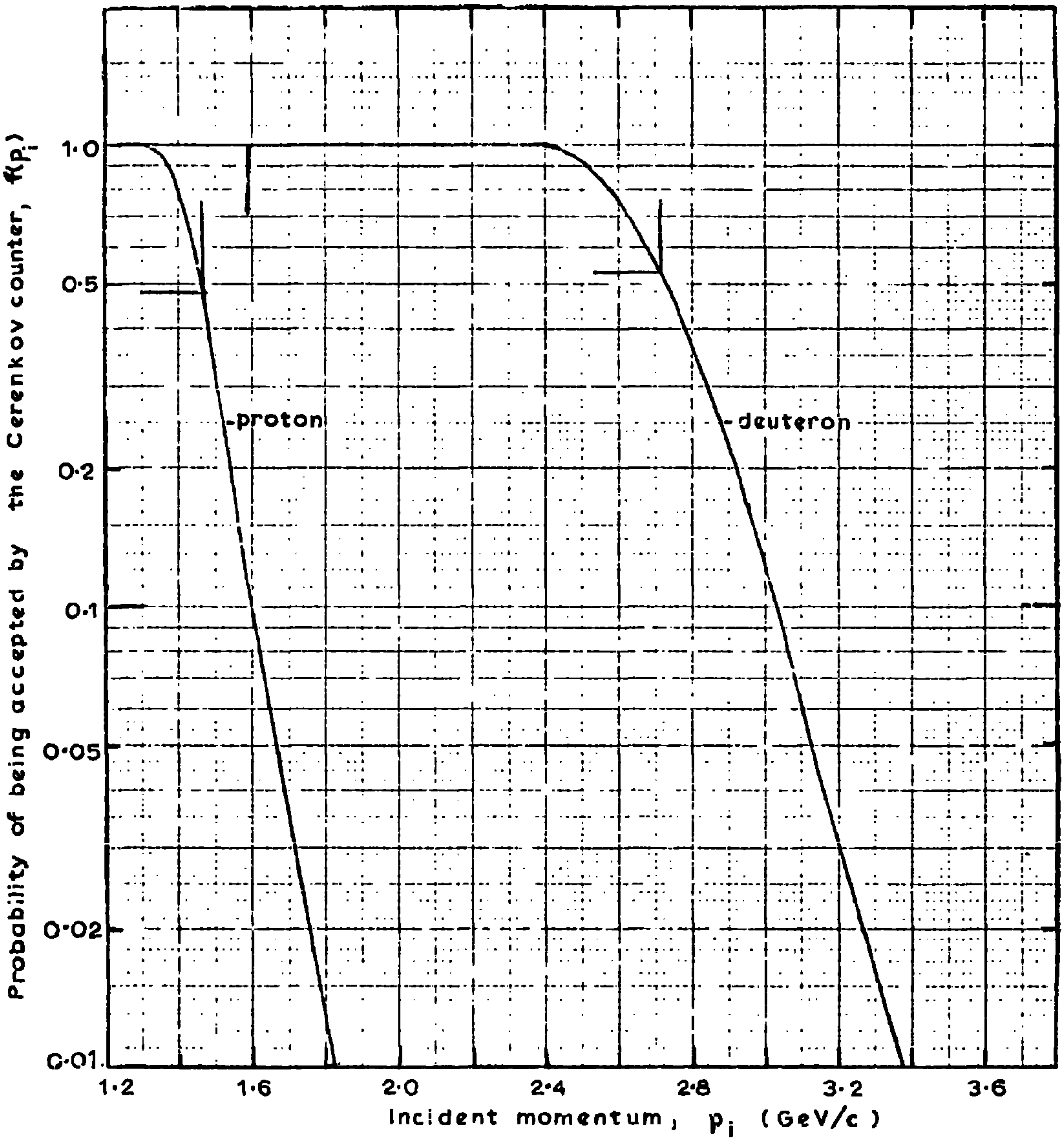

Figure 8.8 Probability of an incident particle being accepted by the Cerenkov counter, $f(p_i)$, as a function of incident momentum. The curves for protons and deuterons are shown with the incident momentum bands indicated by vertical lines on the appropriate curve.

Thus the limiting factor of antiparticle detection is not the error associated with the extraction from a predominate proton background but the small spectrometer aperture, ∿ 19.45 cm^2 sterad, necessitating an extremely long running time before sufficient statistical accuracy is obtained. This factor likewise governs the detection of deuterons (and especially kaons).

The precision on the true intensity estimate of antiparticles (mass < 1.5 GeV/c^2) will be mainly statistical and is not subject to the calculation errors of the expected proton mass distribution.

8.13 Improvement in the precision of intensity measurements

8.13.1 Modifications designed to improve the mass precision

Any method which improves the mass resolutions obtained in Figure 8.6 will accordingly increase the precisions of the resolved constituent particle intensities. The major factor governing the poor resolutions of the asymmetrical mass distributions is the r.m.s scattering displacement, δD_s, and its associated Gaussian distribution. The following modifications to the present conditions are designed to decrease this effect:

1. Increasing the line integral, $\int B d\ell$, by a factor of 3, accordingly decreases

$$\frac{\delta D_s}{D} = \frac{6.509 \times 10^4}{\beta \times \int B d\ell} \qquad \text{from equation 5.23}$$

Reference to Figure 5.22 shows that at 1.4 GeV/c the above ratio becomes ∿ 10%. Temperature recordings have so far limited the magnet exciting current to 36 amp.

2. Decrease in the r.m.s. scattering displacement, δD_s, would be effected if the number of radiation lengths in the detectors F3a, C, F3b were reduced.

For a 10% error in the mass determination due to the r.m.s. scattering displacement, the radiation lengths in the detectors must be a maximum of 0.04 r.ℓ. Possible methods to approach this mass precision were proposed in Section 4.4.

3. An upper limit on the r.m.s. scattering displacement can be achieved with the imposition of an upper discrepancy cut off on the accepted events.

The mass distributions in Figure 8.6 are cut off at mass limits of:

$0.68 < \text{proton mass} < 1.5 \quad \text{GeV/c}^2$

$1.2 < \text{deuteron mass} < 4.8 \quad \text{GeV/c}^2$

$0.4 < \text{kaon mass} < 0.6 \quad \text{GeV/c}^2$

when an upper limit of 1.67 cm is imposed on the r.m.s. scattering discrepancy values of a particle with a true displacement D_a (Table 8.3). The sharpness of the mass limit not only depends on the range of accepted displacement values about the mean D_a cm (giving a corresponding range of mass cut off values), but also on the contribution of the location error in F1a to the discrepancy value. In the present conditions $\delta F1a = 0.69$ cm with an intercept on the $<X^2>$ versus D^2 plot of 1.25 cm^2. To impose a r.m.s. scattering discrepancy of 1.67 cm, one has to impose a discrepancy cut off, on the accepted events, of 2.79 cm. The accuracy of using this limit would be such as to produce a diffuse mass cut off for each $\bar{D}$ value considered within the range. However, if the location error $\delta F1a \approx 1.5$ mm then the mass limits would consequently be more defined.

8.13.2 Intensity measurements in a proton free background

Resolution of deuterons could be attained by a similar method as that used in the scintillator telescope experiment (Section 3.4.1), which effectively discriminates against the acceptance of protons. Such a spectrometer can easily be constructed to exclude all proton background with the inclusion of a suitable quantity of absorber above counter A, together with, the preservation of the Cerenkov velocity discrimination level such as to satisfy equation 2.2. However, this would also reduce the acceptance of deuterons by $\simeq$ 50 to 4.4 x 10^{-3} day^{-1}.

8.14 Comparison of two techniques for identifying low energy, massive particles

The most important and obvious advantage of the magnetic mass spectrometer (described in Chapters 4 - 8) is in its ability to measure three particle parameters, those of mass, magnitude of charge and sign of charge. However, the magnetic spectrometer is found to be limited in the aperture attainable, $\sim$ 19.45 cm^2 sterad, and thus necessitates long experimental operating times before a statistically significant number of events is accepted. The small aperture, some 43 times smaller than that of the scintillator range telescope, is a consequence of three limiting factors, these being: the length of the spectrometer arm which has to be sufficient to allow measurable time differences; the size of the air gap magnet that is economically viable; the areas of the timing detectors which are limited by the requirement of accurate velocity estimations.

In the preliminary proton experiment (described in Chapters 2 and 3) and in the magnetic mass spectrometer (Chapter 8), identification of deuterons from the observed mass distribution of low energy particles is a problem of extracting likely deuteron events from a proton tail of mass values. Consequently both are subject to extraction errors.

Identification of deuterons by mass determinations from simultaneous momentum and time of flight measurements, is found to be limited by the scattering contributions to the momentum precision and not by the time of flight precision. The method suggested to resolve deuterons from a predominate proton background relies on the initial determination of the expected proton mass distribution, and its subsequent subtraction from the observed mass distribution. The measured deuteron intensities are therefore subject to: the accuracy of the determined proton mass distribution; statistical errors on the accepted number of events; correction factor errors, although these are expected to be comparatively small. Completion of a suitable modification as suggested in Section 8.13, or use of the ideal magnetic spectrometer proposed in Chapter 4, would allow more accurate, mass estimates to be assigned to any low energy, massive particles in the cosmic radiation and would accordingly increase the precision of such particle intensity measurements.

It was concluded in Chapter 2 that a problem of making mass measurements on nuclear active particles with a scintillator range telescope, is the large amount of absorbing material needed to slow particles down for accurate mass estimations. At the same time increasing the amount of absorber:

1. causes the method to break down due to the energy loss through nuclear interactions invalidating the derived theory based on ionisation loss alone, and therefore yields spurious results.
2. increases the minimum velocity needed by particles to traverse the telescope.
3. decreases the accepted particle rates, through interaction losses and therefore increases the error in correcting for such losses.

The ionisation, residual range technique is thus more ideally suited to searching for weakly interacting particles, reliable mass and charge estimates being assigned to such particles.

As the large amount of absorber necessary in the ionisation, residual range technique is not a basic necessity of any magnetic mass spectrometer technique, in principle the beam material can be reduced to a very small amount, thus improving the sensitivity of the spectrometer to the acceptance of nuclear active particles. Mass discrimination against muons is then achieved with a suitable choice of the Cerenkov discrimination level and allows a search for heavy mass particles in a velocity region yet unexplored. However, in practice, with the present spectrometer contributing 1.16 nucleon interaction lengths, while enabling a search for heavy mass particles of velocities ~ 0.8 c. it does not present a great deal of improvement in the interaction losses.

8.15 Conclusion

If long time spans are available, the magnetic mass spectrometer, with its powers of conclusive particle identification, has a valuable future in cosmic ray searches for unknown, heavy mass particles of either strong or weak interaction characteristics. In particular, the magnetic spectrometer has prospects in: not only identifying antiparticles and hence detecting the fundamental antitriplets proposed by Friedländer (1970) to simulate deuterons in the sea level cosmic radiation; but also in detecting quarks of any charge, if they are nuclear active, at lower velocity levels than have previously been reached.

The scintillator range telescope is particularly suited to the detection of weakly interacting particles. The technique lends itself to searches for quarks, of any charge, which have the proposed property of a small inelasticity (Adair and Price, 1966) in nuclear interactions.

CHAPTER 9

SUMMARY

A large aperture, scintillator range telescope has been used to search for low energy, heavy mass particles in the cosmic radiation at sea level, irrespective of their charge. Identification of the stopping particles was deduced from determinations of their mass and charge, by an ionisation, residual range technique. Efficient mass discrimination against muons (and protons if desired) was obtained from a suitable choice of Cerenkov velocity discrimination level in conjunction with the minimum amount of telescope material traversed by the particles.

The result of the heavy mass search, while not detecting any quark events of either fractional or integral charge, set an upper quark intensity limit of 4.9×10^{-10} cm^{-2}sec^{-1}sterad^{-1}, at a 90% confidence level, for the velocity bands shown in Figure 3.11. Thus, for a singly charged particle, mass values > 1.3 GeV/c^2, $\beta \leqslant 0.8$, were accepted. If account is taken of the quark inelastic interactions in the telescope, from the assumption that the quark-nucleon cross section is the same as the nucleon-nucleon cross section and that all interacting quarks are lost, then the upper quark limit is raised by a factor of ~ 17.

The heavy mass search was also sensitive to the detection of low energy U particles, proposed by Callan and Glashow (1968) in order to explain the observations of Bergeson et al. (1967) on the angular distribution of cosmic rays underground. As no such particles were detected, an upper limit was placed on the U particle intensity, at a 90% confidence level, of $\sim 10^{-7}$ of the proton flux, in the mass range 2 - 50 GeV/c^2. This limit is considered either insufficient to explain the observations of Bergeson et al. or to be indicative of a discontinuous spectrum of U particles.

The low energy deuteron flux observed in the heavy mass search, $(4.2^{+3.0}_{-2.4})\ 10^{-9}\mathrm{cm}^{-2}\mathrm{sec}^{-1}\mathrm{sterad}^{-1}(\mathrm{MeV/c})^{-1}$ at 1.65 GeV/c and $(4.8^{+6.8}_{-3.3})10^{-10}$ $\mathrm{cm}^{-2}\mathrm{sec}^{-1}\mathrm{sterad}^{-1}(\mathrm{MeV/c})^{-1}$ at 2.45 GeV/c, is in agreement with the deuteron intensity measurement of Badalian (1959). Further, the fall off in the observed spectrum is consistent with that expected for deuteron production via 'pick up' processes.

Friedländer (1970) has recently suggested that the deuterons observed in the heavy mass search might well be the stable members of the fundamental triplet or antitriplet as was thought to be observed by Dardo et al. (1969). A magnetic mass spectrometer incorporating momentum, ionisation loss and time of flight, measurements for conclusive particle identification was thus constructed. The improvements of this technique lie in its capability to detect mass, charge and sign of charge and therefore in its resolution of antiparticles. However, the precision of particle mass determinations is found to be limited by the scattering contribution to the momentum precision, but not by the time of flight precision. Suitable modifications are suggested to reduce this scattering contribution, so enabling reliable mass estimates to be assigned to any accepted particles.

Using the time of flight technique involving two 5 cm thick, $1\mathrm{m}^2$ area plastic scintillators separated by 530.4 cm and each viewed edgewise on by single Mullard 56 AVP photomultipliers, the distribution in time of flight values, of a relativistic particle travelling between them, has a full width at half height of 2.0 ns. This result is comparatively better than 3.2 ns obtained by Stefanski et al. (1967) for an isochronous counter of a similar area.

Analysis of the time of flight distribution obtained for relativistic particles set an upper limit of $2.2 \times 10^{-5}\,\mathrm{cm}^{-2}\,\mathrm{sec}^{-1}\,\mathrm{sterad}^{-1}$ on the tachyon flux with velocities > 1.6c, in the cosmic rays at sea level. This limit refers to tachyons able to penetrate the spectrometer and deposit > 1.8 MeV in each scintillator. Furthering the time of flight measurements, to ascertain the exact cause of the high velocity tail observed in the time of flight distribution of relativistic muons, is considered worthwhile, in that these tail events present an interesting but, as yet, unsolved problem.

The large aperture, scintillator range telescope is concluded to be more suited to searching for weakly interacting, heavy mass particles in the low energy cosmic radiation. In particular, the scintillator range telescope has future prospects in searching for low energy quarks ($\beta \lesssim 0.8$), irrespective of their charge, which have the property, suggested by Adair and Price (1966), of a small inelasticity in nuclear interactions.

If long time spans are available, the magnetic mass spectrometer, with its powers of conclusive particle identification, has a valuable future in cosmic ray searches for unknown, heavy mass particles, irrespective of their charge or interaction characteristics. In particular, the magnetic spectrometer has worthwhile prospects in: identifying antiparticles and hence the fundamental anti-triplets proposed by Friedländer (1970) to simulate sea level deuterons; detecting quarks of any charge, if they are nuclear active, over lower velocity ranges than have previously been covered.

ACKNOWLEDGEMENTS

The author wishes to thank Professor G. D. Rochester, F.R.S., for the provision of the equipment and laboratory facilities and for his support in this work.

She would also like to acknowledge the help and invaluable guidance from her supervisor Dr. F. Ashton, and also Professor A. W. Wolfendale for his interest and support throughout the work.

Members of the Cosmic Ray Research Group are thanked for helpful discussion and especially Dr. G. N. Kelly and Dr. N. I. Smith are thanked for their friendly assistance.

The technical staff of the Physics Department are thanked for their willing help, in particular Mr. G. Young for his assistance with the difficult construction of the magnetic spectrometer, Mr. W. Leslie, Mr. M. Lee, and in the construction of the scintillator range telescope, Mr. K. Tindale and Mr. J. Webster. The author is especially grateful to Miss P. Wallace for completing the more tedious work so conscientiously and with such willingness.

The Durham Computer Unit is thanked for the provision of the facilities and freely given advice.

The author is grateful to Mrs. J. Moore for her patient and capable work in typing this thesis.

Finally, the Science Research Council is thanked for the provision of a Research Studentship, and the National Institute for Research into Nuclear Science (Rutherford Laboratory) is thanked for providing much of the electronic equipment.

REFERENCES

Adair, R.K., and Price, N.J., (1966), Phys. Rev., 142, 844.

Alväger, T., and Kreisler, M.N., (1968), Phys. Rev., 171, 1357.

Ashton, F., (1965), Proc. Int. Conf. Cosmic Rays, (London), p.1108.

Ashton, F., Coates, R.B., and Simpson, D.A.. (1965a), Proc. Int. Conf. Cosmic Rays, (London), 2, 1079.

Ashton, F., Coates, R.B., Kelly, G.N., Simpson, D.A., Smith, N.I., and Takahashi, T., (1968), J. Phys. A., 1, 569.

Ashton, F., Edwards, H.J., Kelly, G.N., Wolfendale, A.W., (1968a), Phys. Rev. Letts., 21, 303.

Ashton, F., Edwards, H.J., Kelly, G.N., (1969a), Proc. Int. Conf. on Cosmic Rays, (Budapest), (in the press).

Ashton, F., Edwards, H.J., Kelly, G.N., (1969b), CERN Neutrino Meeting, CERN 69, 28, 141.

Ashton, F., Edwards, H.J., Kelly, G.N., (1969c), Proc. Int. Conf. on Cosmic Rays, (Budapest), (in the press).

Ashton, F., Edwards, H.J., Kelly, G.N., (1969d), Phys. Lett., 29B, 249.

Ashton, F., Kelly, G.N., (1969), Proc. Int. Conf. on Cosmic Rays, (Budapest), (in the press).

Baccalini, C., Bassi, P., and Manduchi, C., (1955), Nuovo Cimento, 1, 657.

Bacry, H., Nuyts, J., and Van Hove, L., (1964), Phys. Lett., 9, 279.

Badalian, G.V., (1959), Sov. Phys., J.E.T.P., 8, 209.

Ballam, J., and Lichtenstein, P.J., (1954), Phys. Rev., 93, 851.

Bergeson, H.E., Keuffel, J.W., Larson, M.O., Martin, E.R., and Mason, G.W., (1967), Phys. Rev. Letts., 19, 1487.

Bilanuik, O.M.P., Deshparde, V.K., and Sudarshan, E.C.G., (1962), Am. J. Phys., 30, 718.

Brooke, G., (1964), Ph.D. Thesis (Durham), unpublished.

Brooke, G., and Wolfendale, A.W., (1964), Proc. Phys. Soc., 83, 843.

Callan, C.G., and Glashow, S.L., (1968), Phys. Rev. Letts., 20, 779.

Chen, F.F., Leavitt, C.P., and Shapiro, A.M., (1955), Phys. Rev., 99, 857.

Chilton, F., Horn, D., and Jabbur, R.J., (1966), Phys. Lett., 22, 91.

Chu, W.T., Kim, Y.S., Beam, W.J., Kwak, N., (1970), Phys. Rev. Letts., 24, 917.

Cocconi, G., (1965), Proc. Int. Conf. Cosmic Rays (London), p.616.

Coxell, H., and Wolfendale, A.W., (1960), Proc. Phys. Soc., 75, 378.

Dardo, M., Penenge, P., and Sitte, K., (1968), Nuovo Cimento, 58A, 59.

Davis, M.B., Kreisler, M.N., Alväger, T., (1969), Phys. Rev., 183, 1132.

Einstein, A., (1905), Ann. Physik., 17, 891.

Feinberg, G., (1967), Phys. Rev., 159, 1089.

Feinberg, G., (1970), Sci. Am., 222, 68.

Friedländer, E.M., (1970), Nuovo Cimento, 111, 71.

Gell-Mann, M., (1962), Phys. Rev., 125, 1067.

Gell-Mann, M., (1964), Phys. Letts., 8, 214.

Goldwasser, E.L., and Merkle, T.C., (1951), Phys. Rev., 83, 43.

Gursey, F., Lee, T.D., and Nauenberg, M., (1964), Phys. Rev. Letts., 135, B467.

Hagedorn R., (1967), CERN Report, TH 751.

Hayman, P.J., and Wolfendale, A.W., (1962), Proc. Phys. Soc., 80, 710.

Kasha, H., and Stefanski, R.J., (1968), Phys. Rev., 172, 1297.

Kelly, G. N., (1969), Ph.D. Thesis, (Durham), unpublished

Kisdnasamy, (1958), Ph.D. Thesis, (Durham), unpublished.

Kokkedee, J.J.J., (1969), 'The Quark Model', Published by Benjamin.

Landau, L.D., Belen'kji, S.Z., (1956), Nuovo Cimento Suppl., 3, 15.

Longo, M.J., (1968), CERN Report 68-7, Topical Conference on High Energy Collisions of Hadrons, p.523.

Marshall, J., Marshall, L., and Nedzel, V.A., (1953), Phys. Rev., 93, 767.

Maksimenko, V.M., Sisakyan, I.N., Feinberg, E.L., and Chernavskii, D.S., (1966), Zh. Eksper. Teor. Fiz. Pis'ma., 3, 219.

McCusker, C.B.A., and Cairns, I., (1969), Phys. Rev. Letts., 23, 658.

McDiarmid, I.B., (1959), Canad, J. Phys., 37, 79.

Morpurgo, G., (1967), Acta Physica Academiae Scientianum Hungarieae, 22, 105.

Morpurgo, G., (1968), 14th Int. Conf. on High Energy Physics, (CERN), p.225.

Morpurgo, G., (1968), 'The Quark Model - Results and Problems' (published by Academic Press Inc., New York).

Mylori, M.G., and Wilson, J.G., (1951), Proc. Phys. Soc., A64, 404.

Nedzel, V.A., (1954), Phys. Rev., 94, 174.

Neeman, Y., (1961), Nucl. Phys., 26, 222.

Peters, B., (1965), Proc. Int. Conf. Cosmic Rays (London), p.922.

Rossi, B., (1952), High Energy Particles, (Prentice Hall).

Sakata, S., (1956), Prog. Theor. Phys., Osaka, 16, 686.

Schopper, E., (1967), Handbuch der Physik, 46/2, 414.

Serre, C., (1967), CERN Report 67-5.

Simpson, D.A., (1967), Ph.D. Thesis, (Durham), unpublished.

Sommerfeld, A., (1904), Koninkl. Ned. Akad. Wetenshap. Proc. 8, 346.

Stefanski, R.J., Adair, R.K., Kasha, H., and Larson, R.C., (1967), Rev. Sci. Instr., 38, 1792.

Sternheimer, R.M., (1953), Phys. Rev., 91, 256.

Sternheimer, R.M., (1956), Phys. Rev., 103, 511.

Symon, K.R., (1948), Ph.D. Thesis (Harvard), unpublished.

Taylor, F.E., (1961), Ph.D. Thesis (Durham), unpublished.

York, C.M., (1952), Proc. Phys. Soc., A65, 559.

Zweig, G., (1964), CERN Reports 8182/Th 401 and 841/Th 412.

```
QQ=     10.000   X=      0.350  0.6922Q+00  0.6745Q+00  0.5701Q+00  0.5465Q+00  0.5886Q+00  0.6197Q+00
QQ=     10.000   X=      0.350  0.6072Q+00  0.5802Q+00  0.5759Q+00  0.5937Q+00  0.6061Q+00  0.5986Q+00
QQ=     10.000   X=      0.350  0.5848Q+00  0.5836Q+00  0.5942Q+00  0.6009Q+00  0.5957Q+00  0.5871Q+00

QQ=     10.000   X=      0.400  0.6222Q+00  0.5588Q+00  0.4649Q+00  0.4761Q+00  0.5245Q+00  0.5301Q+00
QQ=     10.000   X=      0.400  0.5010Q+00  0.4887Q+00  0.5054Q+00  0.5199Q+00  0.5120Q+00  0.4981Q+00
QQ=     10.000   X=      0.400  0.4996Q+00  0.5113Q+00  0.5143Q+00  0.5055Q+00  0.4999Q+00  0.5053Q+00

QQ=     10.000   X=      0.450  0.5391Q+00  0.4430Q+00  0.3741Q+00  0.4118Q+00  0.4477Q+00  0.4287Q+00
QQ=     10.000   X=      0.450  0.4040Q+00  0.4138Q+00  0.4327Q+00  0.4282Q+00  0.4131Q+00  0.4143Q+00
QQ=     10.000   X=      0.450  0.4264Q+00  0.4275Q+00  0.4177Q+00  0.4152Q+00  0.4229Q+00  0.4264Q+00

QQ=     10.000   X=      0.500  0.4501Q+00  0.3354Q+00  0.2985Q+00  0.3490Q+00  0.3615Q+00  0.3311Q+00
QQ=     10.000   X=      0.500  0.3250Q+00  0.3460Q+00  0.3495Q+00  0.3339Q+00  0.3317Q+00  0.3439Q+00
QQ=     10.000   X=      0.500  0.3454Q+00  0.3355Q+00  0.3344Q+00  0.3426Q+00  0.3435Q+00  0.3365Q+00

QQ=     10.000   X=      0.550  0.3609Q+00  0.2414Q+00  0.2367Q+00  0.2850Q+00  0.2741Q+00  0.2485Q+00
QQ=     10.000   X=      0.550  0.2614Q+00  0.2759Q+00  0.2637Q+00  0.2555Q+00  0.2665Q+00  0.2706Q+00
QQ=     10.000   X=      0.550  0.2611Q+00  0.2596Q+00  0.2677Q+00  0.2673Q+00  0.2606Q+00  0.2623Q+00

QQ=     10.000   X=      0.600  0.2765Q+00  0.1638Q+00  0.1856Q+00  0.2203Q+00  0.1944Q+00  0.1846Q+00
QQ=     10.000   X=      0.600  0.2049Q+00  0.2037Q+00  0.1898Q+00  0.1960Q+00  0.2042Q+00  0.1962Q+00
QQ=     10.000   X=      0.600  0.1928Q+00  0.2006Q+00  0.2004Q+00  0.1940Q+00  0.1966Q+00  0.2010Q+00

QQ=     10.000   X=      0.650  0.2007Q+00  0.1036Q+00  0.1424Q+00  0.1578Q+00  0.1295Q+00  0.1366Q+00
QQ=     10.000   X=      0.650  0.1504Q+00  0.1378Q+00  0.1351Q+00  0.1459Q+00  0.1419Q+00  0.1357Q+00
QQ=     10.000   X=      0.650  0.1424Q+00  0.1436Q+00  0.1375Q+00  0.1400Q+00  0.1437Q+00  0.1395Q+00

QQ=     10.000   X=      0.700  0.1361Q+00  0.5984Q-01  0.1049Q+00  0.1019Q+00  0.8211Q-01  0.9832Q-01
QQ=     10.000   X=      0.700  0.9871Q-01  0.8741Q-01  0.9553Q-01  0.9789Q-01  0.8997Q-01  0.9401Q-01
QQ=     10.000   X=      0.700  0.9728Q-01  0.9158Q-01  0.9317Q-01  0.9671Q-01  0.9270Q-01  0.9273Q-01

QQ=     10.000   X=      0.750  0.8439Q-01  0.3066Q-01  0.7216Q-01  0.5680Q-01  0.5077Q-01  0.6513Q-01
QQ=     10.000   X=      0.750  0.5576Q-01  0.5447Q-01  0.6230Q-01  0.5610Q-01  0.5588Q-01  0.6091Q-01
QQ=     10.000   X=      0.750  0.5641Q-01  0.5652Q-01  0.6011Q-01  0.5667Q-01  0.5689Q-01  0.5960Q-01

QQ=     10.000   X=      0.800  0.4609Q-01  0.1322Q-01  0.4435Q-01  0.2535Q-01  0.3092Q-01  0.3613Q-01
QQ=     10.000   X=      0.800  0.2693Q-01  0.3328Q-01  0.3285Q-01  0.2863Q-01  0.3361Q-01  0.3142Q-01
QQ=     10.000   X=      0.800  0.2990Q-01  0.3335Q-01  0.3074Q-01  0.3080Q-01  0.3293Q-01  0.3048Q-01

QQ=     10.000   X=      0.850  0.2066Q-01  0.4347Q-02  0.2257Q-01  0.7630Q-02  0.1753Q-01  0.1417Q-01
QQ=     10.000   X=      0.850  0.1215Q-01  0.1695Q-01  0.1228Q-01  0.1464Q-01  0.1516Q-01  0.1266Q-01
QQ=     10.000   X=      0.850  0.1548Q-01  0.1385Q-01  0.1366Q-01  0.1526Q-01  0.1333Q-01  0.1451Q-01

QQ=     10.000   X=      0.900  0.6481Q-02  0.8687Q-03  0.8073Q-02  0.7831Q-03  0.7638Q-02  0.2411Q-02
QQ=     10.000   X=      0.900  0.5563Q-02  0.4647Q-02  0.3735Q-02  0.5726Q-02  0.3509Q-02  0.5196Q-02
QQ=     10.000   X=      0.900  0.4468Q-02  0.4179Q-02  0.5205Q-02  0.3920Q-02  0.4980Q-02  0.4483Q-02

QQ=     10.000   X=      0.950  0.8551Q-03  0.4928Q-04  0.1216Q-02  -.1758Q-03  0.1464Q-02  -.2595Q-03
QQ=     10.000   X=      0.950  0.1467Q-02  -.1052Q-03  0.1221Q-02  0.2363Q-03  0.8451Q-03  0.6134Q-03
QQ=     10.000   X=      0.950  0.5140Q-03  0.8660Q-03  0.3600Q-03  0.9131Q-03  0.4084Q-03  0.7884Q-03

QQ=     10.000   X=      1.000  0.0         0.0         0.0         0.0         0.0         0.0
QQ=     10.000   X=      1.000  0.0         0.0         0.0         0.0         0.0         0.0
QQ=     10.000   X=      1.000  0.0         0.0         0.0         0.0         0.0         0.0

**********************************************************************************************

££££££££££££££££££££££  LAMBDA=     0.550  GEV  ££££££££££££££££££££££££££££££
 ££££££££££££££££££££££££££££££  (1-X)**A, A=  0   X**B. B=  0   ££££££££££££££££££££££££££££££
    1    PHI=  0.3064Q+00
    2    PHI= -0.2940Q+00
    3    PHI=  0.3632Q-01
    4    PHI=  0.6054Q+00
    5    PHI= -0.1236Q+01
    6    PHI=  0.1883Q+01
    7    PHI= -0.3714Q+01
    8    PHI=  0.8498Q+01
    9    PHI= -0.2111Q+02
   10    PHI=  0.5585Q+02
   11    PHI= -0.1546Q+03
```